


Spring 4-21-2011

# Resorbable Polymer-Hydroxyapatite Composites for Bone Trauma Treatment: Synthesis and Properties

Troy E. Wiegand  
*University of Nebraska-Lincoln, [wiegante@gmail.com](mailto:wiegante@gmail.com)*

Follow this and additional works at: <http://digitalcommons.unl.edu/chemistrydiss>

 Part of the [Inorganic Chemistry Commons](#), [Materials Chemistry Commons](#), and the [Polymer Chemistry Commons](#)

---

Wiegand, Troy E., "Resorbable Polymer-Hydroxyapatite Composites for Bone Trauma Treatment: Synthesis and Properties" (2011).  
*Student Research Projects, Dissertations, and Theses - Chemistry Department*. 20.  
<http://digitalcommons.unl.edu/chemistrydiss/20>

This Article is brought to you for free and open access by the Chemistry, Department of at DigitalCommons@University of Nebraska - Lincoln. It has been accepted for inclusion in Student Research Projects, Dissertations, and Theses - Chemistry Department by an authorized administrator of DigitalCommons@University of Nebraska - Lincoln.

Resorbable Polymer-Hydroxyapatite  
Composites for Bone Trauma  
Treatment: Synthesis and Properties

By

Troy Edward Wiegand

A Dissertation

Presented to the Faculty of  
The Graduate College at the University of Nebraska  
In Partial Fulfillment of Requirements  
For the Degree of Doctor of Philosophy

Major: Chemistry

Under the Supervision of Professor Jody G. Redepenning

Lincoln, Nebraska

May 2011

Resorbable Polymer-Hydroxyapatite Composites for  
Bone Trauma Treatment: Synthesis and Properties

Troy Edward Wiegand, Ph.D.

University of Nebraska, 2011

Advisor: Jody G. Redepenning

Contemporary therapies for hard tissue replacement involve allografts, where the donor and recipient are of the same species, or the use of xenogenic transplants. Intraspecies materials are often in short supply and interspecies materials are subject to immunological barriers such as disease and tissue rejection. Synthetic composites are unencumbered by these limitations. Poly lactic acid (PLLA) and its copolymers have been used in medicine due to their ability to be resorbed by the body without adverse effects. PLLA's are currently most commonly used in resorbable sutures and gauzes, but there is increasing interest in using them in conjunction with hydroxyapatite (HA) as bioceramics for hard tissue replacement. Early attempts to create a viable PLLA/HA involved dispersing HA particles in a PLLA matrix. There are well defined phase transitions in these types of mixtures. These transitions readily become material failures when placed under stresses or strains. Fortunately the surface hydroxyls on HA can serve as an effective initiator for the ring-opening-polymerization of lactide and other lactones of biological interest. I have shown that bioceramics made in this manner produce materials with superior interfacial strength and that mammalian sources of HA can be used to prepare biomimetic materials that further enhance the physical properties of the resulting composites. I have examined the kinetics of the ring-opening polymerization

reaction of L-lactide using bovine derived HA under various conditions and found that the sintering temperature and sintering time of the HA plays a major role. Experiments designed to elucidate the influence of these parameters on reaction rate reveal that two competing processes determine the polymerization rates. Firstly, specific surface area decreases with sintering time, and since the polymerization is initiated by surface nucleophiles, decreased surface areas give slower polymerization rates. Secondly, thermal decomposition of carbonate to oxide or hydroxide generates nucleophiles in the HA during sintering, resulting in increased heterogeneous rate constants. I have also performed preliminary tests to examine the basic physical properties that these composites possess.

Dedication

It seems only appropriate to dedicate this to my wife, Andra. Without whose love and support I would never have had the determination and fortitude to complete this.

With love, your husband

A handwritten signature in cursive script that reads "Troy". The letters are fluid and connected, with a prominent loop on the 'y'.

Troy

## Figures, Tables, and Equations

| <u>Title</u>  | <u>Page</u> |
|---------------|-------------|
| Figure 1.1    | 10          |
| Equation 2.1  | 43          |
| Figure 2.1    | 44          |
| Equation 2.2  | 45          |
| Equation 2.3  | 45          |
| Equation 2.4  | 45          |
| Equation 2.5  | 46          |
| Equation 2.6  | 46          |
| Figure 2.2    | 51          |
| Figure 2.3    | 53          |
| Figure 2.4    | 55          |
| Figure 2.5    | 56          |
| Equation 2.7  | 57          |
| Equation 2.8  | 57          |
| Equation 2.9  | 58          |
| Equation 2.10 | 58          |
| Equation 2.11 | 58          |
| Equation 2.12 | 58          |
| Equation 2.13 | 58          |
| Equation 2.14 | 59          |
| Figure 2.6    | 60          |
| Figure 2.7    | 61          |

| <u>Title</u>  | <u>Page</u> |
|---------------|-------------|
| Figure 2.8    | 63          |
| Figure 2.9    | 64          |
| Equation 2.15 | 65          |
| Figure 2.10   | 67          |
| Table 2.1     | 68          |
| Figure 2.11   | 69          |
| Figure 2.12   | 70          |
| Figure 2.13   | 71          |
| Equation 2.16 | 72          |
| Figure 2.14   | 73          |
| Figure 2.15   | 74          |
| Figure 2.16   | 76          |
| Table 2.2     | 77          |
| Figure 2.17   | 78          |
| Figure 2.18   | 79          |
| Figure 2.19   | 81          |
| Figure 2.20   | 82          |
| Figure 2.21   | 83          |
| Figure 2.22   | 86          |
| Figure 2.23   | 87          |
| Table 2.3     | 88          |
| Table 2.4     | 88          |
| Equation 2.17 | 90          |
| Equation 2.18 | 90          |

| <u>Title</u>  | <u>Page</u> |
|---------------|-------------|
| Figure 2.24   | 91          |
| Equation 2.20 | 93          |
| Equation 2.21 | 94          |
| Equation 2.22 | 94          |
| Figure 2.25   | 96          |
| Figure 2.26   | 97          |
| Figure 2.27   | 98          |
| Figure 2.28   | 100         |
| Figure 3.1    | 115         |
| Figure 3.2    | 116         |
| Table 3.1     | 117         |
| Equation 3.1  | 118         |
| Equation 3.2  | 118         |
| Equation 3.3  | 118         |
| Equation 3.4  | 119         |
| Equation 3.5  | 119         |
| Equation 3.6  | 119         |
| Equation 3.7  | 120         |
| Equation 3.8  | 120         |
| Equation 3.9  | 121         |
| Equation 3.10 | 121         |
| Equation 3.11 | 121         |
| Equation 3.12 | 121         |
| Figure 3.3    | 124         |



| <u>Title</u> | <u>Page</u> |
|--------------|-------------|
| Figure 3.4   | 126         |
| Table 3.2    | 127         |
| Figure 3.5   | 128         |
| Figure 3.6   | 130         |
| Figure 3.7   | 131         |
| Figure 3.8   | 132         |
| Table 3.3    | 134         |
| Table 3.4    | 137         |
| Figure 3.9   | 139         |
| Figure 3.10  | 140         |
| Figure 3.11  | 141         |
| Figure 4.1   | 149         |
| Figure 4.2   | 150         |
| Figure 4.3   | 152         |
| Table 4.1    | 153         |
| Equation 4.1 | 154         |
| Figure 4.4   | 155         |
| Equation 4.2 | 156         |
| Equation 4.3 | 157         |
| Figure 4.5   | 158         |
| Table 4.2    | 159         |
| Figure 4.6   | 160         |
| Figure 4.7   | 162         |
| Figure 4.8   | 163         |

| <u>Title</u> | <u>Page</u> |
|--------------|-------------|
| Table 4.3    | 166         |
| Table 4.4    | 167         |
| Figure 5.1   | 175         |
| Equation 5.1 | 177         |
| Figure 5.2   | 178         |
| Figure 5.3   | 179         |
| Figure 5.4   | 180         |
| Table 5.1    | 181         |
| Figure 5.5   | 182         |
| Table 5.2    | 183         |
| Figure 5.6   | 185         |
| Figure 5.7   | 187         |
| Figure 5.8   | 188         |
| Table 5.3    | 189         |
| Figure 5.9   | 191         |
| Figure 5.10  | 192         |
| Figure 5.11  | 194         |
| Figure 5.12  | 195         |
| Figure 5.13  | 196         |
| Figure 5.14  | 197         |
| Figure 5.15  | 198         |
| Figure 5.16  | 200         |
| Figure 5.17  | 202         |
| Table 5.4    | 203         |

| <u>Title</u> | <u>Page</u> |
|--------------|-------------|
| Equation 5.2 | 204         |
| Equation 5.3 | 204         |
| Equation 5.4 | 204         |
| Figure 5.18  | 205         |
| Table 5.5    | 206         |
| Table 5.6    | 207         |
| Equation 5.5 | 208         |
| Equation 5.6 | 208         |
| Figure 5.19  | 209         |
| Figure 5.20  | 210         |
| Equation 5.7 | 211         |
| Equation 5.8 | 211         |
| Figure 5.21  | 212         |
| Figure 6.1   | 218         |
| Equation 6.1 | 219         |
| Equation 6.2 | 219         |
| Equation 6.3 | 220         |
| Equation 6.4 | 220         |
| Figure 6.2   | 221         |
| Figure 6.3   | 222         |
| Equation 6.5 | 223         |
| Equation 6.6 | 223         |
| Equation 6.7 | 223         |
| Equation 6.8 | 224         |

| <u>Title</u>  | <u>Page</u> |
|---------------|-------------|
| Equation 6.9  | 225         |
| Equation 6.10 | 225         |
| Figure 6.4    | 226         |
| Figure 6.5    | 230         |
| Figure 6.6    | 232         |
| Figure 6.7    | 233         |
| Figure 6.8    | 234         |
| Table 6.1     | 235         |
| Table 6.2     | 237         |
| Table 6.3     | 238         |
| Table 6.4     | 239         |
| Equation 6.11 | 240         |
| Table 6.5     | 241         |
| Figure 6.9    | 242         |
| Figure 6.10   | 244         |
| Figure 7.1    | 251         |
| Figure 7.2    | 252         |
| Figure 7.3    | 255         |
| Figure 7.4    | 256         |
| Figure 7.5    | 257         |
| Figure 7.6    | 258         |
| Figure 7.7    | 259         |
| Figure 7.8    | 260         |
| Figure 7.9    | 261         |

| <u>Title</u> | <u>Page</u> |
|--------------|-------------|
| Figure 7.10  | 262         |
| Figure 7.11  | 263         |
| Figure 7.12  | 264         |

## Table of Contents

| <u>Chapter</u> | <u>Title</u>   | <u>Page</u> |
|----------------|--|-------------|
| 1              | Introduction.....  | 1           |
| 2              | Kinetic Analysis of Common Biocompatible Monomers and Polymers with Ring Opening Polymerization Initiated by Bovine Hydroxyapatite Sintered at Various Temperatures for Sixteen Hours..... | 43          |
| 3              | Macroscopic and Microscopic Morphologic Changes to Biologically Derived Hydroxyapatite.....  | 113         |
| 4              | Kinetic Analysis of Common Biocompatible Monomers and Polymers with Ring Opening Polymerization Initiated by Bovine Hydroxyapatite Sintered at Constant Temperature for Various Times..... | 145         |
| 5              | Optimization of Sintering Time and Temperature for Biocomposite Preparation and Evaluation of Alternative Ceramics and Polymers.....   | 170         |
| 6              | Physical Properties of Composite Devices Created from a Bioresorbable Polymer and Bovine Derived Hydroxyapatite...   | 217         |
| 7              | Preliminary Biologic Compatibility Studies and Early Proof of Concept Prototype Devices.....   | 248         |

## Chapter One

### Introduction

Since the commencement of Operation Iraqi Freedom (OIF) and Operation Enduring Freedom (OEF) more than 181,000 soldiers, sailors, marines, and airmen have been deployed to active combat theaters. Of these, 34,300 have sustained a battlefield injury.<sup>1</sup> The most frequent types of injuries are wounds caused by improvised explosive devices (IEDs) to the musculoskeletal system, which account for 70% of the total injuries. Of these musculoskeletal injuries, 55% are extremity wounds to the head, arms, and are classified as traumatic.

Traumatic bone injuries that lead to segmental bone defects are defined as injuries where the gap of the fracture is too large for the normal osteoclast and osteoblast mechanism to rejoin the two segments. This leaves a permanent gap in the bone that requires some secondary process to rectify.<sup>2-4</sup> Throughout the history of orthopaedic medicine, different therapies have been used and modified as the technology has improved. The first and most Draconian treatment for traumatic injuries is amputation of the affected limb. Amputations were performed in Egypt and Babylon as early as 2250 B.C. as documented in the *Code of Hammurabi*.<sup>5,6</sup> While amputation can be used in the most severe cases, it is often avoided unless the patient's life is in mortal risk or the limb will become gangrenous. There are also psychological traumas that are inherent in amputation which are best avoided if possible.

The most common contemporary treatment for bone trauma involves fixation. This requires the immobilization of the bone so that the fracture can heal.<sup>7</sup> The simplest

fractures involve the use of splints or a cast.<sup>8</sup> This method is adequate for clean fractures of large bones but has little application for other wounds. For more complex or multiple fractures fixation is still a viable option but a more sophisticated setup is required.<sup>9</sup> Techniques for multiple fractures usually involve directly affixing titanium screws to the bone fragments and then immobilizing the fragments by attaching the screws to a rigid external metal cage.<sup>10</sup> An advantage of the external apparatus is that it can be removed without an additional surgery. Internal bone fixation is also an option for multiple fractures and compound fractures. Internal fixation relies on the use of permanent metal pins or screws to affix the bone fragments to a metal rod placed in the medullary canal. Healed bone that is internally fixed is never as strong as the preinjury bone.<sup>11</sup> This is mainly due to the differences in flexural properties of the supporting rod and bone. Additionally, while the fixation pins or screws do not initiate any negative immunological responses, they are never integrated into the bone but instead remain as discrete bodies in the bone matrix with well-defined phase boundaries. These phase boundaries serve as propagation sites for future fractures due mainly to the differing elastic modulus of the two materials.<sup>12, 13</sup>

In an attempt to create a material that better mimics human bone, surgeons turned to xenografts, which are sections of bone from a different species than the recipient. The first documented case of a xenogenic bone transplant was in 1668 by the Dutch surgeon Job Janszoon.<sup>14</sup> This transplant was performed on a Russian aristocrat who had sustained a severe head wound from a sword. The injury was treated by using a piece of skull from a dog to repair the defect. The patient recovered completely. However, the use of canine bone was deemed unacceptable by the Catholic Church at the time and the nobleman was



excommunicated. The surgeon was asked to remove the offending bone segment, but it was found to have completely incorporated itself in to the skull and could not be removed. Eventually the patient had to flee Russia to avoid persecution from the church.

In the past two centuries several different sources have been tried with varying level of success. Initial attempts at developing a commercial xenograft material revolved around bovine bone. The first commercially available product was Boplant® from Squibb. It was composed of freeze-dried bovine bone and was available as a powder or compacted block. It was believed that the freeze-drying process would eliminate any antigenicity and greatly reduce any immunological response. However this was not the case. After three to four days, once the remaining proteins and fats in the implant were rehydrated, undesirable inflammation was often apparent. In some cases instead of the body incorporating the implant, it was directly attacked by macrophages or encased in fibrous tissue.<sup>15-18</sup> These materials have since been abandoned.

Contemporary, commercially available material for use as xenogenic transplants is centered on deproteinized bovine bone (DBB). As the name states DBB is derived from bovine sources and the organic portion is removed to avoid the negative immunological effects of previous materials. Currently there are two different modes of organic material removal. The first involves the use of extremely basic solutions such as boiling caustic soda. These products are available under the trade names Bio-Oss®, Lubbock®, and Laddec®. The second method for deproteinization involves sintering the raw bone. Different products are available which have been given different sintering treatments. The temperatures range from 300 °C to 1000 °C for most commercially available

products such as OsteoGraf®, Endobon®, and Cerabone®. The two differing production methods each have their merits and deficiencies. An advantage to the alkaline solution method is that the mineral portion of the bone is largely unchanged and microscopic and macroscopic structures are highly preserved. The disadvantage is that not all of the organic components are removed.<sup>19-21</sup> When using bovine sources as raw materials for products that may be used in implantation environment, it is extremely important to limit any exposure to the prion protein, PrP<sup>Sc</sup> which is responsible for Bovine Spongiform Encephalitis in cows and Creutzfeldt-Jakob disease in humans. The sintering method unequivocally removes all traces of organic material, but at the expense of the chemical composition and structure. At high sintering temperatures carbonate present in the bone is decomposed and the specific surface area is decreased. These two phenomena reduce the speed at which osteogenesis may take place on the surface of the implant.<sup>22, 23</sup> It should also be noted that all DBB implants require some manner of fixation to hold the implant in place. Also DBB implants are not suitable for the repair of load bearing bones due to their extreme brittleness.<sup>24</sup>

An alternative to xenogenic implants is an allograft. In this case the donor and the recipient are of the same species. Initial work on allografts began in the 1960s with mice, but has gained wide spread use recently for the repair of excised tumors and treatment of severe bone damage.<sup>25-32</sup> Using human allografts does not come without a unique set of considerations.<sup>33</sup> The most common impediment to a successful allograft is tissue rejection. For this reason fresh cortical allografts are not suited for tissue transplant. The section to be transplanted must be processed before use. The method recommended by the American Association of Tissue Banks is freezing or freeze drying.<sup>34</sup>

Allograft incorporation into the patient is still a complex process. The initial immunological response to an allograft is hemorrhage and inflammation which serves to kill any remaining donor cells and prepare the surface of the implant for either resorption or incorporation. If the recipients to donor tissue differences are too great the body will treat the allograft as a foreign body and attempt to destroy it or sequester it in fibrous tissue. Either immune response ultimately requires removal of the allograft with additional surgery.<sup>35</sup> After the initial inflammation, successful implants undergo osteoconduction which vascularizes the implant so that osteoprogenitor cells can seed the allograft.<sup>11, 36</sup> Osteoconduction does not require living cells, but is a preparatory step necessary for proper allograft to bone fusion.<sup>11, 37</sup> Once osteoprogenitor cell concentration reaches a critical mass they begin to differentiate into osteoclasts, which dissolve bone, and osteoblasts, which create bone. The next step involves osteoclasts removing the surface of the allograft, just as they do for a DBB implant. After an adequate amount of surface bone has been removed, osteoblasts begin to fuse the allograft to the patient's bone. This process is slow for preserved samples from tissue banks. Recent developments to speed allograft incorporation involve one of two pretreatment routes. The first is to prevascularize the allograft. This is accomplished by mechanically perforating the graft or removing some of the HA from the graft by chemical means. Another step to help speed up incorporation is to preseed the graft with progenitor cells which have been grown from the patient's own bone marrow derived mesenchymal cells.<sup>38-40</sup> In addition to cell seeding, small amounts of bone morphogenetic proteins (BMPs), usually BMP-2, BMP-3, BMP-7, and BMP-9, are added to aid in cell differentiation and multiplication.<sup>33, 41-45</sup> The success rate of allograft

transplants with adjuvant cell seeding and BMP doping has risen to 70% to 75%, ten years after implantation.<sup>46</sup> Even with successful allografts, the implant may remain a mix of newly deposited bone and necrotic tissue for up to 36 months.<sup>47</sup>

Currently, the gold standard for bone repair is the autograft.<sup>5</sup> An autograft is a transplanted portion of bone which is taken from another bone in the patient's body. The three most commonly used sites for donor tissue are the iliac crest for cancellous bone, rib, and tibia for cortical bone. The type of defect and length of defect determine the source of the autograft used. Tibial autografts are preferable for defects greater than 3 cm in load bearing bones.

Cortical bone autografts are neither osteoinductive nor osteogenic in that they do not induce cell differentiation into osteoclasts and osteoblasts nor do they contain sizable populations of progenitor cells or bone forming cells. Such autografts are osteoconductive due to the presence of a limited vascular network.<sup>30, 48</sup> For this reason initial graft incorporation is slow and comparable to that of an allograft, and sometimes lead to substantial bone necrosis within the graft. An alternative is to use vascularized cortical autografts. These are taken from donor sites in the ribs or fibula but closer to the sternum or knee than for a nonvascularized cortical autograft.<sup>49, 50</sup> Grafts with the increased vascularization show accelerated rates of initial incorporation and fewer necrotic osteons.<sup>51</sup> By 24 weeks both types of cortical autograft show similar rates of incorporation with the only difference being the larger amount of necrotic tissue in the nonvascularized autograft. The necrotic tissue is eventually replaced after 24 to 36 months depending on blood flow to the site.<sup>52-56</sup> Several approaches based on cell

seeding work with allografts have been devised to increase the rate of healing and to decrease the amount of necrotic tissue that seems to be inherent with cortical implants. The first cell seeding advance for cortical allografts is to seed the implant with bone marrow-derived osteoblastic and osteoclastic progenitor cells.<sup>57-59</sup> This aids in graft fusion while a vascular network is being evolved or extended into the graft from the surrounding bone. The second is a series of intravenous injections over the first 6 weeks after implantation. The injection is a mixture of platelet derived growth factor (PDGF), autologous growth factor (AGF), and transforming growth factor beta (TGF- $\beta$ ).<sup>60-63</sup>

A cancellous autograft is the implant of choice for large segmental defects that are not in load bearing bones. The increased vascular network speeds bone fusion with no noticeable tissue necrosis. Substantial blood vessel ingrowth and graft resorption is seen after four weeks, and by three months the autograft is completely replaced or remodeled with new bone growth.<sup>51</sup> This has made cancellous autografts the choice for replacement surgeries for the metacarpals in the hand and for anterior lumbar fusions.<sup>64-67</sup>

Autografts have the great advantage of being free from the issues associated with major histocompatibility complex (MHC) tissue typing that leads to tissue rejection, but there are other issues that are difficult to surmount. The first is the extremely limited supply of autogenous material. The amount of graft material that can be removed from one section of the body and transplanted to another is limited. The greatest problem that deters surgeons from using autografts is donor site morbidity. Many studies have reported higher than normal complication rates when using allografts from the iliac crest.<sup>68, 69</sup> Minor complications include mild infections, superficial seromas and minor hematomas.

Major issues arising that can be life threatening are herniation of abdominal contents, deep infections at the donor site, nerve damage, and deep hematoma formation that can lead to stroke.

The limited supplies of allografts and autografts coupled with the potentially severe side effects of the surgeries have led to research into materials that are still osteogenic, have acceptable physical properties, and have limited side effects when placed in the human body. For hard tissue replacement a large body of research has been developed around using synthetic hydroxyapatite (HA).<sup>70, 71</sup> Hydroxyapatite is the major component of the mineral portion of mammalian bone. Little success has been seen in using single component HA implants for repair of structural defects. This is mainly due to the extreme brittleness of HA. Another factor stifling the development of hydroxyapatite implants is the difficulty in making structurally sound stock from which desired shapes can be machined. Current methodologies require taking synthesized HA powder compacts and sintering them at high temperature to increase density. Results from this type of processing yield very dense, very fragile devices, with limited porosity, which make them only suitable for non-load bearing applications such as the middle ear.<sup>72-80</sup> These shortcomings have led the majority of bioceramic research with HA to be focused on applying coatings to existing orthopaedic devices to enhance biocompatibility.<sup>81-87</sup> The most common industrial method for creating HA coated metal implants is based on plasma spraying. This gives an HA coating 50 to 100  $\mu\text{m}$  thick with an adhesive strength of 5 to 65 MPa.<sup>88</sup> HA coated implants show normal bone attachment to the thin coating layer, usually 0.05 to 0.2 mm thick. This ultrathin bonding layer causes an

extreme modulus gradient which can promote fracture, poor incorporation of the implant, or total implant failure under repeated loading.<sup>89</sup>

Another route to useful resorbable implants for hard tissue repair is the use of bioresorbable polymers. Currently, resorbable polymers are most common in sutures, rotator cuff repair, or fixation plates and screws for maxillofacial fractures such as Lactosorb® and RapidFlap®.<sup>90-96</sup> Both of these products are made from injection molded polylactic acid (PLA) or a copolymer of PLA and polyglycolic acid (PGA). These products have excellent flexibility, elasticity, and tensile properties that make them good choices for reconstruction of non-loadbearing, but because they are elastomers they are not suitable for loadbearing bone replacement. Rapidflap® and LactoSorb® show low immunological response rates and are completely absorbed by the body in 18 to 24 months, depending on exact polymer composition and molecular weight.<sup>97-102</sup> Other common resorbable polymers used in similar applications are polydioxanone (PDX or PDO) and polycaprolactone (PCL)(Figure 1.1).

A variety of recent research efforts are focused on combining the best characteristics of both hydroxyapatite and bioresorbable polymers to create a material that can be used for hard tissue replacement in both loadbearing and non-loadbearing applications. The premise revolves around using HA as a filler in a polymer matrix in much the same way that  $\text{CaCO}_3$  is used as a filler for various polyvinylchloride (PVC) applications. In these formulations the inert inorganic powder is dispersed in the polymer. This has the effect of increasing the modulus and tensile strength, while at the same time decreasing

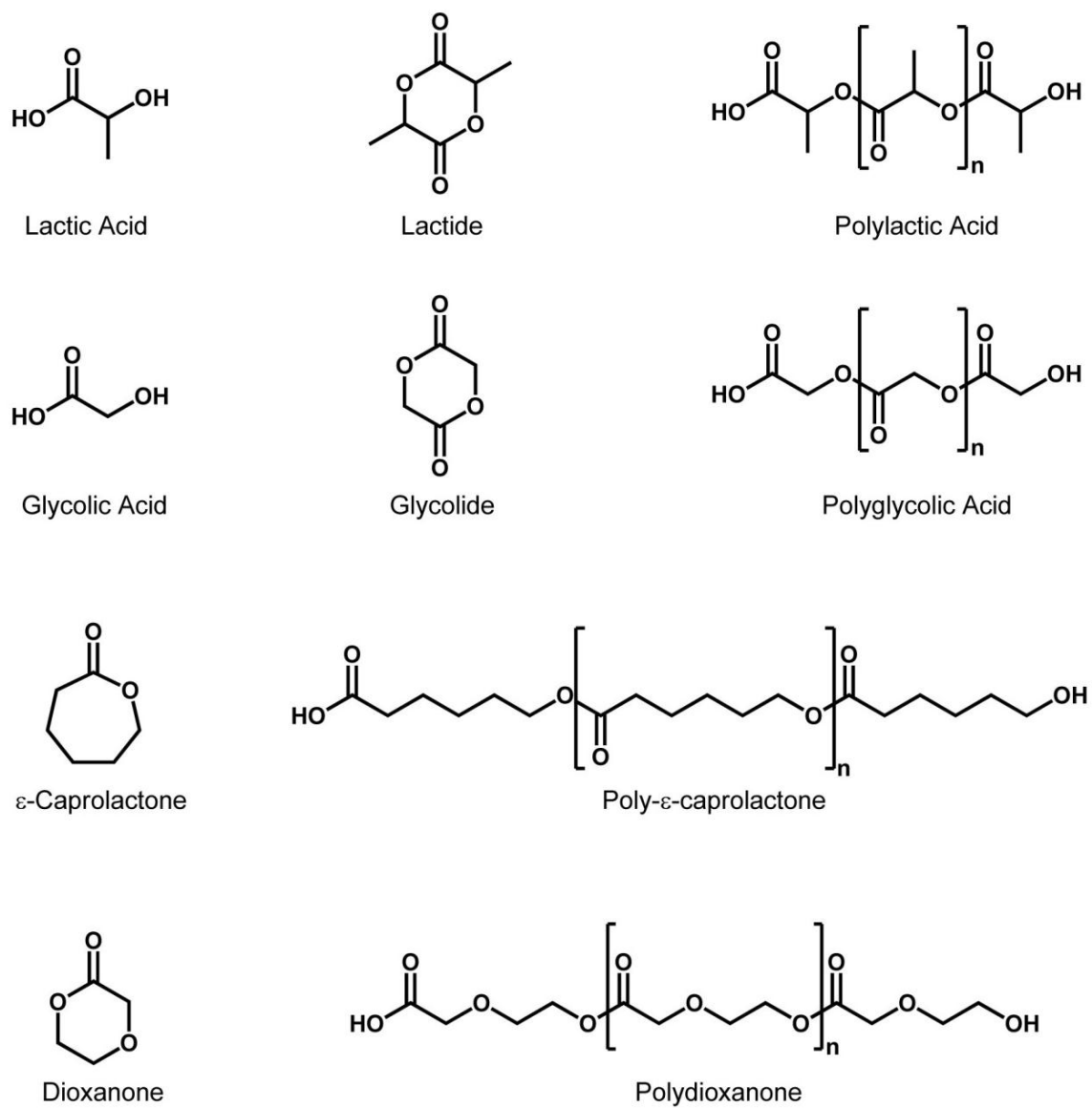


Figure 1.1. Structures of common bioresorbable polymers and their respective monomers



flexibility, elasticity, and toughness. If the filler loading is too high, then tensile strength and elongation will drop off at an exponential rate. This also causes a decrease in the yield stress making the composite more prone to permanent deformations from lower force impacts. Since the filler particles are neither mechanically nor chemically bonded to the polymer, each particle serves as a point of failure and failure propagation. The result is a composite with lowered tensile strength. In order to make a composite of HA and a polymer that contains the same amount of HA as raw bone, the mix needs to be 50% HA and 50% polymer. At this loading the properties of a composite made from powdered HA dispersed in a polymer matrix are only suitable for non-loadbearing applications.<sup>103-108</sup> The most common use of an HA/polymer composite is mixture of polymethylmethacrylate (PMMA) and HA (Cementek®, BiocementD®, and Biopex®), which is used as a bone cement or filler material. These materials are quite brittle and are prone to fatigue failure. Additionally PMMA is not bioresorbable and remains in the body for up to 30 years.

Currently there are no commercially available biocomposites made from HA and a bioresorbable polymer but there have been several studies in animal models reported in the literature.<sup>109-116</sup> To date the studies revolve around taking a relatively high molecular weight PLLA that has been mechanically mixed with various samples of HA. One study in which rods of PLLA/HA composites were constructed and implanted into the medullary canal of rabbit tibias, has reported that, over a period of 7 years, there is bony ingrowth into the implants and that the polymer is gradually absorbed into the body with no late aseptic reactions.<sup>110</sup> It should also be noted that there was no fibrous encapsulation of the implant either. Studies that have been conducted on non-HA filled

PLLA implants report little to no bone ingrowth, fibrous encapsulation of the implant, and substantial localized acidosis from polymer degradation which results in tissue necrosis in some instances.<sup>117-119</sup> Additionally the implant remains for several years and actually inhibits segmental bone defect closure, thus making 100% polymer implants for bone reconstruction impractical.<sup>120</sup>

Improvements have been made in grafting different polymers onto the surface of HA by first treating the HA with a mild solution of lactic acid or other amino acid.<sup>121-124</sup> The respective acids are bonded to the surface of the HA through an acid-base reaction between the carboxylic acid terminus of the acid and the surface hydroxide of the HA. This creates an electrostatic bond between a surface calcium and carboxylate. These surface modifications have been helpful in controlling the particle size of nanoscale HA by inhibiting Ostwald ripening. The distal hydroxyl or amine has also been used to graft longer carboxylic acid terminated polymers and oligomers onto through condensation reactions. These grafting techniques are currently used to primarily control HA crystal size and overall crystallinity in colloidal suspensions and not for bioceramic but do show that surface modification of HA is possible and controllable.

An advance on the theme of polymer grafting to an HA surface is to use the nucleophilic hydroxyls on the surface of HA to initiate the ring opening polymerization of bioresorbable polymers.<sup>125, 126</sup> Traditionally the ring opening polymerization of bioresorbable lactones has been carried out with a tin(II) octoate ( $\text{Sn}(\text{oct})_2$ ) catalyst and an alcohol initiator. Polymerizations of this type proceed via a coordination insertion mechanism and the final polymer has an alcohol and ester end group.<sup>127-132</sup> The ester end

group disables any ability for these polymers to form electrostatic bonds with the surface of the HA. When HA is used as the initiator the mechanism is still a living ring opening polymerization but is anionic instead of coordination insertion. A number of metal oxides, zeolites, and other nucleophiles have been shown to initiate ring opening polymerizations in much same manner as HA.<sup>125, 133-147</sup>

Previous polymerization work with HA has been focused on synthetic HA produced from simple precipitation reactions. There are numerous derivations on the precipitation method that allow for the creation of HA with various crystal sizes and differing degrees of crystallinity.<sup>148-154</sup> These synthetic hydroxyapatites have  $P6_3/m$  space group, and as such form tabular to prismatic crystals.<sup>155-157</sup> This differs from the HA found in mammalian bone in two ways. The first is the chemical composition of biologic HA. Biologic HA has approximately 5 to 8% carbonate substitution for hydroxide or phosphate, as well as common cationic substitutions of magnesium and sodium for calcium.<sup>158-160</sup> Osteoconductivity may also be enhanced by carbonate substitution, but to date there is no definitive research to either support or refute this conclusion. The second is in crystal morphology. Although synthetic HA crystals tend to be tabular to prismatic and very crystalline, biologic HA is poorly crystalline and the crystal morphology is more needle-like than prismatic. This has consequences for the ability of HA to be able to act as a reinforcing material in an organic or polymer matrix. Needle like crystals can enhance the physical properties when used in conjunction with a polymer. This phenomenon is exemplified with fiberglass reinforced polyesters, which have been used in boat hulls, and other structural elements that require high flexibility and strength.<sup>161-169</sup>

Additionally, the lower level of crystallinity in biologic hydroxyapatite reduces brittleness. This helps reduce cracking and failure due to applied stresses and strains.

It can be argued that bioceramic composites are best prepared from biologically sourced HA. Since the mineral component already has the desired crystal morphology, the amount of remodeling that osteoclasts and osteoblasts need to do is greatly decreased. Additionally, the likelihood of enhanced osteoconductivity increases since the chemical makeup of the HA is essentially identical to what is normally found in bone.

Raw mammalian cortical bone is composed of roughly 30% by weight organic material, mainly Type 1 collagen and 70% carbonated hydroxyapatite.<sup>170</sup> It is necessary to remove the organic component without damaging the mineral portion in order to obtain biologic HA that is suitable for bioceramic manufacture. A variety of procedures are reported in the literature, but most are variations on one of two themes. The first involves using highly caustic solutions to dissolve and hydrolyze organic components in the bone.<sup>70, 71, 171-173</sup> The second method involves simply heating the organic components at elevated temperatures in either air or an oxygen enriched atmosphere.<sup>70, 171, 172, 174-176</sup> Each method alone has advantages and disadvantages. The caustic solution methods are gentle toward the mineral component of the bone but do not completely remove all organic matter from the bone. Depending on the source of the bone this can be of grave concern. For bovine sources it is critical to remove all organic matter so that there is no chance of Creutzfeldt-Jakob disease transmission. Heating samples at elevated temperatures does remove all organic material but is much harsher on the sample. It is not uncommon for samples to crack after heating. If the heating temperature is excessive there is also a marked

reduction in surface area, sample dimensional shrinkage, and the carbonate can decompose to carbon dioxide and oxide changing the chemical makeup of the sample.<sup>177-</sup>

181

This thesis describes my efforts to combine a biologically derived HA with resorbable polymers to create a new material that could be used for hard tissue replacement. While there is precedence for using HA and bovine allografts for hard tissue construction there are currently no commercial products that use bovine derived HA in conjunction with a bioresorbable polymer for the same purpose. Bioresorbable polymers have been used for several years as sutures, gauzes, and maxillofacial fixation devices.

The first step in making such a composite would be to derive a reproducible and reliable method for removing all organic matter from the raw bone stock. The ideal method will be gentle enough as to not destroy the macroscopic and microscopic structure of the bone but still remove all organic compounds to eliminate any chances for disease transmission of immunological response. This initial processing involves first the use of an ethylene diamine and water mixture to remove the bulk of the proteins and fats. A heating step is required for complete removal of all biologic compounds, but with the bulk of the organic material removed in the previous step, it is possible to use a much shorter time and lower temperature. In part, this thesis describes my experiments to optimize the exact temperature and time for the sintering step.

There are a number of properties of HA that are affected by temperature. At temperatures above 600 °C carbonate can decompose slowly to oxide and hydroxide. This chemical change has ramifications toward the polymerization reactions. Carbonate

is not nucleophilic, but oxide and hydroxide are both capable of initiating the reaction and as such any increase or decrease in their surface concentrations will affect the rate of reaction and the number of propagation sites for polymer chains.<sup>138, 140, 182, 183</sup> The number of moles of monomer is a fixed quantity because it is determined by the amount that can occupy the void volume in the bone section. Changing the number of initiation sites for the reaction should in theory change the number average molecular weight ( $M_n$ ) of the polymer by altering the number of polymer chains. There are few sources in the literature describing the effects of polymer molecular weight on their resorption properties, but the optimum biologic response is not easily parameterized and is highly dependent on the nature of the specific application. Generally speaking, it is desirable to have a polymer of sufficient molecular weight to impart adequate physical strength to the implant, but still resorb at a rate equivalent to the rate of bony ingrowth and implant incorporation into the surrounding tissue.

For hydroxyapatite, the rate of crystal morphology change increases sharply between 650 °C and 675 °C.<sup>177, 180, 184</sup> Over this temperature range the rate of surface area change, increases by at least an order of magnitude. This is due to increasing the size of individual crystals at the expense of smaller particles. There is also a corresponding density increase in the sample as the particles become more crystalline.<sup>185</sup> A macroscopic manifestation of this is a decrease in the physical dimensions of sections cut from raw bone stock. For powders, shrinkage is not a major concern, but when making a composite device for implantation from sectioned bone it is important to know what the final dimensions will be so that proper sizing can be achieved. The closer the implant is

in size to the defect being repaired, will decrease the amount of remodeling that the body will need to do to the implant and thus decrease healing time.

Once a composite is made from any bioresorbable polymer and HA it is necessary to understand how it will perform for various applications. The idealized composite material will have a modulus, maximum stress at failure, and viscoelastic properties identical to natural wet bone. If the composite is used for maxillofacial reconstruction it will not be subjected to high stresses and strains. However, most segmental bone defects incurred from warfare are in the limbs. Implants in the legs experience mostly compressive and torsional stresses while implants in the arms experience predominantly bending and torsional stresses. Both compression and torsional properties of the composites I have created are quantified and compared to natural wet bovine bone.

In summary, the research presented in this dissertation sets forth a systematic method for the creation of a bioresorbable polymer-ceramic composite material suitable for use in implants for hard tissue replacement. This material can either be fashioned from a powdered bovine derived hydroxyapatite which is more suitable for injection molding of devices such as bone fixation screws or larger pieces of bovine derived bone can be used as the basis of creating implants for segmental bone defects that still contain the morphologic HA structure in mammalian bone. This allows for greater osteoconduction and osteoinduction.

### References

1. Ling, G. S. F.; Rhee, P.; Ecklund, J. M., Surgical Innovations Arising from the Iraq and Afghanistan Wars. *Annu. Rev. Med.* **2010**, 61, 457-468.
2. Egol, K.; Koval, K. J.; Zuckerman, J. D., *Handbook of Fractures*. 4th ed.; Lippincott Williams and Wilkins: 2010; p 816.
3. Ip, D., *Orthopedic Traumatology - A Resident's Guide*. 2nd ed.; Springer: 2008; p 678.
4. Delahay, J. N.; Wiesel, S. W., *Essentials of Orthopedic Surgery*. 3rd ed.; Springer: 2006; p 620.
5. Pietrzak, W. S., *Musculoskeletal Tissue Regeneration: Biological Materials and Methods*. 1st ed.; Humana Press: Totowa, New Jersey, 2008; p 830.
6. Zimmerman, L. M.; Veith, I., *Great Ideas in the History of Surgery*. 1st ed.; Norman Publishing: 1993; p 587.
7. Ellis, E., III, Rigid skeletal fixation of fractures. *Journal of Oral and Maxillofacial Surgery* **1993**, 51, 163-73.
8. Egger, E. L., Instrumentation for external fixation. *The Veterinary Clinics of North America. Small Animal Practice* **1992**, 22, 19-43.
9. Stark, W. J., The Value of External Skeletal Fixation in Elective Orthopedic Surgery. *The Annals of Surgery* **1947**, 125, 372-84.
10. Anzel, S. H., Orthopedics: management of long bone fractures with external fixators. *The Western Journal of Medicine* **1985**, 142, 248.
11. Friedlaender, G. E.; Horowitz, M. C., Immune responses to osteochondral allografts: nature and significance. *Orthopedics* **1992**, 15, 1171-5.



12. Rokkanen, P. U.; Bostman, O.; Hirvensalo, E.; Makela, E. A.; Partio, E. K.; Patiala, H.; Vainionpaa, S.; Vihtonen, K.; Tormala, P., Bioabsorbable fixation in orthopedic surgery and traumatology. *Biomaterials* **2000**, 21, 2607-2613.
13. Sivakumar, M.; Mudali, U. K.; Rajeswari, S., Investigation of failures in stainless steel orthopedic implant devices: fatigue failure due to improper fixation of a compression bone plate. *Journal of Materials Science Letters* **1994**, 13, 142-5.
14. Meekeren, J. H. v., En Geneeskunstige Aanmerkingen. *Commelijn* **1668**.
15. Heiple, K. G.; Kendrick, R. E.; Herndon, C. H.; Chase, S. W., A critical evaluation of processed calf bone. *Journal of Bone and Joint Surgery-American Volume* **1967**, 49, (6), 1119-27.
16. Pieron, A. P.; Bigelow, D.; Hamonic, M., Bone grafting with Boplant. Results in thirty-three cases. *Journal of Bone and Joint Surgery-British Volume* **1968**, 50, (2), 364-8.
17. Elves, M. W.; Salama, R., A study of the development of cytotoxic antibodies produced in recipients of xenografts (heterografts) of iliac bone. *Journal of Bone and Joint Surgery-British Volume* **1974**, 56, (2), 331-9.
18. Cantore, G.; Fortuna, A., Intersomatic fusion with calf bone "Kiel bone splint" in the anterior surgical approach for the treatment of myelopathy in cervical spondylosis. *Acta Neurochirurgica* **1969**, 20, (1), 59-61.
19. Honig, J. F.; Merten, H. A.; Heinemann, D. E., Risk of transmission of agents associated with Creutzfeldt-Jakob disease and bovine spongiform encephalopathy. *Plastic and Reconstructive Surgery* **1999**, 103, (4), 1324-1325.

20. Bundesgesundheitsamt, Bekanntmachung der Sicherheitsanforderungen an Arzneimittel aus KoK rperbestandteilen von Rind, Schaf oder Ziege zur Vemeidung des Risikos einer UG bertragung von BSE bzw. In 1994; Vol. 40, pp 1851-1855.
21. Bundesgesundheitsamt, Bekanntmachung uber die Zulassung und Registrierung von Arzneimitteln. In Bundesanzeiger, Ed. 1996; Vol. 67, pp 4158-4162.
22. Turhani, D.; Cvikl, B.; Watzinger, E.; Weissenbock, M.; Yerit, K.; Thurnher, D.; Lauer, G.; Ewers, R., In vitro growth and differentiation of osteoblast-like cells on hydroxyapatite ceramic granule calcified from red algae. *Journal of Oral and Maxillofacial Surgery* **2005**, 63, (6), 793-799.
23. Turhani, D.; Weissenbock, M.; Watzinger, E.; Yerit, K.; Cvikl, B.; Ewers, R.; Thurnher, D., In vitro study of adherent mandibular osteoblast-like cells on carrier materials. *International Journal of Oral and Maxillofacial Surgery* **2005**, 34, (5), 543-550.
24. Stone, K. R.; Turek, T. J. Xenograft bone matrix for orthopedic applications. US 2002-103613, 2003.
25. Burwell, R. G.; Gowland, G., Lymph node reactivity to homografs of cancellous bone. *Nature* **1960**, 188, 159-60.
26. Burwell, R. G., Studies of the primary and the secondary immune responses of lymph nodes draining homografs of fresh cancellous bone (with particular reference to mechanisms of lymph node reactivity). *Annals of the New York Academy of Sciences* **1962**, 99, 821-60.
27. Burwell, R. G.; Gowland, G., Studies in the transplantation of bone. III. The immune responses of lymph nodes draining components of fresh homologous cancellous

bone treated by different methods. *Journal of Bone and Joint Surgery-British Volume* **1962**, 131-48.

28. Burwell, R. G., Studies in the transplantation of bone. V. The capacity of fresh and treated homografts of bone to evoke transplantation immunity. *Journal of Bone and Joint Surgery-British Volume* **1963**, 45-B, 386-401.

29. Burwell, R. G.; Gowland, G.; Dexter, F., Studies in the Transplantation of Bone. VI Further Observations Concerning the Antigenicity of Homologous Cortical and Cancellous Bone. *Journal of Bone and Joint Surgery-British Volume* **1963**, 45, 597-608.

30. Burwell, R. G., Studies in the Transplantation of Bone. VII. The Fresh Composite Homograft-Autograft of Cancellous Bone; An Analysis of Factors Leading to Osteogenesis in Marrow Transplants and in Marrow-Containing Bone Grafts. *Journal of Bone and Joint Surgery-British Volume* **1964**, 46, 110-40.

31. Burwell, R. G., Osteogenesis in Cancellous Bone Grafts: Considered in Terms of Cellular Changes, Basic Mechanisms and the Perspective of Growth-Control and Its Possible Aberrations. *Clinical Orthopaedics and Related Research* **1965**, 40, 35-47.

32. Burwell, R. G., Studies in the transplantation of bone. 8. Treated composite homograft-autografts of cancellous bone: an analysis of inductive mechanisms in bone transplantation. *Journal of Bone and Joint Surgery-British Volume* **1966**, 48, 532-66.

33. Mankin, H. J.; Friedlaender, G. E.; Tomford, W. W., *Bone Grafts And Bone Graft Substitutes*. 1st ed.; American Academy of Orthopaedic Surgeons: 2006; p 90.

34. Banks, A. A. o. T., Standards for Bone Banking. In Banks, A. A. o. T., Ed. American Association of Tissue Banks: McLean, Virginia, 2001.

35. Stevenson, S.; Xiao, Q. L.; Martin, B., The fate of cancellous and cortical bone after transplantation of fresh and frozen tissue-antigen-matched and mismatched osteochondral allografts in dogs. *Journal of Bone and Joint Surgery-American Volume* **1991**, 73A, (8), 1143-1156.
36. Friedlaender, G. E., Bone allografts: the biological consequences of immunological events. *Journal of Bone and Joint Surgery-American Volume* **1991**, 73, 1119-22.
37. Stevenson, S.; Horowitz, M., The response to bone allografts. *Journal of Bone and Joint Surgery-American Volume* **1992**, 74, 939-50.
38. De Ugarte, D. A.; Morizono, K.; Elbarbary, A.; Alfonso, Z.; Zuk, P. A.; Zhu, M.; Dragoo, J. L.; Ashjian, P.; Thomas, B.; Benhaim, P.; Chen, I.; Fraser, J.; Hedrick, M. H., Comparison of multi-lineage cells from human adipose tissue and bone marrow. *Cells Tissues and Organs* **2003**, 174, 101-9.
39. Dragoo, J. L.; Choi, J. Y.; Lieberman, J. R.; Huang, J.; Zuk, P. A.; Zhang, J.; Hedrick, M. H.; Benhaim, P., Bone induction by BMP-2 transduced stem cells derived from human fat. *Journal of Orthopaedic Research* **2003**, 21, 622-629.
40. Wang, J. C.; Kanim, L. E. A.; Yoo, S.; Campbell, P. A.; Berk, A. J.; Lieberman, J. R., Effect of regional gene therapy with bone morphogenetic protein-2-producing bone marrow cells on spinal fusion in rats. *Journal of Bone and Joint Surgery-American Volume* **2003**, 85-A, 905-11.
41. Bruder, S. P.; Fink, D. J.; Caplan, A. I., Mesenchymal stem cells in bone development, bone repair, and skeletal regeneration therapy. *Journal of Cellular Biochemistry* **1994**, 56, 283-94.

42. Bruder, S. P.; Jaiswal, N.; Ricalton, N. S.; Mosca, J. D.; Kraus, K. H.; Kadiyala, S., Mesenchymal stem cells in osteobiology and applied bone regeneration. *Clinical Orthopaedics and Related Research* **1998**, S247-56.
43. Bruder, S. P.; Kraus, K. H.; Goldberg, V. M.; Kadiyala, S., The effect of implants loaded with autologous mesenchymal stem cells on the healing of canine segmental bone defects. *The Journal of Bone and Joint Surgery* **1998**, 80, 985-96.
44. Bruder, S. P.; Kurth, A. A.; Shea, M.; Hayes, W. C.; Jaiswal, N.; Kadiyala, S., Bone regeneration by implantation of purified, culture-expanded human mesenchymal stem cells. *Journal of Orthopaedic Research* **1998**, 16, 155-62.
45. Bruder, S. P.; Ricalton, N. S.; Boynton, R. E.; Connolly, T. J.; Jaiswal, N.; Zaia, J.; Barry, F. P., Mesenchymal stem cell surface antigen SB-10 corresponds to activated leukocyte cell adhesion molecule and is involved in osteogenic differentiation. *Journal of Bone and Mineral Research* **1998**, 13, 655-663.
46. Clatworthy, M. G.; Ballance, J.; Brick, G. W.; Chandler, H. P.; Gross, A. E., The use of structural allograft for uncontained defects in revision total knee arthroplasty. A minimum five-year review. *Journal of Bone and Joint Surgery-British Volume* **2001**, 83-A, (3), 404-11.
47. Gouin, F.; Passuti, N.; Verrielle, V.; Delecrin, J.; Bainvel, J. V., Histological features of large bone allografts. *Journal of Bone and Joint Surgery-British Volume* **1996**, 78, (1), 38-41.
48. Doi, K.; Tominaga, S.; Shibata, T., Bone grafts with microvascular anastomoses of vascular pedicles: an experimental study in dogs. *Journal of Bone and Joint Surgery-American Volume* **1977**, 59, 809-15.

49. Gabl, M.; Reinhart, C.; Lutz, M.; Bodner, G.; Rudisch, A.; Hussl, H.; Pechlaner, S., Vascularized bone graft from the iliac crest for the treatment of nonunion of the proximal part of the scaphoid with an avascular fragment. *Journal of Bone and Joint Surgery-American Volume* **1999**, 81, 1414-28.
50. Wilden, J. A.; Moran, S. L.; Dekutoski, M. B.; Bishop, A. T.; Shin, A. Y., Results of vascularized rib grafts in complex spinal reconstruction. *Journal of Bone and Joint Surgery-American Volume* **2006**, 88, 832-9.
51. Dell, P. C.; Burchardt, H.; Glowczewskie, F. P., Jr., A roentgenographic, biomechanical, and histological evaluation of vascularized and non-vascularized segmental fibular canine autografts. *Journal of Bone and Joint Surgery-American Volume* **1985**, 67, (1), 105-12.
52. Yajima, H.; Kobata, Y.; Shigematsu, K.; Kawamura, K.; Kawate, K.; Tamai, S.; Takakura, Y., Vascularized fibular grafting in the treatment of methicillin-resistant *Staphylococcus aureus* osteomyelitis and infected nonunion. *Journal of Reconstructive Microsurgery* **2004**, 20, (1), 13-20.
53. Kim, S.-Y.; Kim, Y.-G.; Kim, P.-T.; Ihn, J.-C.; Cho, B.-C.; Koo, K.-H., Vascularized compared with nonvascularized fibular grafts for large osteonecrotic lesions of the femoral head. *Journal of Bone and Joint Surgery-American Volume* **2005**, 87, (9), 2012-8.
54. Marciniak, D.; Furey, C.; Shaffer, J. W., Osteonecrosis of the femoral head. A study of 101 hips treated with vascularized fibular grafting. *Journal of Bone and Joint Surgery-American Volume* **2005**, 87, (4), 742-7.

55. Rose, P. S.; Shin, A. Y.; Bishop, A. T.; Moran, S. L.; Sim, F. H., Vascularized free fibula transfer for oncologic reconstruction of the humerus. *Clinical Orthopaedics and Related Research* **2005**, 438, 80-4.
56. Tuli, S. M., Tibialization of the fibula: a viable option to salvage limbs with extensive scarring and gap nonunions of the tibia. *Clinical Orthopaedics and Related Research* **2005**, 80-4.
57. Connolly, J. F.; Guse, R.; Tiedeman, J.; Dehne, R., Autologous marrow injection as a substitute for operative grafting of tibial nonunions. *Clinical Orthopaedics and Related Research* **1991**, 272, 259-70.
58. Connolly, J.; Guse, R.; Lippiello, L.; Dehne, R., Development of an osteogenic bone-marrow preparation. *Journal of Bone and Joint Surgery-British Volume* **1989**, 71, 684-91.
59. Hernigou, P.; Poignard, A.; Beaujean, F.; Rouard, H., Percutaneous autologous bone-marrow grafting for nonunions. Influence of the number and concentration of progenitor cells. *Journal of Bone and Joint Surgery-American Volume* **2005**, 87, (7), 1430-7.
60. Marx, R. E.; Carlson, E. R.; Eichstaedt, R. M.; Schimmele, S. R.; Strauss, J. E.; Georgeff, K. R., Platelet-rich plasma: Growth factor enhancement for bone grafts. *Oral Surgery, Oral Medicine, Oral Pathology, Oral Radiology, and Endodontology* **1998**, 85, (6), 638-46.
61. Canalis, E.; McCarthy, T. L.; Centrella, M., Effects of platelet-derived growth factor on bone formation in vitro. *Journal of Cell Physiology* **1989**, 140, (3), 530-7.

62. Howes, R.; Bowness, J. M.; Grotendorst, G. R.; Martin, G. R.; Reddi, A. H., Platelet-derived growth factor enhances demineralized bone matrix-induced cartilage and bone formation. *Calcified Tissue International* **1988**, 42, (1), 34-8.
63. Noda, M.; Camilliere, J. J., In vivo stimulation of bone formation by transforming growth factor- $\beta$ . *Endocrinology* **1989**, 124, (6), 2991-4.
64. Brennwald, J., Bone healing in the hand. *Clinical Orthopaedics and Related Research* **1987**, 214, 7-10.
65. Goldberg, V. M.; Stevenson, S., Natural history of autografts and allografts. *Clinical Orthopaedics and Related Research* **1987**, 215, 7-16.
66. Schiffman, M.; Brau, S. A.; Henderson, R.; Gimmestad, G., Bilateral implantation of low-profile interbody fusion cages: subsidence, lordosis, and fusion analysis. *The Spine Journal* **2003**, 3, (1), 377-87.
67. Chen, J.-F.; Wu, C.-T.; Lee, S.-C.; Lee, S.-T., Use of a polymethylmethacrylate cervical cage in the treatment of single-level cervical disc disease. *Journal of Neurosurgery: Spine* **2005**, 3, (1), 24-8.
68. Finkemeier, C. G., Bone-grafting and bone-graft substitutes. *Journal of Bone and Joint Surgery-American Volume* **2002**, 84-A, (3), 454-64.
69. Arrington, E. D.; Smith, W. J.; Chambers, H. G.; Bucknell, A. L.; Davino, N. A., Complications of iliac crest bone graft harvesting. *Clinical Orthopaedics and Related Research* **1996**, 329, 300-9.
70. Araujo, M. V. F.; Mendes, V. C.; Chattopadhyay, P.; Davies, J. E., Low-temperature particulate calcium phosphates for bone regeneration. *Clinical Oral Implants Research* **2010**, 21, (6), 632-641.



71. Fulmer, N. L.; Bussard, G. M.; Gampper, T. J.; Edlich, R. F., Anorganic bovine bone and analogs of bone mineral as implants for craniofacial surgery: a literature review. *J Long-Term Eff Med* **1998**, 8, 69-78.
72. Barinov, S. M., Calcium phosphate-based ceramic and composite materials for medicine. *Russ. Chem. Rev.* **2010**, 79, (1), 13-29.
73. Chevalier, J.; Gremillard, L., Ceramics for medical applications: A picture for the next 20 years. *Journal of the European Ceramic Society* **2009**, 29, (7), 1245-1255.
74. Chissov, V. I.; Sviridova, I. K.; Sergeeva, N. S.; Frank, G. A.; Kirsanova, V. A.; Achmedova, S. A.; Reshetov, I. V.; Filjushin, M. M.; Barinov, S. M.; Fadeeva, I. V.; Komlev, V. S., Study of In Vivo Biocompatibility and Dynamics of Replacement of Rat Shin Defect with Porous Granulated Bioceramic Materials. *Bulletin of Experimental Biology and Medicine* **2008**, 146, (1), 139-143.
75. Dorozhkin, S. V., Calcium orthophosphate-based biocomposites and hybrid biomaterials. *Journal of Materials Science* **2009**, 44, (9), 2343-2387.
76. Douglas, T.; Liu, Q.; Humpe, A.; Wiltfang, J.; Sivananthan, S.; Warnke, P. H., Novel ceramic bone replacement material CeraBall (R) seeded with human mesenchymal stem cells. *Clinical Oral Implants Research* **2010**, 21, (3), 262-267.
77. Okuda, T.; Ioku, K.; Yonezawa, I.; Minagi, H.; Gonda, Y.; Kawachi, G.; Kamitakahara, M.; Shibata, Y.; Murayama, H.; Kurosawa, H.; Ikeda, T., The slow resorption with replacement by bone of a hydrothermally synthesized pure calcium-deficient hydroxyapatite. *Biomaterials* **2008**, 29, (18), 2719-2728.

78. Wands, I.; Shepherd, D. E. T.; Hukins, D. W. L., Viscoelastic properties of composites of calcium alginate and hydroxyapatite. *Journal of Materials Science-Materials in Medicine* **2008**, 19, (6), 2417-2421.
79. Zhao, J.; Lu, X.; Duan, K.; Guo, L. Y.; Zhou, S. B.; Weng, J., Improving mechanical and biological properties of macroporous HA scaffolds through composite coatings. *Colloids and Surfaces B-Biointerfaces* **2009**, 74, (1), 159-166.
80. Muthutantri, A.; Huang, J.; Edirisinghe, M., Novel preparation of graded porous structures for medical engineering. *Journal of the Royal Society Interface* **2008**, 5, (29), 1459-1467.
81. Camazzola, D.; Hammond, T.; Gandhi, R.; Davey, J. R., A Randomized Trial of Hydroxyapatite-Coated Femoral Stems in Total Hip Arthroplasty A 13-Year Follow-Up. *Journal of Arthroplasty* **2009**, 24, (1), 33-37.
82. Elmengaard, B.; Bechtold, J. E.; Chen, X. Q.; Soballe, K., Fixation of Hydroxyapatite-Coated Revision Implants is Improved by the Surgical Technique of Cracking the Sclerotic Bone Rim. *Journal of Orthopaedic Research* **2009**, 27, (8), 996-1001.
83. Gallo, J.; Landor, I.; Cechova, I.; Jahoda, D., Comparison of Hydroxyapatite-Coated Stems in Total Hip Arthroplasty after a Minimum 10-Years Follow-up. *Acta Chirurgiae Orthopaedicae Et Traumatologiae Cechoslovaca* **2008**, 75, (5), 339-346.
84. Garcia-Rey, E.; Munoz, T.; Montejo, J.; Martinez, J., Results of a Hydroxyapatite-Coated Modular Femoral Stem in Primary Total Hip Arthroplasty. A Minimum 5-Year Follow-Up. *Journal of Arthroplasty* **2008**, 23, (8), 1132-1139.

85. Mouttet, A.; Philippot, R.; Farizon, F.; Vallotton, P. H.; Ibnou-Zekri, N., Five-year follow-up of a hydroxyapatite coated stem. *Revue De Chirurgie Orthopedique Et Reparatrice De L Appareil Moteur* **2008**, 94, (8), 746-752.
86. Steens, W.; Schneeberger, A. G.; Skripitz, R.; Fennema, P.; Goetze, C., Bone remodeling in proximal HA-coated versus uncoated cementless SL-Plus(A (R)) femoral components: a 5-year follow-up study. *Archives of Orthopaedic and Trauma Surgery* **2010**, 130, (7), 921-926.
87. Salemyr, M. O. F.; Skoldenberg, O. G.; Boden, H. S. G.; Ahl, T. E.; Adolphson, P. Y., Good results with an uncemented proximally HA-coated stem in hip revision surgery - 62 hips followed for 2-13 years. *Acta Orthopaedica* **2008**, 79, (2), 184-193.
88. Soballe, K.; Hansen, E. S.; Brockstedt-Rasmussen, H.; Bunger, C., Hydroxyapatite coating converts fibrous tissue to bone around loaded implants. *Journal of Bone and Joint Surgery-British Volume* **1993**, 75, (2), 270-8.
89. Hench, L. L.; Wilson, J., *Clinical Performance Of Skeletal Prostheses*. 1st ed.; Chapman and Hall: 1995.
90. Ascherman, J. A.; Foo, R.; Nanda, D.; Parisien, M., Reconstruction of cranial bone defects using a quick-setting hydroxyapatite cement and absorbable plates. *Journal of Craniofacial Surgery* **2008**, 19, (4), 1131-1135.
91. Curtis, N.; Zoellner, H., Resection of an orbital rim intraosseous cavernous hemangioma and reconstruction by chin graft and resorbable fixation plate. *Ophthalmic Plastic and Reconstructive Surgery* **2007**, 23, (3), 232-234.

92. Eppley, B. L.; Pietrzak, W. S., A resorbable rivet system for pediatric craniofacial surgery: Biomechanical testing and clinical experience. *Journal of Craniofacial Surgery* **2006**, 17, (1), 11-14.
93. Kessler, K. J.; Bullens-Borrow, A. E.; Zisholtz, J., LactoSorb plates for rotator cuff repair. *Arthroscopy-the Journal of Arthroscopic and Related Surgery* **2002**, 18, (3), 279-283.
94. Roncevic, R., Lactosorb panel and screws for repair of large orbital floor defects. *Journal of Cranio-Maxillofacial Surgery* **1998**, 26, (3), 191-191.
95. Torre, M.; Jasonni, V.; Asquasciati, C.; Costanzo, S.; Romanini, M. V.; Varela, P., Absorbable Stabilisation of the Bar in Minimally Invasive Repair of Pectus Excavatum. *European Journal of Pediatric Surgery* **2008**, 18, (6), 407-409.
96. Noda, K.; Tanikawa, R.; Sugimura, T.; Kawasaki, K.; Kimura, T.; Izumi, N.; Hashimoto, M., Use of Bioabsorbable Plates for Cranial Fixation -Technical Note. *Neurologia Medico-Chirurgica* **2009**, 49, (11), 559-562.
97. Eppley, B. L.; Morales, L.; Wood, R.; Pensler, J.; Goldstein, J.; Havlik, R. J.; Habal, M.; Losken, A.; Williams, J. K.; Burstein, F.; Rozzelle, A. A.; Sadove, A. M., Resorbable PLLA PGA plate and screw fixation in pediatric craniofacial surgery: Clinical experience in 1883 patients. *Plastic and Reconstructive Surgery* **2004**, 114, (4), 850-856.
98. Pilegaard, H. K.; Licht, P. B., Can absorbable stabilizers be used routinely in the Nuss procedure? *European Journal of Cardio-Thoracic Surgery* **2009**, 35, (4), 561-564.
99. Eppley, B. L.; Reilly, M., Degradation characteristics of PLLA-PGA bone fixation devices. *Journal of Craniofacial Surgery* **1997**, 8, (2), 116-120.

100. Bos, R. R. M., The fate of resorbable poly-L-lactic/polyglycolic acid (LactoSorb) bone fixation devices in orthognathic surgery - Discussion. *Journal of Oral and Maxillofacial Surgery* **2001**, 59, (1), 25-25.
101. Wiltfang, J.; Merten, H. A.; Schultze-Mosgau, S.; Schrell, U.; Wenzel, D.; Kessler, P., Biodegradable miniplates (LactoSorb): Long-term results in infant minipigs and clinical results. *Journal of Craniofacial Surgery* **2000**, 11, (3), 239-243.
102. Edwards, R. C.; Kiely, K. D.; Eppley, B. L., The fate of resorbable poly-L-lactic/polyglycolic acid (LactoSorb) bone fixation devices in orthognathic surgery. *Journal of Oral and Maxillofacial Surgery* **2001**, 59, (1), 19-25.
103. Ignjatovic, N.; Delijic, K.; Vukcevic, M.; Uskokovic, D., Microstructure and mechanical properties of hot-pressed hydroxyapatite/poly-L-lactide biomaterials. In *Bioceramics*, Giannini, S.; Moroni, A., Eds. Trans Tech Publications Ltd: Zurich-Uetikon, 2000; Vol. 192-1, pp 737-740.
104. Ignjatovic, N.; Tomic, S.; Dakic, M.; Miljkovic, M.; Plavsic, M.; Uskokovic, D., Synthesis and properties of hydroxyapatite/poly-L-lactide composite biomaterials. *Biomaterials* **1999**, 20, (9), 809-816.
105. Zhou, Z. H.; Ruan, J. M.; Zhou, Z. C.; Zou, J. P., Synthesis and properties of composite biomaterials based on hydroxyapatite and poly(L-lactide). *Polymer-Plastics Technology and Engineering* **2008**, 47, (5), 496-501.
106. Balac, I.; Uskokovic, P. S.; Aleksic, R.; Uskokovic, D., Predictive modeling of the mechanical properties of particulate hydroxyapatite reinforced polymer composites. *Journal of Biomedical Materials Research* **2002**, 63, (6), 793-799.

107. Nazhat, S. N.; Kellomaki, M.; Tormala, P.; Tanner, K. E.; Bonfield, W., Dynamic mechanical characterization of biodegradable composites of hydroxyapatite and polylactides. *Journal of Biomedical Materials Research* **2001**, 58, (4), 335-343.
108. Wei, G. B.; Ma, P. X., Structure and properties of nano-hydroxyapatite/polymer composite scaffolds for bone tissue engineering. *Biomaterials* **2004**, 25, (19), 4749-4757.
109. Furukawa, T.; Matsusue, Y.; Yasunaga, T.; Shikinami, Y.; Okuno, M.; Nakamura, T., Biodegradation behavior of ultra-high-strength hydroxyapatite/poly (L-lactide) composite rods for internal fixation of bone fractures. *Biomaterials* **2000**, 21, (9), 889-898.
110. Hasegawa, S.; Ishii, S.; Tamura, J.; Furukawa, T.; Neo, M.; Matsusue, Y.; Shikinami, Y.; Okuno, M.; Nakamura, T., A 5-7 year in vivo study of high-strength hydroxyapatite/poly(L-lactide) composite rods for the internal fixation of bone fractures. *Biomaterials* **2006**, 27, (8), 1327-1332.
111. Ignjatovic, N.; Plavsic, M.; Najman, S.; Savic, V.; Uskokovic, D., Analysis of in vivo substitution of bone tissue by HAp/PLLA composite biomaterial with PLLA of different molecular weights using FTIR spectroscopy. In *Trends in Advanced Materials and Processes*, Uskokovic, D. P.; Battiston, G. A.; Nedeljkovic, J. M.; Milonjic, S. K.; Rakovic, D. I., Eds. Trans Tech Publications Ltd: Zurich-Uetikon, 2000; Vol. 352, pp 143-150.
112. Kotani, Y.; Abumi, K.; Shikinami, Y.; Takahata, M.; Kadoya, K.; Kadosawa, T.; Minami, A.; Kaneda, K., Two-year observation of artificial intervertebral disc replacement: results after supplemental ultra-high strength bioresorbable spinal stabilization. *Journal of Neurosurgery* **2004**, 100, (4), 337-342.

113. Cehreli, M. C.; Sahin, S.; Kesenci, K.; Tuzlakoglu, K.; Piskin, E.; Ozturk, S.; Ruacan, S.; Caner, B.; Bozkurt, M. F., Biological reactions to a poly(L-lactide)-hydroxyapatite composite: A study in canine mandible. *Journal of Biomaterials Applications* **2003**, 17, (4), 265-276.
114. Furukawa, T.; Matsusue, Y.; Yasunaga, T.; Nakagawa, Y.; Okada, Y.; Shikinami, Y.; Okuno, M.; Nakamura, T., Histomorphometric study on high-strength hydroxyapatite/poly(L-lactide) composite rods for internal fixation of bone fractures. *Journal of Biomedical Materials Research* **2000**, 50, (3), 410-419.
115. Ishii, S.; Tamura, J.; Furukawa, T.; Nakamura, T.; Matsusue, Y.; Shikinami, Y.; Okuno, M., Long-term study of high-strength hydroxyapatite/poly(L-lactide) composite rods for the internal fixation of bone fractures: A 2-4-year follow-up study in rabbits. *Journal of Biomedical Materials Research Part B-Applied Biomaterials* **2003**, 66B, (2), 539-547.
116. Yasunaga, T.; Matsusue, Y.; Furukawa, T.; Shikinami, Y.; Okuno, M.; Nakamura, T., Bonding behavior of ultrahigh strength unsintered hydroxyapatite particles/poly(L-lactide) composites to surface of tibial cortex in rabbits. *Journal of Biomedical Materials Research* **1999**, 47, (3), 412-419.
117. Matsusue, Y.; Nakamura, T.; Iida, H.; Shimizu, K., A long-term clinical study on drawn poly-L-lactide implants in orthopaedic surgery. *J Long-Term Eff Med* **1997**, 7, (2), 119-137.
118. Matsusue, Y.; Hanafusa, S.; Yamamuro, T.; Shikinami, Y.; Ikada, Y., Tissue reaction of bioabsorbable ultra high strength poly (L-lactide) rod. A long-term study in rabbits. *Clinical Orthopaedics and Related Research* **1995**, 246-53.

119. Yamamuro, T.; Matsusue, Y.; Uchida, A.; Shimada, K.; Shimozaki, E.; Kitaoka, K., Bioabsorbable osteosynthetic implants of ultra high strength poly-L-lactide. A clinical study. *International Orthopaedics* **1994**, 18, 332-40.
120. Walton, M.; Cotton, N. J., Long-term in vivo degradation of poly-L-lactide (PLLA) in bone. *Journal of Biomaterials Applications* **2007**, 21, (4), 395-411.
121. Qiu, X. Y.; Chen, L.; Hu, J. L.; Sun, J. R.; Hong, Z. K.; Liu, A. X.; Chen, X. S.; Jing, X. B., Surface-modified hydroxyapatite linked by L-lactic acid oligomer in the absence of catalyst. *Journal of Polymer Science Part A-Polymer Chemistry* **2005**, 43, (21), 5177-5185.
122. Qiu, X. Y.; Hong, Z. K.; Hu, J. L.; Chen, L.; Chen, X. S.; Jing, X. B., Hydroxyapatite surface modified by L-lactic acid and its subsequent grafting polymerization of L-lactide. *Biomacromolecules* **2005**, 6, (3), 1193-1199.
123. Jack, K. S.; Vizcarra, T. G.; Trau, M., Characterization and surface properties of amino-acid-modified, carbonate-containing hydroxyapatite particles. *Langmuir* **2007**, 23, (24), 12233-12242.
124. Gonzalez-McQuire, R.; Chane-Ching, J. Y.; Vignaud, E.; Lebugle, A.; Mann, S., Synthesis and characterization of amino acid-functionalized hydroxyapatite nanorods. *Journal of Materials Chemistry* **2004**, 14, (14), 2277-2281.
125. Sugiyama, N.; Kunibu, R.; Yoshizawa-Fujita, M.; Takeoka, Y.; Aizawa, M.; Rikukawa, M., Ring-opening bulk polymerization of L-lactide in porous hydroxyapatite. *Chemistry Letters* **2007**, 36, (12), 1476-1477.



126. Wiegand, T.; Karr, J.; Steinkruger, J. D.; Hiebner, K.; Simeich, B.; Beatty, M.; Redepenning, J., Reconstruction of Anorganic Mammalian Bone by Surface-initiated Polymerization of L-lactide. *Chemistry of Materials* **2008**, 20, (15), 5016-5022.
127. Li, H.; Liao, L.; Wang, Q.; Liu, L., Flash-Heating-Enhanced Ring-Opening Polymerizations of epsilon-Caprolactone under Conventional Conditions. *Macromolecular Chemistry and Physics* **2006**, 207, (19), 1789-1793.
128. Kaihara, S.; Matsumura, S.; Mikos, A. G.; Fisher, J. P., Synthesis of poly(L-lactide) and polyglycolide by ring-opening polymerization. *Nature Protocols* **2007**, 2, (11), 2767-2771.
129. Kowalski, A.; Duda, A.; Penczek, S., Mechanism of cyclic ester polymerization initiated with tin(II) octoate. 2. Macromolecules fitted with tin(II) alkoxide species observed directly in MALDI-TOF spectra. *Macromolecules* **2000**, 33, (3), 689-695.
130. Kricheldorf, H. R.; Kreiser-Saunders, I.; Damrau, D. O., Resorbable initiators for polymerizations of lactones. *Macromolecular Symposia* **2000**, 159, 247-257.
131. Ryner, M.; Stridsberg, K.; Albertsson, A. C.; von Schenck, H.; Svensson, M., Mechanism of ring-opening polymerization of 1,5-dioxepan-2-one and L-lactide with stannous 2-ethylhexanoate. A theoretical study. *Macromolecules* **2001**, 34, (12), 3877-3881.
132. Helwig, E.; Sandner, B.; Gopp, U.; Vogt, F.; Wartewig, S.; Henning, S., Ring-opening polymerization of lactones in the presence of hydroxyapatite. *Biomaterials* **2001**, 22, (19), 2695-2702.

133. Kricheldorf, H. R.; Boettcher, C., Polylactones .27. Anionic-Polymerization of L-Lactide - Variation of Endgroups and Synthesis of Block-Copolymers with Poly(Ethylene Oxide). *Makromolekulare Chemie-Macromolecular Symposia* **1993**, 73, 47-64.
134. Schwach, G.; Coudane, J.; Engel, R.; Vert, M., Ring opening polymerization of D,L-lactide in the presence of zinc metal and zinc lactate. *Polymer International* **1998**, 46, (3), 177-182.
135. Williams, C. K.; Breyfogle, L. E.; Choi, S. K.; Nam, W.; Young, V. G.; Hillmyer, M. A.; Tolman, W. B., A highly active zinc catalyst for the controlled polymerization of lactide. *Journal of the American Chemical Society* **2003**, 125, (37), 11350-11359.
136. Zhong, Z. Y.; Dijkstra, P. J.; Birg, C.; Westerhausen, M.; Feijen, J., A novel and versatile calcium-based initiator system for the ring-opening polymerization of cyclic esters. *Macromolecules* **2001**, 34, (12), 3863-3868.
137. Kricheldorf, H. R.; Berl, M.; Scharnagl, N., Poly(lactones). 9. Polymerization mechanism of metal alkoxide initiated polymerizations of lactide and various lactones. *Macromolecules* **1988**, 21, (2), 286-293.
138. Kricheldorf, H. R.; Kreiseraunders, I., Polylactones .19. Anionic-Polymerization of L-Lactide in Solution. *Makromolekulare Chemie-Macromolecular Chemistry and Physics* **1990**, 191, (5), 1057-1066.
139. Penczek, S.; Duda, A., Kinetics and Mechanisms in Anionic Ring-Opening Polymerization. *Makromolekulare Chemie-Macromolecular Symposia* **1993**, 67, 15-42.
140. Dunsing, R.; Kricheldorf, H. R., Polymerization of L,L-LacUde by Means of Magnesium Salts. *Polymer Bulletin* **1985**, 14.

141. Guerra, G. D.; Cerrai, P.; D'Acunto, M.; Krajewski, A.; Maltinti, S.; Mazzocchi, M.; Palla, M.; Ravaglioli, A.; Tricoli, M., Polymerization of epsilon-caprolactone initiated through powders of biological and nonbiological glasses. *Journal of Applied Polymer Science* **2003**, 87, (10), 1579-1586.
142. Kageyama, K.; Tatsumi, T.; Aida, T., Mesoporous Zeolite as a New Catalyst for Polymerization of Lactones. *Polymer Journal* **1999**, 31, (11).
143. Kowalski, A.; Libiszowski, J.; Duda, A.; Penczek, S., Polymerization of L,L-dilactide initiated by tin(II) butoxide. *Macromolecules* **2000**, 33, (6), 1964-1971.
144. Chisholm, M. H.; Eilerts, N. W.; Huffman, J. C.; Iyer, S. S.; Pacold, M.; Phomphrai, K., Molecular design of single-site metal alkoxide catalyst precursors for ring-opening polymerization reactions leading to polyoxygenates. 1. Polylactide formation by achiral and chiral magnesium and zinc alkoxides, (eta(3)-L)MOR, where L = trispyrazolyl- and trisindazolylborate ligands. *Journal of the American Chemical Society* **2000**, 122, (48), 11845-11854.
145. Chisholm, M. H.; Gallucci, J.; Phomphrai, K., Coordination chemistry and reactivity of monomeric alkoxides and amides of magnesium and zinc supported by the diiminato ligand CH(CMeNC6H3-2,6-Pr-i(2))(2). A comparative study. *Inorganic Chemistry* **2002**, 41, (10), 2785-2794.
146. Nederberg, F.; Connor, E. F.; Moller, M.; Glauser, T.; Hedrick, J. L., New paradigms for organic catalysts: The first organocatalytic living polymerization. *Angewandte Chemie-International Edition* **2001**, 40, (14), 2712-2715.
147. Li, Y.; Li, Q. B.; Li, F. X.; Zhang, H. Y.; Jia, L.; Yu, J. Y.; Fang, Q.; Cao, A., Amphiphilic poly(L-lactide)-b-dendritic poly(L-lysine)s synthesized with a metal-free

catalyst and new dendron initiators: Chemical preparation and characterization. *Biomacromolecules* **2006**, 7, (1), 224-231.

148. C. Rey, C. C., C. Drouet, A. Lebugle, H. Sfihi, A. Barroug,, Nanocrystalline apatites in biological systems: characterisation, structure and properties. *Materialwissenschaft Und Werkstofftechnik* **2007**, 38, (12), 996-1002.

149. Fowler, B. O., Infrared Studies of Apatites. 11. Preparation of Normal and Isotopically Substituted Calcium, Strontium, and Barium Hydroxyapatites and SpectraStructure-Composition Correlations. *Inorganic Chemistry* **1974**, 13, (1).

150. Jarcho, M.; Bolen, C. H.; Thomas, M. B.; Bobick, J.; Kay, J. F.; Doremus, R. H., Hydroxylapatite synthesis and characterization in dense polycrystalline form. *Journal of Materials Science* **1976**, 11, (11), 2027-35.

151. Markovic, M.; Fowler, B. O.; Tung, M. S., Preparation and comprehensive characterization of a calcium hydroxyapatite reference material. *J Res Natl Inst Stan* **2004**, 109, (6), 553-568.

152. Roy, D. M. L., Sari K. , Hydroxyapatite formed from coral skeletal carbonate by hydrothermal exchange *Nature* **1974**, 247.

153. Sutorik, A. C.; Paras, M. S.; Lawrence, D.; Kennedy, A.; Hinklin, T., Synthesis, Characterization, and Sintering Behavior of Calcium Hydroxyapatite Powders with Average Particle Diameters of 150 nanometers. In *Bioceramics: Materials and Applications IV*, Wiley-American Ceramic Society 2003.

154. Wei, M.; Evans, J. H.; Bostrom, T.; Grondahl, L., Synthesis and characterization of hydroxyapatite, fluoride-substituted hydroxyapatite and fluorapatite. *Journal of Materials Science-Materials in Medicine* **2003**, 14, (4), 311-320.

155. Bres, E. F.; Cherns, D.; Vincent, R.; Morniroli, J. P., Space-group determination of human tooth-enamel crystals. *Acta Crystallographica Section B: Structural Science* **1993**, B49, (1), 56-62.
156. Aoki, H.; Hata, M.; Akao, M.; Iwai, S.; Kato, K., The crystal structure of hydroxyapatite. *Iyo Kizai Kenkyusho Hokoku* **1978**, 12, 9-17.
157. Elliott, J. C.; Mackie, P. E., Monoclinic hydroxyapatite. *Colloque International* **1975**, 230, 69-76.
158. Biltz, R. M.; Pelligrino, E. D., The Composition of Recrystallized Bone Mineral. *Journal of Dental Research* **1983**, 62, (12).
159. Lafon, J. P.; Champion, E.; Bernache-Assollant, D., Processing of AB-type carbonated hydroxyapatite  $\text{Ca}_{10-x}(\text{PO}_4)_{(6-x)}(\text{CO}_3)_x(\text{OH})_{(2-x-2y)}(\text{CO}_3)_y$  ceramics with controlled composition. *Journal of the European Ceramic Society* **2008**, 28, (1), 139-147.
160. Murugan, R.; Rao, K. P.; Kumar, T. S. S., Heat-deproteinated xenogeneic bone from slaughterhouse waste: Physico-chemical properties. *Bulletin of Materials Science* **2003**, 26, (5), 523-528.
161. Bohdan, Z.; Sikyr, V., Mechanical properties of materials in walls of sandwich construction with polyurethane cores and glass-reinforced plastic sides. *Plastice Hmoty Kaucice* **1969**, 6, 200-3.
162. Chiesi, F., Calculation and method for the designing of fiberglass reinforced polyester bumpers. *Poliplasti Material* **1976**, 24, 47-51.
163. Fesko, D. G., Flexural fatigue of unidirectional fiberglass-reinforced polyester. *Polymer Engineering and Science* **1977**, 17, 242-5.

164. Finsel, J. R.; Younge, K. R., Hybrid BMC's - fiberglass reinforced polyester thermosets displacing traditional molding materials. *Proceedings. Annual Conference - Reinforced Plastics and Composites* **1980**, 35th, 2-F, 1-2-F, 6.
165. Jackson, W. E. Polyester laminates. 1976.
166. Kuroda, T.; Komaki, K.; Hama, T.; Hidaka, T., Mechanical properties of fiberglass-reinforced plastics. Experiments designed in an orthogonal array. *Osaka Kogyo Gijutsu Shikensho Kiho* **1966**, 17, 243-9.
167. Markus, T. H., Measurements of different fiberglass-reinforced polyester supports. *Kunststoffberater vereinigt mit Rundschau Technik* **1970**, 17, 101-6; (3), 157-63.
168. Masi, P.; Nicolais, L.; Mazzola, M.; Narkis, M., Tensile properties of fiberglass-reinforced polyester foams. *Journal of Applied Polymer Science* **1983**, 28, 1517-25.
169. Mazzola, M.; Masi, P.; Nicolais, L.; Narkis, M., Fiberglass-reinforced polyester foams. *Journal of Cellular Plastics* **1982**, 18, 321-4.
170. Legros, R.; Balmain, N.; Bonel, G., Age-related changes in mineral of rat and bovine cortical bone. *Calcified Tissue International* **1987**, 41, (3), 137-44.
171. Bassett, C. A. L.; Hurley, L. A.; Stinchfield, F. E., Fate of long-term anorganic bone implants. *Transplant Biology* **1962**, 29, 51-5.
172. Rapkin, E. Anorganic bone. 2,968,593, January 17, 1961.
173. Williams, J. B.; Irvine, J. W., Jr., Preparation of the inorganic matrix of bone. *Science* **1954**, 119, 771-2.

174. Annalisa, P.; Furio, P.; Ilaria, Z.; Anna, A.; Luca, S.; Marcella, M.; Marzia, A.; Elena, M.; Carinci, F., Anorganic bovine bone and a silicate-based synthetic bone activate different microRNAs. *Journal of Oral Science* **2008**, 50, 301-307.
175. Yukna, R. A.; Krauser, J. T.; Callan, D. P.; Evans, G. H.; Cruz, R.; Martin, M., Multi-center clinical comparison of combination anorganic bovine-derived hydroxyapatite matrix (ABM)/cell binding peptide (P-15) and ABM in human periodontal osseous defects. 6-month results. *Journal of Periodontology* **2000**, 71, (11), 1671-1679.
176. Yukna, R. A.; Krauser, J. T.; Callan, D. P.; Evans, G. H.; Cruz, R.; Martin, M., Thirty-six month follow-up of 25 patients treated with combination anorganic bovine-derived hydroxyapatite matrix (ABM)/cell-binding peptide (P-15) bone replacement grafts in human infrabony defects. I. Clinical findings. *Journal of Periodontology* **2002**, 73, (1), 123-128.
177. Herliansyah, M. K.; Hamdi, M.; Ide-Ektessabi, A.; Wildan, M. W.; Toque, J. A., The influence of sintering temperature on the properties of compacted bovine hydroxyapatite. *Materials Science and Engineering: C* **2009**, 29, (5), 1674-1680.
178. Abdel-Fattah, W. I.; Nour, F. A., Thermal expansion application to assess calcination of bovine hydroxyapatite. *Thermochimica Acta* **1993**, 218, 465-75.
179. Bernache-Assollant, D.; Ababou, A.; Champion, E.; Heughebaert, M., Sintering of calcium phosphate hydroxyapatite  $\text{Ca}_{10}(\text{PO}_4)_6(\text{OH})_2$ . I. Calcination and particle growth. *Journal of the European Ceramic Society* **2002**, 23, 229-241.

180. Haberko, K.; Bucko, M. M.; Brzezinska-Miecznik, J.; Haberko, M.; Mozgawa, W.; Panz, T.; Pyda, A.; Zarebski, J., Natural hydroxyapatite - its behaviour during heat treatment. *Journal of the European Ceramic Society* **2006**, 26, (4-5), 537-542.
181. Haberko, K.; Bucko, M. M.; Mozgawa, W.; Pyda, A.; Brzezinska-Miecznik, J.; Carpentier, J., Behaviour of bone origin hydroxyapatite at elevated temperatures and in O<sub>2</sub> and CO<sub>2</sub> atmospheres. *Ceramic International* **2009**, 35, 2537-2540.
182. Kricheldorf, H. R.; Damrau, D. O., Polylactones .37. Polymerizations of L-lactide initiated with Zn(II) L-lactate and other resorbable Zn salts. *Macromolecular Chemistry and Physics* **1997**, 198, (6), 1753-1766.
183. Kricheldorf, H. R.; Damrau, D. O., Polylactones. 44. Polymerizations of L-lactide catalyzed by manganese salts. *Journal of Macromolecular Science-Pure and Applied Chemistry* **1998**, A35, (11), 1875-1887.
184. Bailliez, S.; Nzihou, A., The kinetics of surface area reduction during isothermal sintering of hydroxyapatite adsorbent. *Chemical Engineering Journal* **2004**, 98, (1-2), 141-152.
185. Figueiredo, M.; Fernando, A.; Martins, G.; Freitas, J.; Judas, F.; Figueiredo, H., Effect of the calcination temperature on the composition and microstructure of hydroxyapatite derived from human and animal bone. *Ceramics International* **2010**, 36, 2383-2393.



## Chapter Two

### Kinetic Analysis of Common Biocompatible Monomers and Polymers with Ring Opening Polymerization Initiated by Bovine Hydroxyapatite Sintered at Various Temperatures for Sixteen Hours

#### Introduction and Background

A logical first step in creating polymer-hydroxyapatite composite materials is to understand how various reaction parameters control reaction rates and properties of the products. It has been shown that hydroxyapatite will initiate the ring-opening polymerization of several lactones.<sup>1-3</sup> The kinetics of homogeneously initiated ring-opening polymerizations have been studied and have been shown to obey the following rate law,

$$Rate = k[I]^x[M]^y \quad (2.1)$$

where  $k$  is the kinetic rate constant,  $[I]$  is the concentration of polymerization initiator and  $[M]$  is the concentration of lactone monomer. Both  $x$  and  $y$  are one.<sup>4-6</sup> Common initiators have been anionic such as hydroxide, oxide, alkoxide, and amide.<sup>7-10</sup> Neutral initiators have also been reported such as alcohols and amines.<sup>11-13</sup>

Ring-opening polymerizations are living reactions where each mole of initiator consumed creates an equivalent number of moles of living polymer chains. (Figure 2.1) Consequently, the number of polymerization sites remains constant throughout the reaction. As such, the  $[I]^x$  term in the general rate equation is a constant and the rate equation can be simplified to the following.

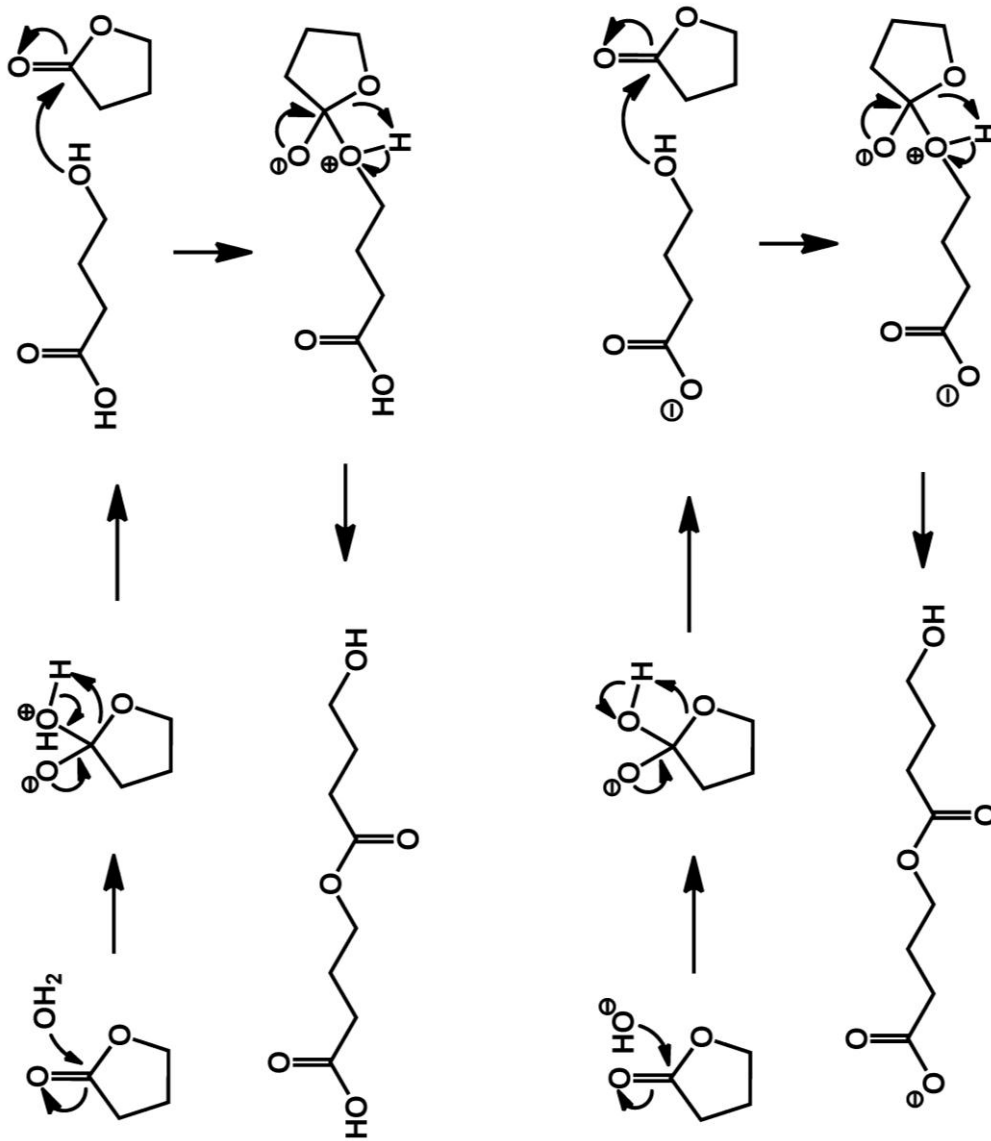


Figure 2.1. General examples of ring opening polymerization with the neutral initiator, water (top) and the anion hydroxide (bottom) with the monomer valerolactone.

$$\text{Rate} = k_{app}[M]^y \quad (2.2)$$

where  $k_{app}$  is equal to  $k[I]^x$ . This equation is rewritten as a differential rate law in terms of disappearance of monomer as shown by Ouhadi et al., Penczek and Duda, and Endo and Sanda is

$$-\frac{dM_t}{dt} = k_{app}M_t \quad (2.3)$$

and its integrated form

$$-\ln \frac{M_t}{M_0} = k_{app}t \quad (2.4)$$

where  $M_0$  is the mole fraction of monomer at time zero and  $M_t$  is the mole fraction of monomer at time,  $t$ .<sup>4, 5, 14</sup> This final rate equation shows a pseudo first order relationship to the monomer concentration and that when  $-\ln \frac{M_t}{M_0}$  is plotted against reaction time the slope of the resulting line is the pseudo first order rate constant for the reaction. By definition, the mole fraction,  $M_0$ , is 1. Equation 2.4 can be used to compare the reaction kinetics for different reaction conditions and for different monomers.

In 2001, Helwig et al. show that the polymerization of lactones could be initiated by  $\text{Sn}(\text{oct})_2$  in the presence of hydroxyapatite to produce a PLLA-HA composite. Tin compounds are not without their drawbacks. Since the early 1980s, several studies have reported that tin compounds adversely affect the gastrointestinal system as well as causing neurological damage in rats.<sup>15-27</sup> Whenever possible, the use of toxic organometallic compounds should be avoided when attempting to make a material for direct human implantation. More recently, it has been shown that hydroxyapatite will

initiate the ring-opening polymerization of several lactones in the absence of any other initiator.<sup>1-3, 28</sup>

Polymerization reactions initiated by hydroxyapatite are different from homogeneous polymerizations in that the initiator is associated with the heterogeneous component. For this reason, treating the initiator in terms of concentration is not entirely correct. A better representation would be to speak of the number of initiation site presented to the bulk monomer. A rate equation analogous to equation 2.1 can be proposed as

$$Rate = kN_i[M]^y \quad (2.5)$$

where  $N_i$  is the number of initiation sites. Based on the mechanism proposed in Figure 2.1 (bottom), the number of initiation sites must remain constant throughout the course of the reaction. Thus,  $kN_i$ , is a constant and equation 2.5 can be rewritten to reflect that giving

$$Rate = k_{app}[M]^y \quad (2.6)$$

where  $k$  and  $N_i$  are combined into  $k_{app}$ . Mathematically, this is equivalent to equation 2.2, so an integrated rate law equivalent to equation 2.4 can also be written. Consequently, heterogeneously initiated polymerization reactions can also be modeled by the same pseudo-first order rate equation

In this thesis, the hydroxyapatite initiated polymerizations were performed using powdered hydroxyapatite derived from biologic sources, more specifically bovine femurs. In part, this was done because bovine femurs provide an inexpensive and readily available source of material. More importantly, bovine bone was used because of our

ultimate goal to prepare devices, possibly from cadaver bone, for repairing segmental bone defects. A review of the relevant literature reveals that there are several methods for the production of hydroxyapatite from biologic sources in the literature. There are two common methods used to remove the organic material from the mineral portion. The first is pyrolysis in either air or an oxygen rich environment. The second employs extremely caustic solvents or solutions to digest the organics. Whichever method is used to remove the proteins and fats from the raw bone, I have found that a subsequent sintering step is needed to remove surface bound water and vestiges of the original organic material. None of the preparation methods in the literature are designed for isolating biologically derived HA for later use as an initiator for ring-opening polymerization of lactones. Consequently, it was necessary to explore all variables in the HA production process and examine how each affects the reaction and the final properties of the composite created.

### Experimental

Chemicals: Deuterated chloroform ( $\text{CDCl}_3$ , 99.8% D from Sigma-Aldrich), deuterated 1,1,2,2-tetrachloroethane ( $\text{C}_2\text{D}_2\text{Cl}_4$ , 99.5% D from Sigma-Aldrich), deuterated dimethylsulfoxide (DMSO, 99.96% from Sigma-Aldrich), 1,4-dioxan-2-one (Dioxanone, DX, from Ethicon),  $\epsilon$ -caprolactone (CL, 99% from Fluka), glycolide (GL, 99.9% from Polysciences Inc.), L-lactic acid (90% from Acros Organics), D-lactic acid (85% from MP Biomedicals), ethylene diamine (99% from Sigma Aldrich), DL-lactic acid (85% from Acros Organics), tin(II) 2-ethyl hexanoate ( $\text{Sn(II)oct}_2$ , 95% from Sigma-Aldrich), tetramethylammonium hydroxide (98% from Alfa Aesar), calcium hydroxide (98% from

Acros Organics), calcium oxide (99.95% from Alfa Aesar), were used as purchased from the respective supplier. L-lactide (from Purac) was sublimed at 90 °C and then transferred into a N<sub>2(g)</sub> atmosphere glove box for further use. Glycolide (≥99% from Sigma Aldrich) was sublimed at 80 °C and then transferred into a N<sub>2(g)</sub> atmosphere glove box for further use. Calcium L-lactate pentahydrate (98% from Fisher) was dehydrated at 120 °C under vacuum and then transferred into a N<sub>2(g)</sub> atmosphere glove box for further use. Biologic hydroxyapatite was sourced from bovine femur (donated by Premium Protein Products, Lincoln, Nebraska).

Preparation of Anorganic Bone from Bovine Femurs. The first step in preparing biologically derived hydroxyapatite, or anorganic bone, was to remove all, or as much as possible, of the organic material from the bone. Sections of bovine femur were cut into pieces that are roughly 15 mm x 15 mm x 10 mm, so that they could fit into a large Soxhlet extractor. The majority of the marrow was manually removed and discarded. Enough bone was added to fill approximately 50% of the volume of the extractor. The extraction solvent was 80% ethylene diamine and 20% water.<sup>29-31</sup> Once the extraction apparatus began cycling, it was wrapped with aluminum foil to reduce heat loss and decrease cycling time. The extraction process was then continued for approximately 2000 cycles over 6 days. The boiling point of the extraction solvent was monitored and determined to be 119 °C. After the 6 days, the extraction solvent was replaced with deionized water. Extractions were run for another 24 hours before the water was exchanged for with fresh water. This process was repeated two additional times to remove the excess ethylene diamine. After all extractions were completed the bone pieces were removed from the Soxhlet extractor and allowed to air dry for 24 hours

before further processing. Once the bone had dried completely, it was ground in a Mister Coffee® coffee grinder to a particle size of less than 10  $\mu\text{m}$ . The bone powder was then stored for further use.

The sintering temperature and the sintering time proved to be the two most important parameters that controlled the reactivity of the powdered anorganic bovine bone. Sintering temperatures from 300  $^{\circ}\text{C}$  to 1300  $^{\circ}\text{C}$  have been reported in the literature.<sup>29, 31-35</sup> In efforts to obtain a general understanding of the effect that sintering temperature plays in determining the efficacy of the HA in initiating subsequent polymerizations, samples of the powdered, extracted bovine bone were heated for 16 hours in increments of 100  $^{\circ}\text{C}$  over a range from 400  $^{\circ}\text{C}$  to 800  $^{\circ}\text{C}$ . Sintering was accomplished by preheating the muffle furnace to the desired temperature and placing cleaned alumina crucibles in the oven to allow them to thermally equilibrate. Crucibles were cleaned by soaking them in *aqua regia* for 4 hours followed by heating in a muffle furnace at 1000  $^{\circ}\text{C}$  for 6 hours. Each time the sintering process was performed, approximately 8 grams of powdered bone were quickly placed in the preheated crucible and then quickly transferred into the preheated muffle furnace. This was done to minimize the amount of time needed to raise the temperature of the sample to the sintering temperature. In this particular set of studies, the samples were then allowed to heat in air for 16 hours at the desired temperature. After the desired sintering time had elapsed the powdered sample was placed into a vacuum desiccator and cooled under vacuum. As soon as the sample was cool enough to handle safely, it was transferred into a  $\text{N}_{2(\text{g})}$  atmosphere glove box and stored for later use.

Summary of Apparatus and Procedures for Kinetic Analyses: The reaction vessel for the kinetics experiments was based on a 50 ml round bottom flask with a 24/40 ground glass joint. The side of the flask was modified by adding an extended arm with a 14/20 ground glass joint at an angle of roughly 30°. The arm was extended so that the top of the 14/20 joint reached a level about 5 mm above the top of the 24/40 joint. This design allowed for the entire reaction vessel to be submerged into a constant temperature oil bath while ensuring that the 14/20 joint could still be used to take samples.

Kinetics reactions were setup by placing a portion of the sintered bone powder and powdered L-lactide in a 1 to 4 mass ratio into the reaction flask. The HA / L-lactide mixture was magnetically stirred at a rate sufficient to ensure that the rate was not limited by mass transfer. The 24/40 joint was fitted with a gas adapter and a hollow glass stopper was placed into the 14/20 joint. Each joint was greased with Krytox® grease, which is a fluoropolymer, not a standard silicone grease. My experience has shown that silicone grease will interfere with the reaction kinetics and must be avoided. The gas adapter was connected to a Schlenk line. The reaction flask was then evacuated and backfilled with N<sub>2(g)</sub>. This evacuation and backfilling was repeated three times. The flask was then kept under a constant positive pressure of flowing N<sub>2(g)</sub>. The reaction vessel was wrapped in aluminum foil and submerged into a 125 °C constant temperature oil bath to begin the polymerization. (Figure 2.2) Upon being submerged in the oil bath, the L-lactide in the flask began to melt. Approximately 2 min was generally required for the entire quantity of L-lactide to liquefy. The first sample aliquot was taken at this point in time, which was defined as time zero. L-lactide is very sensitive to the presence of water and oxygen. Therefore, all samples were taken with the utmost care in assuring that neither entered the



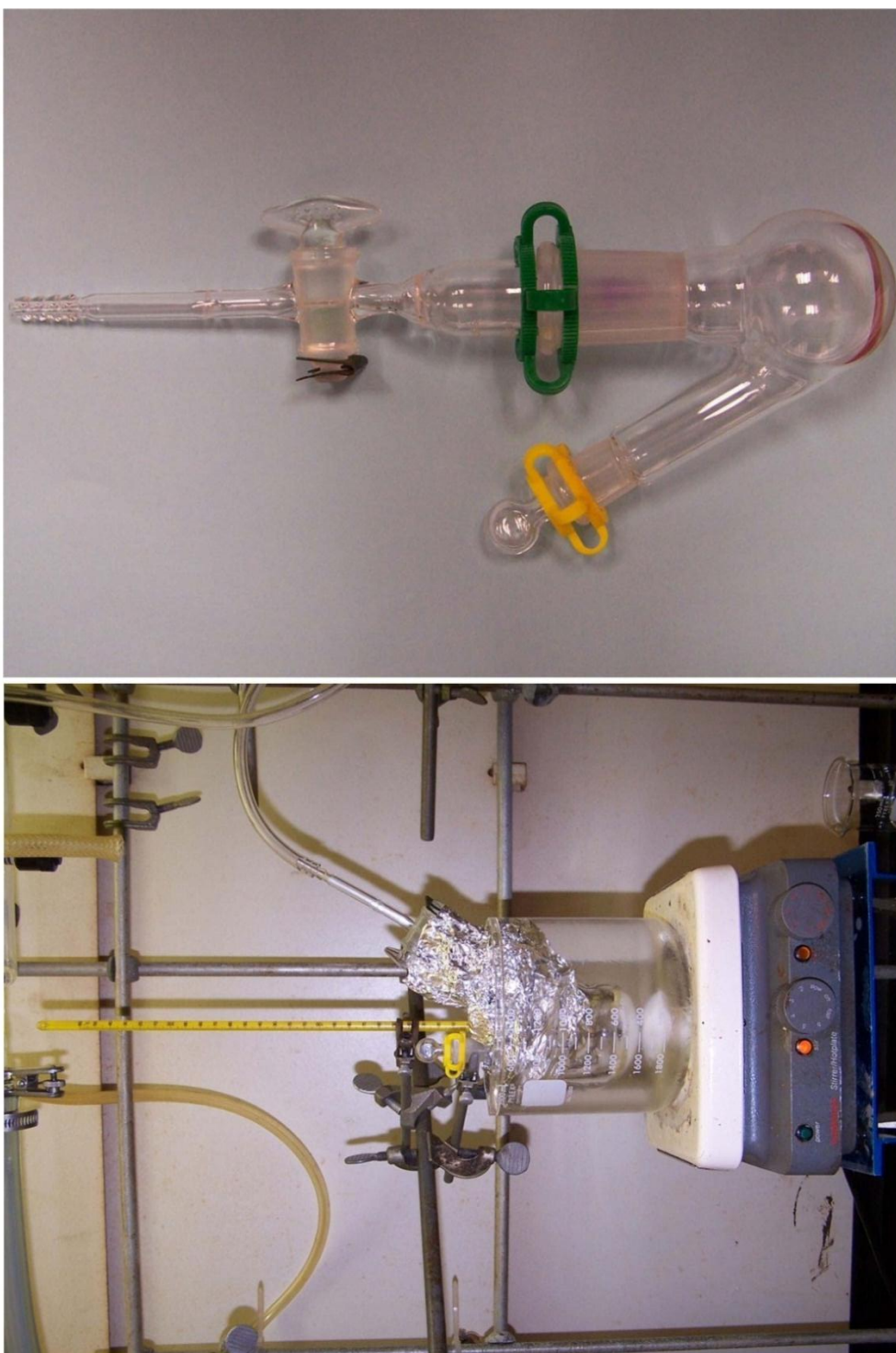


Figure 2.2. Kinetics reaction vessel submerged in a 125 °C oil bath (left) and the empty setup showing the 24/40 joint with gas adapter and 14/20 extended side arm for reaction sampling

reaction vessel, a circumstance that surely would have produced erroneous kinetic data. Samples were taken at regular time intervals to monitor the progression of the reaction. The  $N_{2(g)}$  flow rate was increased to 100 ml/min, and the tip of a 9-inch disposable pipet was quickly dipped into the reaction mixture to obtain a sample aliquot. A small aliquot of sample was drawn into the pipet by capillary action. The pipet was then expeditiously removed and cooled quickly to solidify the aliquot and thermally quench the reaction. The tip of the pipet was then snapped off, crushed, and stored in a small glass vial until needed. The reaction was monitored for several hours or until the viscosity became so great that mass transport effects began to interfere with uniform mixing by the magnetic stir bar.

Once a suitable number of samples were taken from the reaction, each aliquot was dissolved in  $CDCl_3$ . The samples were then centrifuged and 1.0 ml of the solution was placed into an NMR tube for later analysis by  $^1H$  NMR spectroscopy. A  $^1H$  NMR spectrum for each sample was obtained using a Bruker Avance DRX 500 MHz NMR with 5 mm Triple-resonance  $^1H/^{13}C/^{15}N$  cryoprobe and a BACS 120 sample changer. For each separate kinetics trial all the samples were loaded in to the sample changer and run sequentially. Each spectrum was obtained by acquiring 512 scans to ensure excellent signal to noise ratio. Spectral processing was done using Bruker Topspin 3.0.b.8.

It was first necessary to characterize all relevant monomer and polymer peaks to obtain good quality and accurate signals and integrals from the spectra. A reference L-lactide monomer spectra was obtained from the sublimed reagent. (Figure 2.3) It was determined that the methyl protons exhibited the characteristic doublet with chemical

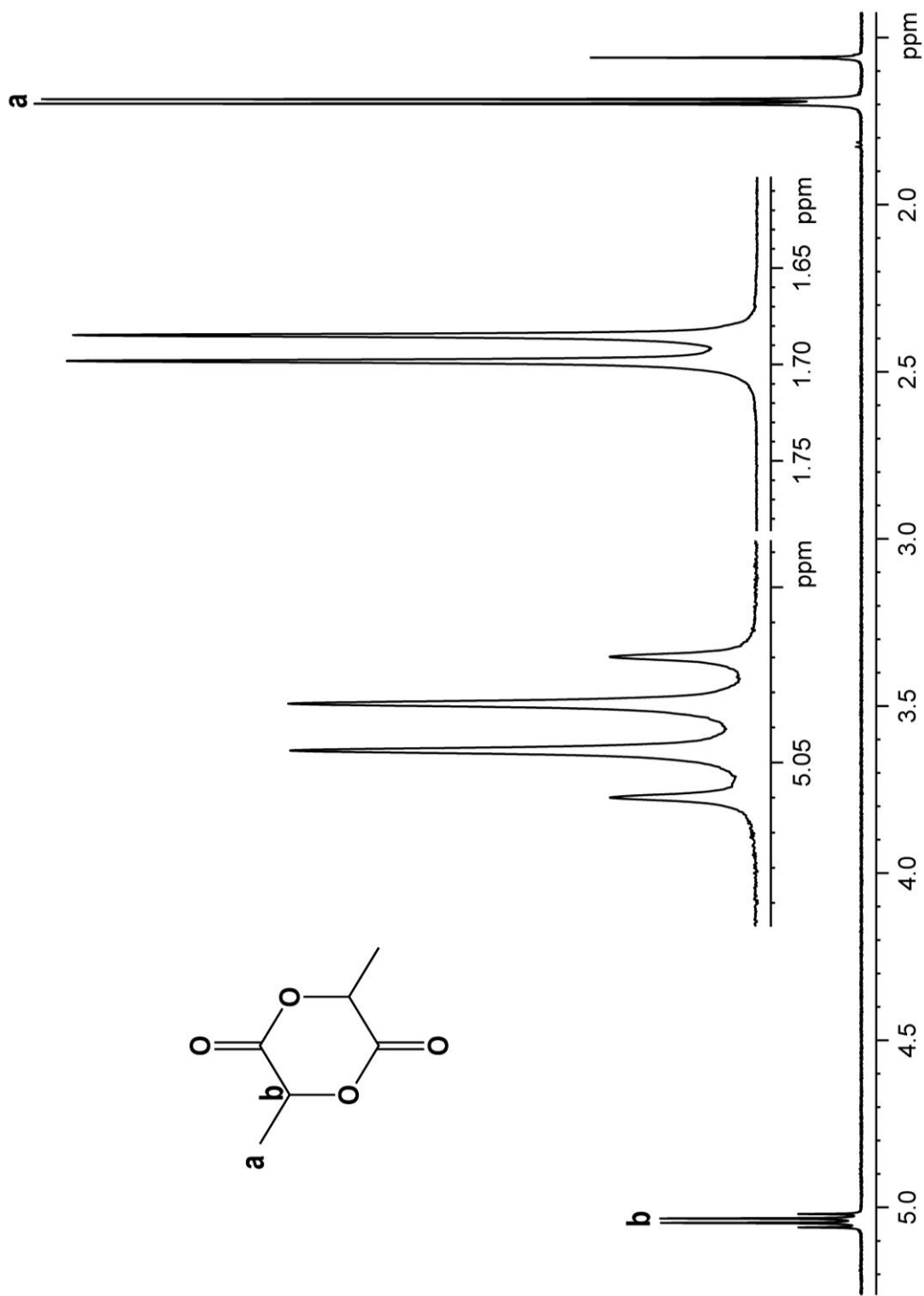


Figure 2.3. 1D <sup>1</sup>H NMR spectrum of L-lactide monomer reagent after purification by sublimation

shift at 1.624 ppm, while the methine quartet is downfield with chemical shift at 5.045 ppm. These chemical shifts are consistent with literature values.<sup>36-39</sup> The  $\text{CDCl}_3$  solvent singlet was used as an internal standard. It was set to a chemical shift of 7.270 ppm.

A pure polymer reference was obtained by allowing 0.250 g of  $\text{Ca}(\text{OH})_{2(s)}$  to react to completion with 2.0 g of L-lactide at 125 °C. The resulting polymer was dissolved in dry chloroform and residual solids were filtered off. The supernatant was then cooled in an ice bath and cold methanol was added. This solution was then cooled with dry ice to recrystallize the polymer as a fluffy white powder.<sup>40</sup> The powder was then collected by vacuum filtration and washed liberally with cold methanol. The purified polymer was dried under vacuum at room temperature for 24 hrs to remove any residual chloroform and methanol. A reference polymer spectrum was obtained in  $\text{CDCl}_3$  with the solvent singlet reference at 7.270 ppm. A methine quartet can be attributed to a hydroxyl end group at 4.36 ppm.<sup>36</sup> The methine quartet attributed to a carboxylate end group overlaps with the internal methines of the polymer to give a broad set of overlapping quartets from 5.28 ppm to 5.10 ppm.<sup>36, 37</sup> (Figure 2.4) An additional polymerization was carried out to verify the results of the polymerization with  $\text{Ca}(\text{OH})_{2(s)}$ . For this reaction 0.150 g dry calcium lactate was used to initiate the polymerization of 2.0 g of L-lactide. The reaction was run at 125 °C and allowed to proceed to completion. The resulting polymer was recrystallized from chloroform and methanol using the method outlined previously. A third polymer sample was synthesized directly from L-lactic acid by refluxing a stirred solution of 50 ml of 85% L-lactic acid and 15% water under hard vacuum in a 250 ml

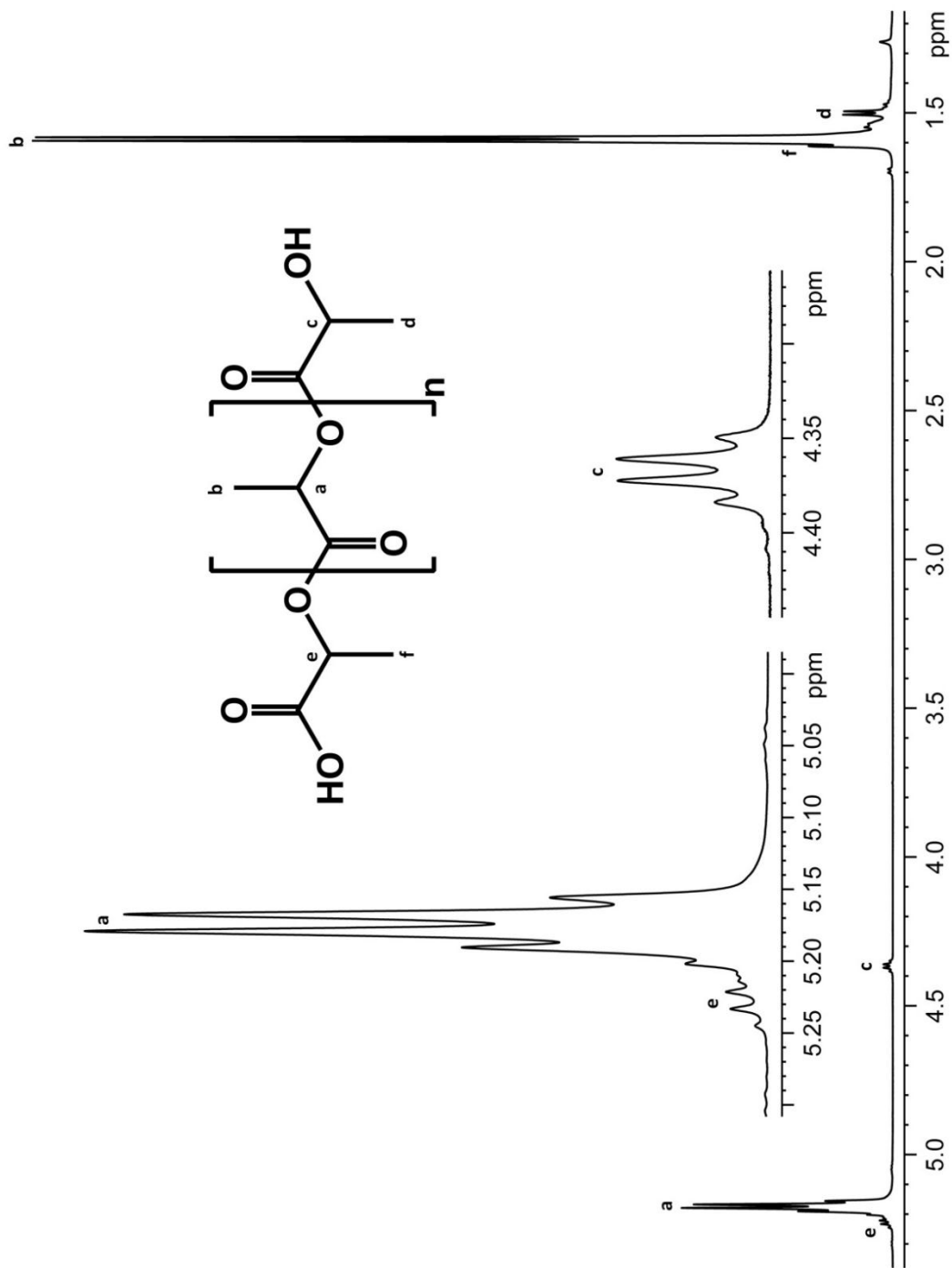


Figure 2.4. 1D  $^1\text{H}$  NMR spectrum of recrystallized PLLA from 0.250g of  $\text{Ca}(\text{OH})_2$  and 2.0g L-lactide

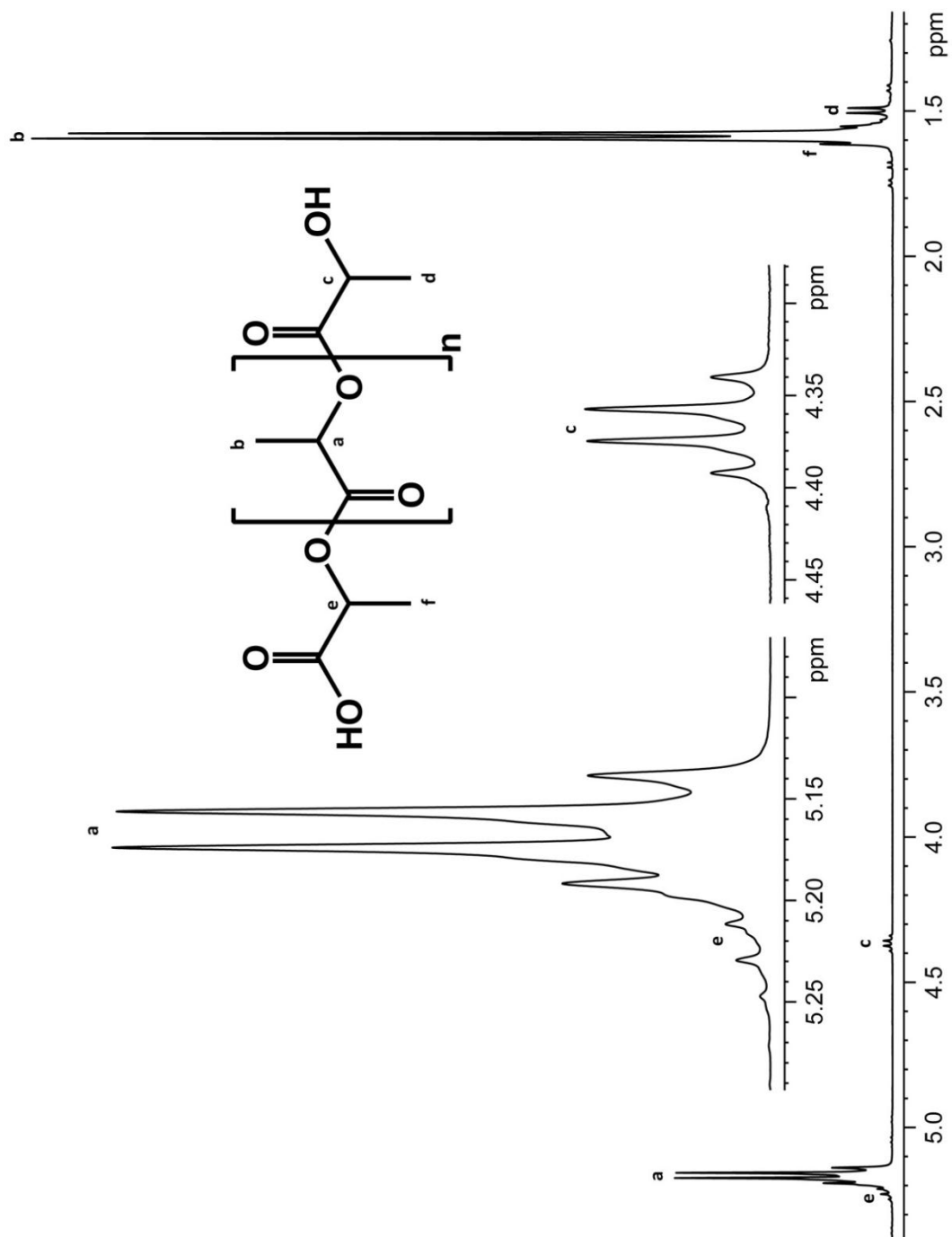


Figure 2.5. 1D  $^1\text{H}$  NMR spectrum of recrystallized PLLA from the polycondensation of 85% L-lactic acid

round bottom flask while stirring.<sup>41-43</sup> This method causes a simple condensation reaction where the alcohol and carboxylic acid condense to the ester. This crude polymer was also recrystallized from chloroform and methanol. (Figure 2.5) <sup>1</sup>H NMR spectra were taken for all polymer and reference samples in CDCl<sub>3</sub> with the solvent singlet referenced to 7.270 ppm. These three spectra were then compared to a commercial sample of poly L-lactic acid. All spectra showed the same characteristic multiplets with chemical shifts that could not be distinguished from one another.

It was possible to determine the mole fraction of monomer in each of the reaction aliquots once the polymer and monomer peaks for L-lactide and poly-L-lactide (PLLA) were identified. The general formula for attaining the mole fraction of using <sup>1</sup>H NMR as tool to determine the amounts of monomer and polymer present equation is

$$M_t = \frac{I_M}{I_M + I_P} \quad (2.7)$$

where I<sub>M</sub> is the integrated area of the monomer methine protons and I<sub>P</sub> is the integrated area of the polymer methine protons.<sup>4, 5, 14</sup>

The integrated area for the polymer consists of the internal polymer chain methine protons (I<sub>I</sub>) as well as the hydroxyl end group at 4.36 ppm (I<sub>A</sub>) (*vide supra*) and the carboxylate end group at (I<sub>C</sub>) .

$$I_P = I_I + I_C + I_A \quad (2.8)$$

Since the carboxylate end group methine quartet is convolved with the methine quartet from the internal polymer chain protons and the monomer <sup>13</sup>C satellites, it is impractical to get each value separately. Instead the entire region from 5.10 ppm to 5.28 ppm is

integrated and taken as one value for the purposes of calculating  $I_I + I_C$ . This region is defined by the equation

$$I_{P_{app}} = (I_I + I_C + I_{M_S}) + I_A \quad (2.9)$$

where  $I_{P_{app}}$  is the apparent polymer integrated area and  $I_{M_S}$  is the integrated area for the monomer  $^{13}\text{C}$  satellites. Early in the reaction the satellites can be anywhere from 50% to 200% of the value of the polymer integral. Not compensating for this would give erroneously low values of  $M_t$  early in the reaction. Since the isotopic abundance of  $^{13}\text{C}$  is 1.1%, the integral value of the satellite can be obtained by multiplying the monomer quartet integral by 0.0055.

$$I_{M_S} = 0.0055(I_M) \quad (2.10)$$

Substituting equation 2.10 into equation 2.9 gives

$$I_{P_{app}} = (I_I + I_C + 0.0055(I_M)) + I_A \quad (2.11)$$

Rearranging equation 2.11 yields

$$I_I + I_C + I_A = I_{P_{app}} - 0.0055(I_M) \quad (2.12)$$

Substituting 2.12 into 2.8 gives

$$I_P = I_{P_{app}} - 0.0055(I_M) \quad (2.13)$$

Integral values for each individual aliquot from the kinetic experiment were then acquired. Spectrum processing consisted of a standard Fourier transform of the free induction decay, automated phase correction, and referencing of the  $\text{CDCl}_3$  singlet to



7.270 ppm. In a small number of samples, it was necessary to manually phase the spectra to obtain optimum quality. Baseline correction was performed using a fifth order polynomial and correcting each region to be integrated separately. In a composite presentation of all spectra for the samples of a single kinetics experiment, the polymer peaks can be seen to grow in intensity while the monomer is decreasing. (Figure 2.6)

In addition to the polymer and monomer species identified above,  $^1\text{H}$  NMR spectra of the reaction mixtures showed the presence of a new species manifested by a new quartet and doublet at 5.081 ppm and 1.722 ppm respectively were quite noticeable. A two-dimensional COSY experiment showed that the unique protons were indeed coupled to each other and integration revealed that they were present in a 3 to 1 ratio of doublet to quartet. Peaks with this same integrated intensity and similar chemical shifts have previously been attributed to meso-lactide.<sup>44-47</sup> The presence of meso-lactide in the reaction mixture was verified as described below. Approximately 1.0 g of the reaction product (containing roughly 50% polymer and 50% mixed monomers) from the kinetics experiment was placed into a 13mm inner-diameter Pyrex® U-tube. (Figure 2.7) The tube was then sealed under vacuum and heated in a controlled manner to separate meso-lactide from L-lactide using the difference in their vapor pressures. The Clausius-Clapeyron equation is given by equation 2.15.

$$\ln(P) = -\frac{\Delta H}{R} \frac{1}{T} + C \quad (2.14)$$

In equation 2.14, P is vapor pressure,  $\Delta H$  is the enthalpy of sublimation, R is the ideal gas constant, T is temperature in Kelvin, and C is a constant. Given the reported vapor

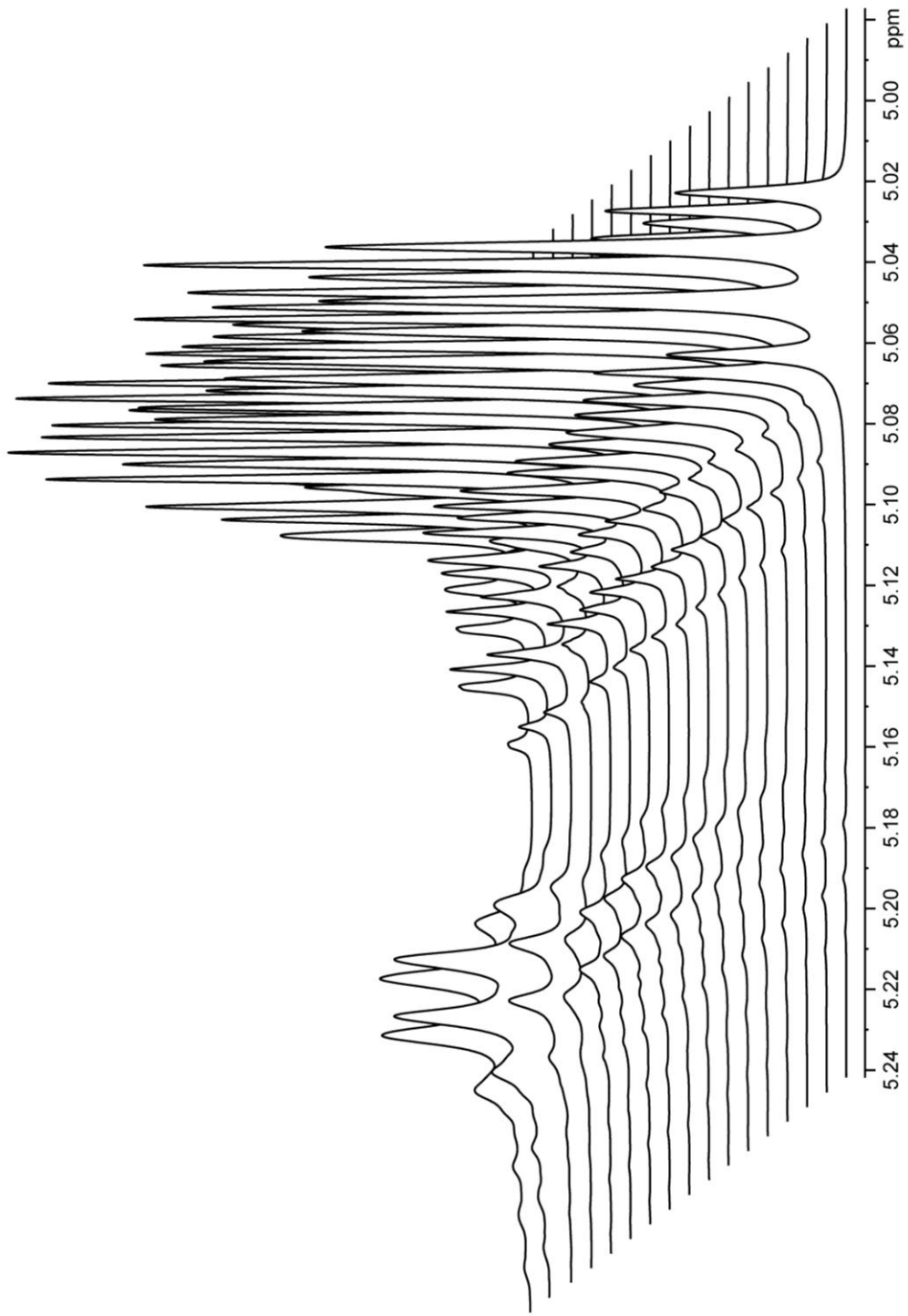


Figure 2.6. Composite 1D <sup>1</sup>H NMR spectra of a typical kinetics reaction of L-lactide initiated by sintered biologically derived hydroxyapatite

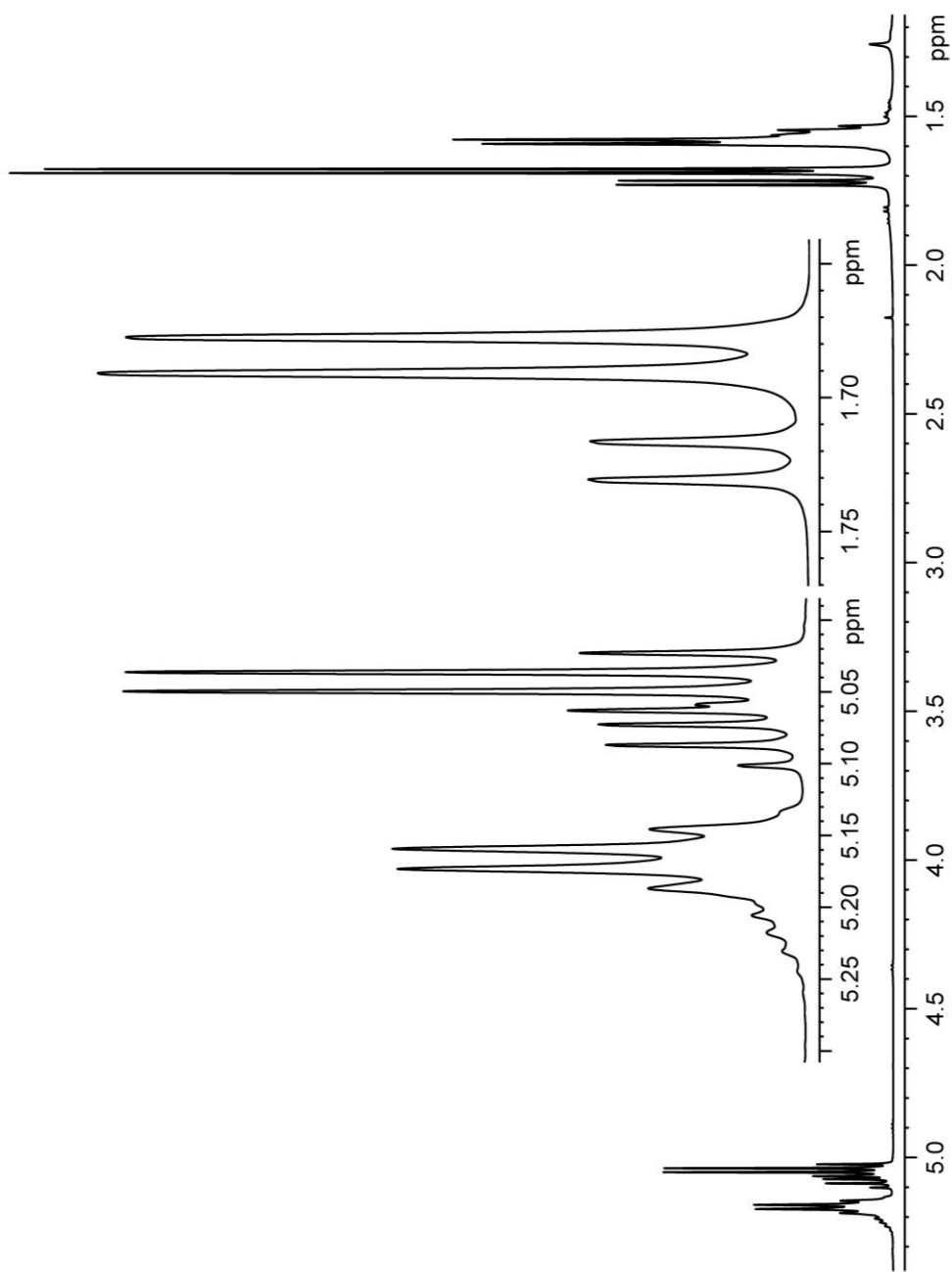


Figure 2.7. 1D  $^1\text{H}$  NMR spectrum of the kinetics reaction product used for the isolation of meso-lactide based on vapor pressure differences at low temperature

pressures for meso-lactide and L-lactide, one can approximate their vapor pressures as a function of temperature to construct plots such as the one shown in Figure 2.8.<sup>41, 48</sup> Note that at low temperatures the vapor pressure of meso-lactide is much greater than that of L-lactide. (Figure 2.8) These calculations suggested that it should be possible to isolate meso-lactide and L-lactide, or a mixture of the two, from the reaction material. This isolation was ultimately achieved using a glass U-tube. The mixture of reaction products was placed in one end of the U-tube and this end was maintained at -5 °C in a constant temperature bath. The other end was placed in liquid nitrogen. After 24hrs a white haze of sublimed materials was observed on the inside of the section of tube submerged in liquid nitrogen. The tube was opened and the sublimate was removed with a cotton swab and dissolved in CDCl<sub>3</sub>. A <sup>1</sup>H NMR spectrum revealed the sample to be a mixture of L-lactide and meso-lactide that was enriched in the meso isomer. (Figure 2.9)

It was necessary to synthesize a pure sample of pure meso-lactide to verify that the isolated material was indeed a mixture of lactides and that the unknown quartet can be attributed to meso-lactide. Comparison to a species purchased from a vendor is not presently possible because meso-lactide is no longer commercially available.

Synthesis of meso-lactide was executed by adapting procedures already found in the literature.<sup>40, 44, 45, 48</sup> A total of 50 ml of L-lactic acid and 50ml of D-lactic acid was added to a 250 ml round bottom flask. The flask was fitted with a gas adapter and placed under hard vacuum to remove any water produced and speed the reaction. The mixture was refluxed for 24 hrs to initiate the polycondensation reaction. At the end of this time 5 g of the raw prepolymer was placed in the bottom of a small sublimator and 0.100 g of

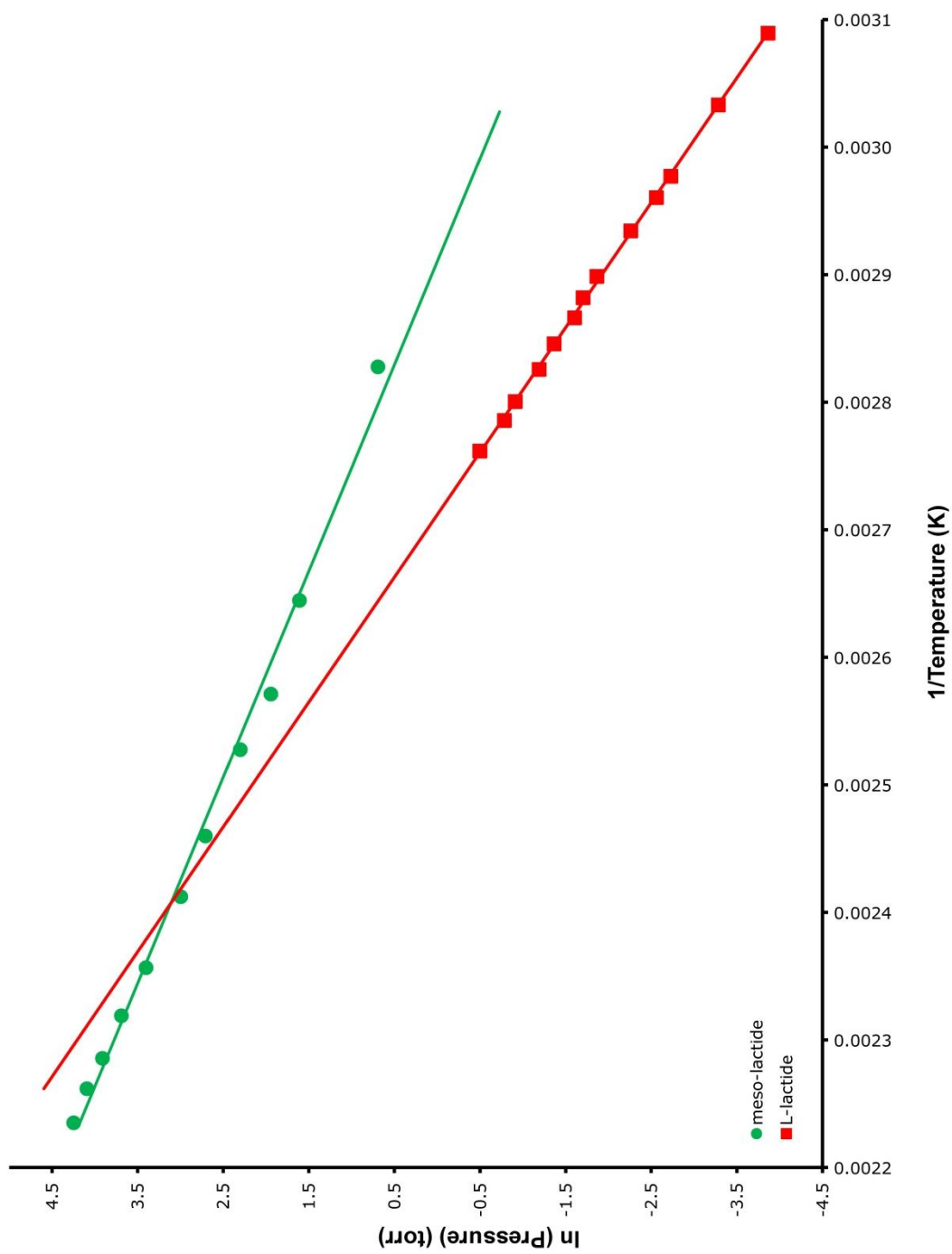


Figure 2.8. Clausius-Clapeyron plot of L-lactide and meso-lactide

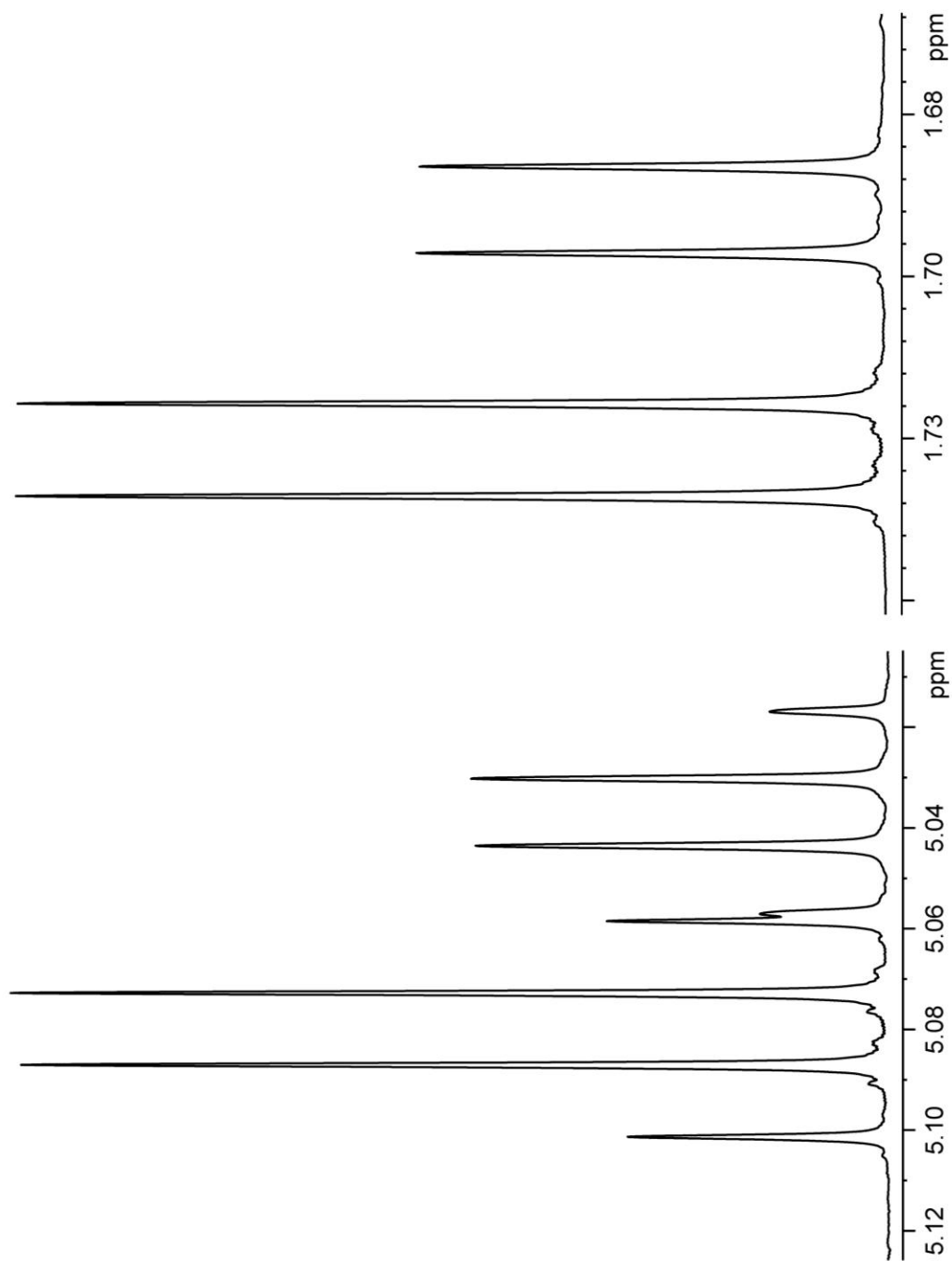


Figure 2.9. 1D  $^1\text{H}$  NMR spectrum of meso-lactide and L-lactide collected from kinetics reaction product

Sn(II)oct<sub>2(1)</sub> was added. The cold finger was attached to a chiller unit for which the bath temperature was set to -5 °C. The reaction setup was submerged to the middle of the cold finger in a 200 °C oil bath and placed under vacuum. The addition of the tin catalyst, high temperature, and vacuum cause a depolymerization reaction to occur where polylactones are cracked back to their respective lactone monomers.<sup>46</sup> The monomer was then captured on the cold finger. The reaction was allowed to run for 24 hrs, at which time a layer of fine white crystals were seen on the cold finger. <sup>1</sup>H NMR spectroscopy showed that the crystals were a roughly 60% meso-lactide and 40% a mixture of the two enantiomers, L-lactide and D-lactide. (Figure 2.10) Further purification was not pursued due to the elaborate condenser setup required. Because the unknown quartet in the reaction of L-lactide with hydroxyapatite was identified as meso-lactide, a diastereomer of the monomer L-lactide, in all kinetics reactions the mole fraction of monomer is treated as the sum of the mole fractions of meso and L-lactides. Both are eventually consumed and converted to polymer at rates that appear to be indistinguishable for the kinetics reactions I completed. The individual monomer components can now be represented in the equation

$$I_M = I_{M_L} + I_{M_{meso}} \quad (2.15)$$

where  $I_{M_L}$  is the integrated area of L-lactide monomer,  $I_{M_{meso}}$  is the integrated area for meso-lactide, and where  $I_{M_{meso}} \ll I_{M_L}$ . This approximation is particularly useful because there is some overlap of the meso-lactide and L-lactide peaks over chemical shifts ranging from 5.120 ppm to 5.011 ppm. It is noteworthy that if the kinetics of meso-lactide incorporation during chain propagation steps were significantly different

than that for L-lactide, significant deviations from linearity would be observed in plots of  $-\ln \frac{M_t}{M_0}$  versus t. Integral values were then entered into an Excel® spreadsheet for further analysis. (Table 2.1) When  $-\ln \frac{M_t}{M_0}$  is plotted versus time for the desired kinetics experiments with L-lactide a line is obtained with slope of  $k_{app}$ . (Figure 2.11)

I also examined the influence of HA sintering temperature on the polymerization of  $\epsilon$ -caprolactone, another biocompatible lactone that is known to undergo ring opening polymerization.<sup>1, 3</sup> It was necessary to assign all peaks in the  $^1\text{H}$  NMR spectra for  $\epsilon$ -caprolactone and its respective polymer before being able to calculate  $M_t$ .  $\epsilon$ -Caprolactone monomer poly- $\epsilon$ -caprolactone have been well characterized in the literature but it was still necessary to locate at least one end group in the polymer to make assignments that could be used to interpret the kinetic results. First, a  $^1\text{H}$  NMR spectrum of  $\epsilon$ -caprolactone was obtained in  $\text{CDCl}_3$ , and the chemical shifts were verified to be consistent with literature values.<sup>49-51</sup> (Figure 2.12) A “standard sample” of poly- $\epsilon$ -caprolactone was prepared by polymerizing  $\epsilon$ -caprolactone with  $\text{Ca}(\text{OH})_{2(s)}$ . A 0.250 g sample of dry  $\text{Ca}(\text{OH})_{2(s)}$  was mixed with 4.0 g of  $\epsilon$ -caprolactone in a 50ml round bottom flask with a 24/40 ground glass joint. The flask was fitted with a gas adapter and then the reaction was heated to 125 °C and kept under a positive pressure of flowing  $\text{N}_{2(g)}$ . The reaction was allowed to run several days to reach completion. At the end of this time a small amount of the reaction product was dissolved in  $\text{CDCl}_3$  and filtered through a 0.45  $\mu\text{m}$  syringe filter to remove the solids. A  $^1\text{H}$  NMR spectrum was run and the chemical shifts of the protons were assigned based on reported literature values.<sup>52</sup> (Figure 2.13)



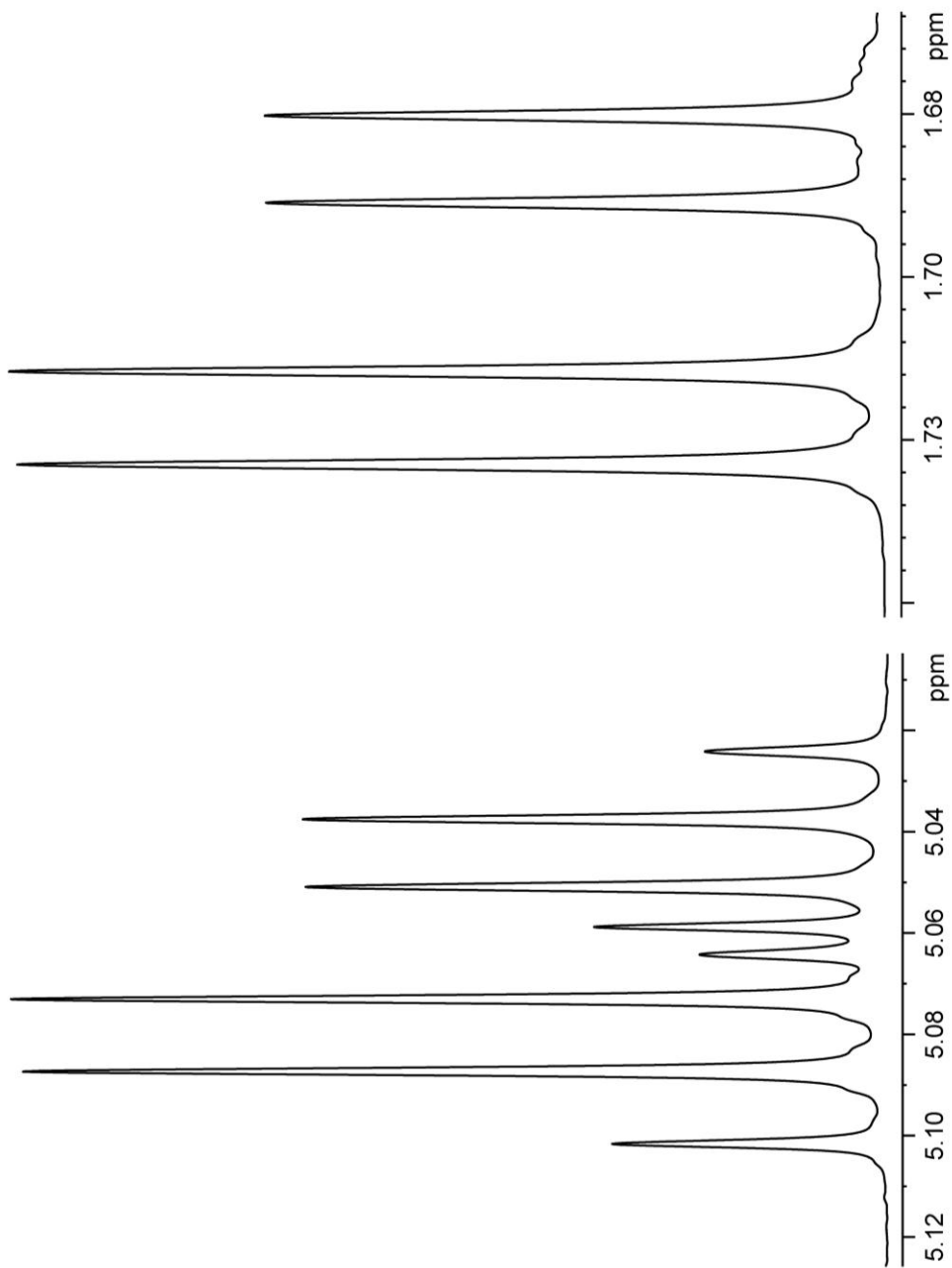


Figure 2.10. 1D  $^1\text{H}$  NMR spectrum of meso-lactide, and D-lactide and L-lactide obtained from the cracking of low molecular weight atactic polylactic acid

| Sample | Elapsed Time (min) | Polymer and Acid End Group (5.120 to 5.280ppm) (Integrated Area) | Monomers (5.011 to 5.110ppm) (Integrated Area) | Hydroxyl End Group (4.35ppm) (Integrated Area) | Calculated Monomer <sup>13</sup> C Satalites | Mole Fraction of Monomer | -ln (Mole Fraction of Monomer) |
|--------|--------------------|--|--|--|--|--------------------------|--------------------------------|
| 1      | 0                  | 0.5395   | 99.4212  | 0.0392   | 0.546817                                     | 0.9997                   | 0.0003206                      |
| 2      | 13                 | 1.0727   | 98.8637  | 0.0636   | 0.543750                                     | 0.9940                   | 0.0059757                      |
| 3      | 27                 | 2.0609   | 97.8251  | 0.1139   | 0.538038                                     | 0.9835                   | 0.0165931                      |
| 4      | 54                 | 2.4972   | 97.3656  | 0.1371   | 0.535511                                     | 0.9789                   | 0.0213267                      |
| 5      | 81                 | 3.8223   | 96.0282  | 0.1495   | 0.528155                                     | 0.9654                   | 0.0352327                      |
| 6      | 115                | 6.0943   | 93.6521  | 0.2535   | 0.515087                                     | 0.9414                   | 0.0604182                      |
| 7      | 136                | 5.9842   | 93.7995  | 0.2162   | 0.515897                                     | 0.9429                   | 0.0588373                      |
| 8      | 163                | 7.2329   | 92.5182  | 0.2488   | 0.508850                                     | 0.9299                   | 0.0726623                      |
| 9      | 190                | 8.3006   | 91.4606  | 0.2388   | 0.503033                                     | 0.9192                   | 0.0842189                      |
| 10     | 217                | 9.7767   | 89.9203  | 0.3029   | 0.494562                                     | 0.9037                   | 0.1012876                      |
| 11     | 245                | 11.1930  | 88.4969  | 0.3099   | 0.486733                                     | 0.8893                   | 0.1173214                      |
| 12     | 272                | 11.6182  | 88.0622  | 0.3195   | 0.484342                                     | 0.8849                   | 0.1222706                      |
| 13     | 299                | 12.4303  | 87.2323  | 0.3373   | 0.479778                                     | 0.8765                   | 0.1317852                      |
| 14     | 326                | 14.6760  | 84.8629  | 0.4611   | 0.466746                                     | 0.8526                   | 0.1594548                      |
| 15     | 583                | 22.5685  | 76.9658  | 0.4656   | 0.423312                                     | 0.7729                   | 0.2575659                      |
| 16     | 1349               | 45.2032  | 54.3037  | 0.4930   | 0.298670                                     | 0.5447                   | 0.6075856                      |
| 17     | 1417               | 46.8078  | 52.6823  | 0.5098   | 0.289753                                     | 0.5284                   | 0.6379879                      |

Table 2.1. Representative Excel® spreadsheet for a kinetics reaction of L-lactide polymerization initiated by sintered hydroxyapatite

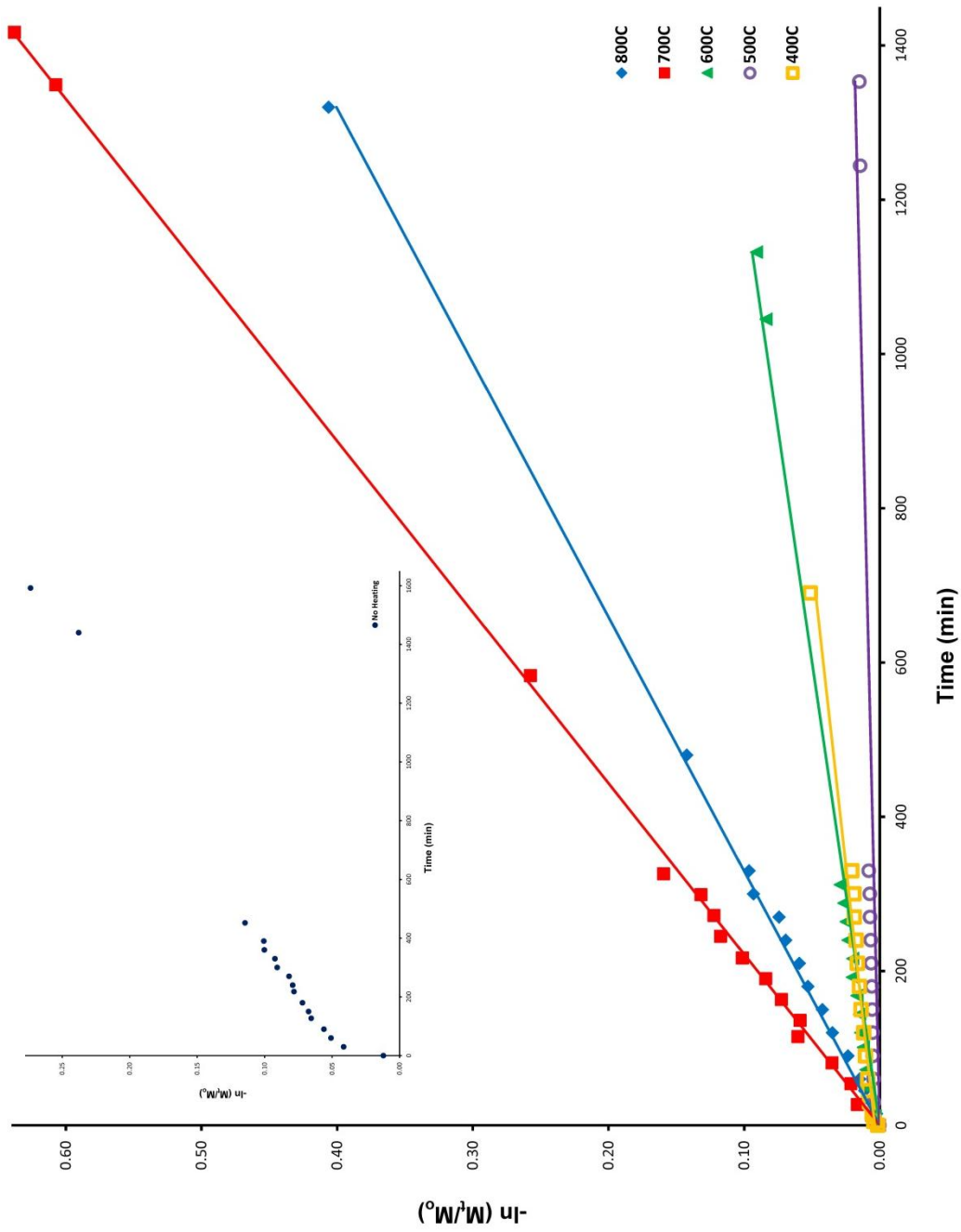


Figure 2.11. main: Kinetics plots for L-lactide reacted with bovine hydroxyapatite samples sintered at 100 °C inset: Kinetic plot of L-lactide reacted with non-sintered bovine hydroxyapatite increments

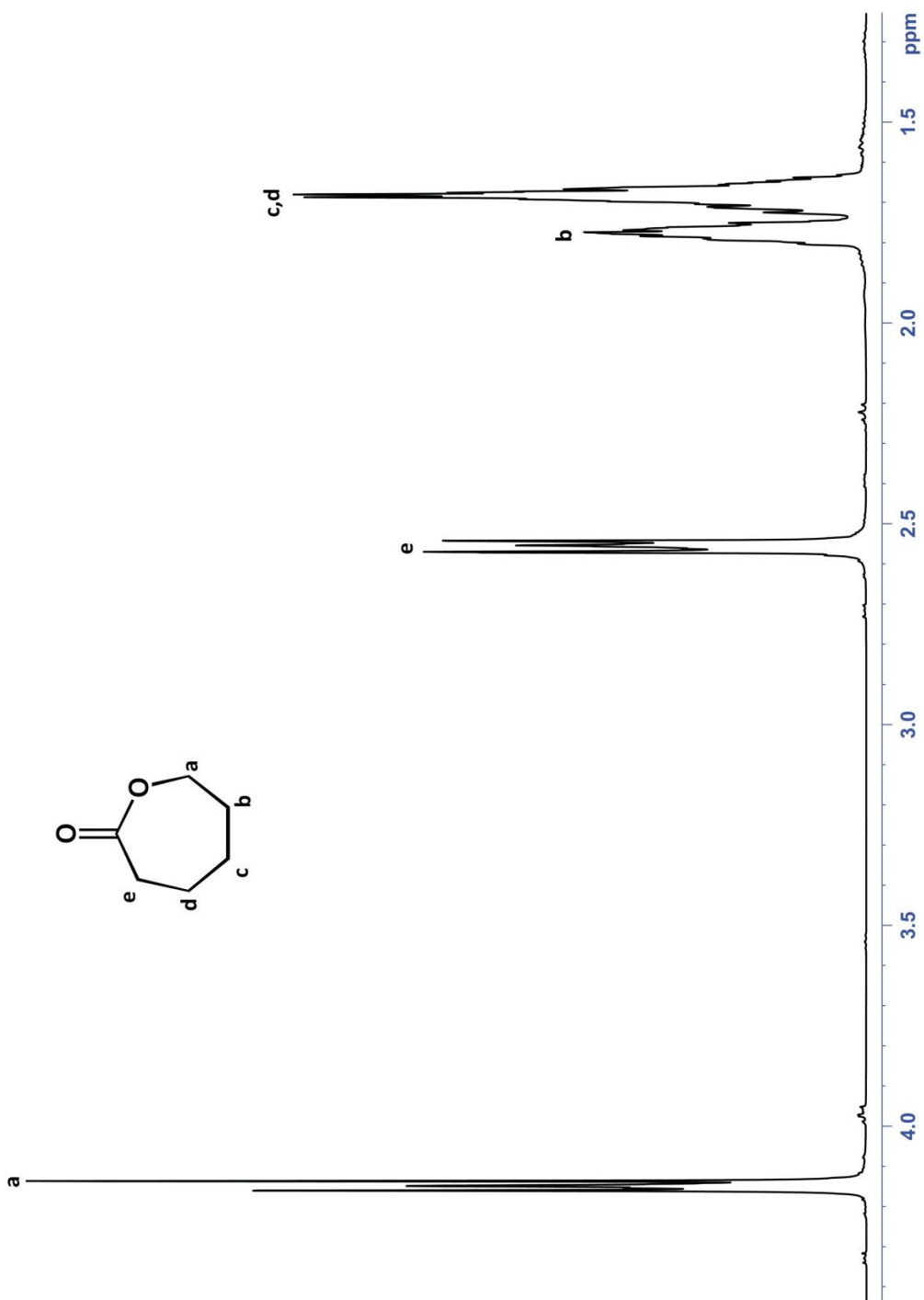


Figure 2.12. 1D  $^1\text{H}$  NMR spectrum of  $\epsilon$ -caprolactone monomer

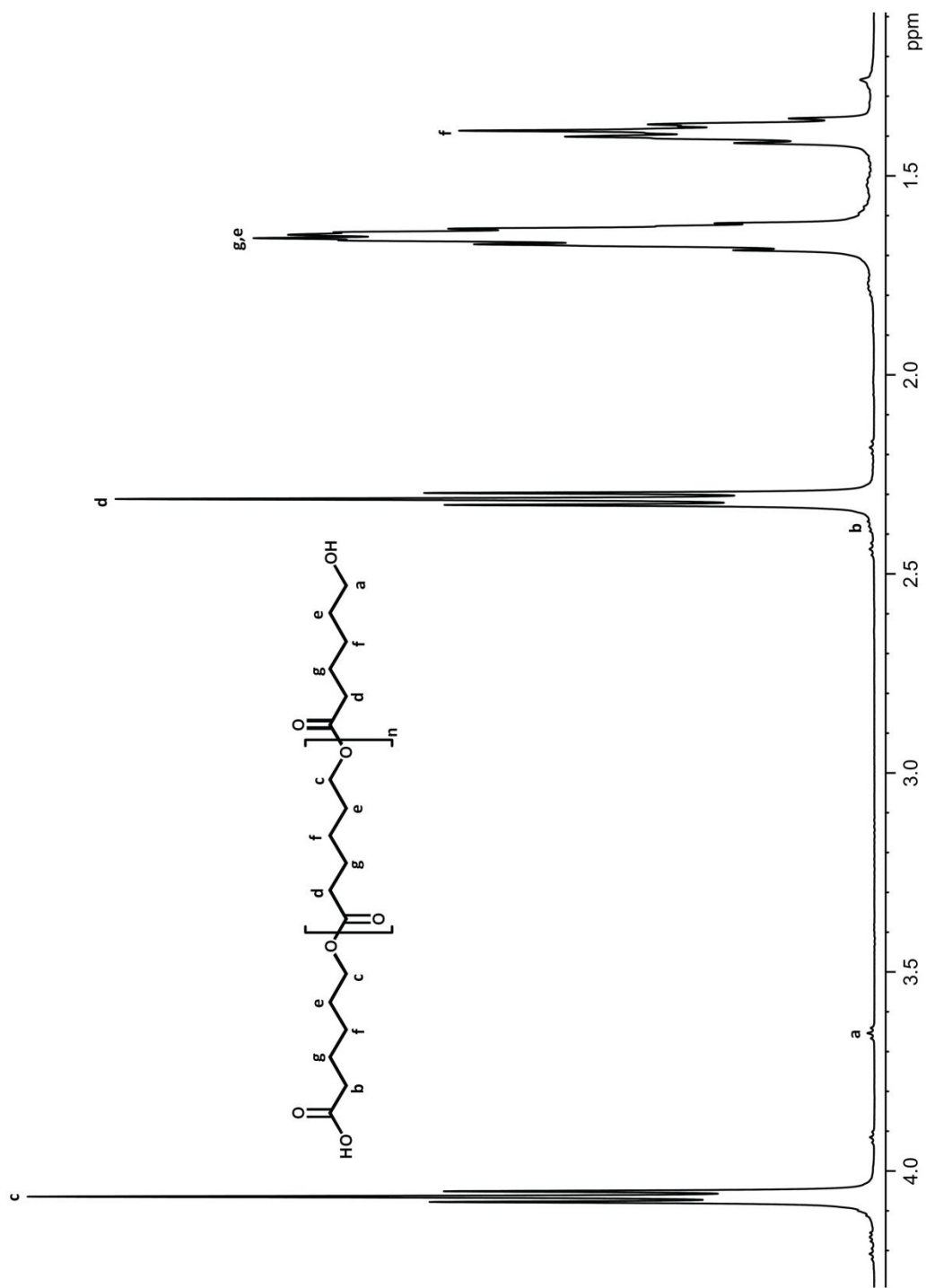


Figure 2.13. 1D <sup>1</sup>H NMR spectrum of poly-ε-caprolactone made from 0.250g Ca(OH)<sub>2</sub> and 4.0g of ε-caprolactone

A second procedure was also used to prepare a “standard sample” of poly- $\epsilon$ -caprolactone. The most common method for polymerizing lactone monomers is to employ  $\text{Sn}(\text{Oct})_{2(l)}$  as a catalyst in concert with a weakly nucleophilic initiator. I selected water as the weak nucleophile. More specifically, 10ml of  $\epsilon$ -caprolactone and 0.01ml of water were added to a 25 ml round bottom flask. One drop of  $\text{Sn}(\text{Oct})_{2(l)}$  was added to catalyze the reaction before lowering the reaction vessel into a 125 °C oil bath. The resulting polymerization reached completion in approximately 4 hours. (Figure 2.14) Finally, a sample of poly- $\epsilon$ -caprolactone was also purchased and its  $^1\text{H}$  NMR spectrum was used in concert with the polymer samples described above to identify the polymeric components of the reaction between poly- $\epsilon$ -caprolactone and hydroxyapatite. (Figure 2.15)

The process of using  $^1\text{H}$  NMR spectroscopy to assess rates of polymerization is much more straightforward for  $\epsilon$ -caprolactone than it is for L-lactide. The monomer does not isomerize. Consequently, the kinetics can be parameterized by identifying and integrating single discrete monomer and polymer groups in the  $^1\text{H}$  NMR. In addition, the molecular weight of the polymer can be quantified if a polymer end group can be identified and successfully integrated. For the purposes of the kinetics described in this thesis, the monomer proton at 2.646 ppm, the polymer peak at 2.313 ppm, and the hydroxyl end group at 3.655 ppm were selected. Thus mole fraction of  $\epsilon$ -caprolactone,  $M_t$ , is defined in the following equation.

$$M_t = \frac{I_M}{I_M + I_I + I_C + I_A} \quad (2.16)$$

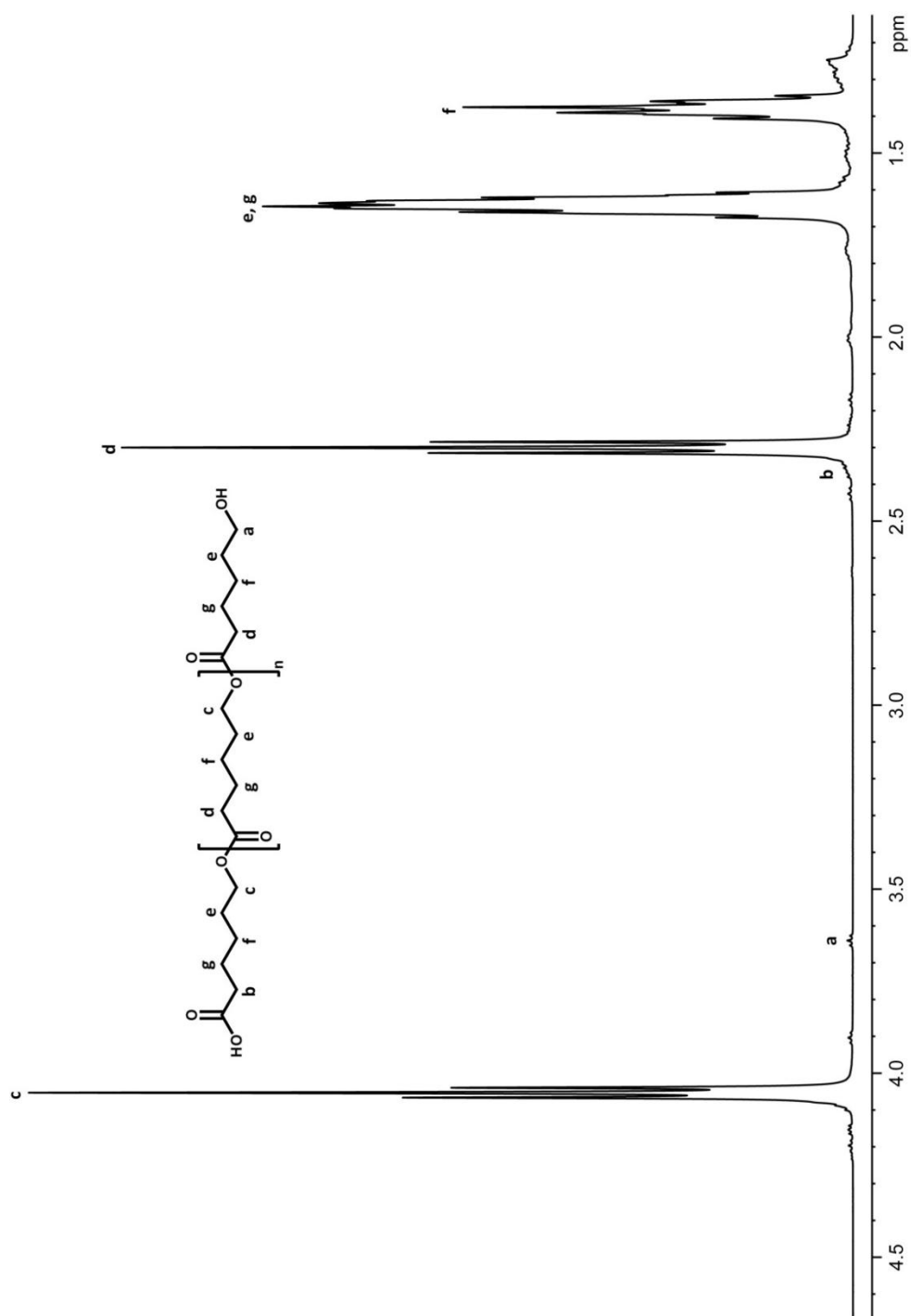


Figure 2.14. 1D <sup>1</sup>H NMR spectrum of poly-ε-caprolactone made by coordination insert with water initiator and Sn(oct)<sub>2</sub> catalyst

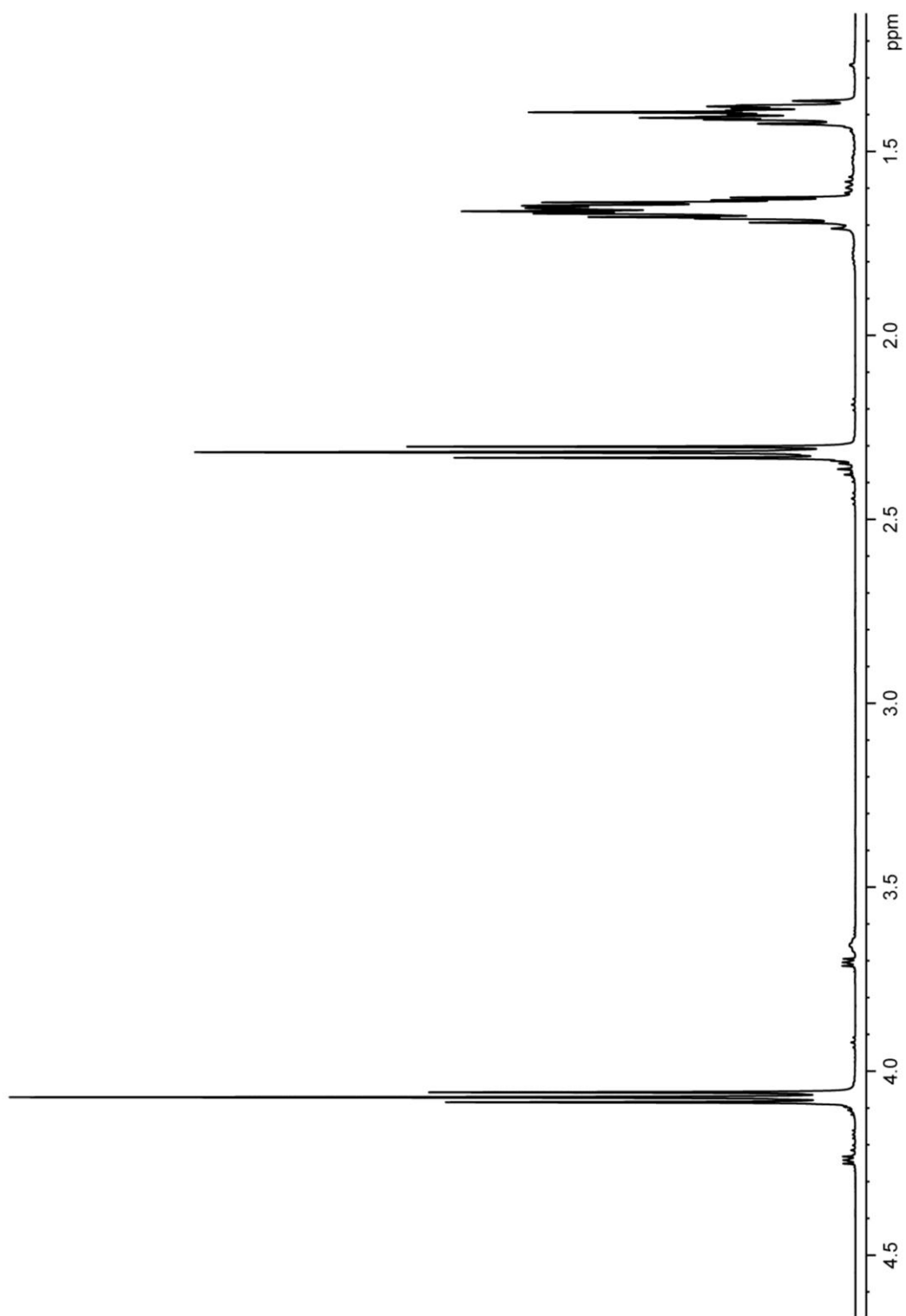


Figure 2.15. 1D  $^1\text{H}$  NMR spectrum of commercially available poly- $\epsilon$ -caprolactone,  $M_n = 10,000$ ,  $M_w = 12,000$



Polymerizations of  $\epsilon$ -caprolactone were executed using the same powdered, extracted, bovine bone that was used for the polymerization of L-lactide (*vide supra*). HA sintering temperatures ranged from 400 °C to 800 °C in 100 °C increments. Additionally, the apparatus and polymerization methodology for polymerizing  $\epsilon$ -caprolactone was the same as that outlined earlier for L-lactide. A representative  $^1\text{H}$  NMR spectrum of the reaction mixture at one time point in a kinetics experiment is shown in Figure 2.16. A representative composite of all  $^1\text{H}$  NMR spectra acquired for a kinetics experiment run using HA sintered at 700 °C is shown in Figure 2.17. Note the time dependent decrease in monomer concentration with concomitant increases attributed to polymer and hydroxyl end groups. Integrated intensities of the three chosen peaks were entered into an Excel® spreadsheet for further processing and plotting. Figure 2.18 shows first order kinetics plots for the polymerization of  $\epsilon$ -caprolactone with HA sintered at various temperatures for 16 hrs. The slopes of these plots give the apparent first order rate constants,  $k_{\text{app}}$ , which are tabulated in Table 2.2. A discussion of the apparent first order rate constants will be presented following the characterization of the sintered HA by surface area measurements, X-ray powder diffraction (XRD) and Fourier Transform Infrared Spectroscopy (FTIR). The discussion of these characterizations begins immediately below. One technique utilized for the characterization of sintered HA was X-ray powder diffraction (XRD). XRD is a spectroscopic method where a powdered sample of material is irradiated by a collimated x-ray beam. In single crystal diffraction only one crystal orientation is present so any beam diffraction is represented as a dot on the detector. These are referred to as Laue spots. In powder diffraction, it is assumed that every possible crystal orientation is present in equal quantity. The consequence of this is that

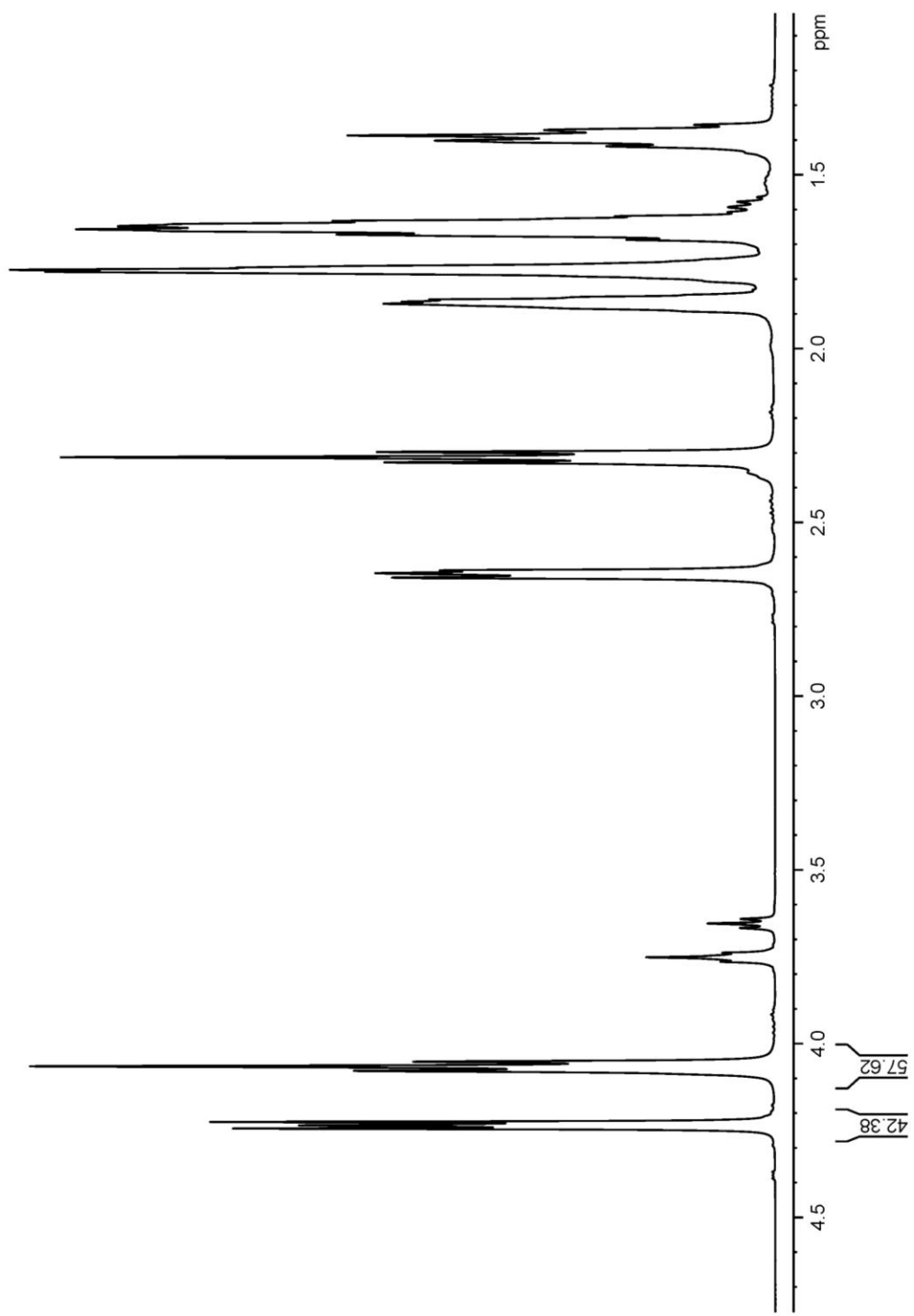


Figure 2.16. Intermediate time  $^1\text{H}$  NMR spectrum of a  $\epsilon$ -caprolactone kinetics reaction showing roughly 40% monomer and 60% polymer

| Sample | Elapsed Time<br>(min) | Monomer<br>(2.65ppm)<br>(Integrated Area) | Polymer<br>(2.31ppm)<br>(Integrated Area) | Hydroxyl End<br>Group (3.65ppm)<br>(Integrated Area) | Mole Fraction<br>of Monomer | -ln (Mole Fraction<br>of Monomer) |
|--------|-----------------------|---|---|--|-----------------------------|-----------------------------------|
| 1      | 0                     | 1   | 0.0076                                    | 0.0060   | 0.986582                    | 0.01350835                        |
| 2      | 60                    | 1   | 0.0252                                    | 0.0066   | 0.969180                    | 0.03130485                        |
| 3      | 188                   | 1   | 0.0329                                    | 0.0078   | 0.960892                    | 0.039893564                       |
| 4      | 244                   | 1   | 0.0563                                    | 0.0131   | 0.935104                    | 0.067097744                       |
| 5      | 1263                  | 1   | 0.2855                                    | 0.0134   | 0.769882                    | 0.261517752                       |
| 6      | 1363                  | 1   | 0.3040                                    | 0.0134   | 0.759071                    | 0.275660097                       |
| 7      | 1489                  | 1   | 0.3411                                    | 0.0148   | 0.737518                    | 0.30446544                        |
| 8      | 1605                  | 1   | 0.3791                                    | 0.0186   | 0.715461                    | 0.334828029                       |
| 9      | 1729                  | 1   | 0.4020                                    | 0.0200   | 0.703235                    | 0.352064331                       |
| 10     | 2711                  | 1   | 0.7443                                    | 0.0220   | 0.566155                    | 0.568886963                       |
| 11     | 2824                  | 1   | 0.7710                                    | 0.0249   | 0.556824                    | 0.585506289                       |
| 12     | 2944                  | 1   | 0.8605                                    | 0.0265   | 0.529942                    | 0.634988266                       |
| 13     | 3064                  | 1   | 0.9021                                    | 0.0364   | 0.515863                    | 0.661914478                       |
| 14     | 3184                  | 1   | 0.9435                                    | 0.0412   | 0.503854                    | 0.685467769                       |

Table 2.2. Representative Excel® spreadsheet for a kinetics reaction of  $\epsilon$ -caprolactone polymerization initiated by sintered hydroxyapatite

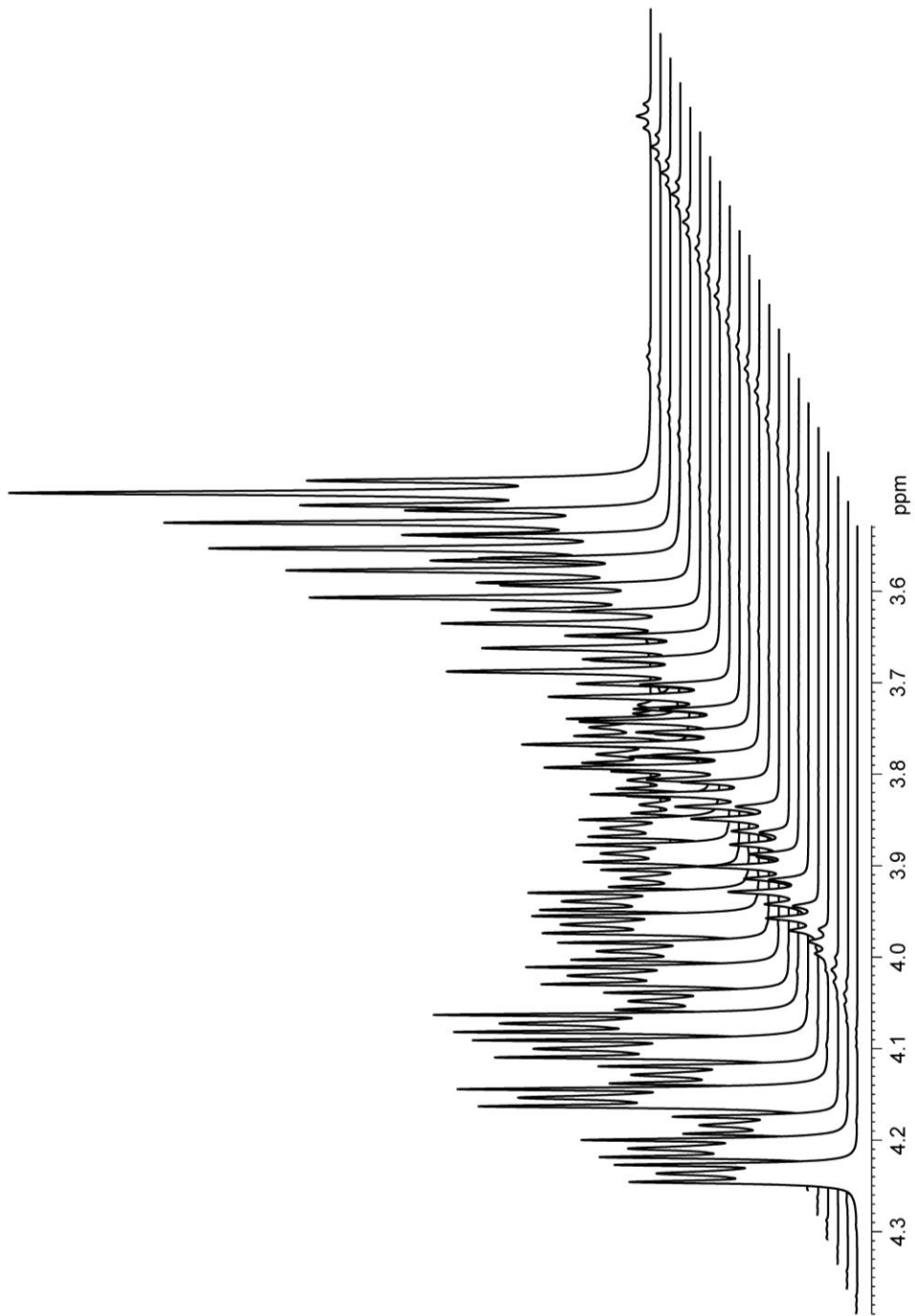


Figure 2.17. Composite 1D <sup>1</sup>H NMR spectra of a typical kinetics reaction of  $\epsilon$ -caprolactone initiated by sintered biologically derived hydroxyapatite

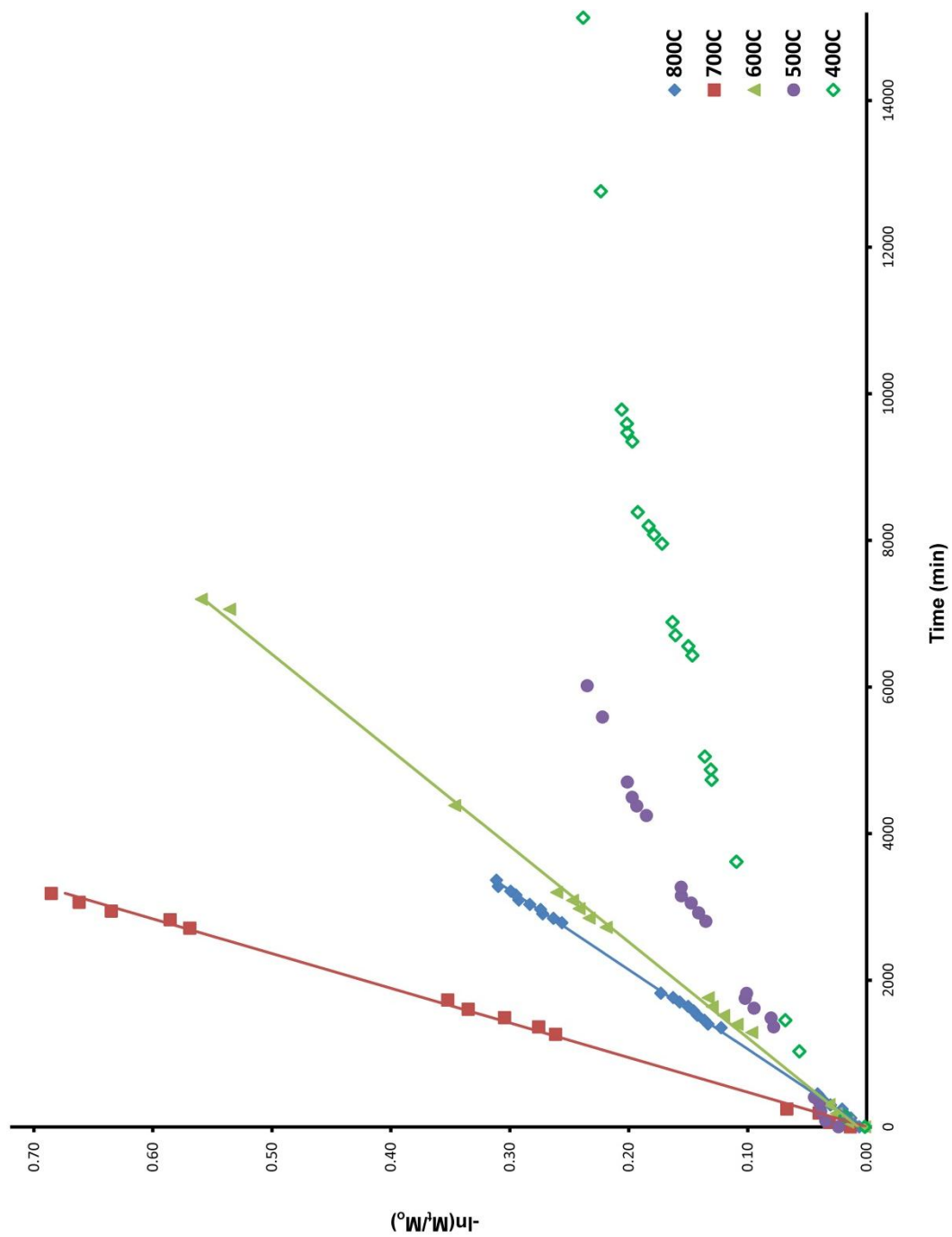


Figure 2.18. Kinetics plots for  $\epsilon$ -caprolactone reacted with bovine hydroxyapatite samples sintered at 100 °C increments

the Laue spots now show up as concentric rings around the initial point of beam contact with the sample. The angle formed between the incident beam and diffracted beam path is referred to as the scattering angle and is denoted as  $2\theta$  in the literature. The resulting refraction of the beam is recorded on a linear plate detector. The diffraction patterns of apatites, biologic, synthetic, and geologic, have been well characterized in the literature for a number of decades. (Figure 2.19) Particularly good reflections for characterizing HA are the (002) at  $25.9^\circ$ , (211) at  $31.8^\circ$ , (112) at  $32.2^\circ$ , (300) at  $32.9^\circ$ , (202) at  $34.1^\circ$ , and (310) at  $39.8^\circ$  with a  $K_\alpha$  of  $\lambda = 154.4$  pm x-ray source.<sup>53-58</sup>

XRD patterns for the sintered HA samples were obtained by placing approximately 30mg of each sample was placed in the concave sample holder of a Rigaku D/Max-B Horizontal powder diffractometer. The source was a 2 kW Cu target with  $K_\alpha$  of  $\lambda = 154.4$  pm. Diffraction patterns were obtained by plotting intensity vs.  $2\theta$  for values of  $2\theta$  ranging from  $10^\circ$  to  $60^\circ$ . (Figure 2.20) Data was then exported to an Excel® spreadsheet for further analysis.

In addition to XRD, Fourier transform infrared spectroscopy (FTIR) was also performed on each sintered HA sample. All spectra were obtained on a Nicolet Avatar 380 FTIR spectrophotometer. Many derivatives of hydroxyapatite have been characterized using FTIR, the body of literature that describes these characterizations is now extensive enough to make interpretation of the spectra relatively straightforward. (Figure 2.21) The IR activity of pure HA is due exclusively to phosphate and hydroxide. Vibrations for phosphate are observed at  $1092\text{ cm}^{-1}$ ,  $1039\text{ cm}^{-1}$ ,  $963\text{ cm}^{-1}$ ,  $602\text{ cm}^{-1}$ , and  $570\text{ cm}^{-1}$ . Hydroxide exhibits a hydrogen-oxygen stretch at  $3572\text{ cm}^{-1}$  and a libration at  $632\text{ cm}^{-1}$ .

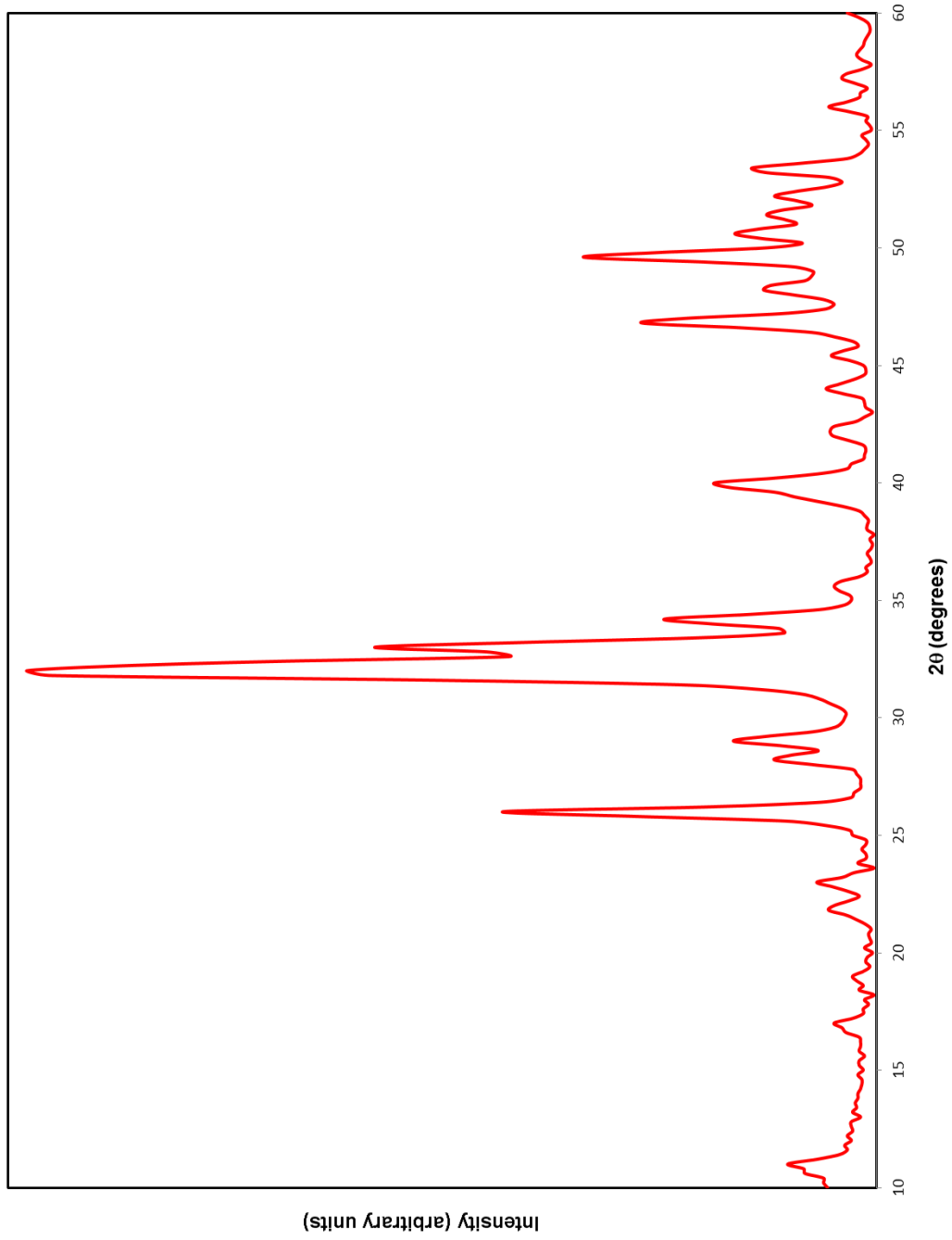


Figure 2.19. X-ray powder diffraction pattern of synthetic hydroxyapatite

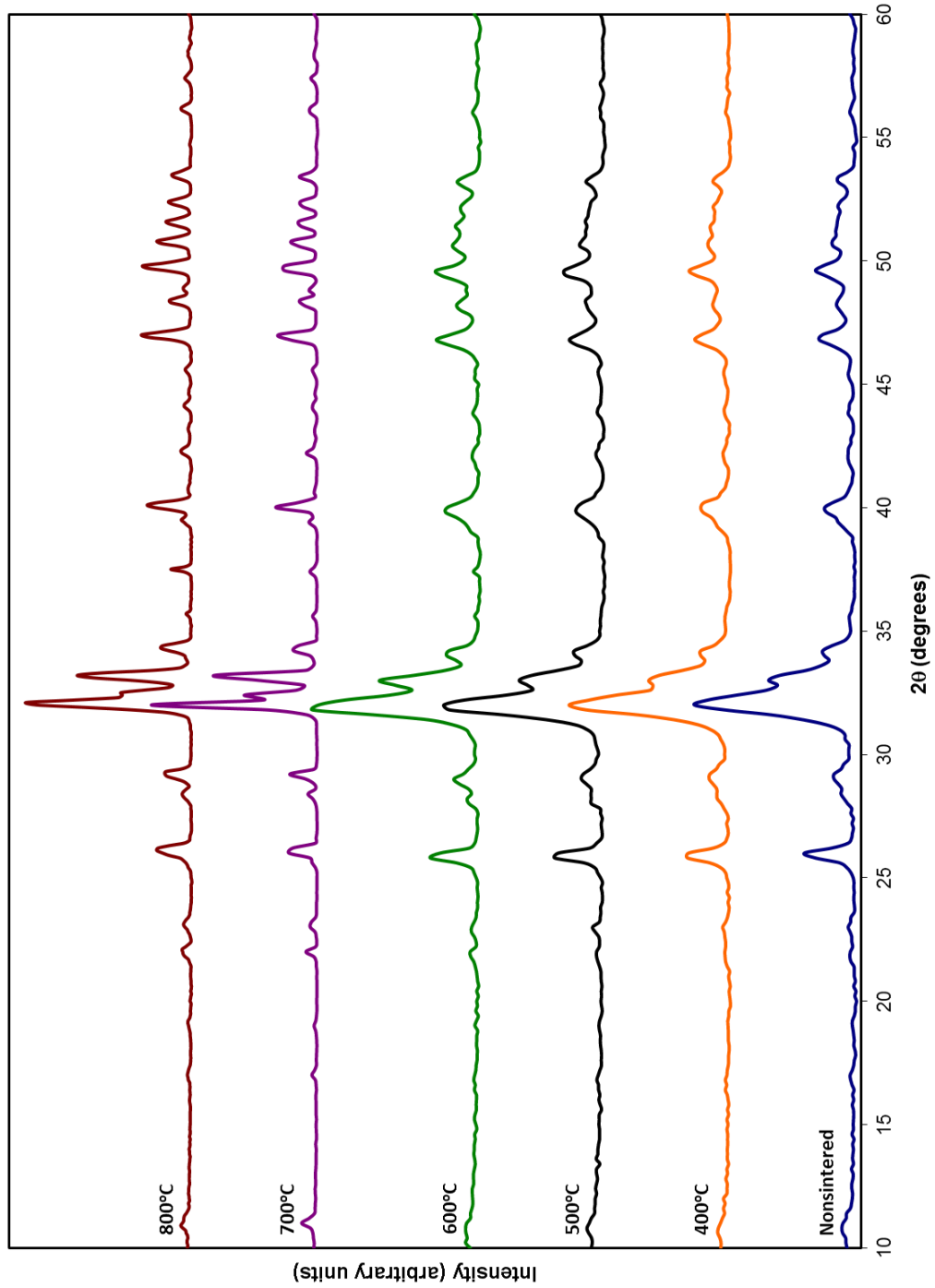


Figure 2.20. X-ray powder diffraction patterns of bovine bone derived hydroxyapatite sintered at various temperatures



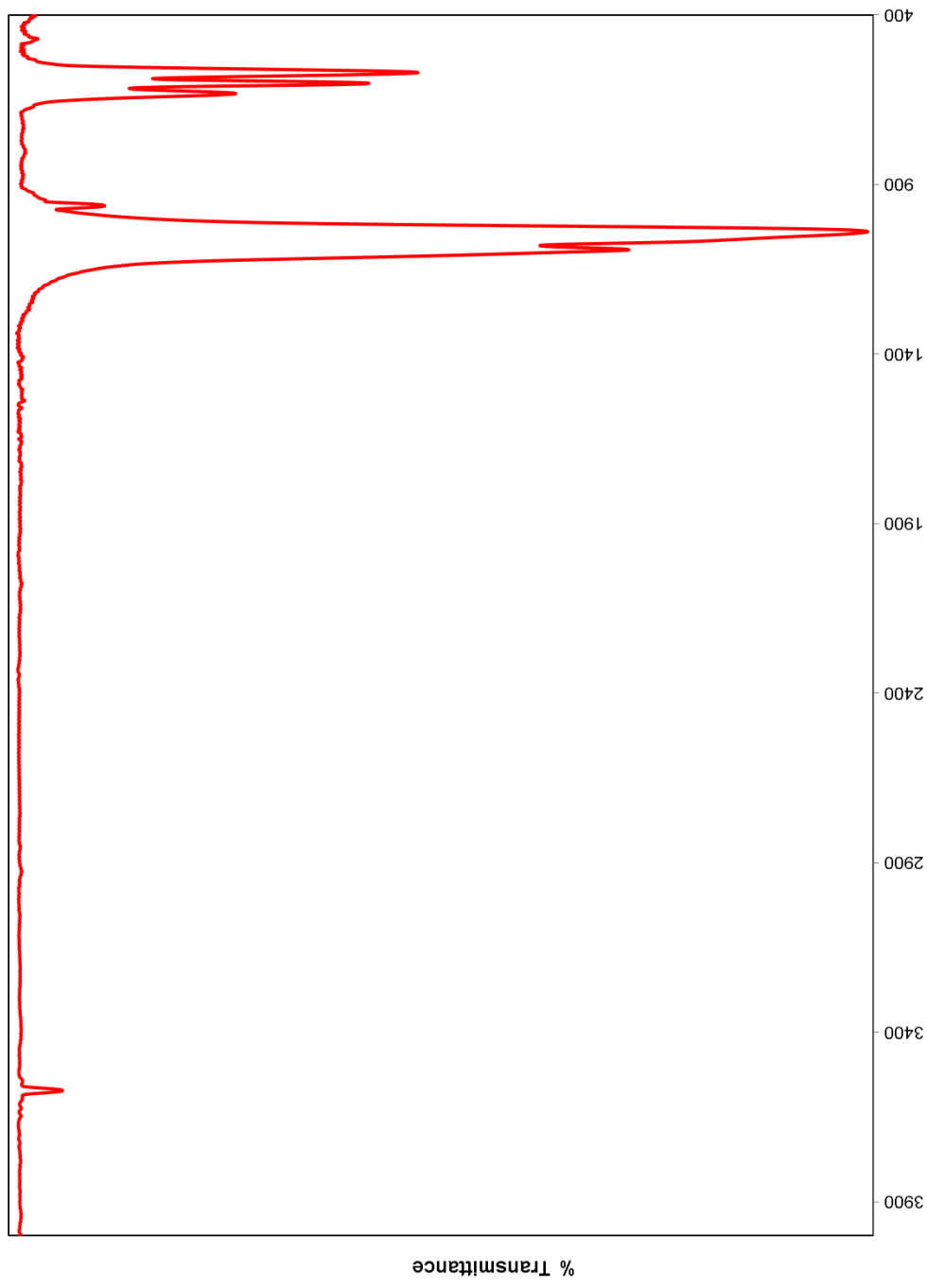


Figure 2.21. FTIR spectrum of synthetic hydroxyapatite

Biologically derived hydroxyapatites also contain large amounts of carbonate which appears in the FTIR spectrum as a pair of broad and poorly defined peaks at  $1451\text{ cm}^{-1}$  and  $1420\text{ cm}^{-1}$ , and a low intensity narrow peak at  $873\text{ cm}^{-1}$ .<sup>57, 59-61</sup> (Figure 2.22) Biologic HA is also less crystalline than synthetic and geologic sourced HA. This lower level of crystallinity is evident from the peak broadening that presents itself in the IR spectrum.

Since HA is extremely prone to adsorbing water from the atmosphere, all samples characterized by FTIR spectroscopy were prepared under the dry  $\text{N}_{2(g)}$  atmosphere of a glove box containing a fine grind mortar and pestle, and pellet press. In a typical sample preparation, approximately 2 mg of sintered HA was added in the glove box to 50 mg of KBr. The mixture was then ground to a fine powder in the mortar and pestle. After being powdered, about 30 mg of the HA/KBr mixture was placed in the pellet press and pressed to form a clear disc. If the disc was slightly opaque it was pressed again until it was clear. A pure KBr pellet was pressed to serve as a background sample. Transferring the pellets to the spectrometer, while minimizing exposure to  $\text{CO}_2$  and water in air was critical. Before being removed from the glove box, finished pellets were placed in a small jar and sealed. The jars were wrapped in aluminum foil and then transported to the FTIR spectrometer. A background spectrum for the pure KBr pellet was obtained. Each background spectrum consisted of 32 scans acquired with a spectral resolution of  $2\text{ cm}^{-1}$ . Once the background spectrum had been obtained, the sample pellet was transferred quickly into the instrument and scanning was started immediately. This was done to minimize absorption or reaction of the sample with  $\text{CO}_2$  and water in the air. Like the background spectrum, the FTIR spectrum of each sample consisted of 32 scans acquired

with a spectral resolution of  $2\text{ cm}^{-1}$ . (Figure 2.23) Approximately 45 seconds were required to acquire the 32 scans. Under these conditions and over this time period, no reactions with air were apparent. Resulting spectra were processed using Omnic 7.2a software from Thermo Electron Corporation in Franklin, Massachusetts.

### Results and Discussion

Some unanticipated but useful results were obtained from kinetics experiments performed using powdered samples of bovine bone sintered at various temperatures for 16 hours. (Tables 2.3 and 2.4) When the sintering temperature is  $600\text{ }^{\circ}\text{C}$  or higher the kinetics are fit well by a pseudo first order equation. (Equation 2.4) At reaction temperatures of  $500\text{ }^{\circ}\text{C}$  and below, there is a great deal of deviation from linearity in first order plots. Although the reaction rates generally increase as the sintering temperature increases from  $400\text{ }^{\circ}\text{C}$  to  $700\text{ }^{\circ}\text{C}$ , reactions run using bone powder sintered at  $800\text{ }^{\circ}\text{C}$  are much slower ones using material sintered at  $700\text{ }^{\circ}\text{C}$ .

The kinetics experiments performed using powdered bone that was not sintered were particularly anomalous. Plausible explanations of these results include the presence of residual extraction solvent (water or ethylene diamine) or organic material that competes with or inhibits the dominant reaction mechanism by providing different mechanistic routes to polymerization or concurrent mechanistic routes to deleterious depolymerization. Samples sintered at  $400\text{ }^{\circ}\text{C}$  for 16 hrs are noticeably grey when compared to samples that were not sintered or sintered at high temperatures. This suggests the presence of remnant organic matter from the bone that was partially

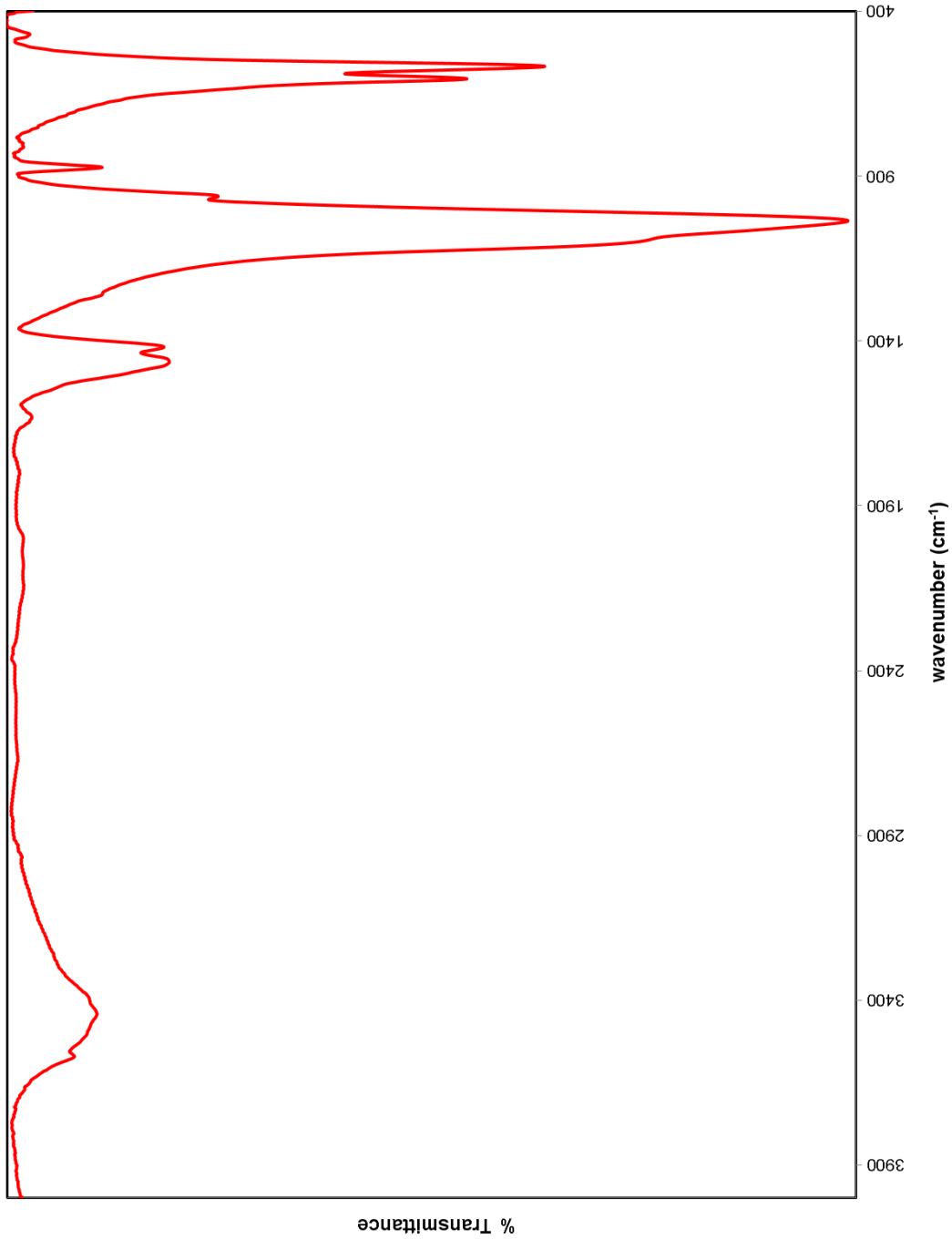


Figure 2.22. FTIR spectrum of extracted, powdered, bovine hydroxyapatite

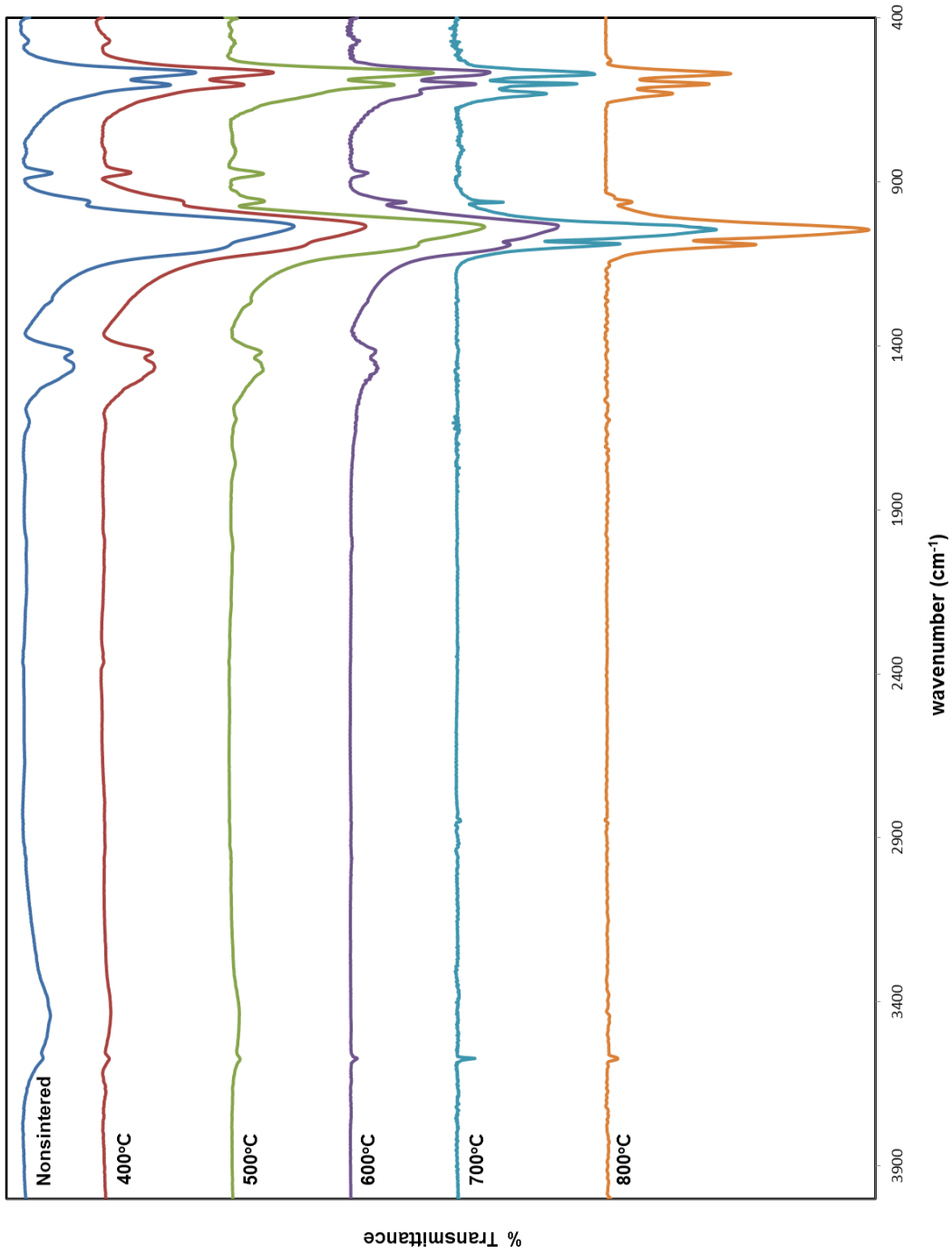


Figure 2.23. FTIR spectra of bovine hydroxyapatite sintered at 100 °C increments

| Sintering<br>Temperature (°C) | Apparent<br>Rate Constant<br>(10 <sup>-7</sup> s <sup>-1</sup> ) |
|-------------------------------|--|
| None                          | 31.9 ± 2.5   |
| 400                           | 12.3 ± 0.6   |
| 500                           | 2.2 ± 0.3  |
| 600                           | 13.9 ± 0.3   |
| 700                           | 75.2 ± 0.4   |
| 800                           | 50.6 ± 0.4   |

Table 2.3. Apparent first order rate constants for the polymerization of L-lactide initiated by bovine hydroxyapatite sintered at various temperatures for 16 hours

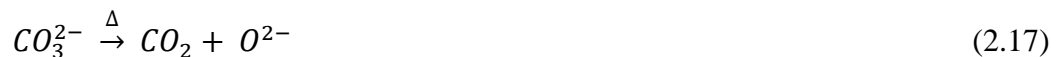
| Sintering<br>Temperature<br>(°C) | Apparent<br>Rate Constant<br>(10 <sup>-7</sup> s <sup>-1</sup> ) |
|----------------------------------|--|
| 400                              | 3.5 ± 0.1  |
| 500                              | 7.4 ± 0.2  |
| 600                              | 13.1 ± 0.1   |
| 700                              | 35.3 ± 0.3   |
| 800                              | 15.53 ± 0.05   |

Table 2.4. Apparent first order rate constants for the polymerization of  $\epsilon$ -caprolactone initiated by bovine hydroxyapatite sintered at various temperatures for 16 hours

pyrolyzed, not fully combusted by the oxygen in air. IR spectra of these samples also reveal that a good deal of surface and lattice water present, as is evidenced by a broad peak at  $3446\text{ cm}^{-1}$ . Both of these types of water can serve as a nucleophile to open a lactone ring and start polymerization. Samples sintered at  $500\text{ }^{\circ}\text{C}$  showed no discoloration, but IR spectroscopy does show that water is still present, albeit a smaller amount than observed for samples sintered at  $500\text{ }^{\circ}\text{C}$ . Infrared spectroscopy does not indicate the presence of any water in samples sintered at  $600\text{ }^{\circ}\text{C}$  and above. At  $600\text{ }^{\circ}\text{C}$  and below, the peaks in the FTIR spectra are still quite broad indicating that HA crystallinity has not increased to any appreciable degree. The low level of crystallinity of these samples is also manifested by the broad peaks in their XRD powder diffraction patterns. Also notable at these lower sintering temperatures is the presence of carbonate, which can be identified by broad peaks at  $1454\text{ cm}^{-1}$  and  $1413\text{ cm}^{-1}$ , and a relatively small narrow peak at  $869\text{ cm}^{-1}$ . The presence of carbonate substitutions in the HA crystal reduce crystallinity and increase solubility.<sup>62, 63</sup> This increase in solubility aids in osteoclast dissolution of HA in the bone remodeling process.<sup>64</sup>

As was mentioned in the introduction during the discussion of rate equations used to fit this class of reactions, the reaction rate is proportional to the number of moles of nucleophile present in any given reaction. The number of moles of nucleophile per gram of HA is clearly influenced by the temperature at which the HA is sintered. It has been shown that hydroxide can initiate ring opening polymerization of lactones, but in samples sintered at  $500\text{ }^{\circ}\text{C}$  or lower much less hydroxide is present, as is evident in infrared spectra by the relatively small vibration at  $3571\text{ cm}^{-1}$  and libration at  $628\text{ cm}^{-1}$ . Infrared spectra indicate that the amount of hydroxide in samples sintered at  $600\text{ }^{\circ}\text{C}$  greater than

the amount found in samples sintered at 600 °C. This can be attributed to decomposition of the carbonate found naturally in bovine bone. As represented in equations 2.17 and 2.18, these solid state decompositions can yield one of two nucleophiles depending on the presence or absence of water.<sup>59, 65, 66</sup>



Decomposition without water evolves carbon dioxide and the concomitant production of one nucleophile, the oxide. Oxide is known to initiate polymerization, but it is believed the reaction rate is slightly hindered due to a charge separation effect. It seems improbable to form the zwitterion with a calcium dication and a negatively charged alkoxide separated by a five member chain. (Figure 2.24) Since the sintering is being performed in air and there is a fair amount of water already present in the starting sample it is reasonable to believe that the hydroxide being formed is coming from the decomposition of carbonate in the presence of a water molecule. At 600 °C the first evidence appears that hydroxides are being formed, albeit very slowly. A decrease in the amount of carbonate can also be seen in the FTIR spectra when comparing 600 °C to 500 °C.

If the sintering temperature is increased from 600 °C to 700 °C, the apparent kinetic rate constant for the polymerization of L-lactide increases by over a factor of five. One factor influencing this change is the complete decomposition of carbonate, possibly to hydroxide or oxide. While calcium oxide is not visible by FTIR in the 400 cm<sup>-1</sup> to 4000



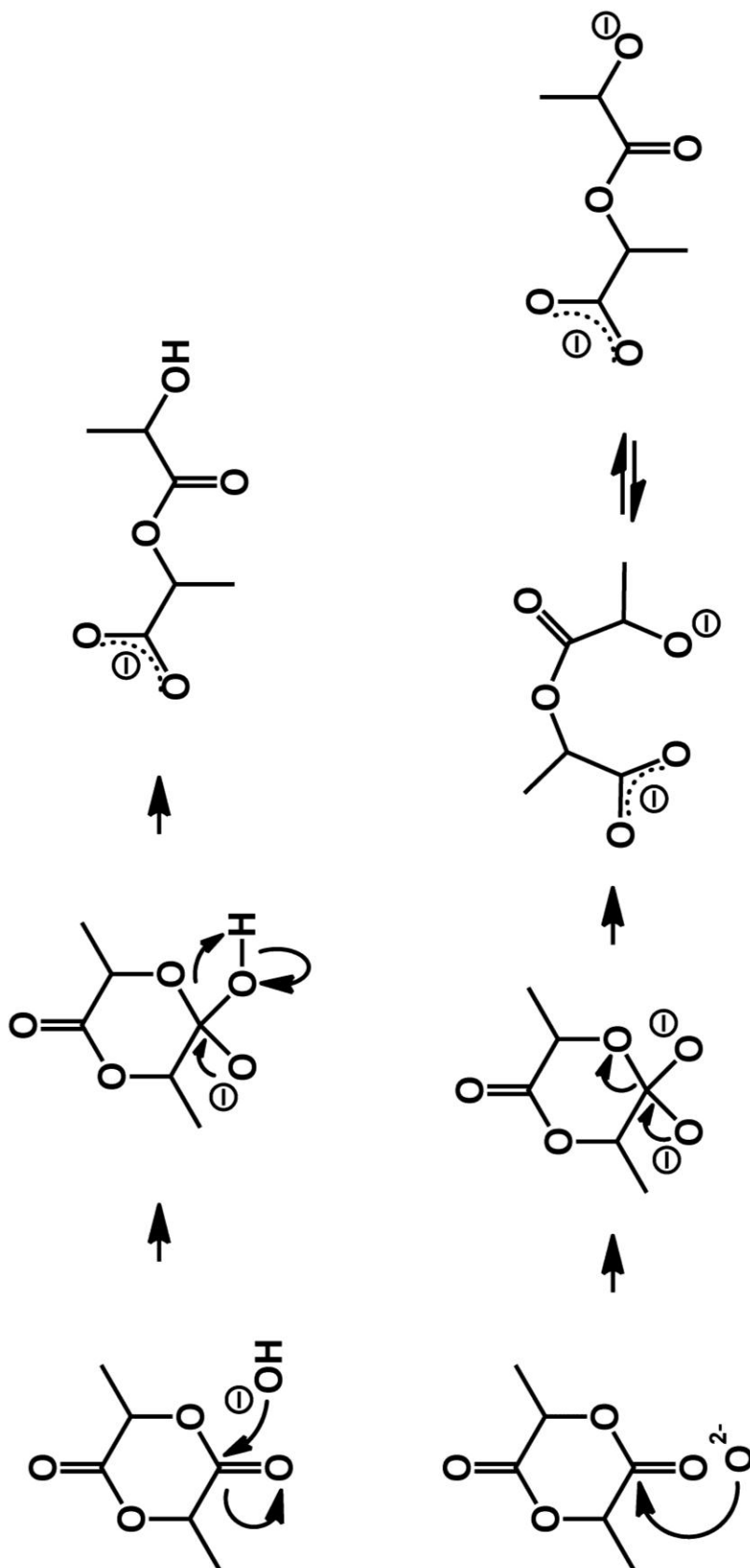


Figure 2.24. First step in ring opening polymerization of L-lactide by hydroxide (top) and oxide (bottom)

$\text{cm}^{-1}$ , it is clear that the amount of hydroxide present increases. This gives some evidence that equation 2.18 applies to the sintering of bovine hydroxyapatite in air. The presence of a calcium oxide phase can be tracked by a peak at  $37.5^\circ$  in the XRD pattern.<sup>55</sup> At sintering temperatures of  $500^\circ\text{C}$  and below, there is no sign of this peak, but at  $600^\circ\text{C}$  and above the oxide diffraction peak begins to appear. This coincides with the appearance of hydroxide and disappearance of carbonate in the FTIR spectrum, giving more evidence that the decomposition of carbonate is responsible for the generation of the reactive nucleophiles that leads to the increased polymerization rates at hydroxyapatite sintered at higher temperatures.

Increasing the HA sintering temperature by another  $100^\circ\text{C}$  from  $700^\circ\text{C}$  to  $800^\circ\text{C}$  does not further increase the kinetics rate constant for L-lactide polymerization. The trend observed at lower sintering temperatures comes to an end, and the rate constant actually decreases by about one third. As will be described in much more detail in Chapter 3, part of this decrease can be attributed to a large decrease in the specific surface area of HA sintered at  $800^\circ\text{C}$  for 16 hours. Characterizations by XRD and FTIR suggest some subtle chemical changes that are noteworthy. Although XRD and FTIR characterizations indicate no change in the crystallinity of the sample, there does appear to be a difference in the amount of hydroxide present. Since there appears to be no carbonate present in either the  $700^\circ\text{C}$  or  $800^\circ\text{C}$  samples, one can assume that all of the carbonate is transformed into either oxide or hydroxide. When comparing the XRD patterns of the  $700^\circ\text{C}$  and the  $800^\circ\text{C}$  samples the oxide reflection at  $37.5^\circ$  is much more prevalent in the higher temperature sample, indicating that there is a higher amount of oxide present.

A more detailed discussion of the stoichiometry for carbonate decomposition and possible impacts of this stoichiometry on the rates of polymerization is warranted. As was mentioned above, samples of bovine bone sintered at 700 °C show evidence for more hydroxide and less oxide than are observed in samples sintered for the same period at 800 °C. Since hydroxide is formed in a two to one ratio from carbonate decomposition in the presence of water, while oxide is formed in a one to one ratio in the absence of water, thermal treatments that favor the formation of hydroxide will favor the formation of more nucleophiles. If the changes in propagation steps for polymerization are the same for initiation by oxide and hydroxide, and if the initiation step is not rate limiting in either case, one would anticipate that kinetic rate constants would be higher for the sintering process that produces more nucleophiles, i.e., the decomposition mechanism that leads to hydroxide. Additional insight can be gained by a more careful comparative analysis of the FTIR spectra obtained for samples sintered at 700 °C and 800 °C. The hydroxide libration at 630 cm<sup>-1</sup> and the two phosphate stretches between 661 cm<sup>-1</sup> and 503 cm<sup>-1</sup> can be deconvoluted and the areas of the three peaks can be determined by integration. Since phosphate does not decompose until well above 1000 °C, it was assumed that the amount of phosphate present was identical in the 700 °C and 800 °C samples.<sup>67</sup> When the hydroxide libration at 630 cm<sup>-1</sup> and the phosphate vibration at 600 cm<sup>-1</sup> are deconvoluted and integrated, phosphate to hydroxide peak absorbance ratios of 0.91 and 1.31 are obtained for 700 °C and 800 °C samples respectively. (Equation 2.20)

$$\text{Absorbance Ratio} = \frac{PO_4^{3-} \text{ } \nu=600 \text{ cm}^{-1}}{OH^- \text{ } \nu=630 \text{ cm}^{-1}} \quad (2.20)$$

$$\text{Absorbance Ratio} = \frac{PO_4^{3-} \quad \nu=1050 \text{ cm}^{-1}}{OH^- \quad \nu=3570 \text{ cm}^{-1}} \quad (2.21)$$

Although the complexity of quantitative IR spectroscopy is duly noted, the simple analysis above clearly indicates that the amount of hydroxide available to act as a nucleophile has increased substantially, by approximately one third. The same phosphate to hydroxide ratio and percent increase in hydroxide is obtained using the same method with the hydroxide stretch at  $3570 \text{ cm}^{-1}$  and phosphate stretch at  $1050 \text{ cm}^{-1}$ . (Equation 2.21) There are at least two plausible explanations for these observations. One explanation is that in the initial decomposition of the carbonate the formation of oxide is preferential to the formation of hydroxide. A second possibility is that the hydroxyapatite is dehydrated. It is known that calcium hydroxide can be dehydrated at moderate temperature to form calcium oxide.<sup>68-70</sup> The same is true for hydroxyapatite, although the temperature requirements are much higher.<sup>71-75</sup>



Whichever mechanism for the generation of oxide is predominate, the end is the same; a reduction in number of nucleophiles available to initiate the polymerization. Both mechanisms should result in decreased numbers of nucleophiles and decreases in the apparent first order rate constants.

Some insight into the mechanism of this class of polymerizations can be gained by using the FTIR characterizations to interpret the observed kinetics. Consistent with less detailed analyses reported previously, the reaction hydroxyapatite with L-lactide (and  $\epsilon$ -caprolactone) is clearly first order in monomer and first order in amount of

hydroxyapatite.<sup>2</sup> The hydroxyls in the HA are one of the initiating species. This was verified by comparing the FTIR spectrum of the HA before using it as the initiator with a subsequent FTIR spectrum of the composite material once the polymerization reaction had run to completion. (Figure 2.25) Special interest was paid to the hydroxyl libration at  $632\text{ cm}^{-1}$ . Before the reaction, this peak is well distinguished from the two neighboring phosphate stretches at  $602\text{ cm}^{-1}$  and  $570\text{ cm}^{-1}$ . There is no evidence that the polymerization influences the amount phosphate in the inorganic phase of the resulting composite. Consequently, the phosphate stretches can be used as an internal standard for the amount of hydroxide that remains after polymerization. It is clear from the spectra that the amount of hydroxide is markedly decreased. Along with hydroxide initiation, the proposed mechanism also shows the formation of a carboxylate end group electrostatically tethered to a calcium ion. Evidence for this assertion can be seen when comparing the FTIR spectrum of a PLLA/HA composite material prepared as described above, the FTIR spectrum of a PLLA sample made with an alcohol initiator (so the polymer has no carboxylate end group), and the FTIR spectrum of calcium lactate. (Figure 2.26) The peak in the calcium lactate spectrum at  $1588\text{ cm}^{-1}$  has previously been assigned to the asymmetric carboxylate stretch.<sup>76, 77</sup> The peak at  $1753\text{ cm}^{-1}$  is attributed to the ester carbonyl stretch in the spectrum for PLLA prepared using an alcohol initiator. The spectrum of the PLLA/HA composite shows the asymmetric carboxylate stretch at  $1606\text{ cm}^{-1}$  and the ester carbonyl stretch at  $1759\text{ cm}^{-1}$  both of which can be attributed to the polymer. These data support a mechanism of anionic initiated ring opening polymerization. The data also support the assertion that the resulting polymer is electrostatically attached to calcium by the carboxylate end group. (Figure 2.27)

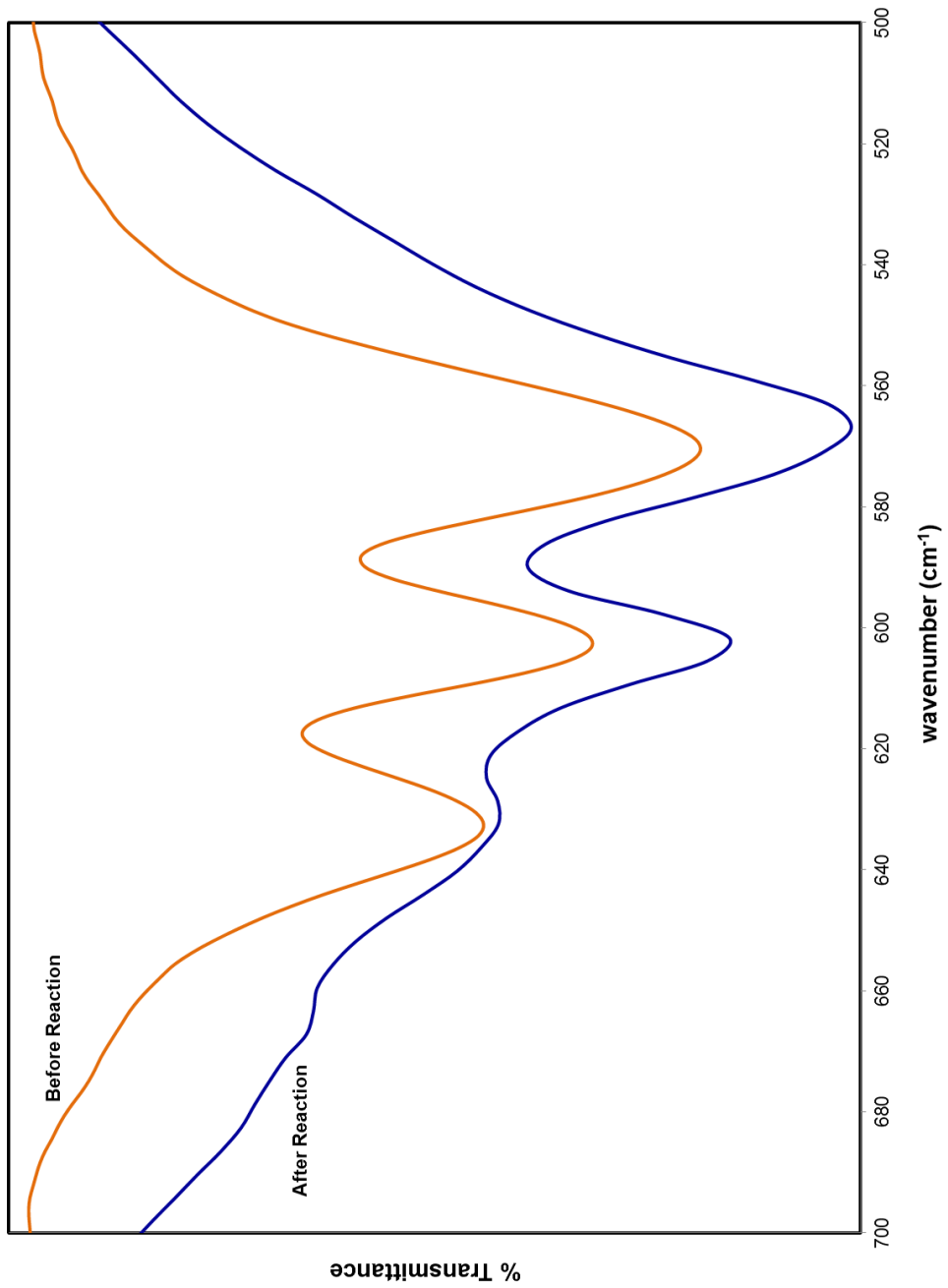


Figure 2.25. FTIR spectra of sintered hydroxyapatite before (top) and after (bottom) a polymerization reaction with L-lactide showing the hydroxyl libration at 632  $\text{cm}^{-1}$  and phosphate vibrations at 602  $\text{cm}^{-1}$  and 570  $\text{cm}^{-1}$

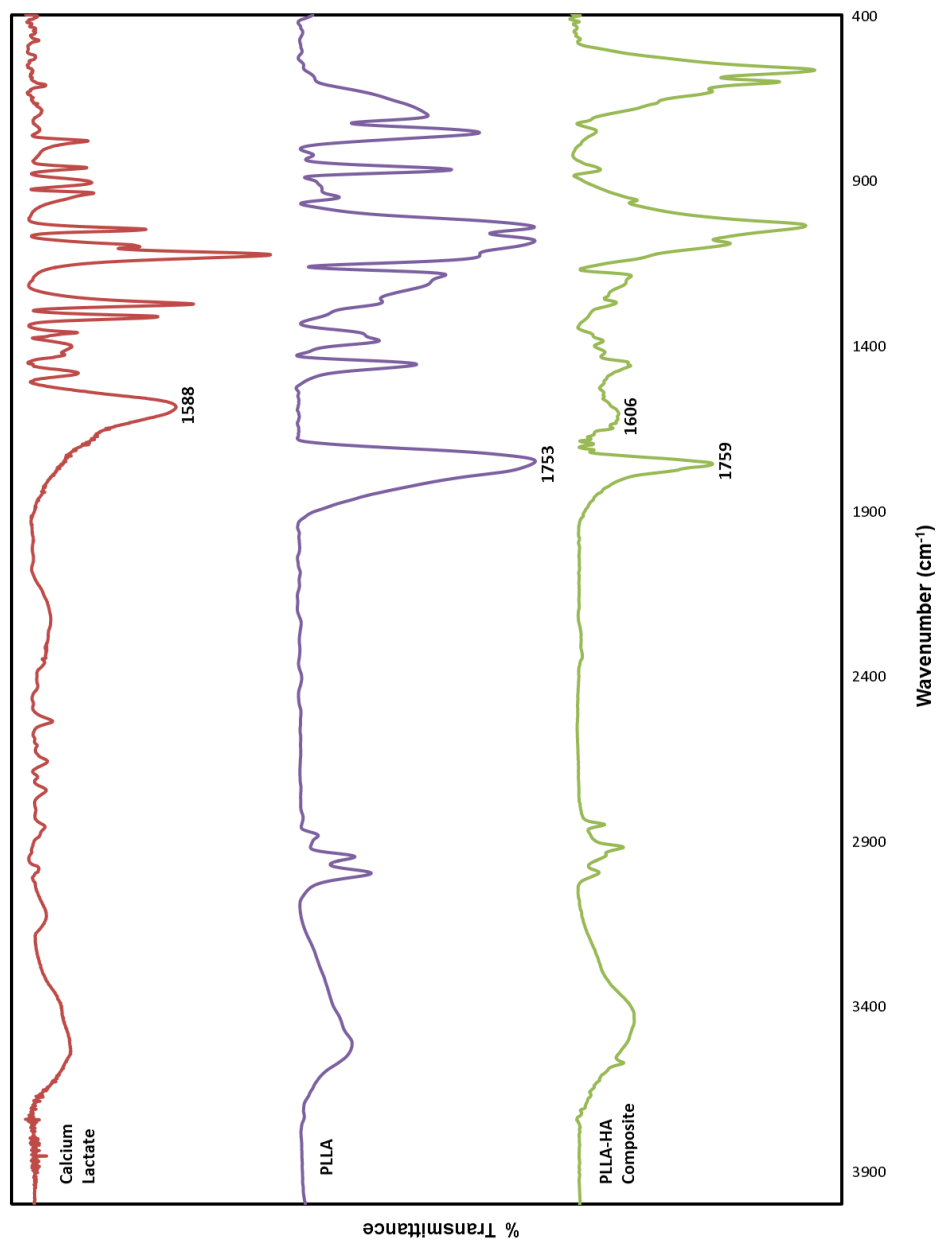


Figure 2.26. FTIR spectra comparing calcium lactate, PLLA, and a PLLA/HA composite. The carboxylate stretch is identified at  $1588\text{ cm}^{-1}$  for calcium lactate and  $1606\text{ cm}^{-1}$  for the PLLA/HA composite. The ester carbonyl stretch is identified at  $1753\text{ cm}^{-1}$  for PLLA and  $1759\text{ cm}^{-1}$  for the PLLA/HA composite.

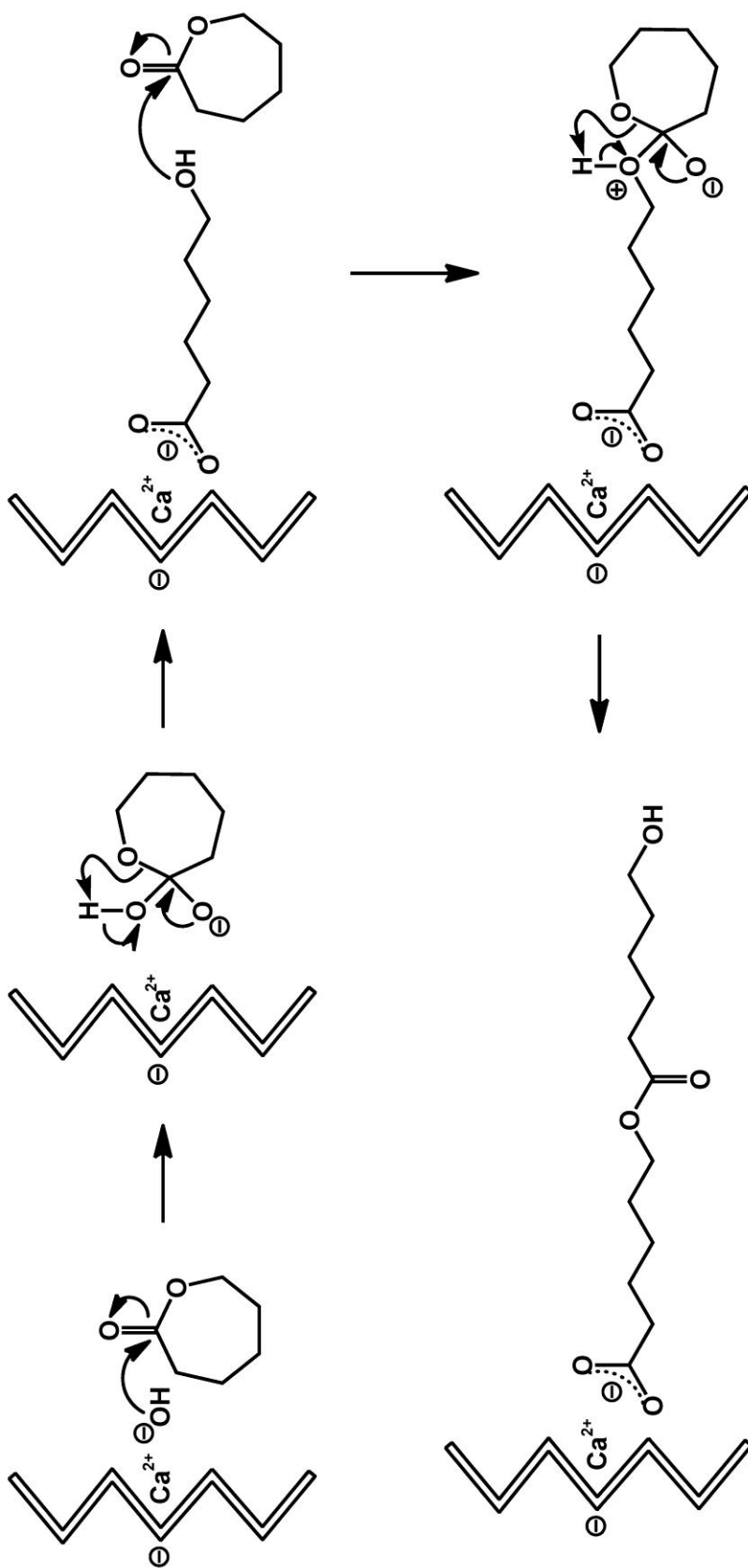


Figure 2.27. Representative mechanism of ring-opening polymerization initiated by hydroxyapatite using  $\epsilon$ -caprolactone



L-lactide has two stereocenters, both (*S*). When polymerization reactions are performed with HA as the initiator at 125 °C, some epimerization to the meso-lactide monomer is observed. There are three potential routes to meso-lactide. (Figure 2.28) One involves the keto-enol tautomerizations of L-lactide. The second involves the polymer. In the polymer chain the stereochemistry at one center may change from (*S*) to (*R*) via a keto-enol tautomerization. Next the subsequent attack of the hydroxyl end group on the ester bond in the polymer chain effectively shortens the chain by one monomer unit and generates one meso-lactide unit.<sup>78, 79</sup> A third mechanism requires the carboxylate to act as the attacking nucleophile in performing an  $S_n^2$  type reaction. This would invert the stereochemistry at one chiral carbon giving the meso-lactide product. This is extremely unlikely as the carboxylate is generally considered to be a weak nucleophile and in this case is electrostatically attached to a calcium ion.

Stereochemistry may not play a large part in determining the rate of a reaction but it will affect the final properties of any polymer. Changes in stereochemistry influence the percent crystallinity of a polymer. Crystallinity plays a major part in determining whether a polymer such as a polyesters or polycarbonates, which are very crystalline, will be brittle. Polymers with low crystallinity, such as styrene-ethylene-butadiene-styrene (SEBS) block copolymers, are elastomeric and exhibit properties that resemble rubber. These properties include high elasticity, bend and twist flexibility, and low compression set. Highly crystalline polymers also tend to have much higher and more sharply defined glass transition temperatures. Sintering conditions play a great role in determining the chemical makeup of biologic hydroxyapatite.

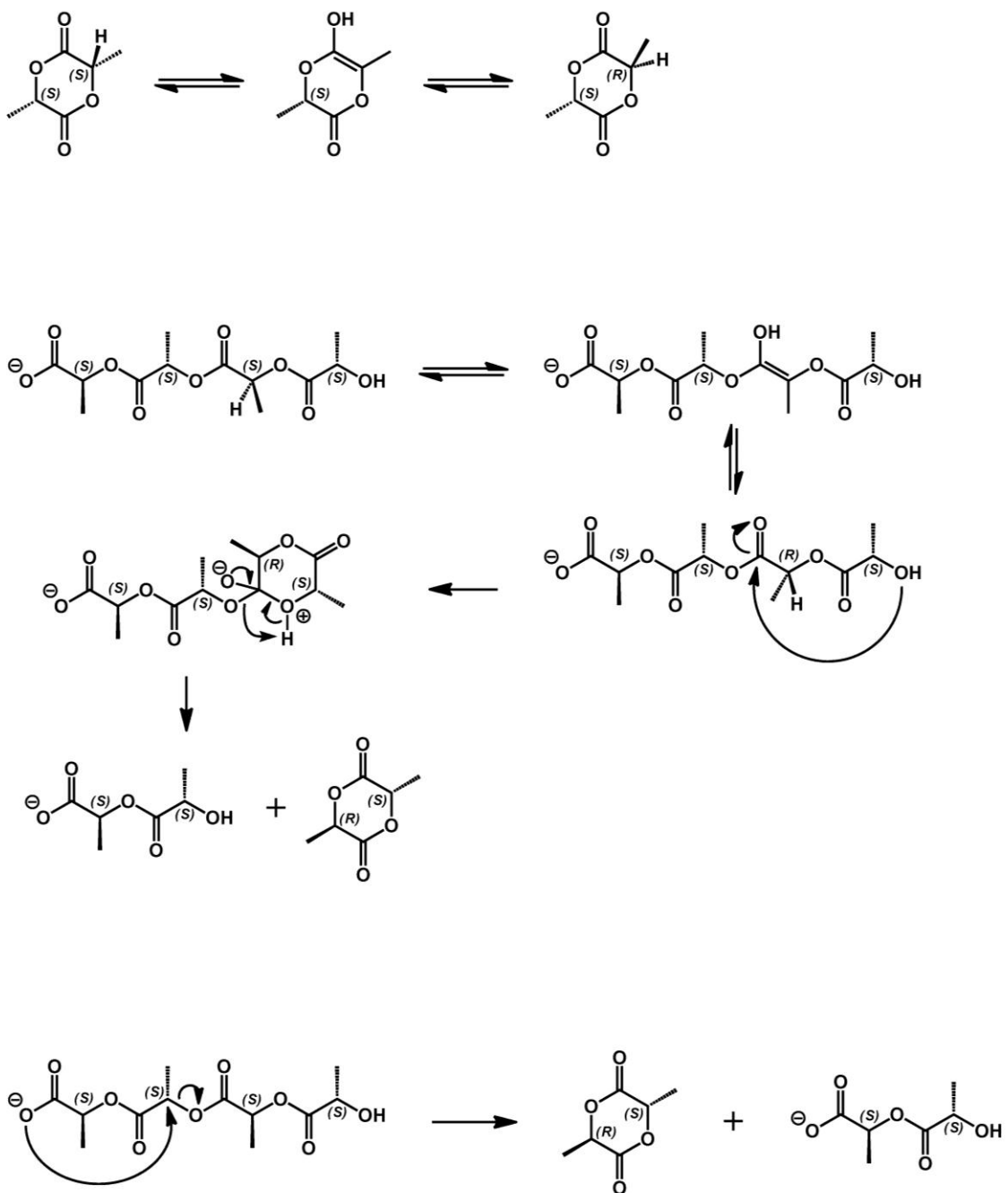


Figure 2.28. Potential mechanisms for the generation of meso-lactide from L-lactide and PLLA

Sintering at 600 °C and lower does not decompose carbonate and as such the kinetic rate constants obtained from polymerization reactions with HA sintered at these lower temperatures are small. When the sintering temperature is raised to 700 °C, the carbonate decomposes to hydroxide or oxide. These two new species are quite nucleophilic and as such the rates of polymerization reaction increase. If the sintering temperature is raised even further then the ratio of oxide to hydroxide is shifted toward oxide. This effectively reduces the number of nucleophiles present subsequently causing a decrease in the rate of polymerization reaction. Further analysis will examine how the sintering atmosphere affects the chemical composition of the hydroxyapatite as well as how sintering affects the surface area.

### References

1. Helwig, E.; Sandner, B.; Gopp, U.; Vogt, F.; Wartewig, S.; Henning, S., Ring-opening polymerization of lactones in the presence of hydroxyapatite. *Biomaterials* **2001**, *22*, (19), 2695-2702.
2. Wiegand, T.; Karr, J.; Steinkruger, J. D.; Hiebner, K.; Simeich, B.; Beatty, M.; Redepening, J., Reconstruction of Anorganic Mammalian Bone by Surface-initiated Polymerization of L-lactide. *Chemistry of Materials* **2008**, *20*, (15), 5016-5022.
3. Guerra, G. D.; Cerrai, P.; Tricoli, M.; Krajewski, A.; Ravaglioli, A.; Mazzocchi, M.; Barbani, N., Composites between hydroxyapatite and poly(epsilon-caprolactone) synthesized in open system at room temperature. *Journal of Materials Science-Materials in Medicine* **2006**, *17*, (1), 69-79.
4. Penczek, S.; Duda, A., Kinetics and Mechanisms in Anionic Ring-Opening Polymerization. *Makromolekulare Chemie-Macromolecular Symposia* **1993**, *67*, 15-42.
5. Ouhadi, T.; Hamitou, A.; Jerome, R.; Teyssie, P., Soluble Bimetallic  $\mu$ -Oxo-alkoxides. 8. Structure and Kinetic Behavior of the Catalytic Species in Unsubstituted Lactone Ring-Opening Polymerization. *Macromolecules* **1976**, *9*, (6), 927-931.
6. Miola-Delaite, C.; Hamaide, T.; Spitz, R., Anionic coordinated polymerization of epsilon-caprolactone with aluminium, zirconium and some rare earths alkoxides as initiators in the presence of alcohols. *Macromolecular Chemistry and Physics* **1999**, *200*, (7), 1771-1778.
7. Chisholm, M. H.; Eilerts, N. W.; Huffman, J. C.; Iyer, S. S.; Pacold, M.; Phomphrai, K., Molecular design of single-site metal alkoxide catalyst precursors for ring-opening polymerization reactions leading to polyoxygenates. 1. Polylactide

formation by achiral and chiral magnesium and zinc alkoxides, ( $\eta^3$ -L)MOR, where L = trispyrazolyl- and trisindazolylborate ligands. *Journal of the American Chemical Society* **2000**, 122, (48), 11845-11854.

8. Chisholm, M. H.; Gallucci, J.; Phomphrai, K., Coordination chemistry and reactivity of monomeric alkoxides and amides of magnesium and zinc supported by the diiminato ligand CH(CMeNC<sub>6</sub>H<sub>3</sub>-2,6-Pr-i(2))(2). A comparative study. *Inorganic Chemistry* **2002**, 41, (10), 2785-2794.

9. Kricheldorf, H. R.; Boettcher, C., Polylactones .27. Anionic-Polymerization of L-Lactide - Variation of Endgroups and Synthesis of Block-Copolymers with Poly(Ethylene Oxide). *Makromolekulare Chemie-Macromolecular Symposia* **1993**, 73, 47-64.

10. Kricheldorf, H. R.; Berl, M.; Scharnagl, N., Poly(lactones). 9. Polymerization mechanism of metal alkoxide initiated polymerizations of lactide and various lactones. *Macromolecules* **1988**, 21, (2), 286-293.

11. Albertsson, A.-C.; K.Varma, I., Recent Developments in Ring Opening Polymerization of Lactones for Biomedical Applications. *Biomacromolecules* **2003**, 4.

12. Westerhausen, M.; Schneiderbauer, S.; Kneifel, Alexander N.; Sörtl, Y.; Mayer, P.; Nöth, H.; Zhong, Z.; Dijkstra, Pieter J.; Feijen, J., Organocalcium Compounds with Catalytic Activity for the Ring-Opening Polymerization of Lactones. *European Journal of Inorganic Chemistry* **2003**, 2003, (18), 3432-3439.

13. Schwach, G.; Coudane, J.; Engel, R.; Vert, M., Ring opening polymerization of D,L-lactide in the presence of zinc metal and zinc lactate. *Polymer International* **1998**, 46, (3), 177-182.

14. Takeshi Endo, Y. S., Fumio Sanda,, Controlled ring-opening polymerization of cyclic carbonates and lactones by an activated monomer mechanism. *Journal of Polymer Science Part A: Polymer Chemistry* **2002**, 40, (13), 2190-2198.
15. Bulten, E. J. In *Tin [toxicity]*, 1984; Verlag Chemie: 1984; pp 631-44.
16. Florea, A.-M. Toxicity of alkylated derivatives of arsenic, antimony and tin in vitro. Cellular uptake, cytotoxicity, genotoxic effects, perturbation of Ca<sup>2+</sup> homeostasis, and cell death. 2005.
17. Greger, J. L.; Lane, H. W. In *The toxicology of dietary tin, aluminum, and selenium*, 1987; Academic: 1987; pp 223-47.
18. Hassett, J. M.; Johnson, D. L.; Myers, J. A.; Al-Mudamgha, A.; Melcer, M. E.; Kutscher, C. L.; Sembrat, M. M., The exposure of rats to inorganic tin: behavioral and systemic effects of different levels and modes of exposure. *Trace Substances and Environmental Health* **1984**, 18, 487-96.
19. Janssen, P. *Effects of feeding of stannous chloride (SnCl<sub>2</sub>) on different parts of the gastrointestinal tract of the rat*; TNO: 1983; p 21 pp.
20. Janssen, P. J. M.; Bosland, M. C.; Van, H. J. P.; Spit, B. J.; Willems, M. I.; Kuper, C. F., Effects of feeding stannous chloride on different parts of the gastrointestinal tract of the rat. *Toxicology and Applied Pharmacology* **1985**, 78, 19-28.
21. Krigman, M. R.; Silverman, A. P., General toxicology of tin and its organic compounds. *Neurotoxicology* **1984**, 5, 129-39.
22. Kungolos, A.; Hadjispyrou, S.; Samaras, P.; Petala, M.; Tsiridis, V.; Aravossis, K.; Sakellaropoulos, G. P. In *Assessment of toxicity and bioaccumulation of organotin*

*compounds*, 2001; University of the Aegean, Dep. of Environmental Studies: 2001; pp 499-505.

23. Miller, K.; Scott, M. P., Immunological consequences of dioctyltin dichloride (DOTC)-induced thymic injury. *Toxicology and Applied Pharmacology* **1985**, 78, 395-403.

24. Sandhu, G. K.; Sandhu, G. K., Toxicology of organometallic compounds of silicon, germanium, tin and lead. *Journal of Chemical Sciences* **1983**, 9, 36-50.

25. Thayer, J. S. In *Toxicity of tin in humans*, 1995; Dekker: 1995; pp 726-9.

26. Tsuji, M.; Inoue, Y.; Sugaya, C.; Tsunoda, M.; Sugaya, T.; Takahashi, M.; Yuba, T.; Tsuchiya, T.; Aizawa, Y., Higher toxicity of dibutyltin and poly-L-lactide with a large amount of tin but lower toxicity of poly-L-lactide of synthetic artificial dura mater exhibited on murine astrocyte cell line. *Yakugaku Zasshi* **2010**, 130, 847-855.

27. Zhihui, S.; Tianyi, C., Toxicity of tributyltin to *Lemna minor* L. and *Azolla filiculoides* Lamk. *Bull Environ Contam Toxicol - Bulletin of Environmental Contamination and Toxicology* **1998**, 60, 318-322.

28. Sugiyama, N.; Kunibu, R.; Yoshizawa-Fujita, M.; Takeoka, Y.; Aizawa, M.; Rikukawa, M., Ring-opening bulk polymerization of L-lactide in porous hydroxyapatite. *Chemistry Letters* **2007**, 36, (12), 1476-1477.

29. Rapkin, E. Anorganic bone. 2,968,593, January 17, 1961.

30. Bassett, C. A. L.; Hurley, L. A.; Stinchfield, F. E., Fate of long-term anorganic bone implants. *Transplant Biology* **1962**, 29, 51-5.

31. Williams, J. B.; Irvine, J. W., Jr., Preparation of the inorganic matrix of bone. *Science* **1954**, 119, 771-2.

32. Ababou, A.; Bernacheassollant, D.; Heughebaert, M., Influence of the Calcination Conditions on the Morphological Evolution of Hydroxyapatite. *Annales De Chimie-Science Des Materiaux* **1994**, 19, (4), 165-175.
33. Bailliez, S.; Nzihou, A., The kinetics of surface area reduction during isothermal sintering of hydroxyapatite adsorbent. *Chemical Engineering Journal* **2004**, 98, (1-2), 141-152.
34. Bernache-Assollant, D.; Ababou, A.; Champion, E.; Heughebaert, M., Sintering of calcium phosphate hydroxyapatite  $\text{Ca}_{10}(\text{PO}_4)_6(\text{OH})_2$  - I. Calcination and particle growth. *Journal of the European Ceramic Society* **2003**, 23, (2), 229-241.
35. Haberko, K.; Bucko, M. M.; Brzezinska-Miecznik, J.; Haberko, M.; Mozgawa, W.; Panz, T.; Pyda, A.; Zarebski, J., Natural hydroxyapatite - its behaviour during heat treatment. *Journal of the European Ceramic Society* **2006**, 26, (4-5), 537-542.
36. Nederberg, F.; Connor, E. F.; Moller, M.; Glauser, T.; Hedrick, J. L., New paradigms for organic catalysts: The first organocatalytic living polymerization. *Angewandte Chemie-International Edition* **2001**, 40, (14), 2712-2715.
37. Kalmi, M.; Lahcini, M.; Castro, P.; Lehtonen, O.; Belfkira, A.; Leskela, M.; Repo, T., Tetrakis Sn(IV) alkoxides as novel initiators for living ring-opening polymerization of lactides. *Journal of Polymer Science Part A-Polymer Chemistry* **2004**, 42, (8), 1901-1911.
38. Thakur, K. A. M.; Kean, R. T.; Hall, E. S.; Kolstad, J. J.; Munson, E. J., H-1 NMR spectroscopy in the analysis and characterization of poly(lactide). *International Journal of Polymer Analysis and Characterization* **1998**, 4, (5), 379-391.



39. Espartero, J. L.; Rashkov, I.; Li, S. M.; Manolova, N.; Vert, M., NMR analysis of low molecular weight poly(lactic acid)s. *Macromolecules* **1996**, *29*, (10), 3535-3539.
40. Kaihara, S.; Matsumura, S.; Mikos, A. G.; Fisher, J. P., Synthesis of poly(L-lactide) and polyglycolide by ring-opening polymerization. *Nature Protocols* **2007**, *2*, (11), 2767-2771.
41. Entenmann, G.; Bendix, D. Preparation of meso-lactide for use in resorbable (co)polymers. DE 3820299 A1, December 29, 1988.
42. Noda, M., LL-lactide formation from thermal depolymerization reaction of poly(L-lactic acid) oligomer. I. Organic stannic compound as catalyst. *Shimadzu Hyoron* **1999**, *56*, 83-86.
43. Noda, M.; Okuyama, H., L,L-Lactide formation from thermal depolymerization reaction of poly(L-lactic acid) oligomer. II. *Shimadzu Hyoron* **2000**, *56*, 169-173.
44. Darensbourg, D. J.; Karroonnirun, O., Stereoselective Ring-Opening Polymerization of rac-Lactides Catalyzed by Chiral and Achiral Aluminum Half-Salen Complexes†. *Organometallics* **2010**, 100811082732073.
45. Entenmann, G.; Bendix, D. meso-Lactide, Process for its Preparation and Polymers and Copolymers Prepared Therefrom DE 3820299 A2, December 12, 1988.
46. Muller, M. B., (DE), Hess, Joachim (Bingen, DE), Schnell, Wilhelm-gustav (Ingelheim am Rhein, DE), Bendix, Dieter (Ingelheim am Rhein, DE), Entenmann, Gunther (Ingelheim an Rhein, DE) Meso-lactide. 1993.
47. Mariage, P.-A.; Hottois, D.; Coszach, P. Method of obtaining lactide using ethers as solvents. WO 2010/018209 A1, February 18, 2010.

48. Emel'yanenko, V. N.; Verevkin, S. P.; Pimerzin, A. A., The Thermodynamic Properties of DL- and L-lactides. *Russian Journal of Physical Chemistry A* **2009**, 83, (12), 2013-2021.
49. Lee, S. H.; Kim, B. S.; Kim, S. H.; Choi, S. W.; Jeong, S. I.; Kwon, I. K.; Kang, S. W.; Nikolovski, J.; Mooney, D. J.; Han, Y. K.; Kim, Y. H., Elastic biodegradable poly(glycolide-co-caprolactone) scaffold for tissue engineering. *Journal of Biomedical Materials Research Part A* **2003**, 66A, (1), 29-37.
50. Stolt, M.; Viljanmaa, M.; Sodergard, A.; Tormala, P., Blends of poly(epsilon-caprolactone-b-lactic acid) and poly(lactic acid) for hot-melt applications. *Journal of Applied Polymer Science* **2004**, 91, (1), 196-204.
51. Zhang, J.; Wang, L. Q.; Wang, H. J.; Tu, K. H.; Liu, L., Amphiphilic block copolymers based on methoxy poly(ethylene glycol) and either crystalline or amorphous poly(caprolactone-b-lactide): Synthesis, solid-state and aqueous solution characterizations. *Journal of Applied Polymer Science* **2007**, 105, (2), 915-927.
52. Zhong, Z. Y.; Ankone, M. J. K.; Dijkstra, P. J.; Birg, C.; Westerhausen, M.; Feijen, J., Calcium methoxide initiated ring-opening polymerization of epsilon-caprolactone and L-lactide. *Polymer Bulletin* **2001**, 46, (1), 51-57.
53. Herliansyah, M. K.; Hamdi, M.; Ide-Ektessabi, A.; Wildan, M. W.; Toque, J. A., The influence of sintering temperature on the properties of compacted bovine hydroxyapatite. *Materials Science and Engineering: C* **2009**, 29, (5), 1674-1680.
54. Gibson, I. R.; Bonfield, W., Preparation and characterization of magnesium/carbonate co-substituted hydroxyapatites. *Journal of Materials Science-Materials in Medicine* **2002**, 13, (7), 685-693.

55. Gibson, I. R.; Bonfield, W., Novel synthesis and characterization of an AB-type carbonate-substituted hydroxyapatite. *Journal of Biomedical Materials Research* **2002**, 59, (4), 697-708.
56. Barinov, S. M.; Rau, J. V.; Cesaro, S. N.; Durisin, J.; Fadeeva, I. V.; Ferro, D.; Medvecky, L.; Trionfetti, G., Carbonate release from carbonated hydroxyapatite in the wide temperature range. *Journal of Materials Science-Materials in Medicine* **2006**, 17, (7), 597-604.
57. Rau, J. V.; Cesaro, S. N.; Ferro, D.; Barinov, S. M.; Fadeeva, I. V., FTIR study of carbonate loss from carbonated apatites in the wide temperature range. *Journal of Biomedical Materials Research Part B-Applied Biomaterials* **2004**, 71B, (2), 441-447.
58. Slosarczyk, A.; Paszkiewicz, Z.; Paluszkiewicz, C., FTIR and XRD evaluation of carbonated hydroxyapatite powders synthesized by wet methods. *Journal of Molecular Structure* **2005**, 744, 657-661.
59. Biltz, R. M.; Pelligrino, E. D., The Composition of Recrystallized Bone Mineral. *Journal of Dental Research* **1983**, 62, (12).
60. Ooi, C. Y.; Hamdi, M.; Ramesh, S., Properties of hydroxyapatite produced by annealing of bovine bone. *Ceramics International* **2007**, 33, (7), 1171-1177.
61. Dahm, S.; Risnes, S., A comparative infrared spectroscopic study of hydroxide and carbonate absorption bands in spectra of shark enameloid, shark dentin, and a geological apatite. *Calcified Tissue International* **1999**, 65, (6), 459-465.
62. Redey, S. A.; Nardin, M.; Bernache-Assolant, D.; Rey, C.; Delannoy, P.; Sedel, L.; Marie, P. J., Behavior of human osteoblastic cells on stoichiometric hydroxyapatite

and type A carbonate apatite: Role of surface energy. *Journal of Biomedical Materials Research* **2000**, 50, (3), 353-364.

63. Landi, E.; Celotti, G.; Logroscino, G.; Tampieri, A., Carbonated hydroxyapatite as bone substitute. *Journal of the European Ceramic Society* **2003**, 23, (15), 2931-2937.

64. Mezahi, F. Z.; Oudadesse, H.; Harabi, A.; Lucas-Girot, A.; Le, G. Y.; Chaair, H.; Cathelineau, G., Dissolution kinetic and structural behaviour of natural hydroxyapatite vs. thermal treatment. Comparison to synthetic hydroxyapatite. *Journal of Thermal Analysis and Calorimetry* **2009**, 95, 21-29.

65. Ababou, A.; Bernache-Assollant, D.; Heughebaert, M., Influence of water vapor on grain growth during the calcination of hydroxyapatite. *Ceramic Transactions* **1995**, 51, 111-15.

66. Haberko, K.; Bucko, M. M.; Mozgawa, W.; Pyda, A.; Brzezinska-Miecznik, J.; Carpentier, J., Behaviour of bone origin hydroxyapatite at elevated temperatures and in O<sub>2</sub> and CO<sub>2</sub> atmospheres. *Ceramic International* **2009**, 35, 2537-2540.

67. Lin, F. H.; Liao, C. J.; Chen, K. S.; Sun, J. S., Thermal reconstruction behavior of the quenched hydroxyapatite powder during reheating in air. *Materials Science & Engineering C-Biomimetic and Supramolecular Systems* **2000**, 13, (1-2), 97-104.

68. Chatterji, S.; Jeffrey, J. W., The oriented conversion of Ca(OH)<sub>2</sub> to CaO. *Mineralogist Magazine* **1966**, 35, 867-70.

69. Chaix-Pluchery, O.; Bouillot, J.; Ciosmak, D.; Niepce, J. C.; Freund, F., Calcium hydroxide dehydration early precursor states. *Journal of Solid State Chemistry* **1983**, 50, 247-55.

70. Vitkovskii, R. E., Effect of calcium hydroxide dehydration determined on DTA patterns of cement stone. *Zhurnal Prikladnoi Khimii* **1984**, 57, 1295-8.
71. Bertinetti, L.; Tampieri, A.; Landi, E.; Ducati, C.; Midgley, P. A.; Coluccia, S.; Martra, G., Surface structure, hydration, and cationic sites of nanohydroxyapatite: UHR-TEM, IR, and microgravimetric studies. *Journal of Physical Chemistry C* **2007**, 111, (10), 4027-4035.
72. Liao, C. J.; Lin, F. H.; Chen, K. S.; Sun, J. S., Thermal decomposition and reconstitution of hydroxyapatite in air atmosphere. *Biomaterials* **1999**, 20, (19), 1807-1813.
73. Ruys, A. J.; Brandwood, A.; Milthorpe, B. K.; Dickson, M. R.; Zeigler, K. A.; Sorrell, C. C., The effects of sintering atmosphere on the chemical compatibility of hydroxyapatite and particulate additives at 1200 °C. *Journal of Materials Science-Materials in Medicine* **1995**, 6, (5), 297-301.
74. Sugiyama, S.; Nakanishi, T.; Ishimura, T.; Moriga, T.; Hayashi, H.; Shigemoto, N.; Moffat, J. B., Preparation, characterization, and thermal stability of lead hydroxyapatite. *Journal of Solid State Chemistry* **1999**, 143, (2), 296-302.
75. Yamashita, K.; Kitagaki, K.; Umegaki, T., Thermal instability and proton conductivity of ceramic hydroxyapatite at high temperatures. *Journal of the American Ceramic Society* **1995**, 78, (5), 1191-1197.
76. Qiu, X. Y.; Hong, Z. K.; Hu, J. L.; Chen, L.; Chen, X. S.; Jing, X. B., Hydroxyapatite surface modified by L-lactic acid and its subsequent grafting polymerization of L-lactide. *Biomacromolecules* **2005**, 6, (3), 1193-1199.

77. Socrates, G., *Infrared Characteristic Group Frequencies: Tables and Charts. Second Edition*. 3rd ed.; Wiley: 2001; p 249 pp.
78. Tsukegi, T.; Motoyama, T.; Shirai, Y.; Nishida, H.; Endo, T., Racemization behavior of L,L-lactide during heating. *Polymer Degradation and Stability* **2007**, *92*, 552-559.
79. Matsuo, T.; Kamikawa, M.; Okamoto, N., Lowering of meso-lactide formation at thermal cracking in PLA production. *Journal of Chemical Engineering of Japan* **2008**, *41*, 1049-1054.

## Chapter Three

### Macroscopic and Microscopic Morphologic Changes to Biologically Derived

### Hydroxyapatite

#### Introduction and Background

In the preceding chapter a relationship was established between sintering temperature and the kinetics of a ring-opening polymerization reaction for lactones. This relationship is influenced by the number of nucleophiles present and the distribution of these nucleophiles. The number of nucleophiles and their distribution can be controlled by sintering biologically derived hydroxyapatite to decompose-carbonate substitutions in the crystal lattice to either hydroxide or oxide. The sintering temperature affects the total number of nucleophiles and the distribution between the two species possible. Another factor that has direct bearing on the use of hydroxyapatite derived from biologic sources is surface area. The polymerization reaction is initiated by surface oxides and hydroxides. Occluded oxides and hydroxides are sterically prohibited from participating in the polymerization. Thus, the higher the surface area the more nucleophiles that can be presented to the monomer melt. This effectively increases the  $N_i$  term in equation 2.5, and since  $N_i$  is a constant and grouped with  $k$ , an increase in the apparent rate constant,  $k_{app}$ , is observed.

This chapter describes the influence of specific surface area on the surface-initiated polymerization of cyclic lactones at nucleophilic interfaces. The chapter begins with an introduction to basic gas adsorption theories that can be used in order to reliably measure the specific surface area of a wide variety of materials. Examined next are my results

showing the influence of sintering time and sintering temperature on the specific surface area of hydroxyapatite derived from bovine femurs. This is followed by a discussion of the influence of specific surface area on reactions kinetics. Chapter 3 concludes by correlating changes in specific surface area with macroscopic morphological changes, which are manifested in dimensional changes in hydroxyapatite rods, and microscopic changes in crystallinity, which are revealed through scanning electron microscopy.

Two types of gas adsorption phenomena are typically used to determine specific surface areas, chemisorption and simple physical adsorption. In general, gas adsorption to a solid is exothermic, and it increases at low temperature and higher pressure. Most measurements are performed at liquid nitrogen's boiling point, which is 77.35 K at one atmosphere. Chemisorption involves an irreversible chemical reaction between a gas-phase or liquid-phase molecule and the surface of a solid to produce a surface layer that is only one molecule. A common chemisorption reaction is the corrosion of a metal surface in air. For iron and steel the process yields rust and for copper the reaction is apparent by the formation of the turquoise patina that coats the surface. Early attempts at the beginning of the Twentieth Century capitalized on chemisorption reactions to measure the surface area of solids. The first measurements were performed by Isaac Langmuir and involved the bonding of carbon monoxide or oxygen to a platinum surface.<sup>1</sup> An experimental adsorption isotherm is obtained when the molar volume of gas taken up by the solid,  $V_a$ , is plotted against  $P/P_o$ , where  $P$  is the actual pressure of the gas and  $P_o$  is its partial pressure. (Figure 3.1, Figure 3.2, Table 3.1) The experimental results can be fit by a variety of isotherm models, the most common of which are Type 2 and Type 4 isotherms, which deal with adsorbents containing no pores or adsorbents containing



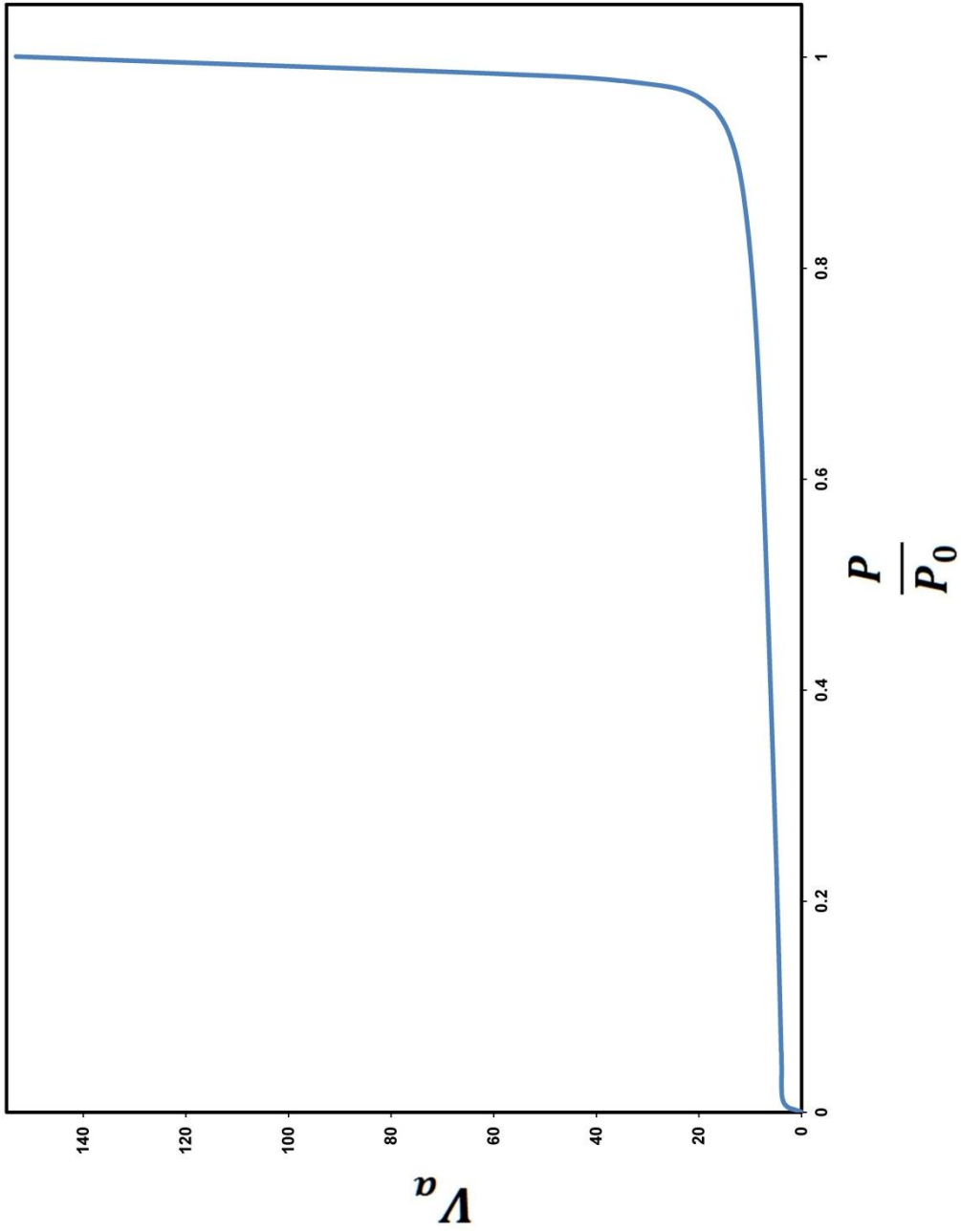


Figure 3.1.1. Example Type 2 isotherm taken on a standard alumina reference material

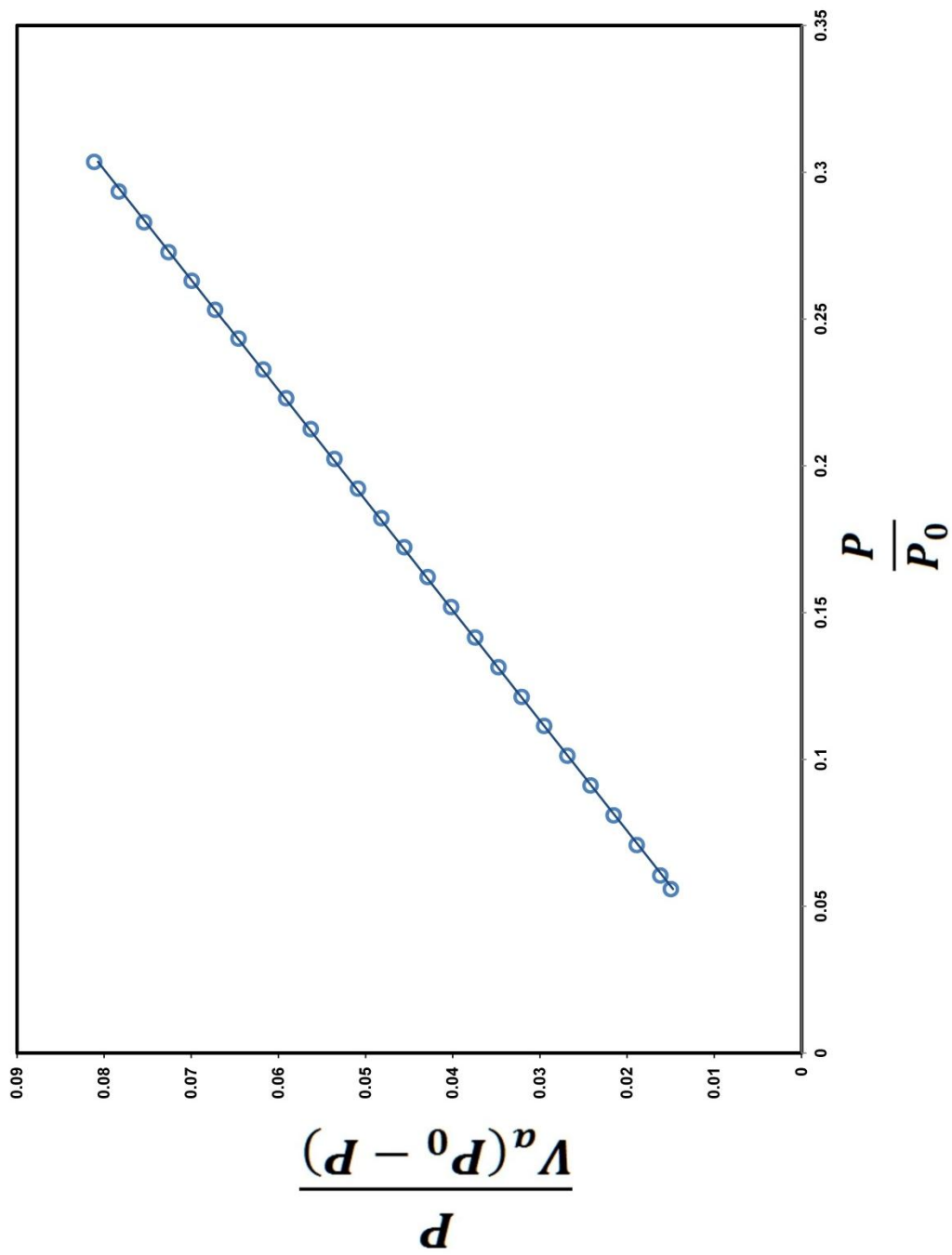


Figure 3.2. BET transform plot over the region 0.05 to 0.30 for  $\frac{P}{P_0}$  for a standard alumina reference material

| Absolute<br>Pressure (mmHg) | $\frac{P}{P_0}$ | $V_a$       | $\frac{P}{V_a(P_0 - P)}$ |
|-----------------------------|-----------------|-------------|--------------------------|
| 33.611728668                | 0.045669919     | 3.887555995 | 0.012309913              |
| 41.088726044                | 0.055839640     | 3.950412246 | 0.014971125              |
| 44.486953735                | 0.060467930     | 3.977887047 | 0.016179349              |
| 52.112365723                | 0.070844433     | 4.036296456 | 0.018890099              |
| 59.551383972                | 0.080970966     | 4.090552805 | 0.021538630              |
| 67.016235352                | 0.091134321     | 4.144113007 | 0.024196395              |
| 74.462432861                | 0.101277203     | 4.196306548 | 0.026854603              |
| 81.903549194                | 0.111422246     | 4.248428277 | 0.029515367              |
| 89.135070801                | 0.121282014     | 4.299676848 | 0.032100446              |
| 96.571113586                | 0.131421041     | 4.351568959 | 0.034770403              |
| 103.988708496               | 0.141541071     | 4.404387641 | 0.037434964              |
| 111.588882446               | 0.151913322     | 4.458786523 | 0.040173432              |
| 119.071083069               | 0.162125434     | 4.513479945 | 0.042870705              |
| 126.506629944               | 0.172280769     | 4.568423754 | 0.045560384              |
| 133.737945557               | 0.182157938     | 4.622205886 | 0.048186943              |
| 141.129409790               | 0.192260326     | 4.678613649 | 0.050874608              |
| 148.530380249               | 0.202379329     | 4.736247080 | 0.053571697              |
| 155.949462891               | 0.212522403     | 4.794629197 | 0.056287438              |
| 163.639266968               | 0.223042229     | 4.856419458 | 0.059111706              |
| 170.788742065               | 0.232824571     | 4.915381114 | 0.061741465              |
| 178.481933594               | 0.243356301     | 4.980266478 | 0.064580082              |
| 185.653823853               | 0.253150003     | 5.040887043 | 0.067241530              |
| 192.888031006               | 0.263018688     | 5.103283365 | 0.069932725              |
| 200.030242920               | 0.272762832     | 5.166581500 | 0.072594854              |
| 207.497024536               | 0.282949937     | 5.233086425 | 0.075405360              |
| 215.177536011               | 0.293428882     | 5.303300744 | 0.078307025              |
| 222.583343506               | 0.303532976     | 5.371618480 | 0.081133491              |

| y=mx+b         |             |
|----------------|-------------|
| Slope (m)      | 2.66185E-01 |
| Intercept (b)  | -1.0773E-04 |
| S <sub>m</sub> | 4.51391E-04 |
| S <sub>b</sub> | 8.54633E-05 |
| R <sup>2</sup> | 9.99928E-01 |

| BET Surface Area               |  |
|--------------------------------|--|
| 16.36 ± 0.03 m <sup>2</sup> /g |  |

Table 3.1. Example of tabulated data over the region 0.05 to 0.30 for  $\frac{P}{P_0}$  used to determine surface area for a standard alumina reference material

extremely large pores relative to the size of gas molecules adhering to it. Over 95% of materials studied fall into either Type 2 or Type 4. A general equation that came from Langmuir's research relates the amount of gas adsorbed to the increase in pressure that is measured.

$$V_a = \frac{V_m b P}{1 + b P} \quad (3.1)$$

In equation (3.1)  $V_m$  is the quantity of gas adsorbed when the surface is completely saturated with one layer of molecules,  $V_a$  is the amount of gas adsorbed at pressure,  $P$ , and  $b$  is an empirical constant. This equation can be rewritten in a linear format to yield the equation 3.2.

$$\frac{P}{V_a} = \frac{1}{V_m b} + \frac{P}{V_m} \quad (3.2)$$

So if  $\frac{P}{V_a}$  is plotted against  $P$  then the result should be a straight line. One can determine the value of the specific surface area using the slope and intercept from linear equation 3.2 and equation 3.3

$$S = \frac{V_m \sigma N_a}{m V_o} \quad (3.3)$$

where  $S$  is the surface area of sample in  $\text{m}^2/\text{g}$ ,  $\sigma$  is the area of surface occupied by one molecule of adsorbent gas,  $N_a$  is Avogadro's number,  $m$  is the mass of adsorbent sample, and  $V_o$  is the molar volume of the gas at standard temperature and pressure.

These equations fit experimental results well for a monolayer of gas that is irreversibly chemisorbed to the surface of the material being studied, but fits are much poorer for reversible adsorptions.

The next advance in surface area measurement that has application to a wider range of applications came in 1938 with the advent of BET theory.<sup>2</sup> The BET acronym represents the scientists who discovered it, Stephen Brunauer, Paul Emmett, and Edward Teller. These researchers were the first to describe the process of gas condensation on the surface of a solid as being a multilayer process where the same forces responsible for condensation of the first layer were also responsible for condensation of subsequent layers. They also were able to account for the reversible adsorption and desorption of gas molecules. Braunauer, Emmett and Teller thus refined Langmuir's equations to get

$$V_a = \frac{V_m C P}{(P_0 - P) \left[ 1 + (C - 1) \frac{P}{P_0} \right]} \quad (3.4)$$

where

$$C = e^{\frac{q_a - q_L}{RT}} \quad (3.5)$$

The term  $q_a$  is the heat of adsorption of the first layer of gas molecules,  $q_L$  is the heat of liquefaction of the adsorptive gas,  $R$  is the ideal gas constant, and  $T$  is temperature in Kelvin. Rewriting equation 3.4 in linear form yields

$$\frac{P}{V_a(P_0 - P)} = \frac{1}{V_m C} + \frac{C - 1}{V_m C} \left( \frac{P}{P_0} \right) \quad (3.6)$$

The region between  $0.05 \leq P/P_0 \leq 0.30$  is usually chosen for optimum linearity. With the volume of the monolayer now determined from a regression line, it is possible to find the surface area using the number of molecules present in the monolayer and the area occupied by one gas molecule assuming closest packing orientation. The mean area occupied per gas molecule is

$$\sigma = 3.464 \left[ \frac{M}{4(2N_A\rho)^{1/2}} \right]^{2/3} \quad (3.7)$$

where  $M$  is the molecular weight of the gas,  $N_A$  is Avogadro's number, and  $\rho$  is the density of the liquid adsorbate.

The intercept term  $\frac{1}{V_m C}$  in equation 3.6 is extremely small and is usually approximated as zero. This approximation has little effect on the slope of the line obtained. Equation 3.6 now becomes

$$\frac{P}{V_a(P_0 - P)} = \frac{C-1}{V_m C} \left( \frac{P}{P_0} \right) \quad (3.8)$$

which is referred to as the BET single point relationship. With this equation it is possible to get an accurate surface area by taking one data point at the higher end of the linear region of the isotherm.

Surface area changes with respect to temperature were studied with greater frequency during in the 1960s following the advent of reliable instruments to measure surface area accurately. For example, several studies focused on surface area changes associated with heating simple, chemically stable oxides such as MgO and Fe<sub>2</sub>O<sub>3</sub>.<sup>3</sup> It was found that

surface area changed with sintering time under isothermal conditions according to the equation

$$\frac{dS}{dt} = -k_{SA}(S_0 - S_t) \quad (3.9)$$

where  $S_0$  is the initial specific surface area of the material,  $S_t$  is the specific surface area of the sample after sintering time,  $t$ , and  $k_s$  is the kinetics rate constant for surface area decrease. If the “back reaction” is also included in the kinetic model, equation 3.8 can be rewritten in exponential form as shown in equation 3.9

$$\frac{S_t - S_e}{S_0 - S_e} = e^{-k_{SA}t} \quad (3.10)$$

where the new term,  $S_e$ , is the equilibrium surface area.<sup>4, 5</sup> If a sample were allowed to sinter for an infinite amount of time, and if no restrictions were placed on particle size, then the surface area of the sample is  $S_e$ . For some equilibria, many small particles are favored leading to a large value for  $S_e$ , and for others fewer, larger particles are favored making  $S_e$  very small. For hydroxyapatite,  $S_e$  approaches zero, allowing one to simplify equation 3.9 as shown in equation 3.10.

$$\frac{S_t}{S_0} = e^{-k_{SA}t} \quad (3.11)$$

Rewriting equation 3.10 into a linear form gives

$$\ln(S_t) = -k_{SA}t + \ln(S_0) \quad (3.12)$$

In all instances  $S_0$  is a constant that need not be measured to obtain a linear relationship for the purposes of predicting surface area changes as a function of sintering time. The value of  $S_0$  can be determine from the y-intercept when  $\ln(S_t)$  is plotted vs. time.

For chemically stable solids the surface area generally decreases as described by equation 3.11 while crystal size increases. In a phenomenon similar to Ostwald ripening, small crystals are sacrificed to form fewer large crystals.<sup>6-8</sup> In solids, ion diffusion is the mechanism of mass transfer that leads to recrystallization. At points where any two crystals touch, the point of contact will slowly grow larger until the two crystals fuse into one. This is the first stage in any particle growth since the ions on the surface are the most able to diffuse. Higher temperatures allow facile diffusion of the ions due to increased kinetic energy. In my samples, two macroscopic consequences of this crystal growth are the densification of the HA and the shrinkage of the sample. At high sintering temperatures, dense materials that have undergone significant shrinkage form quickly. For a powder these morphological changes may be of little consequence, but it is extremely important that the final dimensions of the implant be predictable when trying to reconstitute a bone section for segmental defect treatment. Furthermore, extreme shrinkage can lead to cracking of a sample, introducing failure points into the implant.

### Experimental

Chemicals: Ethylene diamine (99% from Sigma-Aldrich) was used as purchased, and biologic hydroxyapatite was derived from bovine femurs (Premium Protein Products).

Methodology: Biologically derived hydroxyapatite, or anorganic bone, was prepared by extracting bovine bone and then sintering it as described on page 47 in Chapter 2.



All surface area measurements were performed on the Micromeritics ASAP® 2020 Physisorption Analyzer. The combined mass of an empty sample tube and seal frit were measured (Figure 3.3). Enough HA powder to fill about half of the sample ball was then placed into the sample tube. Between 1.5 g and 6.0 g of sample was used to assure that at least 10 m<sup>2</sup> of sample surface area would be measured. The manufacturer of the ASAP 2020 analyzer states that for surface areas below 10 m<sup>2</sup>, small volumes of adsorbed gas lead to imprecise measurements with large uncertainties. The total mass of the sample setup and sample was then recorded. The next step in measuring the surface area was to remove any adherent gas molecules from the surface of the sample powder by degassing it under vacuum at elevated temperatures. First the sample tube was placed on the instrument and a heating mantle placed over the bowl of the sample tube. The sample tube was placed under a constant vacuum and the sample heated at 10 °C/min to a temperature of 95 °C. The evacuation rate was set to 25.0 mmHg/s until a pressure of 5.0 mmHg was reached. At this pressure the evacuation rate was increased to the maximum the pumping system could deliver until the pressure in the tube fell to 300 µmHg. The sample was held at this pressure for an additional 30 minutes, at which point a more aggressive heating phase of the degassing process was initiated. The temperature of the sample was increased to 250 °C at a ramp rate of 10.0 °C/min. Once the sample had reached 250 °C it was allowed to remain at this temperature for an additional 120 minutes. The sample was then allowed to cool to room temperature and the sample tube was backfilled with N<sub>2(g)</sub>. With degassing complete, the sample tube, seal frit, and sample were reweighed. It is noteworthy that the resulting weight difference serves as a



Figure 3.3. Typical surface area setup tube used in the Micromeritics® ASAP 2020

rough indicator of the moisture content of the sample. Once this final step of the degassing procedure was completed, the sample was transferred to the analysis port of the ASAP Analyzer.

As was described above, when nitrogen gas is the adsorbate and when  $\frac{P}{P_0}$  ranges from 0.05 to 0.30, plots of  $\frac{P}{V_a(P_0-P)}$  against  $\frac{P}{P_0}$  are highly linear. This range was used for all of the surface area measurements described in this thesis. Within this linear range, 17 data points were taken at regular intervals using the default conditions of the control software. All sampling and control of the instrument was performed using proprietary software provided by Micromeritics. Raw data for  $\frac{P}{P_0}$  and  $V_a$  were transferred to an Excel® spreadsheet for further processing to verify the surface area results determined by the instrument software (Figure 3.4, Table 3.2).

Frozen, raw, bovine femurs were cut into roughly ½ inch thick sections perpendicular to the long axis of the bone on a band saw to manufacture samples for dimensional stability tests. From these sections 6mm diameter plugs were cut using a custom plug cutting tool. The plugs were cut on a Bridgeport knee mill. A mill was used instead of a standard drill press to ensure that the cuts were consistent from plug to plug. (Figure 3.5) The organic material was then removed from the cut plugs in a standard Soxhlet as described on page 47 in Chapter 2. Enough cut bone plugs were added to fill approximately 50% of the volume of the extractor. After all extractions were completed the bone plugs were removed from the Soxhlet extractor and allowed to air dry for 24 hours before further

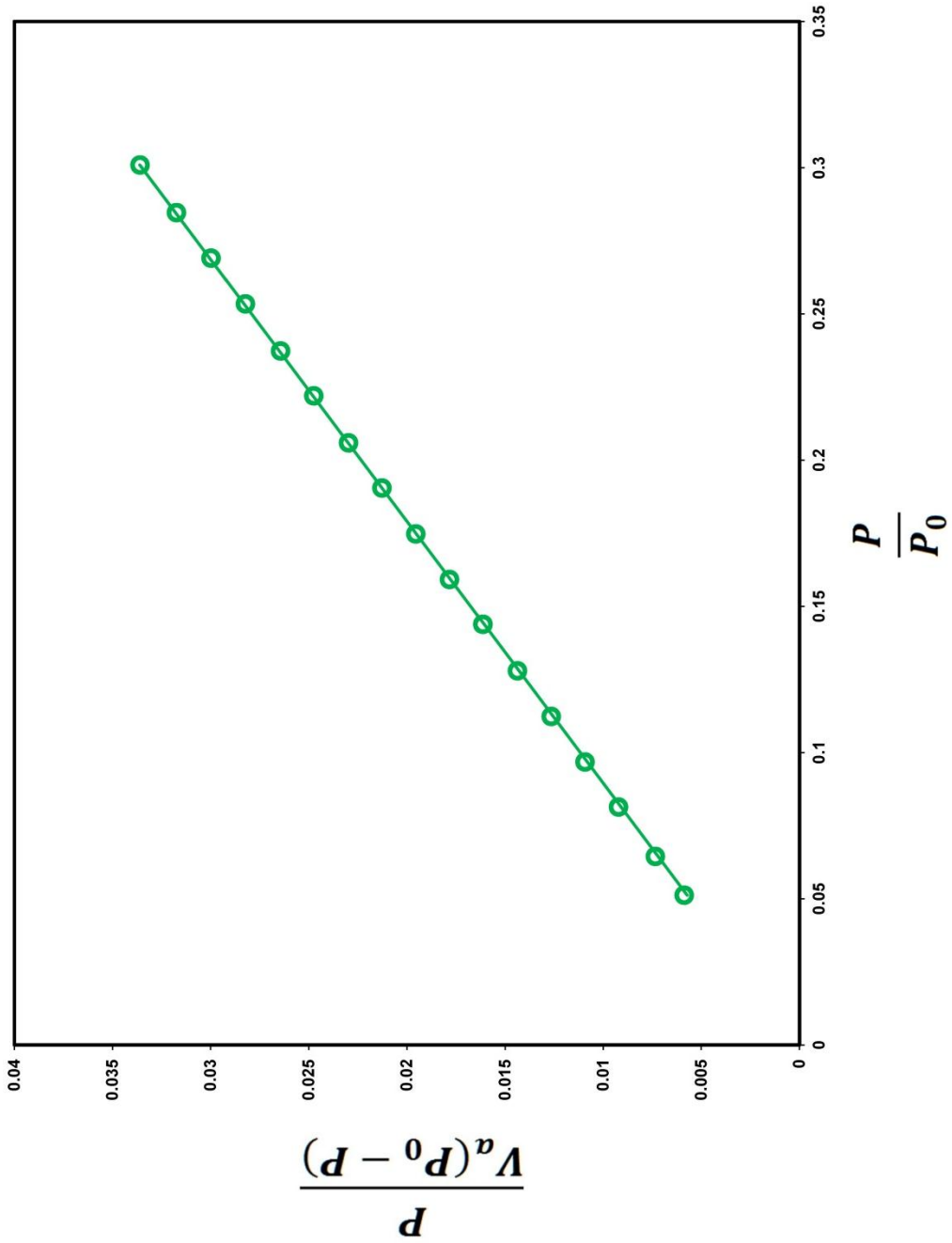


Figure 3.4. Representative BET transform plot using data from the sintering of hydroxyapatite at 700 °C for 1 hour

| Absolute Pressure<br>(mmHg) | $\frac{P}{P_0}$ | $V_a$       | $\frac{P}{V_a(P_0 - P)}$ |
|-----------------------------|-----------------|-------------|--------------------------|
| 37.65331650                 | 0.05119670      | 9.19653998  | 0.00586734               |
| 47.39600754                 | 0.06444370      | 9.38453325  | 0.00734003               |
| 59.82259369                 | 0.08133996      | 9.60673208  | 0.00921666               |
| 71.15759277                 | 0.09675201      | 9.80561313  | 0.01092391               |
| 82.62177277                 | 0.11233970      | 10.00523768 | 0.01264908               |
| 94.08158112                 | 0.12792144      | 10.20670793 | 0.01437150               |
| 105.78554530                | 0.14383516      | 10.41559228 | 0.01612960               |
| 117.06773380                | 0.15917540      | 10.62098999 | 0.01782401               |
| 128.50596620                | 0.17472781      | 10.83525867 | 0.01954004               |
| 140.05886840                | 0.19043613      | 11.05930926 | 0.02127013               |
| 151.43013000                | 0.20589748      | 11.28748721 | 0.02297086               |
| 163.24995420                | 0.22196873      | 11.52925229 | 0.02474535               |
| 174.51660160                | 0.23728784      | 11.76870104 | 0.02643542               |
| 186.37864690                | 0.25341650      | 12.02375215 | 0.02823036               |
| 197.86791990                | 0.26903831      | 12.28013829 | 0.02997204               |
| 209.33439640                | 0.28462912      | 12.53781062 | 0.03173411               |
| 221.30041500                | 0.30089915      | 12.81204721 | 0.03359407               |

| y=mx+b        |              |
|---------------|--------------|
| Slope (m)     | 1.10721E-01  |
| Intercept (b) | 1.99152E-04  |
| $S_m$         | 8.695553E-05 |
| $S_b$         | 1.66152E-05  |
| $R^2$         | 9.99991E-01  |

| BET Surface Area (m <sup>2</sup> /g) |
|--------------------------------------|
| 39.25 ± 0.03                         |

Table 3.2. Representative Excel® spreadsheet for the BET transform plot of bovine derived hydroxyapatite sintered at 700 °C for 1 hour used to determine BET surface areas



Figure 3.5. Image of a standard 6mm diameter bovine bone plug being cut from a section of bovine femur

experimentation. Between 6 and 8 extracted bone plugs were selected at random. Their heights and diameters were measured with a set of Starrett® 799 digital calipers. The weight of each plug was also measured. To determine the effect that sintering has on a portion of intact bone, I placed each plug in a separate crucible and the crucible was then placed into a preheated muffle furnace at the desired temperature. The minimum temperature chosen was 600 °C. This temperature was chosen based on the previous FTIR spectroscopy that showed water remains in the sample at 500 °C and is not driven off until a sintering temperature of at least 600 °C is reached. 600 °C was also the lowest temperature that gave reliable kinetics data. A temperature of 1100 °C was chosen for the upper limit of the sintering experiments. The plugs were maintained at the selected sintering temperature for 16 hours before being removed and allowed to cool in a vacuum desiccator under hard vacuum of less than 50 millitorr. Once the plugs had cooled to room temperature, they were quickly weighed. Water quickly adsorbs to the surface of HA so haste was key to getting reliable weights for desiccated samples. After the weights of all plugs were determined, the height and diameter of each plug were measured again with the calipers.

### Results and Discussion

The surface area experiments clearly indicate a greatly accelerated decrease in surface area when the sintering temperature is raised from 600 °C to 800 °C. Once a temperature of 800 °C or above is reached, the surface area decreases to 9.3 m<sup>2</sup>/g in approximately 30 minutes. While at 700 °C almost seven hours is required to reach a surface area of approximately 9.4 m<sup>2</sup>/g. (Figure 3.6, Figure 3.7, Figure 3.8) At 600 °C

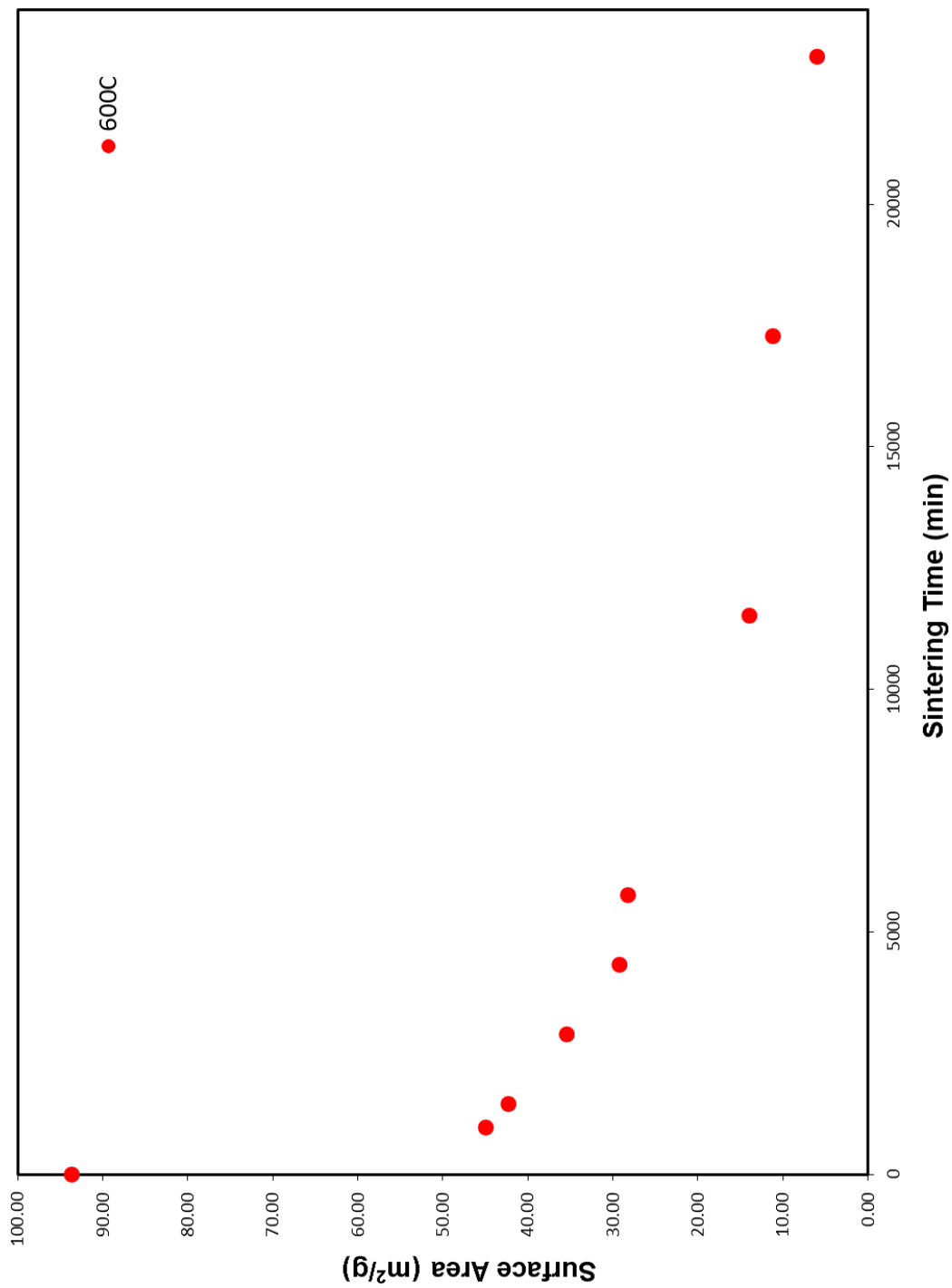


Figure 3.6. Plot of surface area versus time for bovine derived hydroxyapatite sintered at 600 °C



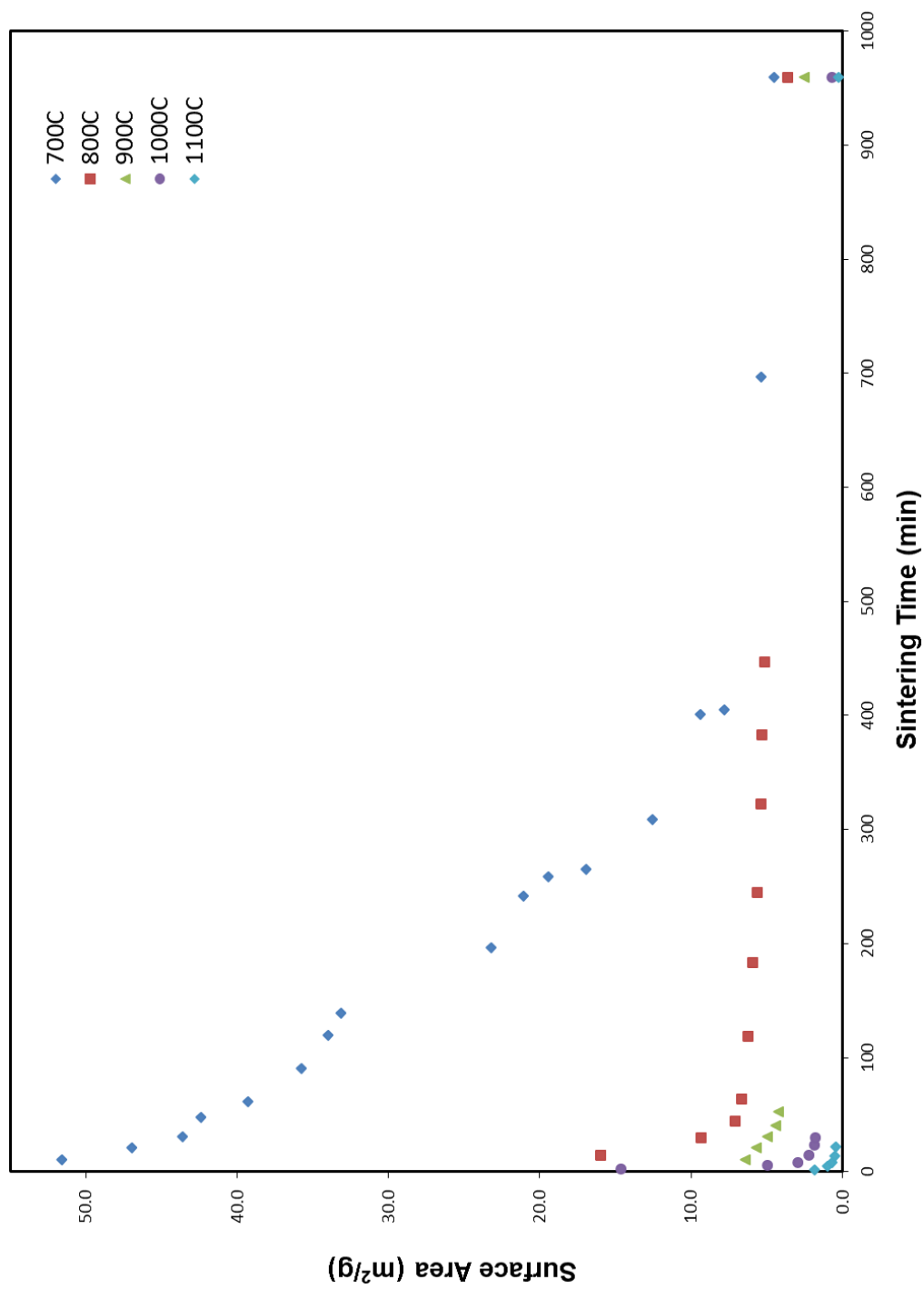


Figure 3.7. Plots of surface area versus time for bovine derived hydroxyapatite samples sintered at temperatures from 700 °C to 1100 °C in 100 °C increments

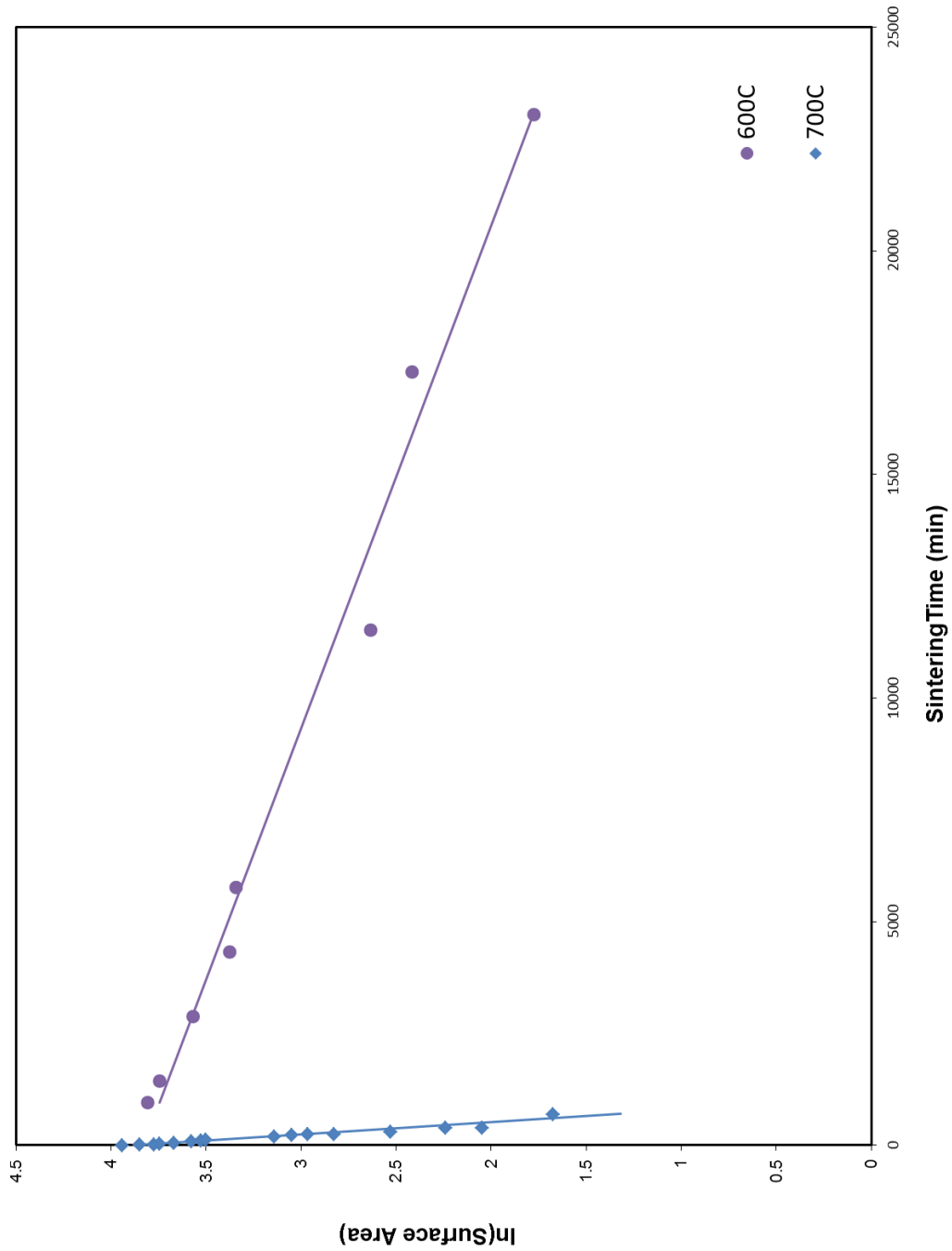


Figure 3.8. Kinetic plots for the decrease in surface area of bovine derived hydroxyapatite sintered at 600 °C and 700 °C

the rate of decrease in surface area is very slow. At this temperature the surface area changes very little over a period of several days. When the data from the 600 °C and 700 °C surface area experiments is plotted according to equation 3.11, the predicted linear relationship manifests itself. Kinetic rate constants for the surface area change ( $k_{SA}$ ) can be determined from the slope of each line. Values of  $3.7 \pm 0.2 \times 10^{-3} \text{min}^{-1}$  and  $8.9 \pm 0.4 \times 10^{-5} \text{min}^{-1}$  are obtained for sintering temperatures of 700 °C and 600 °C respectively. Using the y-intercept to determine the initial specific surface area of the sample, I obtained a value of  $46.0 \pm 0.3 \text{ m}^2/\text{g}$  for the sample sintered for 16 hours at 600 °C and  $48.9 \pm 0.3 \text{ m}^2/\text{g}$  for the sample sintered for 16 hours at 700 °C.

It is not practical to use higher temperature experiments for determining the surface area decrease kinetics because the reaction proceeds at such a fast rate that sampling becomes unreliable, and the thermal lag in bringing the entire sample up temperature and cooling it in a uniform manner results in nonhomogeneity throughout the sample.

In Chapter 2 kinetics for the ring opening polymerization reaction for various sintering temperatures of the initiating hydroxyapatite were explained in terms of the nucleophile type and distribution. The final piece in characterizing how the heat treatment of the HA will affect the reaction is to know the surface area. To find this piece of information, the surface areas were measured, using the BET method, for the HA samples, nonsintered and sintered from 400 °C to 800 °C, previously used to determine the kinetic rate constants. (Table 3.3) For the lower temperature sintering conditions there is some doubt about the value measured for the surface area obtained. At these low temperatures there is some organic matter left behind that may be giving an abnormally high surface

| Sintering Temperature (°C) | Rate Constant (10 <sup>-7</sup> s <sup>-1</sup> ) | Surface Area (m <sup>2</sup> /g) | 10 <sup>7</sup> × k <sub>app</sub> /SA (g/sm <sup>2</sup> ) |
|----------------------------|---|----------------------------------|---|
| None                       | 31.9 ± 2.5  | 93.68 ± 0.25                     | 0.34 ± 0.03   |
| 400                        | 12.3 ± 0.6  | 87.81 ± 0.15                     | 0.14 ± 0.01   |
| 500                        | 2.2 ± 0.3   | 70.84 ± 0.11                     | 0.03 ± 0.01   |
| 600                        | 13.9 ± 0.3  | 46.76 ± 0.08                     | 0.30 ± 0.01   |
| 700                        | 75.2 ± 0.4  | 4.79 ± 0.02                      | 15.7 ± 0.1  |
| 800                        | 50.6 ± 0.4  | 3.61 ± 0.02                      | 14.0 ± 0.2  |

Table 3.3. Surface area data and kinetics data normalized for surface area for samples sintered for 16 hours at 100 °C temperature increments from 400 °C to 800 °C

area. At 500 °C the residual organic material is burned away and it is believed that the surface area measurements become very reliable at this temperature. At sintering temperatures of 500 °C and below the surface area loss is relatively small but does increase at 600 °C. This also agrees with spectroscopic data showing little increase in crystallinity of the sample. The observations combine to show that little particle size growth is occurring at the macroscopic level. Upon increasing from 600 °C to 700 °C the surface area plummets by over 95%. This extreme decrease in surface area also corresponds to the increase in crystallinity of the sample seen in both the FTIR spectra and XRD patterns. Increasing even further to 800 °C has only a marginal effect on the surface area and crystallinity of the sample, so it appears that the critical temperature for crystal growth and rapid surface area decrease is between 600 °C and 700 °C.

If the apparent kinetic rate constant is normalized by dividing it by the surface area it is possible to directly compare the reactivity of the surface. As expected from the raw kinetics data, below 600 °C shows very little activity toward reaction. Increasing the temperature to 700 °C and above gives a surface that is far more reactive as is attested by the 50 fold increase in  $k_{\text{app}}/SA$ . This increase in reactivity must be due to the increase in surface nucleophiles since the decrease in surface area alone would predict a decrease in the rate of reaction. As described in Chapter 2, decomposition of carbonate to hydroxide and oxide cause an increase in the rate of polymerization. Normalization of the rate constants using the specific surface area demonstrates that the surface activity for initiation of the polymerization is far greater than is obvious from a simple comparison of rates that are not normalized. In Chapter 2 evidence was also presented showing that

sintering at 800 °C leads to a higher percentage of oxide nucleophiles relative to hydroxide to reduce the total number of nucleophiles available to initiate the polymerization. After the kinetic rate constants are normalized using the specific surface areas, the rates of polymerization do appear to decrease for samples sintered at 800 °C. Consequently, if the chain propagation steps for hydroxide-initiated and oxide-initiated polymerizations are the same, it appears that the polymerization rates decreased at the highest sintering temperatures due to reduced numbers of surface nucleophiles.

Keeping in mind the ultimate goal of using reconstituted bone to construct implants for repair of segmental defects, I determined the influence of sintering temperature on bone plugs that have not been powdered. The ideal conditions for device construction would minimize dimensional shrinkage while maintaining the microscopic and macroscopic morphologies of native bone. The results of my dimension study correlate well with the previous trends of surface area decrease and changes in crystallinity described above (Table 3.4). At sintering temperatures of 500 °C and below, dimensional changes in the bone plugs were negligible over 16 hours, never rising above 1%; however, it should be emphasized that my kinetic data shows that the reaction rates are undesirably slow for bone that is powdered under this condition. At a sintering temperature of 600 °C a modest volume decrease of  $3.2 \pm 0.5\%$  was observed, but this decrease was not accompanied by densification of the samples. In fact the overall density decreased, indicating that the weight loss occurred without major structural changes to the bone. At a sintering temperature of 700 °C the shrinkage rises to  $13.1 \pm 0.5\%$ . This volume change can be attributed to a decrease in the dimensions of the long axis and a decrease in the diameter. This anisotropy in shrinkage is almost certainly related to the anisotropic

| Plug    | Before Heating |             |          |                           | After Heating  |               |             |          | % Density Change |                           |                |               |              |
|---------|----------------|-------------|----------|---------------------------|----------------|---------------|-------------|----------|------------------|---------------------------|----------------|---------------|--------------|
|         | Diameter (mm)  | Height (mm) | Mass (g) | Volume (mm <sup>3</sup> ) | Density (g/ml) | Diameter (mm) | Height (mm) | Mass (g) |                  | Volume (mm <sup>3</sup> ) | Density (g/ml) | % Volume Loss | % Mass Loss  |
| 1       | 6.52           | 24.62       | 1.1596   | 822.0 ± 2.9               | 1.41 ± 0.01    | 6.46          | 24.53       | 1.0954   | 804.0 ± 2.8      | 1.36 ± 0.01               | 2.2% ± 0.5%    | 5.5% ± 0.1%   | -3.4% ± 0.7% |
| 2       | 6.34           | 23.90       | 1.0813   | 755.5 ± 2.7               | 1.43 ± 0.01    | 6.31          | 23.63       | 1.0044   | 738.9 ± 2.7      | 1.36 ± 0.01               | 2.2% ± 0.5%    | 7.1% ± 0.1%   | -5.0% ± 0.7% |
| 3       | 6.41           | 13.88       | 0.6482   | 447.9 ± 1.7               | 1.45 ± 0.01    | 6.32          | 13.75       | 0.6062   | 431.3 ± 1.7      | 1.41 ± 0.01               | 3.7% ± 0.6%    | 6.5% ± 0.1%   | -2.9% ± 0.7% |
| 4       | 6.47           | 19.23       | 0.9398   | 632.2 ± 2.3               | 1.49 ± 0.01    | 6.34          | 19.04       | 0.8775   | 601.1 ± 2.2      | 1.46 ± 0.01               | 4.9% ± 0.5%    | 6.6% ± 0.1%   | -1.8% ± 0.7% |
| 5       | 6.53           | 19.10       | 0.9581   | 639.7 ± 2.3               | 1.50 ± 0.01    | 6.45          | 18.97       | 0.9028   | 619.8 ± 2.3      | 1.46 ± 0.01               | 3.1% ± 0.5%    | 5.8% ± 0.1%   | -2.8% ± 0.7% |
| 6       | 6.52           | 20.68       | 1.0462   | 690.5 ± 2.5               | 1.52 ± 0.01    | 6.45          | 20.53       | 0.9656   | 670.8 ± 2.4      | 1.44 ± 0.01               | 2.8% ± 0.5%    | 7.7% ± 0.1%   | -5.0% ± 0.6% |
| 7       | 6.54           | 21.76       | 1.0883   | 731.0 ± 2.6               | 1.49 ± 0.01    | 6.45          | 21.59       | 1.0258   | 705.4 ± 2.5      | 1.45 ± 0.01               | 3.5% ± 0.5%    | 5.7% ± 0.1%   | -2.3% ± 0.7% |
| Average |                |             |          |                           |                |               |             |          |                  |                           | 3.2% ± 0.5%    | 6.4% ± 0.1%   | -3.3% ± 0.7% |
| Plug    | Before Heating |             |          |                           | After Heating  |               |             |          | % Density Change |                           |                |               |              |
|         | Diameter (mm)  | Height (mm) | Mass (g) | Volume (mm <sup>3</sup> ) | Density (g/ml) | Diameter (mm) | Height (mm) | Mass (g) |                  | Volume (mm <sup>3</sup> ) | Density (g/ml) | % Volume Loss | % Mass Loss  |
| 1       | 6.33           | 13.66       | 0.6293   | 429.9 ± 1.7               | 1.46 ± 0.01    | 6.02          | 13.55       | 0.5911   | 385.7 ± 1.6      | 1.53 ± 0.01               | 10.3% ± 0.6%   | 6.1% ± 0.1%   | 4.7% ± 0.7%  |
| 2       | 6.50           | 22.42       | 1.1168   | 744.0 ± 2.6               | 1.50 ± 0.01    | 6.25          | 21.75       | 1.0399   | 667.3 ± 2.4      | 1.56 ± 0.01               | 10.3% ± 0.5%   | 6.9% ± 0.1%   | 3.8% ± 0.7%  |
| 3       | 6.53           | 21.01       | 1.0660   | 703.6 ± 2.5               | 1.52 ± 0.01    | 6.22          | 20.58       | 0.9863   | 625.3 ± 2.3      | 1.58 ± 0.01               | 11.1% ± 0.5%   | 7.5% ± 0.1%   | 4.1% ± 0.7%  |
| 4       | 6.64           | 14.30       | 0.7123   | 495.2 ± 1.8               | 1.44 ± 0.01    | 6.25          | 13.87       | 0.6590   | 425.5 ± 1.7      | 1.55 ± 0.01               | 14.1% ± 0.5%   | 7.5% ± 0.1%   | 7.7% ± 0.8%  |
| 5       | 6.63           | 15.25       | 0.7813   | 526.5 ± 1.9               | 1.48 ± 0.01    | 6.25          | 14.66       | 0.7186   | 449.8 ± 1.7      | 1.60 ± 0.01               | 14.6% ± 0.5%   | 8.0% ± 0.1%   | 7.7% ± 0.7%  |
| 6       | 6.28           | 20.99       | 0.9595   | 650.2 ± 2.4               | 1.48 ± 0.01    | 5.85          | 20.13       | 0.8806   | 541.1 ± 2.1      | 1.63 ± 0.01               | 16.8% ± 0.5%   | 8.2% ± 0.1%   | 10.3% ± 0.8% |
| 7       | 6.23           | 15.83       | 0.7155   | 482.6 ± 1.9               | 1.48 ± 0.01    | 5.88          | 15.23       | 0.6556   | 413.6 ± 1.7      | 1.59 ± 0.01               | 14.3% ± 0.6%   | 8.4% ± 0.1%   | 6.9% ± 0.7%  |
| Average |                |             |          |                           |                |               |             |          |                  |                           | 13.1% ± 0.5%   | 7.5% ± 0.1%   | 6.4% ± 0.7%  |

Table 3.4. Tabulated data for dimension stability of bovine bone plugs sintered for 16 hours at 600 °C (Top) and 700 °C (Bottom)

nature of the native bone plugs, which were acquired with the long axis of the plug being parallel to the long axis of the cortical bone in the original femur.

Scanning electron microscopy images of sintered bovine bone show growth in crystal size that is consistent with measurements of specific surface area. (Figure 3.9, Figure 3.10, Figure 3.11) The crystal size is clearly larger for sintered samples than it is for samples that have not been heated. Some grain growth is observed after sintering for 16 hours at 600 °C, but the extent of remodeling is far more pronounced in samples sintered for 16 hours at 700 °C. Grain coalescence is far more apparent in the higher temperature sample. Additionally, the aspect ratio of the hydroxyapatite changes during the sintering process. Synthetic and geologic hydroxyapatite crystals are hexagonal and somewhat flat to globular in shape. Biologic hydroxyapatite crystals are hexagonal, but needle-like. At high sintering temperatures the needle shape is lost in favor of a more globular form. In short, as the crystallinity increases the microscopic biologic morphology is lost. This loss may influence the performance of polymer-ceramic composite devices. In mammals, carbonated hydroxyapatite with low crystallinity is remodeled faster than highly crystalline samples.<sup>9, 10</sup> Changing the crystal shape and chemical composition by removing the carbonate may affect device resorption and remodeling.

It is clear from the dimensional analysis experiments that both the mass of hydroxyapatite bone plugs and their volume decrease upon extensive sintering. It is also evident that the amount of shrinkage and mass loss increases with increasing temperature. Comparisons of the initial and final densities show that the reactions which cause mass loss through evolution of water and decomposition of carbonate do not cause macroscopic



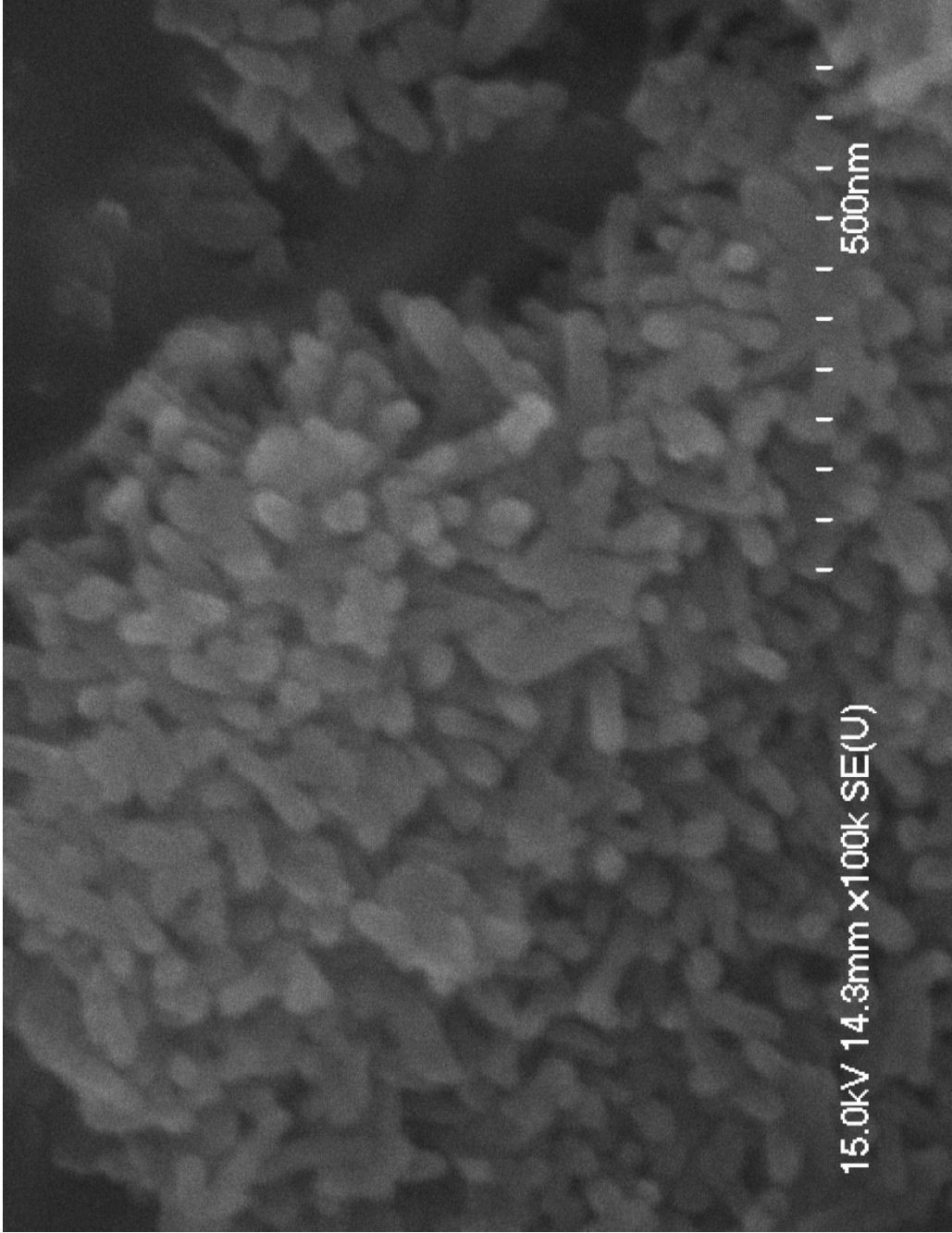


Figure 3.9. Scanning electron microscopy image of nonsintered, extracted, bovine hydroxyapatite powder

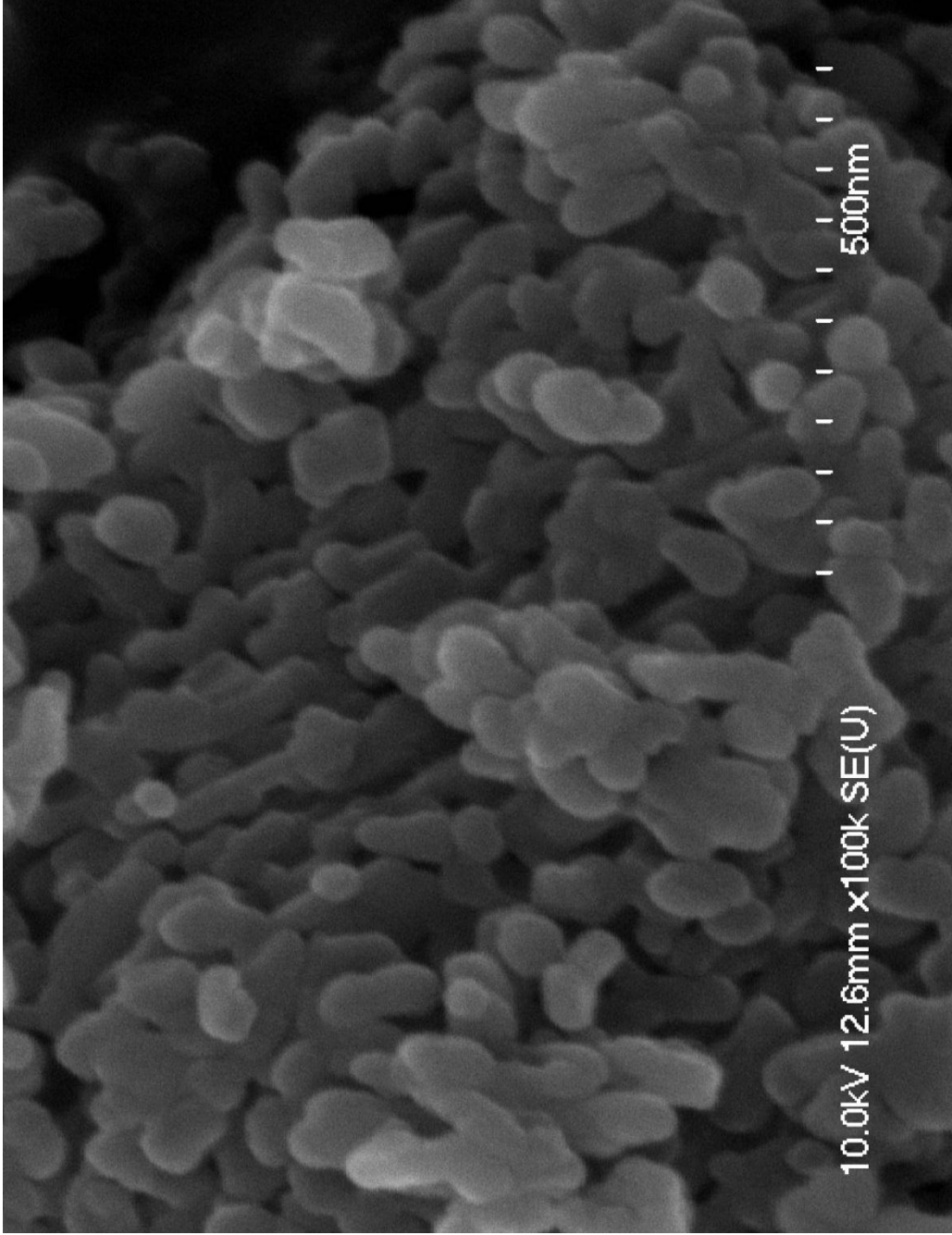


Figure 3.10. Scanning electron microscopy image of extracted bovine hydroxyapatite powder sintered at 600 °C for 16 hours

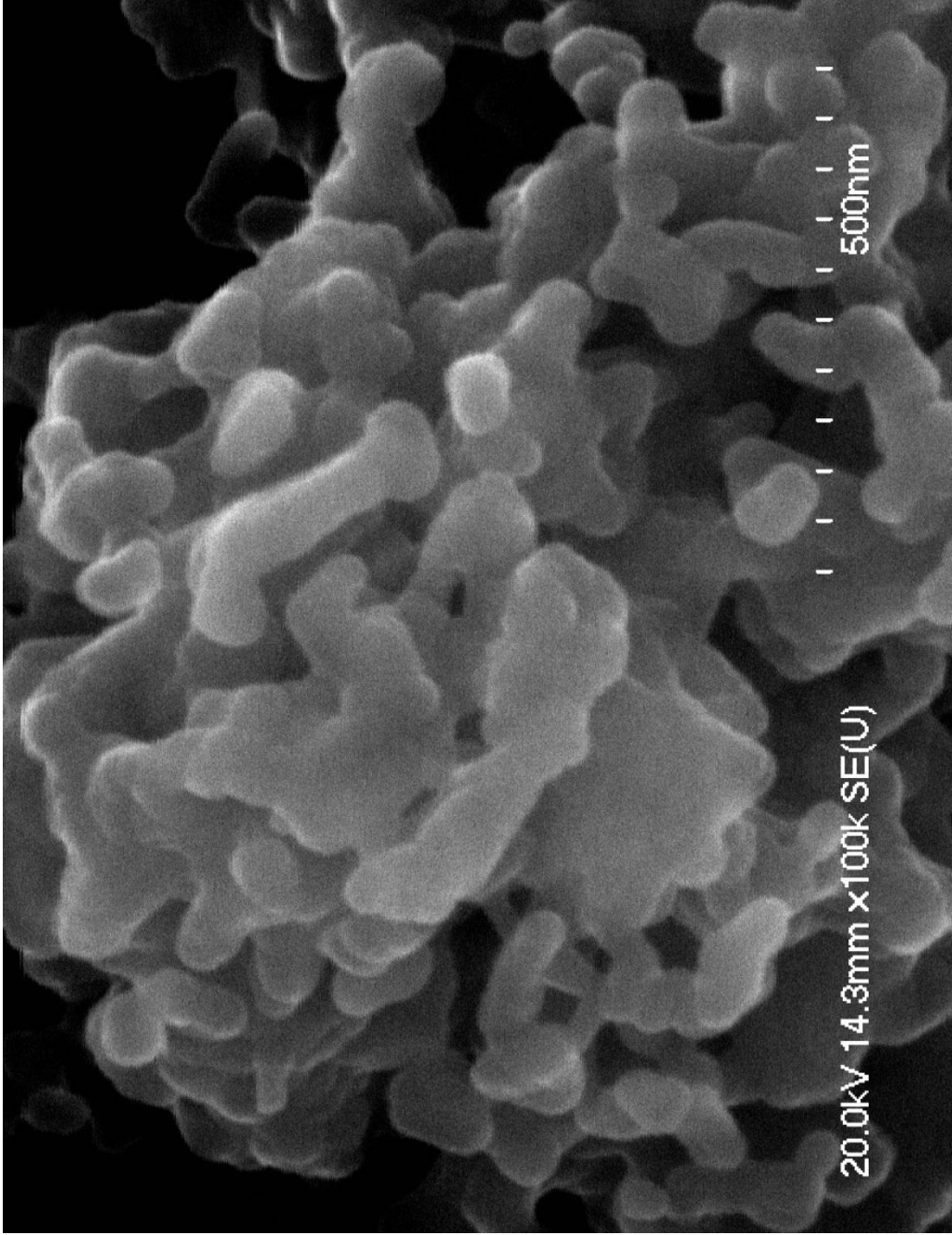


Figure 3.11. Scanning electron microscopy image of extracted bovine hydroxyapatite powder sintered at 700 °C for 16 hours

dimensional changes that influence the bulk density. Looking at the density change at 700 °C reveals an increase in density, which is consistent with surface area decrease and crystal size increase seen in the SEM images. At 600 °C, I did observe a mass loss due to water loss and limited carbonate decomposition, but the volume occurs more slowly, as attested by the differences in the kinetic rate constants for the two temperatures. This creates a scenario where the density is higher for nonsintered samples than it is for samples sintered at 600 °C for 16 hours.

It is important to note that after 16 hours at a sintering temperature of 700 °C the bone plugs appear bright white upon cooling and there is no macroscopic evidence of cracking or flaking. When bone plugs are heated to 800 °C and above there is noticeable cracking that could lead to a device failure in load bearing applications. These deformities prevented accurate dimensional measurements of samples sintered at 800 °C and above and suggest that such materials should not be used in load bearing applications. I conclude that the sintering temperature should be kept at 700 °C or below.

### References

1. Langmuir, I., The adsorption of gases on plane surfaces of glass, mica and platinum. *Journal of the American Chemical Society* **1918**, 40, (9), 1361-1402.
2. Brunauer, S.; Emmett, P. H.; Teller, E., Adsorption of Gases in Multimolecular Layers. *Journal of the American Chemical Society* **1938**, 60, (2), 309-319.
3. Nicholson, D., Variation of Surface Area During the Thermal Decomposition of Solids. *Transactions of the Faraday Society* **1965**, 61, (501), 990-998.
4. Nzihou, A.; Bailliez, S., Mechanisms of Sintering of Macroporous Hydroxyapatite Adsorbents. *Journal of High Temperature Materials and Processes* **2002**, 21, (5), 281-295.
5. Bailliez, S.; Nzihou, A., The kinetics of surface area reduction during isothermal sintering of hydroxyapatite adsorbent. *Chemical Engineering Journal* **2004**, 98, (1-2), 141-152.
6. Raynaud, S.; Champion, E.; Bernache-Assollant, D., Calcium phosphate apatites with variable Ca/P atomic ratio II. Calcination and sintering. *Biomaterials* **2001**, 23, 1073-1080.
7. Bernache-Assollant, D.; Ababou, A.; Champion, E.; Heughebaert, M., Sintering of calcium phosphate hydroxyapatite  $\text{Ca}_{10}(\text{PO}_4)_6(\text{OH})_2$ . I. Calcination and particle growth. *Journal of the European Ceramic Society* **2002**, 23, 229-241.
8. Ababou, A.; Bernache-Assollant, D.; Heughebaert, M., Influence of water vapor on grain growth during the calcination of hydroxyapatite. *Ceramic Transactions* **1995**, 51, 111-115.

9. Zakaria, F. A.; Marsad, N. H.; Manaf, A. Y. A.; Villamil, M.; Montes, T.; Carretero, C.; Mikan, J., Characterisation of carbonated apatite for possible application in biomedical implants. *Materials Research Innovations* **2009**, 13, (3), 309-312.
10. Landi, E.; Celotti, G.; Logroscino, G.; Tampieri, A., Carbonated hydroxyapatite as bone substitute. *Journal of the European Ceramic Society* **2003**, 23, (15), 2931-2937.

## Chapter Four

### Kinetic Analysis of Common Biocompatible Monomers and Polymers with Ring Opening Polymerization Initiated by Bovine Hydroxyapatite Sintered at Constant Temperature for Various Times

#### Introduction and Background

As was established in Chapters 2 and 3, two properties of sintered anorganic bone are important in determining the rate of polymerization of cyclic lactones. These two properties are the number of surface nucleophiles and their identity. FTIR spectra and XRD patterns show that the number of nucleophiles can be increased in a sample of biologically derived hydroxyapatite by sintering the sample at 600 °C or higher. The temperature chosen also influences the distribution between two nucleophiles that are possible, oxide and hydroxide. The general trend is that at lower temperatures hydroxide is the favored species, while at increasing temperature oxide becomes more prevalent. The reactions favoring hydroxide generation favor faster reaction rates since one mole of carbonate can decompose into two moles of hydroxide, but only one mole of oxide. The temperature also influences the surface area of biologically derived hydroxyapatite. When sintering for 16 hours at 600°C or below there is relatively little decrease in the surface area. The rate of change of specific surface area is greatly accelerated at a sintering temperature of 700 °C. At 600 °C the rate constant for surface area decrease is  $8.9 \pm 0.4 \times 10^{-5} \text{ min}^{-1}$  and at 700 °C it rises by over an order of magnitude to  $3.7 \pm 0.2 \times 10^{-3} \text{ min}^{-1}$ . (Figure 3.8) In a matter of minutes at 800 °C and higher, the specific surface area decreases to less than 5% of its original value. There is also a large difference in the

crystal morphology and crystallinity at 600 °C and 700 °C. At the lower temperature the hydroxyapatite is much less crystalline than the sample sintered at higher temperatures. This lower level of crystallinity is due to carbonate ion substitution that is still present at low temperatures. At elevated temperatures, the crystal morphology changes in tandem with the increase in crystallinity. Biologic hydroxyapatite is needle like in shape as opposed to synthetic sources which are more tabular to globular in shape. Accompanying the crystallinity change during sintering, the crystal morphology also changed to become more like synthetically manufactured samples as was seen from SEM images. (Figures 3.9, 3.10, and 3.11)

Although my characterizations of sintering on bone plugs reveals that the rates of carbonate decomposition and surface area decrease are increased at elevated sintering temperatures, the density does not follow the same trend. At 600 °C the density of the plugs actually decreases relative to its value before sintering. At 700 °C the density of the plugs decreases relative to its value before sintering. This begs the question, is it possible to sinter biologically derived HA at a low temperature so that it retains its higher surface area while still enhancing the concentration of nucleophiles? The search for an answer to this question is the focus of Chapter 4.

When attempting to create a material for hard tissue replacement, it seems logical that preservation of the original biological structure might lead to better compatibility and more rapid integration of the device with its host. In theory, use of high specific area hydroxyapatite with a high surface concentration of nucleophiles should afford rapid



polymerization rates. Additionally, high HA specific surface areas should aid osteoclast remodeling of any implants constructed from the resulting composites.

### Experimental

Chemicals: Ethylene diamine (99% from Sigma-Aldrich) was used as purchased, and biologic hydroxyapatite was sourced from bovine femur (from Premium Protein Products). L-lactide (from Purac) was sublimed at 90 °C and then transferred into a N<sub>2(g)</sub> atmosphere glove box for further use.

Methodology: The FTIR spectroscopy and powder x-ray diffraction described in this chapter were performed and processed as described on pages 80 and 84 of Chapter 2. Biologically derived hydroxyapatite powder for kinetics studies was prepared as described on pages 50 through 52 in Chapter 2. Once the powder was isolated from bovine femurs, it was processed as follows. A muffle furnace was heated to 600 °C. Several crucibles were preheated to the desired temperature. Roughly 6 to 7 grams of powdered HA was placed into the preheated crucibles and allowed to heat in air in the furnace. The samples were removed at regular intervals and allowed to cool in a vacuum desiccator under vacuum at 50 millitorr. Once the samples had cooled enough to handle they were transferred into a N<sub>2(g)</sub> atmosphere glove box for further characterization and experimentation. These experiments include kinetics experiments to characterize the efficacy of the sintered bone in initiating the polymerization of L-lactide. The methods used to perform the kinetics experiments can be found on page 52 of this thesis. NMR analysis of aliquots selected from the reaction mixtures was described on page 58.

## Results and Discussion

Several samples of powdered bovine HA were sintered at 600 °C from 16 hours to 384 hours. These samples were then analyzed by FTIR. The FTIR spectra show that at short sintering times the HA is poorly crystalline and contains little hydroxide, but does have some carbonate substitutions. (Figure 4.1) As was described on page 93 in Chapter 2, the relative hydroxide concentration in these samples was determined using the vibration at 3567  $\text{cm}^{-1}$  and the libration at 607  $\text{cm}^{-1}$ . The presence of carbonate is evident by the broad stretch from 1490  $\text{cm}^{-1}$  to 1301  $\text{cm}^{-1}$ . As would be expected, as the sintering time is increased the amount of carbonate decreases and the amount of hydroxide increases. By 192 hours the carbonate had completely decomposed. At this time there is a marked increase in the crystallinity that seems to correlate to the loss of the carbonate. This is consistent with literature reports that the carbonate ion substitution is the cause of irregularities in the lattice that lead to increased solubility and lowered crystallinity.<sup>1-4</sup> This increase in crystallinity, with the loss of carbonate is also consistent with results seen in variable temperature sintering experiments described in Chapter 3. It was observed that some carbonate remained after sintering 16 hours at 600 °C, but carbonate appeared to be completely removed after sintering the bone powder for 16 hours at 700 °C.

The changes in crystallinity observed in FTIR spectra are also apparent in XRD patterns. (Figure 4.2) At 192 hours there is a large increase in the crystallinity of the sample. At higher temperatures a calcium oxide reflection can be seen at 37.5°, but at 600 °C no peak corresponding to an oxide phase is present at any sintering time. Together, XRD and

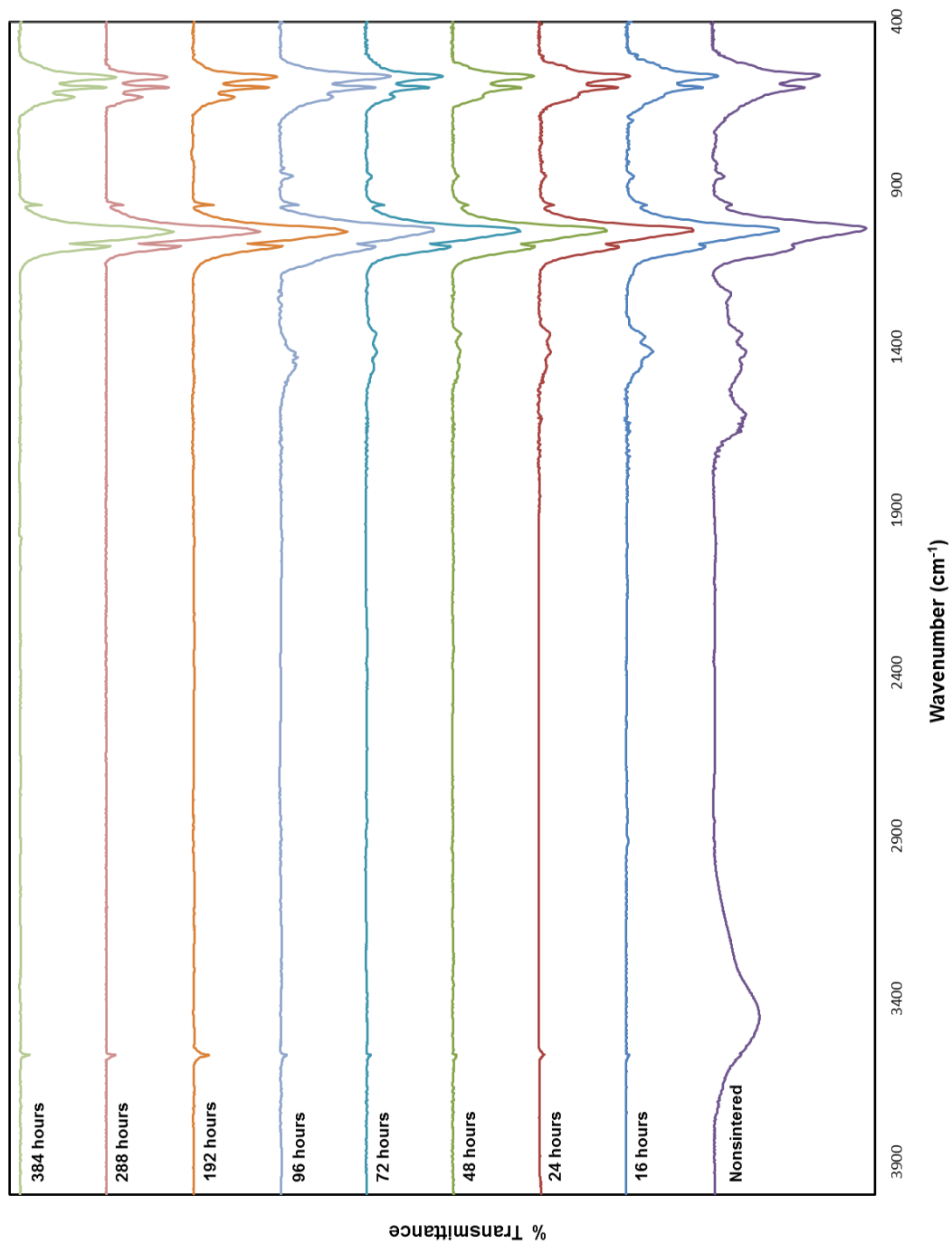


Figure 4.1. FTIR transmittance spectra for bovine hydroxyapatite sintered at 600 °C for various times

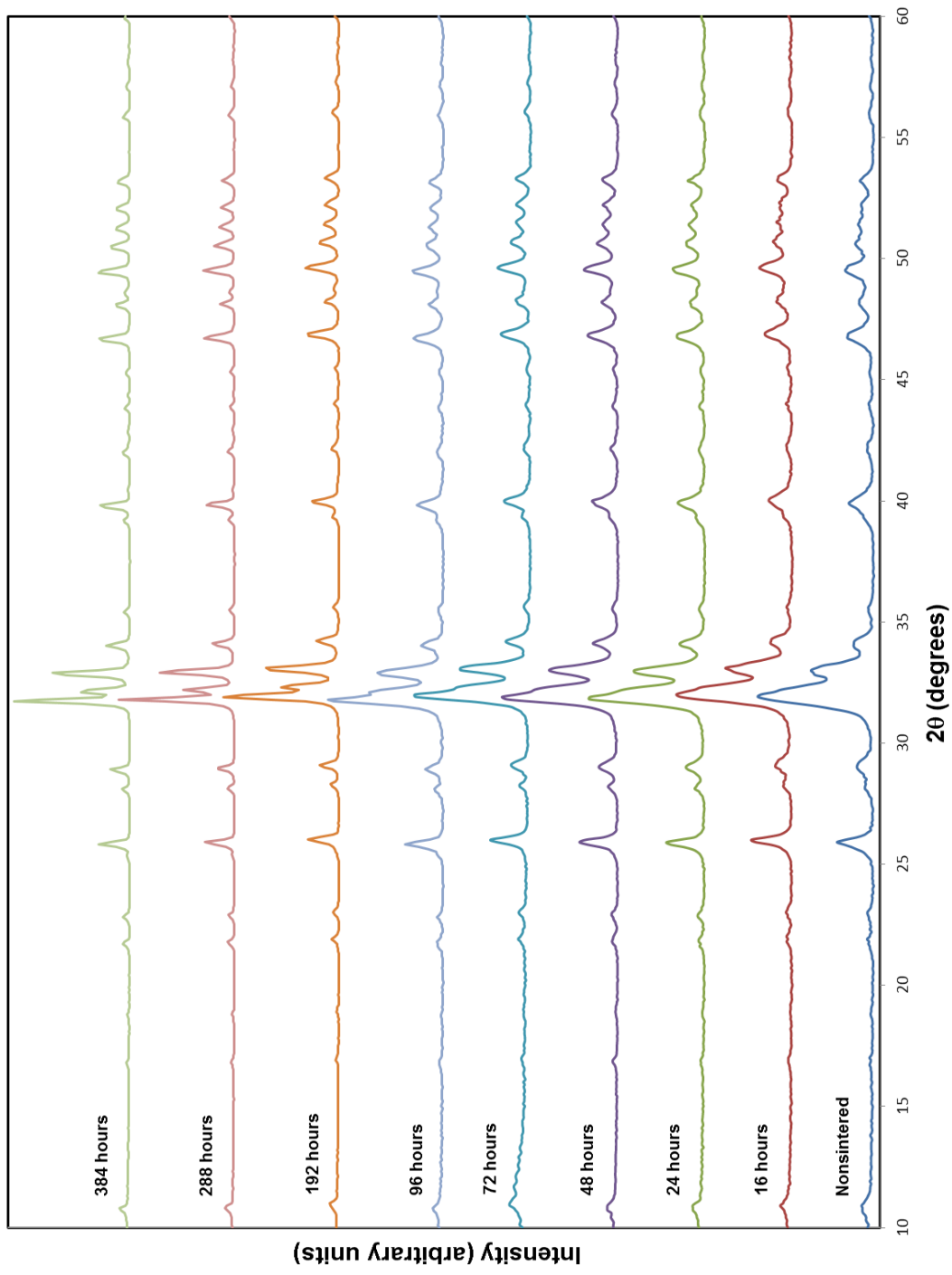


Figure 4.2. XRD patterns for bovine hydroxyapatite sintered at 600 °C for various times

FTIR results indicate that all the carbonate has been successfully converted to hydroxide. Also evident in both the XRD and FTIR is a gradual increase in crystallinity until the carbonate is gone, followed by a significant event in which the crystallinity increases. Later, the rate of change in crystallinity slows again, as seen by comparing relative peak widths.

A series of kinetics experiments were performed to accompany the spectroscopic analysis of the HA samples sintered at 600 °C from 16 hours to 384 hours. A sintering temperature of 600 °C was chosen to examine the effect that sintering time has on the ring opening polymerization of lactones initiated by hydroxyapatite. At 600 °C the same reactions and processes that occur at higher temperatures also occur, but they do so at greatly reduced rates. These reduced rates allow for easier elucidation of subtle changes that take place as the sintering proceeds. With the empirically determined equation to describe the surface area decrease, it was possible to calculate how long a sample must be sintered at 600 °C to have the same surface area as a sample sintered at 700 °C for 16 hours. That time was determined to be 384 hours.

For each polymerization reaction, the plot of  $-\ln \frac{M_t}{M_0}$  versus time obtained from NMR integrations, gave lines with excellent correlation. (Figure 4.3) The slope of each line was used to calculate  $k_{app}$  according to equation 2.4. (Table 4.1) Up to a sintering time of 288 hours, the rate of the reaction increased as the sintering time was increased. At longer sintering times the rate gradually decreased. This trend was not expected, because FTIR spectra and XRD patterns provided no prior indication of a reduction in the number of nucleophiles. When surface area is added to the analysis, a new relationship becomes

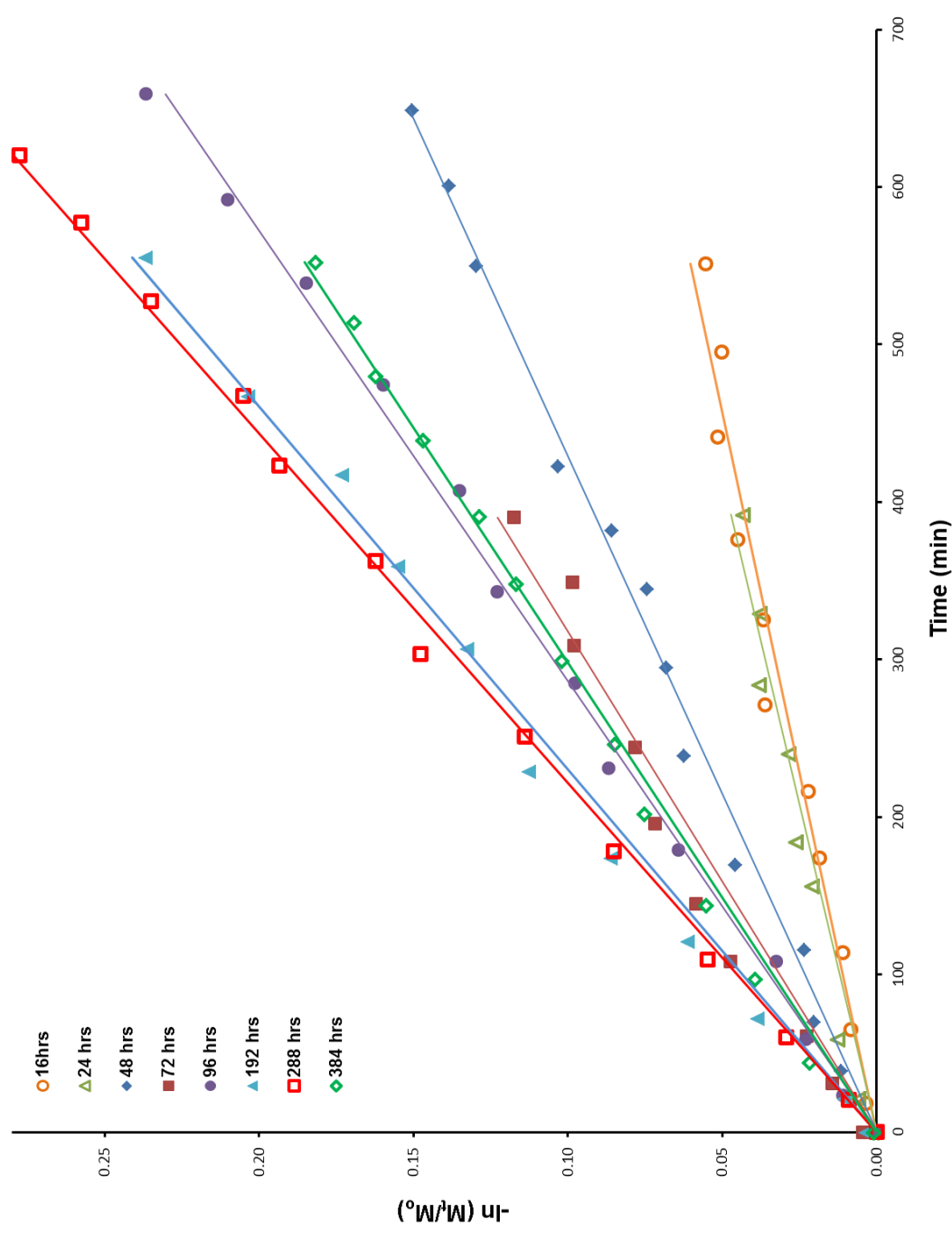


Figure 4.3. Kinetics plots for L-lactide reacted with bovine hydroxyapatite samples sintered at 600 °C for various times

| Sintering Time (hrs) | Apparent Rate Constant ( $10^{-7} \text{ s}^{-1}$ ) | Surface Area ( $\text{m}^2/\text{g}$ ) | $10^7 \times k_{\text{app}}/\text{SA}$ ( $\text{g}/\text{sm}^2$ ) |
|----------------------|---|--|---|
| 16                   | 14.9 $\pm$ 0.3                                      | 44.9 $\pm$ 0.1                         | 0.33 $\pm$ 0.01   |
| 24                   | 17.4 $\pm$ 0.5                                      | 42.2 $\pm$ 0.1                         | 0.41 $\pm$ 0.01   |
| 48                   | 38.9 $\pm$ 0.5                                      | 35.5 $\pm$ 0.1                         | 1.10 $\pm$ 0.02   |
| 72                   | 45.7 $\pm$ 1.4                                      | 29.3 $\pm$ 0.1                         | 1.56 $\pm$ 0.05   |
| 96                   | 58.3 $\pm$ 0.6                                      | 28.24 $\pm$ 0.03                       | 2.06 $\pm$ 0.02   |
| 192                  | 72.4 $\pm$ 1.2                                      | 13.94 $\pm$ 0.03                       | 5.2 $\pm$ 0.1   |
| 288                  | 78.6 $\pm$ 1.0                                      | 11.21 $\pm$ 0.02                       | 7.0 $\pm$ 0.1   |
| 384                  | 55.9 $\pm$ 0.6                                      | 5.91 $\pm$ 0.01                        | 9.5 $\pm$ 0.1   |

Table 4.1. Tabulated kinetic data and surface area results for the reaction of L-lactide reacted with bovine hydroxyapatite samples sintered at 600 °C for various times

apparent. When the rate constants are normalized by dividing through by the surface area to give  $k_{\text{app}}/S_A$ , a direct comparison of the rates of reaction at different sintering times can be made for samples with different surface areas. Such comparisons can be made by examining the data plotted in Figure 4.4. Higher values of  $k_{\text{app}}/S_A$  reflect a surface that is more reactive. The general trend observed in Figure 4.4 indicates that as the sintering time is increased, the surface becomes more reactive toward initiating ring opening polymerization with lactones.

The dependence of  $k_{\text{app}}/S_A$  on sintering temperature can be explained by two competing processes. The first is nucleophile generation. As the sintering time is increased, more nucleophiles are created through the decomposition of carbonate until all of the carbonate is gone. At a sintering temperature of 600 °C, the moles of hydroxide remain constant. At this temperature hydroxide does not appear to dehydrate to form one mole of water and one mole of oxide; however,



carbonate decomposition serves to increase the rate of the polymerization reaction as shown by equations 2.17 and 2.18.

The second process that is a major influence on  $k_{\text{app}}/S_A$  is the time dependent decrease in surface area. As is evident in equations introduced on page 120 and 132 of Chapter 3, the



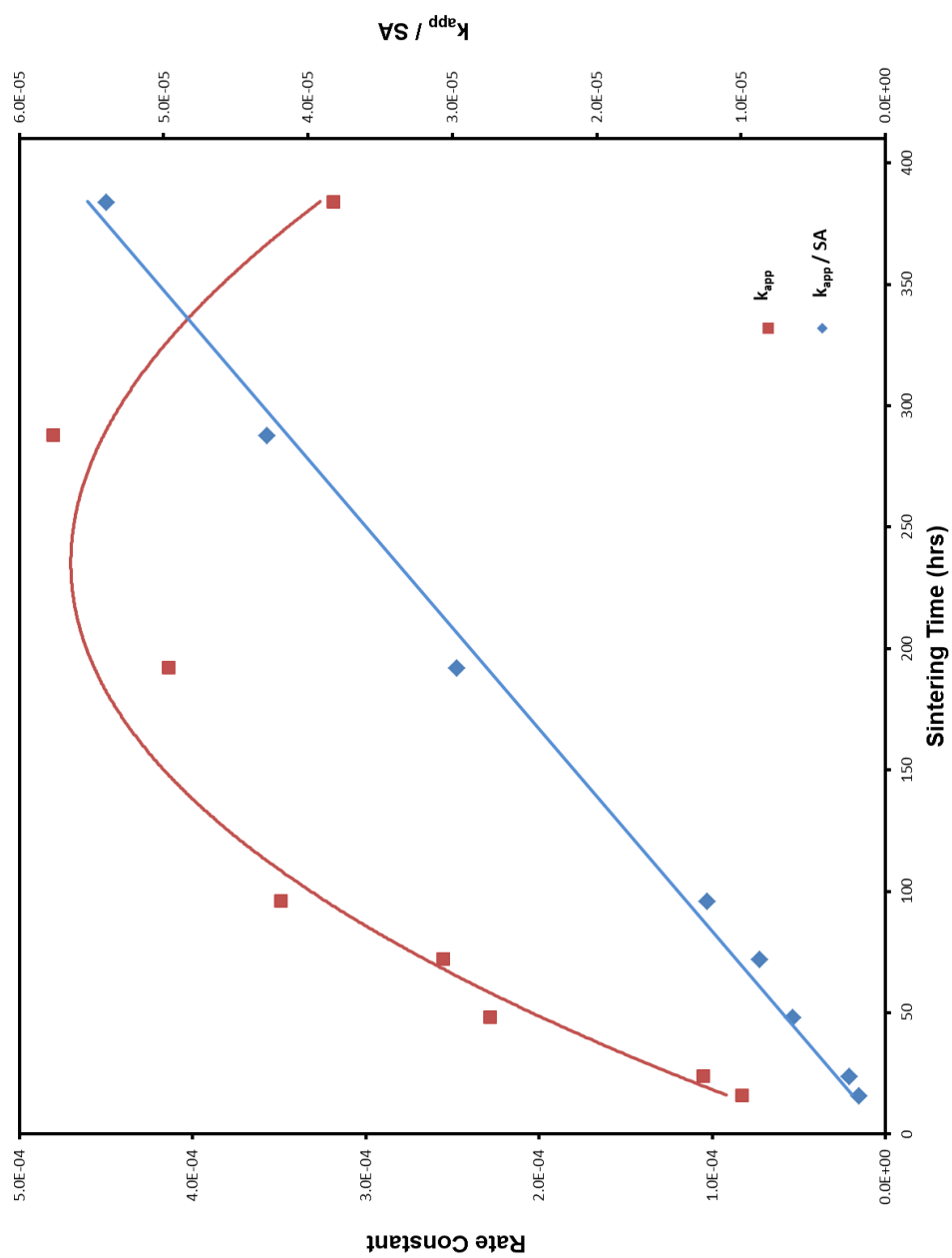


Figure 4.4. The apparent kinetic rate constant for the ring-opening polymerization reaction of L-lactide initiated by bovine hydroxyapatite sintered at 600 °C for various times plotted against sintering time and the apparent kinetic rate constant normalized for surface area plotted against sintering time

surface area of hydroxyapatite gradually decreases during sintering and does not stop at any point. This decrease in specific surface area reduces the number of nucleophiles that are exposed to the monomer, in effect decreasing the  $N_i$  term in equation 2.5. This reduction decreases the apparent rate constant,  $k_{app}$ , since it is equal to  $kN_i$ .

The results plotted in Figure 4.4 make it clear that the process of nucleophile generation ultimately comes to an end and the decrease in surface area becomes the dominant factor controlling the rate constant of polymerization reaction. Another relationship evident in the data plotted in Figure 4.4 is one between the normalized kinetic rate constant,  $k_{app}/SA$ , and time. When  $k_{app}/SA$  is plotted against time a linear relationship is seen giving the empirical relationship

$$1.469 \times 10^{-7}t + 7.759 \times 10^{-7} = \frac{k_{app}}{SA} \quad (4.2)$$

for hydroxyapatite sintered at 600 °C.

Surface areas can be predicted through equation 3.11 for sintered samples and these surface areas can be related to  $k_{app}$  and time through equation 4.2. With this empirical evidence it is possible to project the kinetic rate constant and surface area for samples sintered for as long as 384 hours at 600 °C.

To explore the generality of the proportional relationship between  $k_{app}/SA$  and sintering time, I examined polymerization kinetics and made surface area measurements for samples sintered at 700 °C for various times. The resulting data were treated in the same manner as the 600 °C data. Samples were sintered at 700 °C over times ranging from 1

hour to 16 hours. For each reaction a plot of  $-\ln \frac{M_t}{M_0}$  versus time gave a straight line with excellent correlation. The slope of each line was then used to calculate values of  $k_{app}$ , which are tabulated in Table 4.2 and plotted in Figure 4.5. It is evident in Table 4.2 and Figure 4.5 that the apparent rate constant increases as the sintering time increases from one hour to four hours, at which time it reaches a maximum. Values of  $k_{app}$  for longer sintering times progressively decrease. These changes are accompanied by a monotonic decrease in surface area. As was true for the data collected at a sintering temperature of 600 °C, interpretation of the polymerization kinetics for HA samples sintered at 700 °C becomes clearer when  $k_{app}/SA$  is plotted versus time.

When the rate constants for 700 °C sintering are plotted against time, the same general trend present at 600 °C is revealed. The normalized rate constants increase to a maximum value followed by a rapid decrease. (Figure 4.6) At this sintering temperature, a maximum rate of reaction is seen when the bone powder is sintered at 700 °C for 240 minutes. After this point the rate falls precipitously. These results are similar to the 600 °C results except for the compressed time frame which is due to the more rapid rates of carbonate decomposition and surface area change at elevated temperature. If  $k_{app}/SA$  for the 700 °C sintered material is plotted against time a linear relationship is apparent over the examined range of sintering times giving the equation

$$1.039 \times 10^{-7}t + 3.004 \times 10^{-6} = \frac{k_{app}}{SA} \quad (4.3)$$

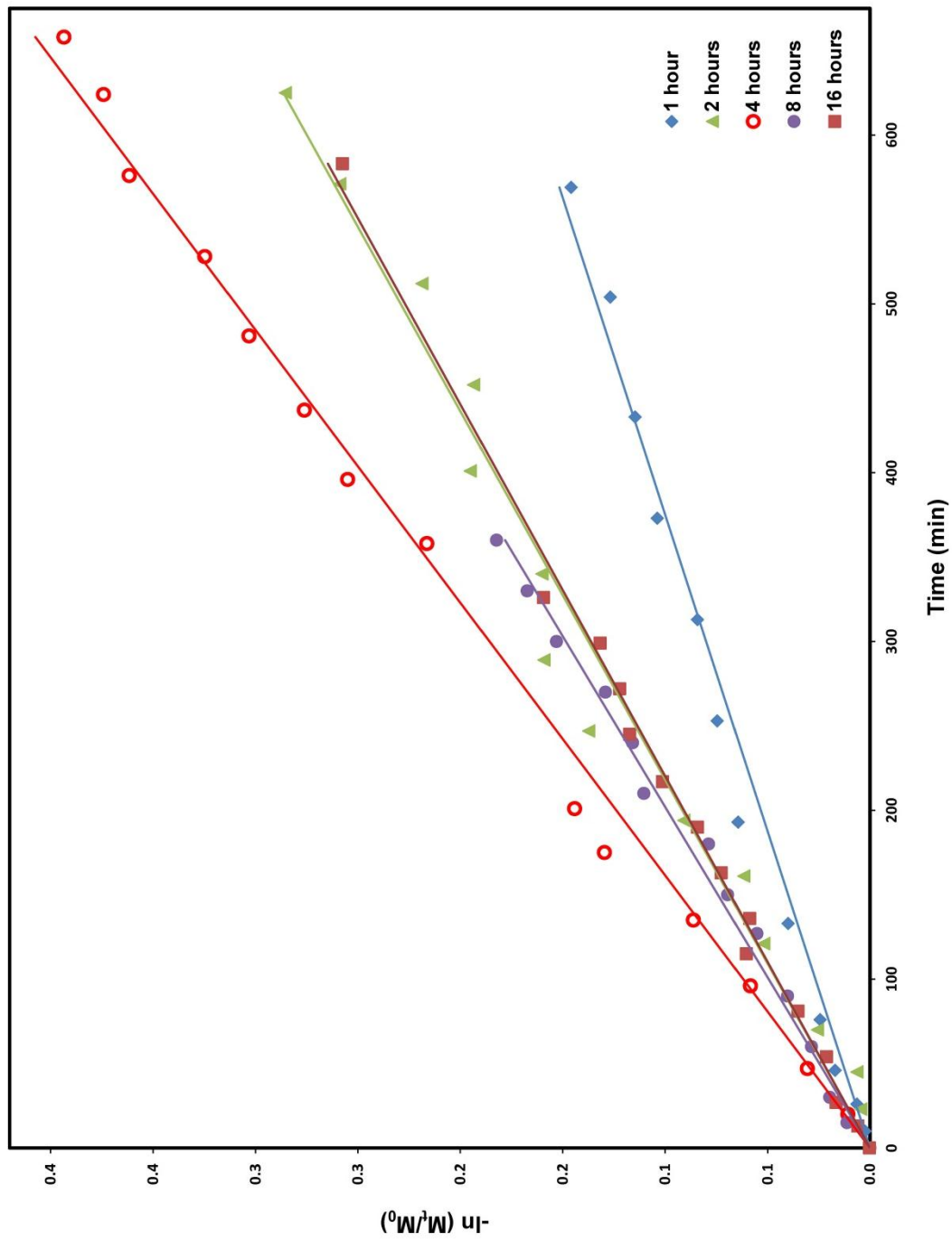


Figure 4.5. Kinetics plots for L-lactide reacted with bovine hydroxyapatite samples sintered at 700 °C for various times

| Sintering Time (hrs) | Apparent Rate Constant ( $10^{-6} \text{ s}^{-1}$ ) | Surface Area ( $\text{m}^2/\text{g}$ ) | $10^6 \times k_{\text{app}}/\text{SA}$ ( $\text{g}/\text{sm}^2$ ) |
|----------------------|---|--|---|
| 1                    | 4.44 $\pm$ 0.09                                     | 39.25 $\pm$ 0.03                       | 0.113 $\pm$ 0.002   |
| 2                    | 7.64 $\pm$ 0.17                                     | 33.98 $\pm$ 0.03                       | 0.22 $\pm$ 0.01   |
| 4                    | 10.32 $\pm$ 0.11                                    | 21.08 $\pm$ 0.03                       | 0.49 $\pm$ 0.01   |
| 8                    | 8.25 $\pm$ 0.12                                     | 8.42 $\pm$ 0.03                        | 0.98 $\pm$ 0.02   |
| 16                   | 7.52 $\pm$ 0.04                                     | 4.52 $\pm$ 0.03                        | 1.66 $\pm$ 0.02   |

Table 4.2. Tabulated kinetic data and surface area results for the reaction of L-lactide reacted with bovine hydroxyapatite samples sintered at 700 °C for various times

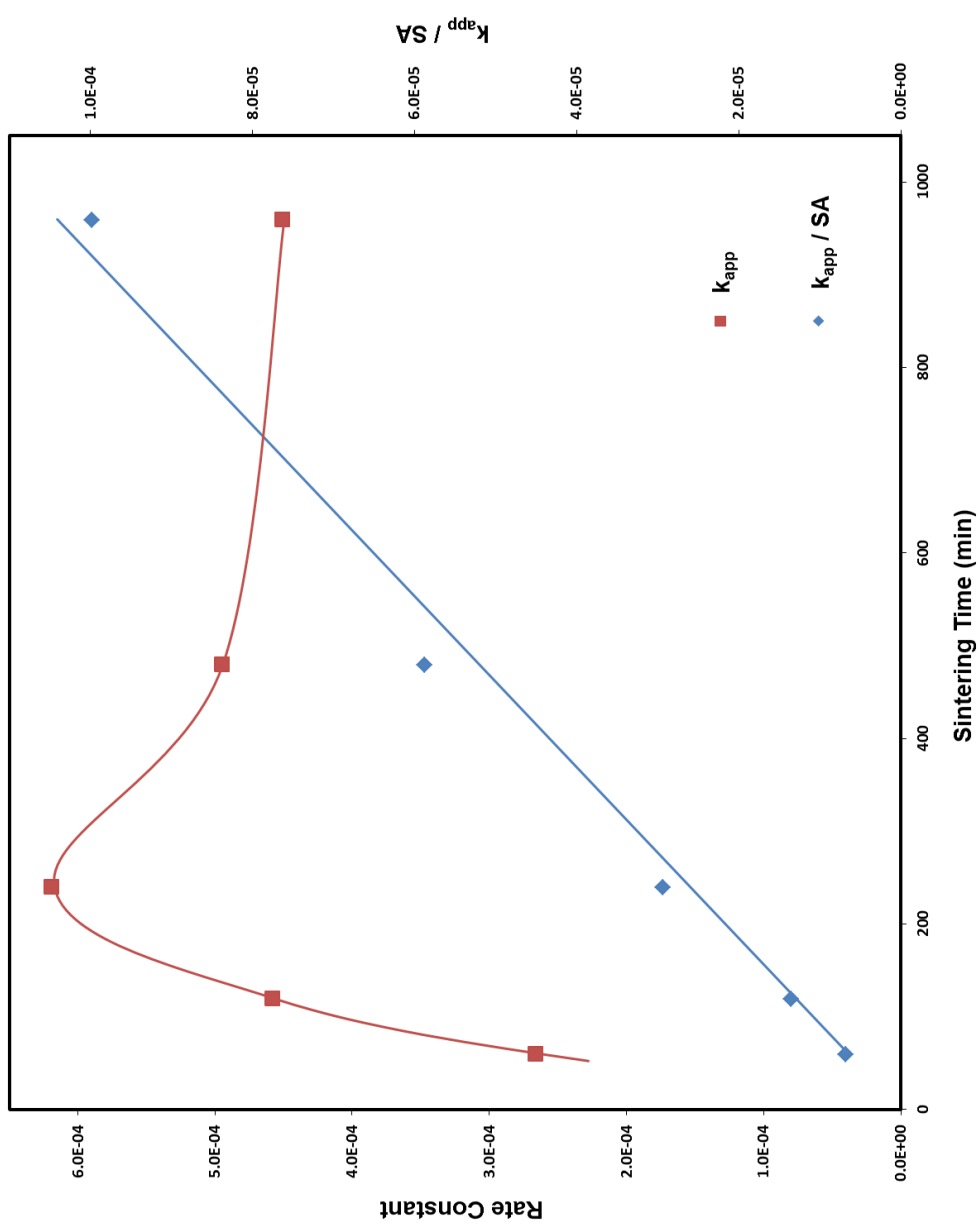


Figure 4.6. The apparent kinetic rate constant for the ring-opening polymerization reaction of L-lactide initiated by bovine hydroxyapatite sintered at 700 °C for various times plotted against sintering time and the apparent kinetic rate constant normalized for surface area plotted against sintering time

Both the 600 °C and 700 °C sintering temperatures yield the same pattern of behavior when  $k_{app}/S_A$  is plotted against time. Both yield linear relationships with good correlation. With these data available combined with a mathematical representation of how surface area decreases with sintering time, it is possible to predict the polymerization rates of L-lactide at HA sintering over a broad range of times at either 600 °C or 700 °C.

FTIR spectroscopy shows that after 1 hour of heating at 700 °C all water is removed, and some carbonate has been decomposed to hydroxide as is evident by the libration at 628  $cm^{-1}$  and the vibration at 3572  $cm^{-1}$ . Only a small amount of carbonate remains. (Figure 4.7) The peak narrowing observed in XRD powder diffraction patterns show some increase in crystallinity, but no buildup of oxide since the reflection at 37.5° is absent. (Figure 4.8) After 2 hours of sintering at 700 °C, little change is observed. Under this condition a small amount of carbonate was converted to hydroxide, but the XRD pattern gave no indication of oxide presence. Four hours into sintering, the FTIR spectrum showed another slight decrease in carbonate and concomitant increase in hydroxide. The crystallinity also increased from the initial nonsintered sample, but FTIR spectroscopy showed little change in crystallinity from the first hour of sintering through the fourth, as is evident by the lack of noticeable peak narrowing from 1 to 4 hours. After sintering for 4 hours, the XRD is a better indication of the crystallinity increase. By this point in time the (112) reflection began to resolve from the (211) reflection, whereas before it was merely a shoulder on the larger peak. When the sintering was allowed to continue to the eighth hour, a much larger portion of the carbonate was seen to decompose to hydroxide. Corresponding to this step, the crystallinity of the sample increased as well, as is

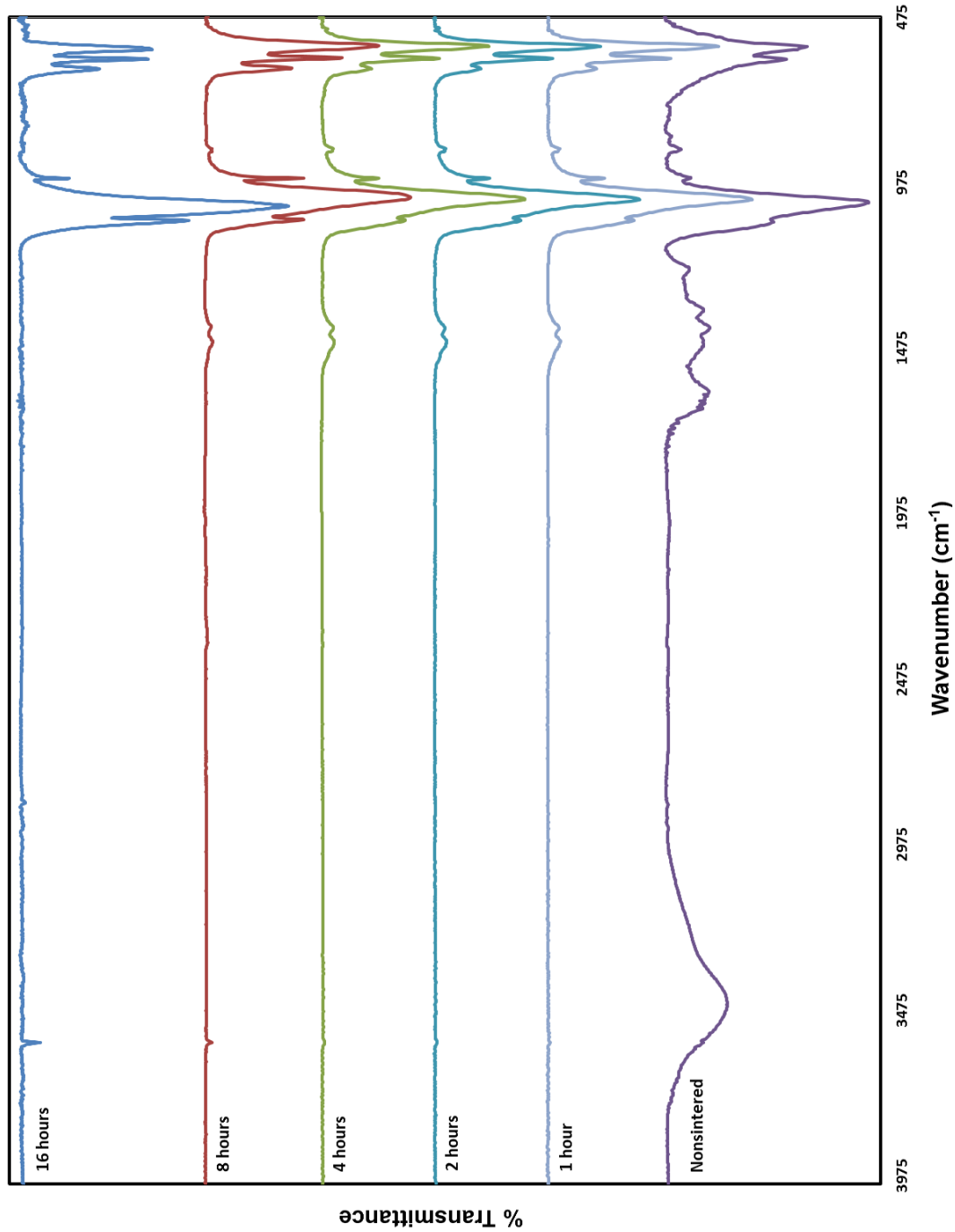


Figure 4.7. FTIR transmittance spectra for bovine hydroxyapatite sintered at 700 °C for various times



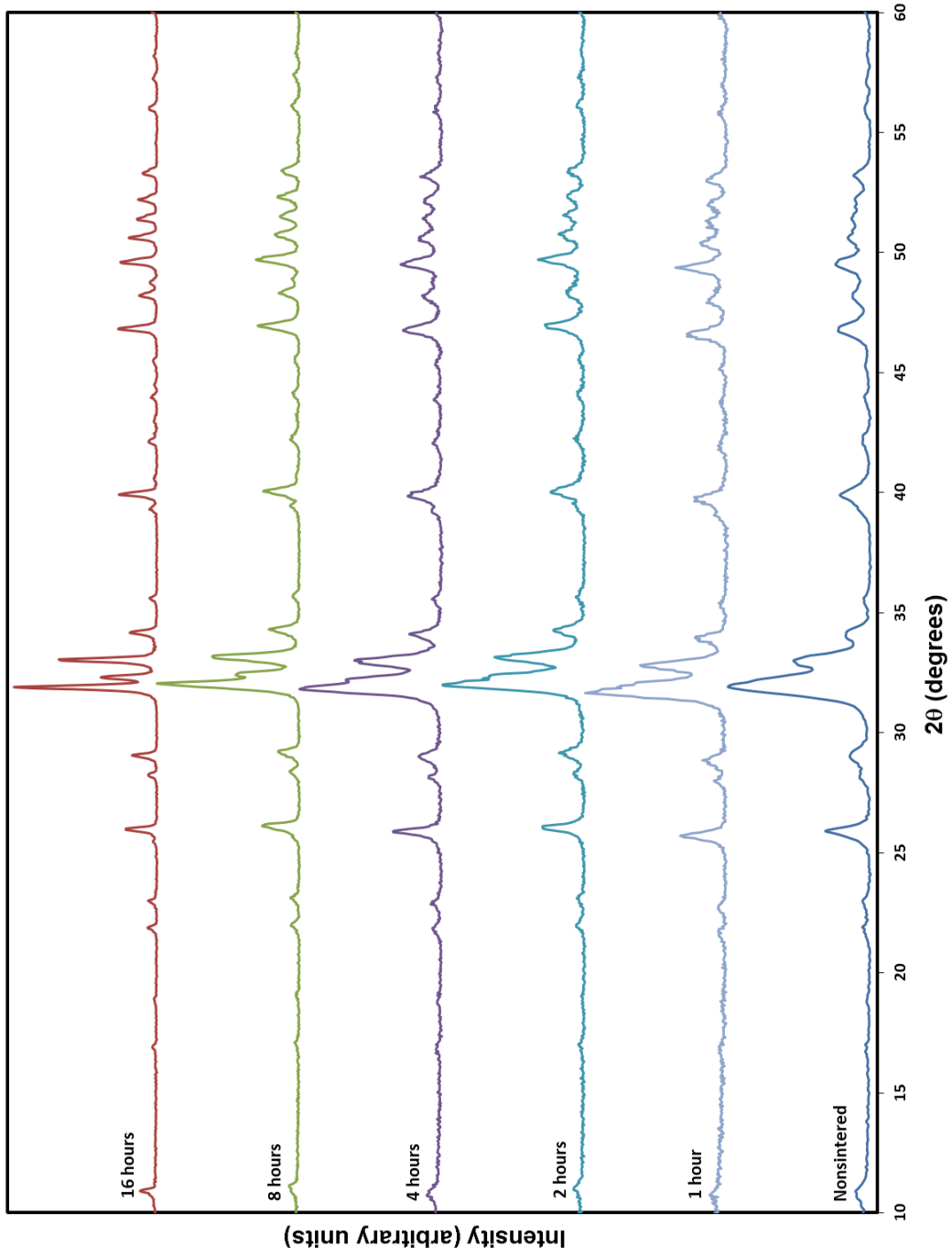


Figure 4.8. XRD patterns for bovine hydroxyapatite sintered at 700 °C for various times

evidenced by the peak narrowing in the FTIR spectrum and XRD diffraction pattern. When the sintering was allowed to run for the standard 16 hours, the FTIR spectrum shows that all carbonate in the sample was completely removed. A consequence of the prolonged time at elevated temperature and the removal of all carbonate substitution is that the hydroxyapatite is now free to become more crystalline. Peaks widths were distinctly narrower and the hydroxide stretches (from carbonate decomposition in the presence of water) were more pronounced. After sintering the samples for 16 hours, the XRD diffraction pattern showed that the sintered bone powder is highly crystalline. The (112) reflection is completely separate from the (211) reflection and all peaks are sharp, narrow, and well resolved. It is interesting to note that there is no peak at  $37.5^\circ$  in the XRD pattern, indicating that there is no oxide, or very little present.

#### Summary

In chapter 2, bone plugs were sintered at  $600^\circ\text{C}$  and  $700^\circ\text{C}$  for 16 hours. The  $600^\circ\text{C}$  plugs showed an average mass loss of 6.4% and a shrinkage of 3.2%. Because the mass loss was observed to be greater than the volume change, the density of the sample sintered at  $600^\circ\text{C}$  actually decreases. When the temperature is raised to  $700^\circ\text{C}$  the mass loss and shrinkage increase to 7.5% and 13.1%, respectively, and the density of the plugs increases by 6.4%. The shrinkage at these temperatures is consistent with literature studies on synthetically produced hydroxyapatite.<sup>5-8</sup> Contemporary studies also show that the rate of surface area decrease and dimensional changes accelerate rapidly at temperatures between  $650^\circ\text{C}$  and  $680^\circ\text{C}$ , depending on the exact chemical makeup of the sample. The theoretical ratio of calcium to phosphorus in hydroxyapatite is 1.67. For samples with to phosphorus ratios above ideality, rapid rates of shrinkage are

observed at lower temperatures. For hydroxyapatite synthesized with a calcium to phosphorus ratio below 1.67, rapid rates of shrinkage are observed only at relatively high temperatures.<sup>6,9</sup>

In concurrence with the decrease in specific surface area over time, mass loss continues until the surface water and lattice water are eliminated. (Table 4.3) Once this happens, the rate of mass loss tapers off, but the surface area decreases, crystal morphology changes, and dimensional changes continue because they are not caused by a specific chemical reaction as shown from the results in chapter 3. Eventually the volume change of the plugs surpasses their mass loss. Consequently, the density begins to increase. This increase continues and at 192 hours of sintering, the density decrease is roughly equivalent to that of samples sintered at 700 °C for 16 hours. Sample plugs sintered at 600 °C for 288 hours and 384 hours were severely cracked and lost physical integrity making dimensional analysis impossible.

Using the normalized rate constant,  $k_{app}/SA$ , it is possible to compare the surface reactivities of samples sintered at different temperatures and with different surface areas. With equations 4.2 and 4.3 it is also possible to identify the required sintering times to create hydroxyapatites with equivalent surface reactivities utilizing different sintering temperatures. An example of this can be seen in table 4.4 where sintering times for 600 °C and 700 °C are shown for equivalent values of  $k_{app}/SA$ .

| Plug Number | Sintering Time (hrs) | % Mass Loss | % Volume Loss | % Density Change | Surface Area (m <sup>2</sup> /g) |
|-------------|----------------------|-------------|---------------|------------------|----------------------------------|
| 1           | 24                   | 6.5 ± 0.1   | 3.2 ± 0.4     | -3.4 ± 0.7       | 42.2 ± 0.1                       |
| 2           | 24                   | 7.5 ± 0.1   | 3.0 ± 0.5     | -4.6 ± 0.6       | 35.5 ± 0.1                       |
| 3           | 48                   | 7.2 ± 0.1   | 2.4 ± 0.5     | -4.9 ± 0.7       | 29.3 ± 0.1                       |
| 4           | 48                   | 7.8 ± 0.1   | 3.2 ± 0.4     | -4.7 ± 0.7       | 28.2 ± 0.1                       |
| 5           | 72                   | 8.8 ± 0.1   | 2.9 ± 0.5     | -6.2 ± 0.7       | 13.9 ± 0.1                       |
| 6           | 72                   | 7.7 ± 0.1   | 3.1 ± 0.5     | -4.7 ± 0.6       |                                  |
| 7           | 96                   | 8.6 ± 0.1   | 3.0 ± 0.5     | -5.7 ± 0.7       |                                  |
| 8           | 96                   | 7.9 ± 0.1   | 3.4 ± 0.5     | -4.7 ± 0.7       |                                  |
| 9           | 192                  | 9.7 ± 0.1   | 13.2 ± 0.5    | 4.0 ± 0.7        |                                  |
| 10          | 192                  | 7.9 ± 0.1   | 12.7 ± 0.5    | 5.4 ± 0.6        |                                  |

Table 4.3. Dimension analysis data for cylindrical bovine hydroxyapatite plugs machined from femoral cortical bone sintered at 600 °C for various times

| <u>700 °C</u><br><u>(hrs)</u> | <u><math>10^7 \times k_{app}/SA</math></u><br><u>(g/sm<sup>2</sup>)</u> | <u>600 °C</u><br><u>(hrs)</u> |
|-------------------------------|---|-------------------------------|
| 1                             | 32.1  | 15.9                          |
| 2                             | 33.2  | 16.6                          |
| 3                             | 34.2  | 17.3                          |
| 4                             | 35.2  | 18.0                          |
| 5                             | 36.3  | 18.7                          |

Table 4.4 Calculated values for hydroxyapatite sintering at 700 °C and 600 °C that yield equivalent values of  $k_{app}/SA$ .

### References

1. Mezahi, F. Z.; Oudadesse, H.; Harabi, A.; Lucas-Girot, A.; Le, G. Y.; Chaair, H.; Cathelineau, G., Dissolution kinetic and structural behaviour of natural hydroxyapatite vs. thermal treatment. Comparison to synthetic hydroxyapatite. *Journal of Thermal Analysis and Calorimetry* **2009**, 95, 21-29.
2. Landi, E.; Celotti, G.; Logroscino, G.; Tampieri, A., Carbonated hydroxyapatite as bone substitute. *Journal of the European Ceramic Society* **2003**, 23, (15), 2931-2937.
3. Suetsugu, Y.; Takahashi, Y.; Cho, S. B.; Okamura, F. P.; Tanaka, J., Space group determination of hydroxyapatite and carbonate apatite. *Key Engineering Materials* **1997**, 132-136, 2037-2039.
4. Bres, E. F.; Cherns, D.; Vincent, R.; Morniroli, J. P., Space-group determination of human tooth-enamel crystals. *Acta Crystallographica Section B: Structural Science* **1993**, B49, (1), 56-62.
5. Haberko, K.; Bucko, M. M.; Brzezinska-Miecznik, J.; Haberko, M.; Mozgawa, W.; Panz, T.; Pyda, A.; Zarebski, J., Natural hydroxyapatite - its behaviour during heat treatment. *Journal of the European Ceramic Society* **2006**, 26, (4-5), 537-542.
6. Bernache-Assollant, D.; Ababou, A.; Champion, E.; Heughebaert, M., Sintering of calcium phosphate hydroxyapatite  $\text{Ca}_{10}(\text{PO}_4)_6(\text{OH})_2$ . I. Calcination and particle growth. *Journal of the European Ceramic Society* **2002**, 23, 229-241.
7. Abdel-Fattah, W. I.; Nour, F. A., Thermal expansion application to assess calcination of bovine hydroxyapatite. *Thermochimica Acta* **1993**, 218, 465-75.

8. Bailliez, S.; Nzihou, A., The kinetics of surface area reduction during isothermal sintering of hydroxyapatite adsorbent. *Chemical Engineering Journal* **2004**, 98, (1-2), 141-152.
9. Raynaud, S.; Champion, E.; Bernache-Assollant, D., Calcium phosphate apatites with variable Ca/P atomic ratio II. Calcination and sintering. *Biomaterials* **2001**, 23, 1073-1080.

## Chapter Five

### Optimization of Sintering Time and Temperature for Biocomposite Preparation and Evaluation of Alternative Ceramics and Polymers

#### Introduction and Background

In previous chapters the relationships between sintering time, sintering temperature, and the final properties of hydroxyapatite as an initiator for ring opening polymerization of lactones were examined. From variable temperature experiments it was determined that sintering for 4 hours at 700 °C offered that fastest rate of reaction with L-lactide, with complete loss of carbonate and substantial crystal morphology change. Samples sintered at 600 °C reacted far slower, did not have the same degree of morphology change, and carbonate was still observed in FTIR spectra. When the pre-polymerization sintering temperature is increased from 600 °C to 700 °C, the primary cause of increased polymerization rate is the increase in the amount of hydroxide that serves as the initiating nucleophile. When the sintering temperature is raised even higher from 700 °C to 800 °C, a higher proportion of oxide is formed at the expense of hydroxide, thus reducing the total number of nucleation sites because one oxide can be created for every two hydroxides.

When sintering time was examined as a variable, it was found that at lower temperatures the decomposition of carbonate to hydroxide was not the only factor that could affect the rate of reaction. At temperatures high enough to decompose carbonate, the crystal morphology also changes. As a consequence, the surface area also decreases. This surface area decrease has an inhibitory effect on the rate of reaction by effectively



reducing the number of nucleophiles,  $N_i$ , presented to the monomer melt. For samples sintered at 600 °C, it is possible to create a material that reacts with comparable efficacy toward L-lactide, but the extremely long sintering time required to achieve this level of surface activity makes the process prohibitive.

For synthetically prepared hydroxyapatite, literature sources report that the critical temperature for the rapid increase in these morphology changes and surface area decrease lies somewhere between 650 °C and 680 °C.<sup>1-4</sup> With this information in mind, in addition to my own results described in previous chapters, I sought to fine tune the sintering time and temperature of anorganic bone to achieve a fast reacting, high surface area hydroxyapatite surface that could be used to initiate the polymerization of lactones to produce composite materials in short times.

### Experimental

Chemicals: Deuterated chloroform ( $CDCl_3$ , 99.8% D from Sigma-Aldrich), deuterated 1,1,2,2-tetrachloroethane ( $C_2D_2Cl_4$ , 99.5% D from Sigma-Aldrich), deuterated dimethylsulfoxide (DMSO, 99.96% from Sigma-Aldrich), 1,4-dioxan-2-one (Dioxanone, DX, from Ethicon),  $\epsilon$ -caprolactone (CL, 99% from Fluka), glycolide (GL, 99.9% from Polysciences Inc.), L-lactic acid (90% from Acros Organics), D-lactic acid (85% from MP Biomedicals), ethylene diamine (99% from Sigma Aldrich), DL-lactic acid (85% from Acros Organics), tin(II) 2-ethyl hexanoate ( $Sn(II)oct_2$ , 95% from Sigma-Aldrich), tetramethylammonium hydroxide (98% from Alfa Aesar), calcium hydroxide (98% from Acros Organics), calcium oxide (99.95% from Alfa Aesar), were used as purchased from the respective supplier. L-lactide (from Purac) was sublimed at 90 °C and then

transferred into a  $N_{2(g)}$  atmosphere glove box for further use. Glycolide ( $\geq 99\%$  from Sigma Aldrich) was sublimed at  $80\text{ }^{\circ}\text{C}$  and then transferred into a  $N_{2(g)}$  atmosphere glove box for further use. Calcium L-lactate pentahydrate (98% from Fisher) was dehydrated at  $120\text{ }^{\circ}\text{C}$  under vacuum and then transferred into a  $N_{2(g)}$  atmosphere glove box for further use. Biologic hydroxyapatite was sourced from bovine femur (from Premium Protein Products). Bioglass was manufactured and supplied by Professor Matthew Hall from Alfred University in Alfred, New York and used as received.

Methodology: Biologically derived hydroxyapatite powder for kinetics studies, FTIR, XRD, and surface area analysis was processed as described in Chapter 2. Temperatures between  $600\text{ }^{\circ}\text{C}$  and  $700\text{ }^{\circ}\text{C}$  were chosen to refine the sintering conditions (in air) with the goal of optimizing polymerization rates and the properties of the resulting composites. In addition to the samples sintered in air, samples were sintered under vacuum as described below. Sections of anorganic bone (*vide supra*) were placed in a  $\frac{1}{2}$  inch inner diameter quartz tube that was sealed at one end. One end of a piece of flexible vacuum tube was placed over the end of the quartz tube, and the other end was attached directly to a rotary vane vacuum pump and the pressure inside the tube was reduced to approximately 50 millitorr. The quartz tube was lowered into the preheated muffle furnace until the anorganic bone was well within the heating chamber. About nine inches of quartz tube protruded from the top of the furnace so that the vacuum tube was not subjected to excess heat that could soften it and compromise the vacuum. After 16 hours the quartz tube was removed from the furnace and the sections of sintered bone were transferred, while still hot, to a vacuum desiccator. The plugs were then allowed to cool under vacuum and then transferred to a  $N_{2(g)}$  atmosphere glove box. Once in the glove box, the plugs were

powdered in a Mister Coffee® coffee grinder to a particle size of less than 10  $\mu\text{m}$ . The powder was stored under  $\text{N}_{2(\text{g})}$  for subsequent use.

Along with bone pieces for powdering, whole bone plugs were also sintered for dimensional stability analysis. The lengths and diameters of seven plugs were measured. Each of the plugs was also weighed. The plugs were then placed in a quartz tube, sintered under vacuum as described above for 16 hours, and then cooled to room temperature. The weights and the dimensions of sintered rods were then determined and compared to their values before sintering. For other comparative purposes, an additional set of anorganic bone plugs was prepared, characterized, and then sintered in air at the same temperatures used for the vacuum sintering. The plug dimensions and weights determined after sintering were ultimately compared to the initial values and to the values obtained after vacuum sintering.

Thermogravimetric analyses of extracted powdered bovine bone were performed on a Perkin Elmer STA 6000. Approximately 40 mg samples of powdered bone were placed into the alumina sample crucible for subsequent analysis under a stream of air flowing at 20  $\text{ml}/\text{min}$ . The initial temperature of each analysis was set to 25  $^{\circ}\text{C}$  and the temperature was quickly ramped from this value to a selected value at a ramp rate of 100  $^{\circ}\text{C}/\text{min}$ . The selected values were identical to the sintering temperatures described above for the anorganic bone plugs. Once each sample had reached the desired temperature, it was held there for an additional 16 hours to simulate the sintering process. Percent mass loss was monitored over time and plotted against time for each temperature tested.

## Results and Discussion

Two kinetics experiments with L-lactide were run and compared to previously described results. One involved sintering HA at 675 °C in air and the other involved HA sintered for 700 °C under hard vacuum. The reaction flask was setup according to previously performed experiments. Sintered HA and monomer were added to the reaction vessel in a 1 to 4 ratio. The masses were kept as close to 1.000 g and 4.000 g as possible.

In addition to L-lactide, three other monomers and their respective polymers are used in orthopedic applications where biocompatibility and timely resorption are required. These three monomers are  $\epsilon$ -caprolactone, dioxanone, and DL-lactide, which is actually a mixture of 50% L-lactide and 50% D-lactide. The polymerization kinetics for each of these monomers was performed as previously described by initiating the polymerization at the surface of sintered samples of hydroxyapatite powder derived from bovine bone. For all of these polymerizations the biologically derived hydroxyapatite was sintered for 16 hrs at 700 °C in air, cooled in a vacuum desiccator and stored in a glove box under  $N_{2(g)}$  for subsequent use.  $^1H$  NMR chemical shift assignments for L-lactide and  $\epsilon$ -caprolactone were previously completed and assignments for DL-lactide were straight forward as they are the same as those determined for L-lactide. L-lactide and D-lactide are enantiomers and as such there will be no difference in their respective chemical shifts for analogous protons. The fourth monomer and polymer combination that was studied is dioxanone and polydioxanone. (Figure 5.1) The  $^1H$  NMR spectra for dioxanone and polydioxanone merit further discussion. Dioxanone is highly soluble in chloroform but

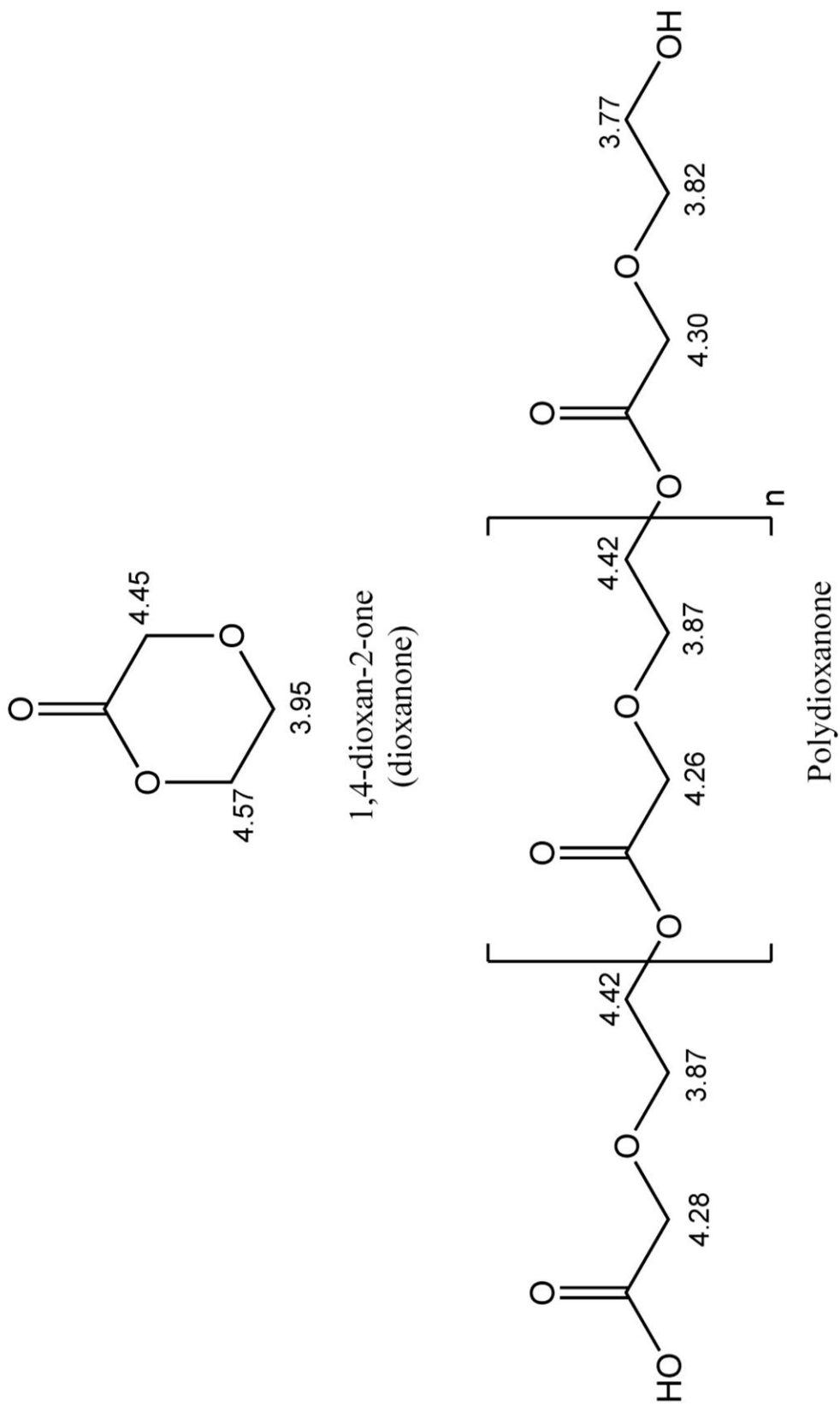


Figure 5.1. Structures and  $^1\text{H}$  NMR chemical shift assignments for dioxanone monomer and polydioxanone

polydioxanone is not. For this reason it is common to use 1,1,2,2-tetrachloroethane as a solvent for the polymer.  $^1\text{H}$  NMR chemical shift assignments for the dioxanone monomer were obtained by dissolving approximately 5 milligrams of the compound in approximately 1.0 milliliters of  $\text{C}_2\text{D}_2\text{Cl}_4(\text{l})$ . The singly protonated solvent was set to 6.080 ppm as an internal reference for the chemical shifts. Interpreting the spectra is relatively straightforward because dioxanone contains only three chemically nonequivalent sets of protons, only two of which are coupled to each other.  $^1\text{H}$  NMR peak assignments were made using polymer synthesized as follows. First, 0.100 g of dry  $\text{Ca}(\text{OH})_{2(\text{s})}$  and 2.0 g of dioxanone were added to a 25 ml round bottom flask. The flask was then fitted with a gas adapter. Next, the reaction mixture was placed under a positive pressure of flowing  $\text{N}_{2(\text{g})}$  and submerged in a 125 °C oil bath. The reaction was allowed to proceed for 24 hrs before being removed from the oil bath. The melt polymerization of dioxanone typically proceeds to about 80% completion, so the crude product typically contains a large fraction of monomer.<sup>5</sup> This was also found to be true for my polymerizations of dioxanone. Fortunately, removal of the excess monomer can be accomplished in one simple step because dioxanone is easily sublimed at room temperature under vacuum. I was able to obtain a relatively pure sample of polydioxanone by powdering my crude reaction product and placing it in a sublimator pumping the vessel down to a vacuum of approximately 50 millitorr. The temperature of the circulating coolant in the sublimator cold finger was set to -5 °C and the entire sublimator assembly was then placed into a 35 °C oil bath. The sample was allowed to sublime for 24 hours, after which time,  $^1\text{H}$  NMR indicated that all monomer had been removed from the crude reaction mixture. The resulting polymer product was used to

make chemical shift assignments for the protons on the internal polymer chain. In order to identify polymer end groups, a low molecular weight sample of polymer was made. To this end 2.0 g of dioxanone were mixed with 0.500 g of dry  $\text{Ca(OH)}_{2(s)}$  and reacted at 125 °C under nitrogen. The large number of hydroxide initiators led to a large number of short polymer chains. Since each chain has a hydroxyl end group, the number of these end groups must increase as well. I was able to assign the end groups by identifying NMR peaks or sets of peaks that increased in proportion to the internal proton peaks. (Figures 5.2, 5.3, and 5.4) With the NMR assignments in hand for the monomer and the polymer, necessary assignments now made for monomer, polymer and hydroxyl end group, the mole fraction of dioxanone,  $M_t$  can be determined using the following formula,

$$M_t = \frac{I_M}{I_M + I_P + 2I_A} \quad (5.1)$$

where  $I_M$  is the integrated area for the dioxanone monomer,  $I_P$  is the integrated area for the internal polymer protons, and  $I_A$  is the integrated area for the alcohol end group. The values obtained from the integrals of the three chosen peaks were entered into an Excel® spreadsheet for further processing and plotting (Table 5.1).

Hydroxyapatite is not the only ceramic material that has application in hard tissue replacement. Bioglasses have been used for several decades as a bioceramic for bone adhesion (Figure 5.5).<sup>6-12</sup> All bioglasses contain nucleophilic species such as oxides and hydroxides in high loading. Consequently, their surfaces are quite effective in initiating the ring opening polymerization of cyclic lactones. The composition of the particular bioglass that I used is 45S5 and is shown in Table 5.2. To investigate the potential of

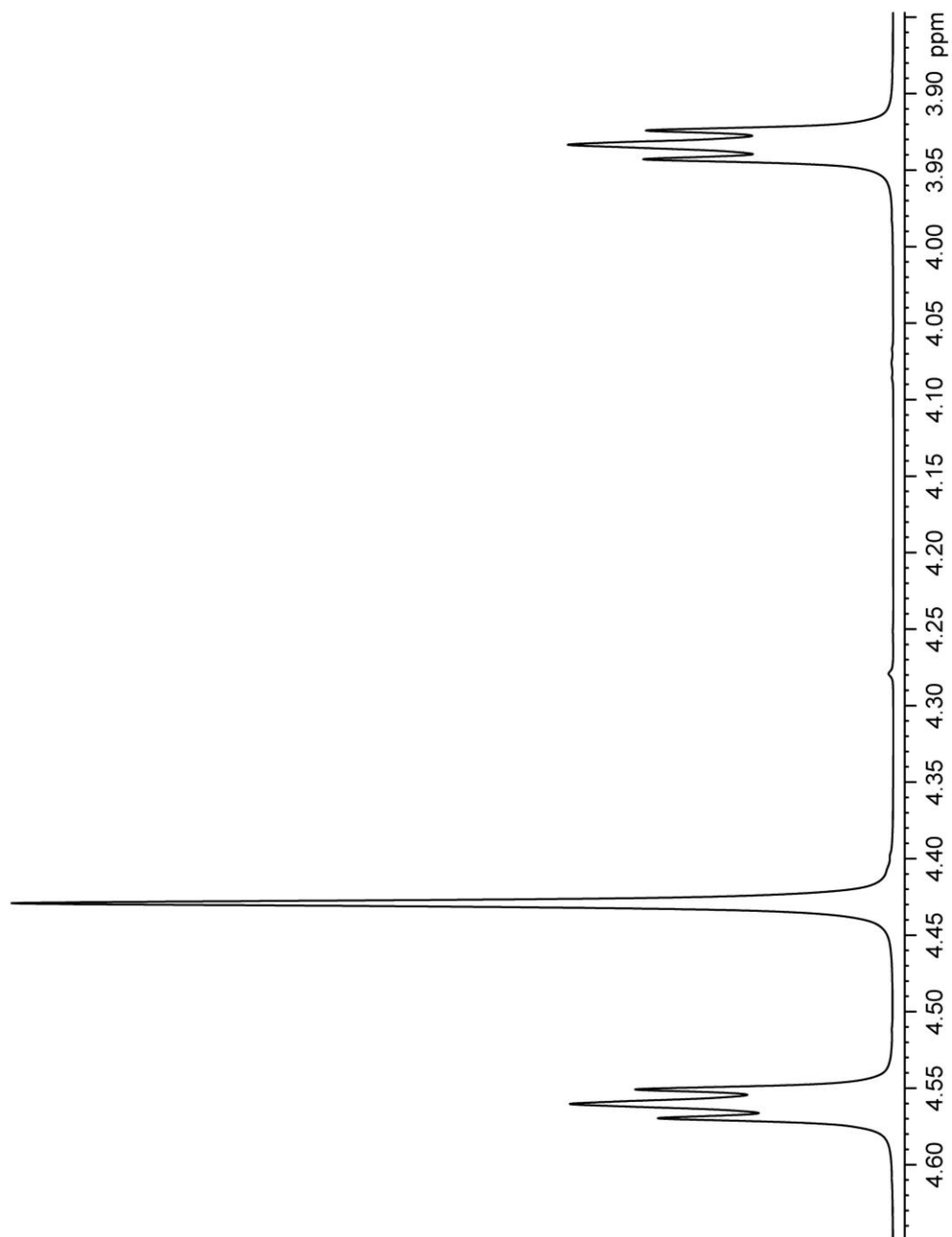


Figure 5.2.  $^1\text{H}$  NMR spectrum of dioxanone monomer in  $\text{C}_2\text{D}_2\text{Cl}_4$



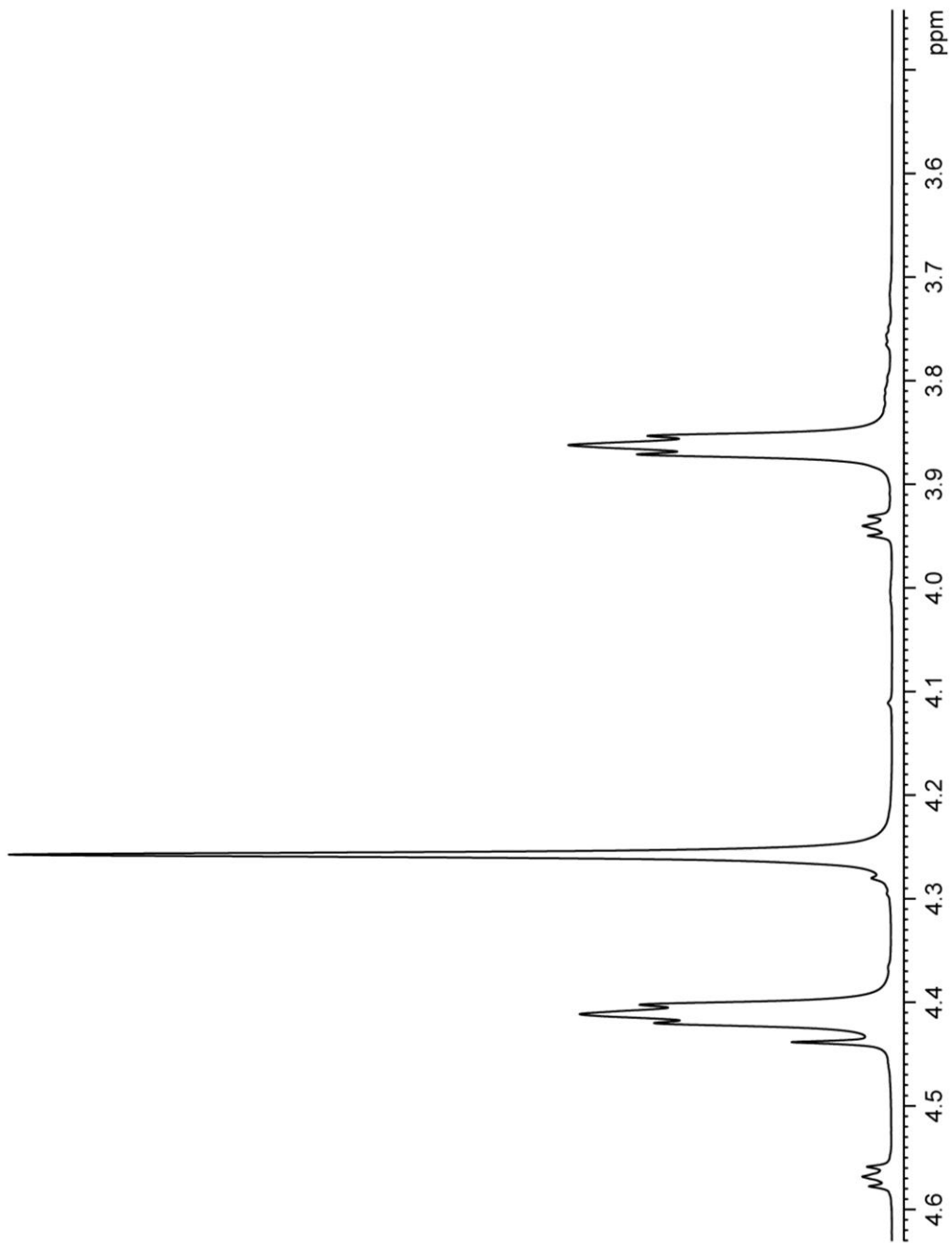


Figure 5.3.  $^1\text{H}$  NMR spectrum of polydioxanone in  $\text{C}_2\text{D}_2\text{Cl}_4$  synthesized from 0.100g of  $\text{Ca}(\text{OH})_2(\text{s})$  and 2.0g of dioxanone

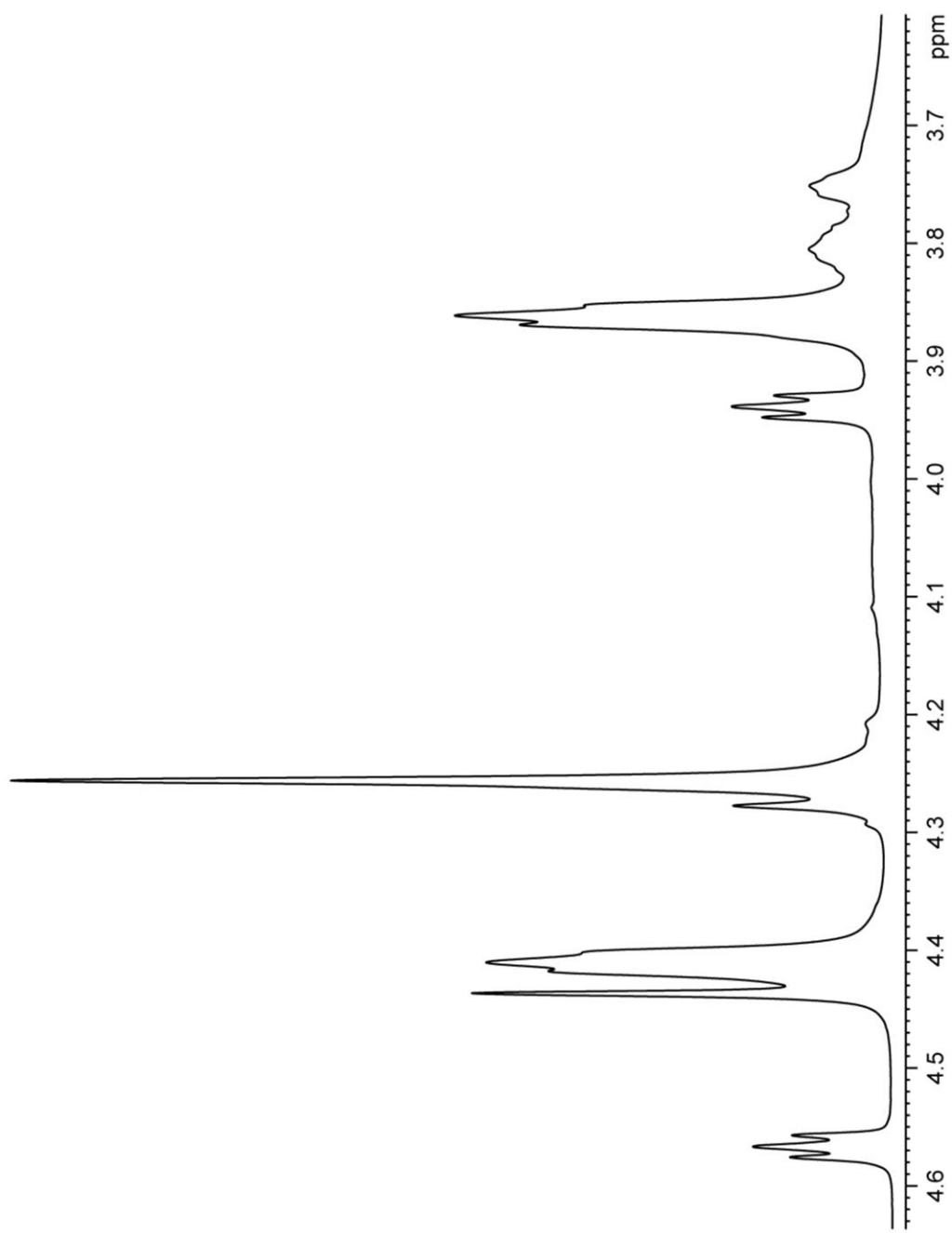


Figure 5.4.  $^1\text{H}$  NMR spectrum of polydioxanone in  $\text{C}_2\text{D}_2\text{Cl}_4$  synthesized from 0.500g of  $\text{Ca}(\text{OH})_{2(s)}$  and 2.0g of dioxanone

| Sample | Elapsed Time (min) | Monomer (4.51ppm) | Polymer (3.82ppm) | Hydroxyl End Group (3.71ppm) | Mole Fraction of Monomer | -ln (Mole Fraction of Monomer) |
|--------|--------------------|-------------------|-------------------|------------------------------|--------------------------|--------------------------------|
| 1      | 0                  | 100.0000          | 0.0000            | 0.0000                       | 1.000000000              | 0.000000000                    |
| 2      | 17                 | 97.7961           | 2.0768            | 0.1272                       | 0.979205570              | 0.021013679                    |
| 3      | 43                 | 89.0568           | 10.7041           | 0.2392                       | 0.892702452              | 0.113501955                    |
| 4      | 83                 | 82.2944           | 17.3828           | 0.3228                       | 0.825609066              | 0.191633903                    |
| 5      | 115                | 79.9543           | 19.7155           | 0.3303                       | 0.802191837              | 0.220407501                    |
| 6      | 146                | 76.3187           | 23.1774           | 0.5039                       | 0.767052176              | 0.265200454                    |
| 7      | 183                | 74.0859           | 25.4782           | 0.4359                       | 0.744102543              | 0.295576427                    |
| 8      | 243                | 68.4271           | 31.0730           | 0.4998                       | 0.687708857              | 0.374389704                    |
| 9      | 288                | 60.4952           | 38.9495           | 0.5553                       | 0.608330057              | 0.497037688                    |
| 10     | 328                | 56.7257           | 42.6886           | 0.5856                       | 0.570598998              | 0.561068596                    |
| 11     | 371                | 53.7400           | 45.6598           | 0.6003                       | 0.540644951              | 0.614992498                    |
| 12     | 401                | 49.9757           | 49.5888           | 0.4355                       | 0.501942962              | 0.689268788                    |

Table 5.1. Representative Excel® spreadsheet used to generate kinetics plots for the polymerization reaction of dioxanone

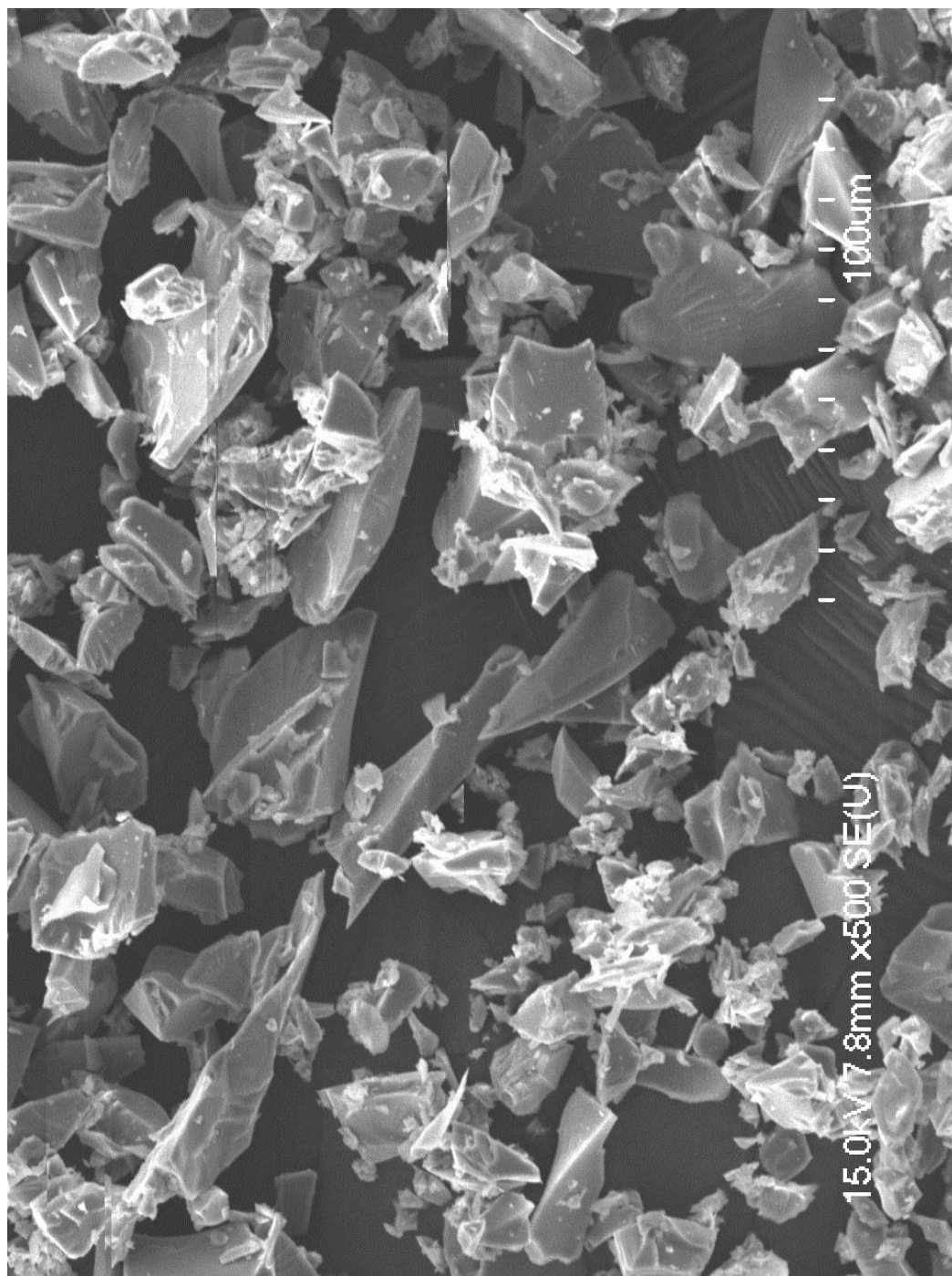


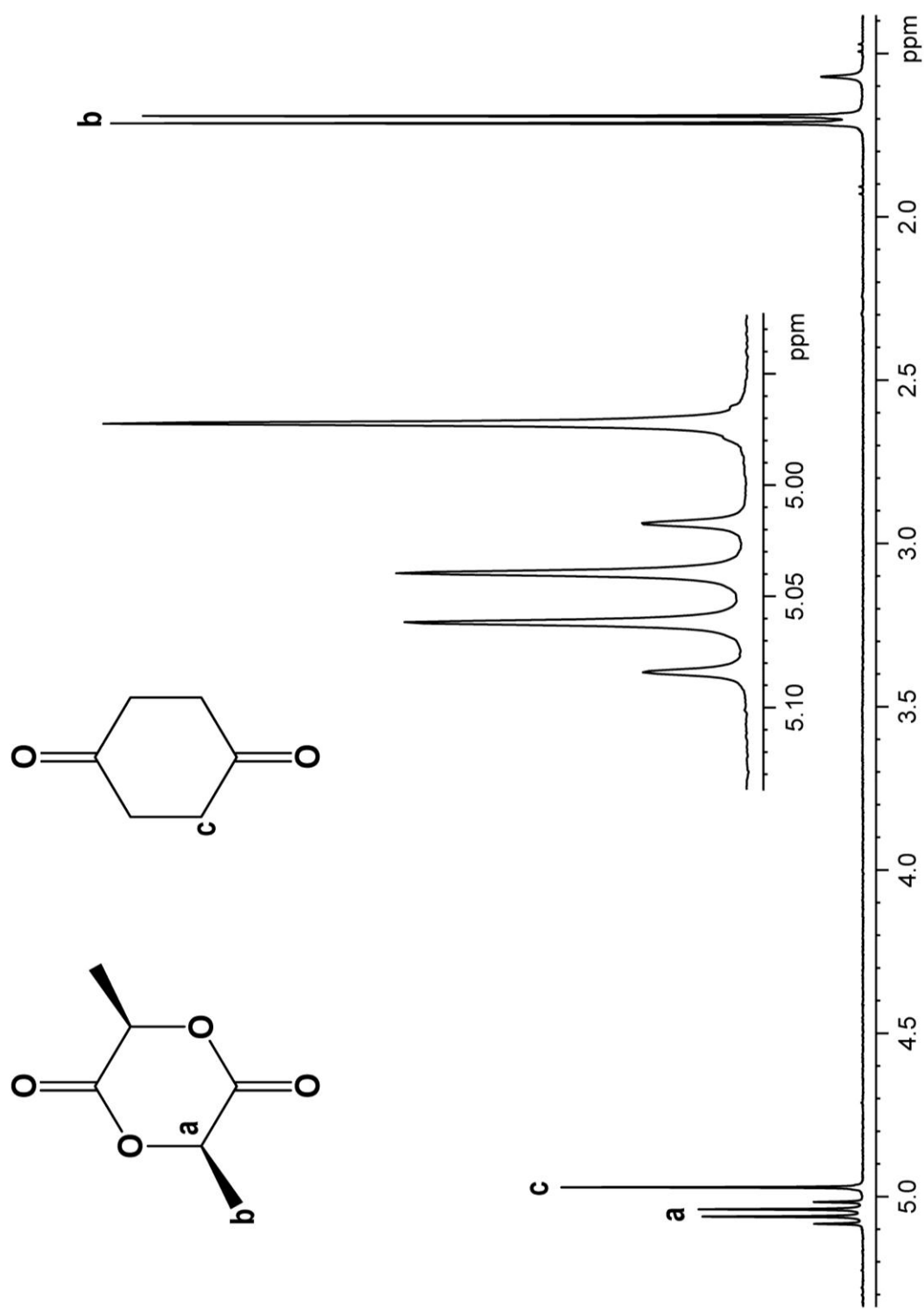
Figure 5.5. SEM image of bioglass at 500X magnification

| <u>Bioglass<br/>Designation</u> | <u>SiO<sub>2</sub></u> | <u>P<sub>2</sub>O<sub>5</sub></u> | <u>CaO</u> | <u>Na<sub>2</sub>O</u> |
|---------------------------------|------------------------|-----------------------------------|------------|------------------------|
| 45S5                            | 45.0                   | 6.0                               | 24.5       | 24.5                   |
| 42S5.6                          | 46.1                   | 2.6                               | 29.0       | 26.3                   |
| 46S5.2                          | 46.1                   | 2.6                               | 26.9       | 24.4                   |
| 49S4.9                          | 49.1                   | 2.6                               | 25.3       | 23.8                   |
| 52S4.6                          | 52.1                   | 2.6                               | 23.8       | 21.5                   |
| 60S3.8                          | 60.1                   | 2.6                               | 19.6       | 17.7                   |
| 55S4.3                          | 55.0                   | 6.0                               | 19.5       | 19.5                   |

Table 5.2 Common bioglass formulation showing the molar percentages of each component

creating a bioglass-polymer composite material, I performed three kinetics experiments in which the L-lactide to bioglass ratio was changed. The first used a mixture of L-lactide and bioglass in a 4 to 1 ratio, the second used a 15 to 1 ratio of L-lactide to bioglass, and the third used a 31 to 1 ratio. When  $-\ln \frac{M_t}{M_0}$  is plotted versus time for the desired kinetics experiments with L-lactide a straight line is obtained with slope of  $k_{app}$ . The surface area of the bioglass was also measured. About 4.0 g of sample was used to assure that there was at least a minimum of 10 m<sup>2</sup> of area to be measured.

One of the most commercially common bioresorbable polymers used in resorbable sutures and fixation devices consists of a single polymer that is made from 82% polylactide and 18% polyglycolide. To investigate the feasibility of using a mix of monomers to synthesize this copolymer, I attempted to use bioglass to polymerize a homogeneous mixture of 82% L-lactide and 18% glycolide. A description of the preparation of the mixture and the attempted preparation of copolymer follows below. Glycolide and L-lactide are water and oxygen sensitive. To prepare the desired monomer mixture, 82 g of L-lactide and 18 g of glycolide were placed into a beaker and slowly heated to melting in a N<sub>2(g)</sub> glove box. Once the mixture melted it was stirred briefly to ensure complete mixing. It was quickly removed from the heat source and allowed to cool. After solidifying, the mixture was powdered in a mortar and pestle. The monomer ratio was verified by <sup>1</sup>H NMR using chemical shift assignments established in previous chapters. (Figure 5.6) To identify the chemical shifts attributed to the glycolide portion of the polymer, I purchased a commercial sample of a 50% PLA-50% PGA polymer and

Figure 5.6.  $^1\text{H}$  NMR spectra of 82% L-lactide and 18% glycolide

characterized it with  $^1\text{H}$  NMR spectroscopy (Figure 5.7). Peak assignments were taken from literature references.<sup>13-16</sup> To characterize the polymerization reaction with a mixed monomer system, I placed the 82% L-lactide / 18% glycolide mixture in reaction vessel with bioglass in a 15 to 1 mass ratio. This reaction was run at 125 °C under a positive pressure of flowing  $\text{N}_{2(\text{g})}$ . Several aliquots were taken during the reaction for  $^1\text{H}$  NMR analysis.

### Results and Discussion

The FTIR spectra for hydroxyapatite sintered at 600 °C, 650 °C, 675 °C and 700 °C in air for 16 hours show that as the temperature is raised, the amount of carbonate remaining in the sample decreases as the amount of hydroxide increases. This process continues until no carbonate remains (Figure 5.8). This is the same pattern that was seen during the sintering experiments performed at 100 °C intervals. My results show that there was a great deal more hydroxide present after sintering at 675 °C than there was after sintering at 600 °C. Still more was present when the bone was sintered at 700 °C. The crystallinity of the samples also increases as the temperature is increased. When the surface areas were measured, a general trend of decreasing surface area with increasing temperature was revealed. When sintering hydroxyapatite at 675 °C, the surface area is 17.69  $\text{m}^2/\text{g}$ . This is over four times the surface area of the sample sintered at 700 °C (Table 5.3). At 675 °C, there is a large increase in hydroxide and the surface area still remains relatively high.

Results of the dimensional analysis study reveal that the shrinkage and mass loss for samples sintered at 600 °C to 675 °C remain relatively constant at 3 to 4% shrinkage and



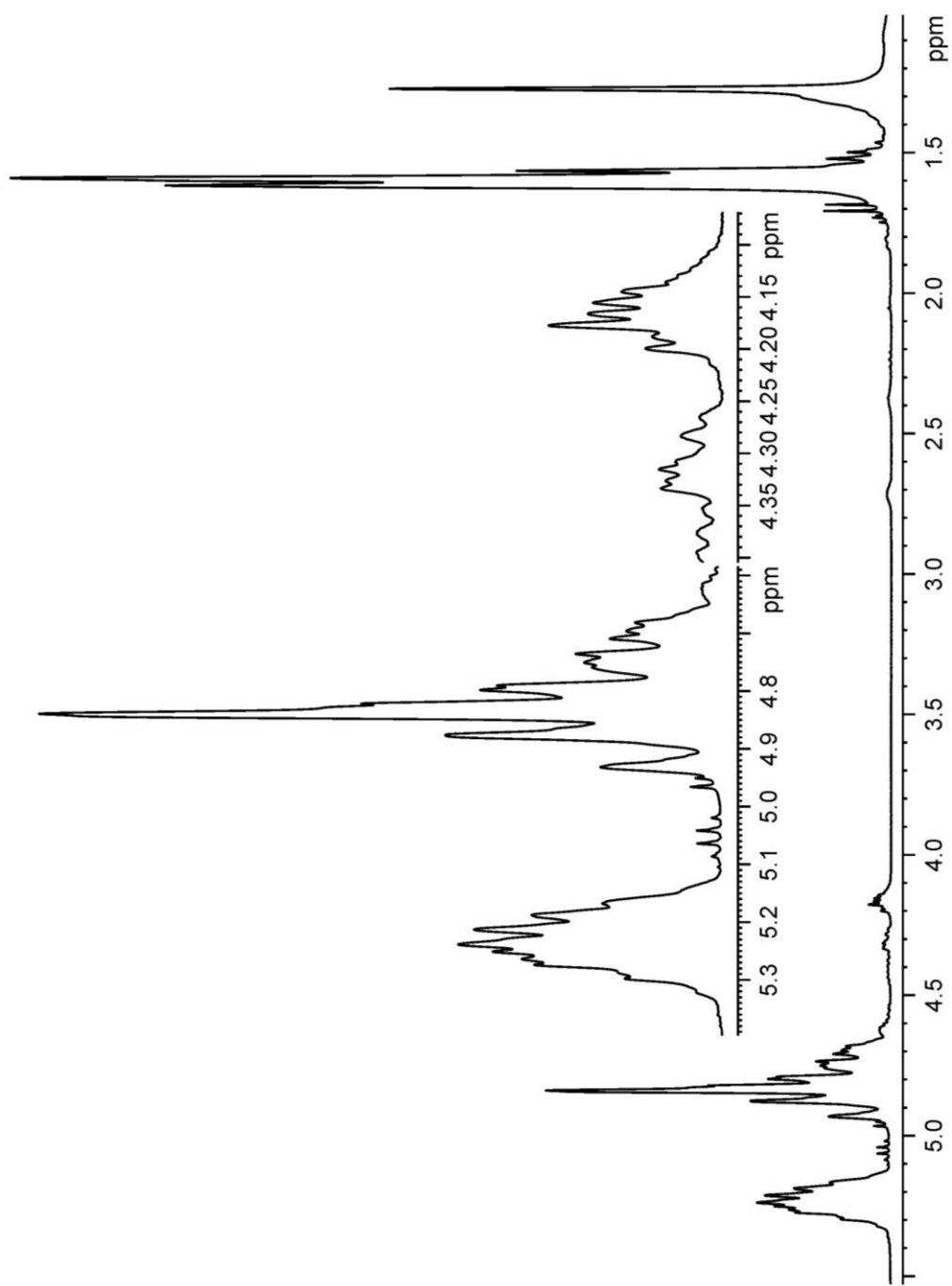


Figure 5.7.  $^1\text{H}$  NMR spectra of commercially available 50% PLLA / 50% PGA polymer

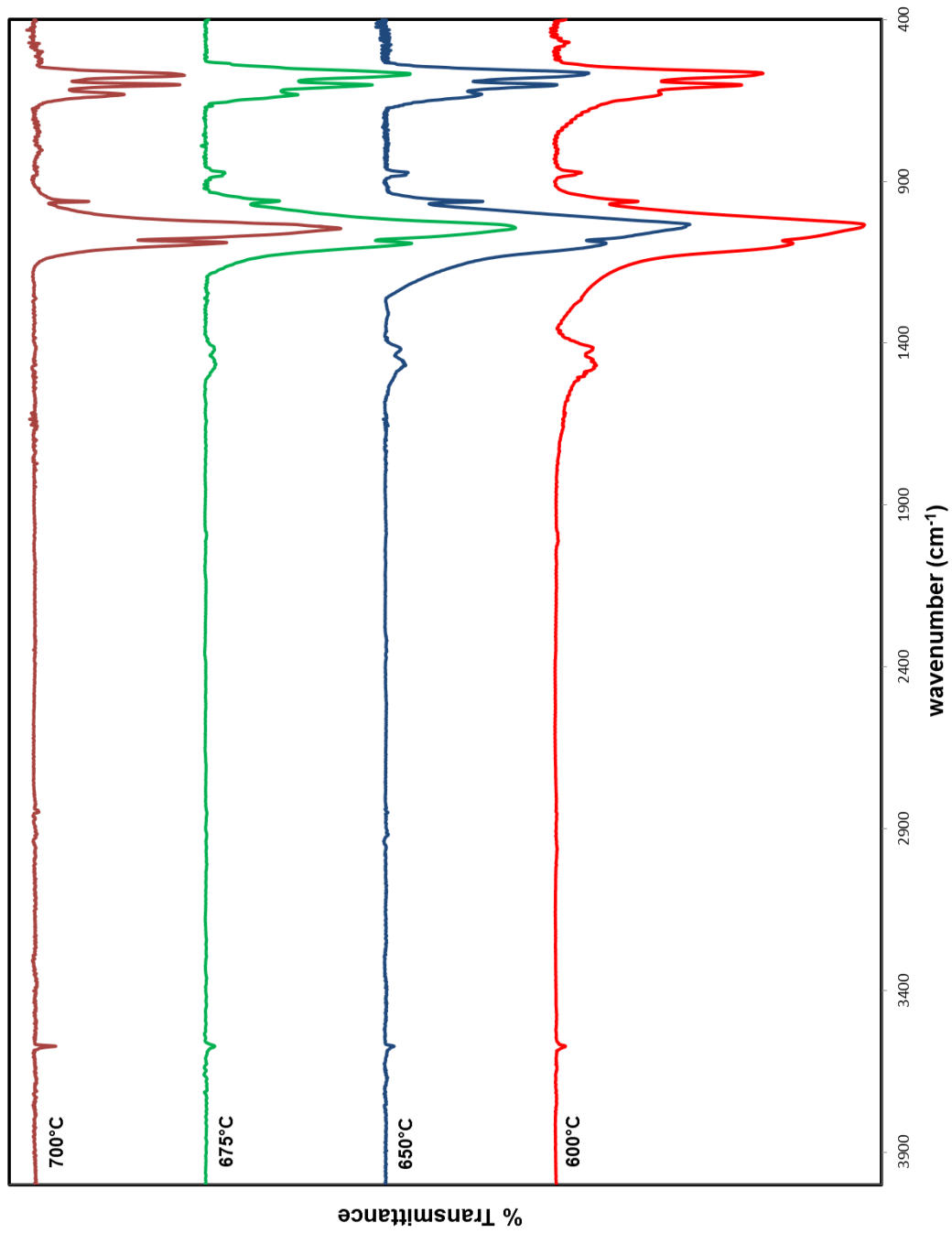


Figure 5.8. FTIR spectra of bovine HA sintered in air at 700 °C, 675 °C, 650 °C, and 600 °C for 16 hours

| Sintering Temperature (°C) | Sintering Time (hrs) | Sintering Atmosphere | Volume Loss (%) | Mass Loss (%) | Surface Area (m <sup>2</sup> /g) |
|----------------------------|----------------------|----------------------|-----------------|---------------|----------------------------------|
| 700                        | 16                   | Vacuum               | 5.89%           | 8.33%         | 21.38                            |
| 700                        | 16                   | Air                  | 13.06%          | 7.50%         | 4.79                             |
| 675                        | 16                   | Vacuum               | 3.85%           | 6.91%         | 26.89                            |
| 675                        | 16                   | Air                  | 5.48%           | 6.51%         | 17.69                            |
| 650                        | 16                   | Vacuum               | 3.05%           | 6.62%         | 35.06                            |
| 650                        | 16                   | Air                  | 3.25%           | 6.42%         | 33.88                            |
| 600                        | 16                   | Vacuum               | 3.20%           | 6.60%         | 51.11                            |
| 600                        | 16                   | Air                  | 3.41%           | 6.45%         | 46.80                            |
| 600                        | 192                  | Vacuum               | 4.44%           | 7.36%         | 41.33                            |
| 600                        | 192                  | Air                  | 12.95%          | 8.80%         | 13.90                            |

Table 5.3. Tabulated dimensional analysis data for bovine bone plugs sintered in air and in vacuum

6 to 7% mass loss. These are all well below the values obtained at 700 °C. The mass loss was also confirmed by thermogravimetric analysis (Figure 5.9). It is noteworthy that the combination of high hydroxide content, reasonably high surface area, stable dimensions, and retention of some carbonate, make a sintering temperature of 675 °C at 16 hours an excellent set of conditions for the production of PLLA-HA composite materials. When  $-\ln \frac{M_t}{M_0}$  versus time is plotted for the kinetics reaction run with HA sintered at 675 °C for 16 hours in air, the results can be fit to a straight line with excellent correlation (Figure 5.10). This indicates that the pseudo-first order rate relationship is valid for this reaction. From the slope of the line a rate constant of  $3.72 \pm 0.03 \times 10^{-6} \text{s}^{-1}$  is obtained. This value is roughly half of the value of  $7.52 \pm 0.04 \times 10^{-6} \text{s}^{-1}$  calculated for the reaction performed with HA sintered at 700 °C in air. Normalizing the rate constant for surface area gives a  $k_{\text{app}}/SA$  value of  $2.1 \times 10^{-8} \text{g/sm}^2$  which is much lower than the  $1.66 \times 10^{-7} \text{g/sm}^2$  calculated for 700 °C. These normalized values show that even though the surface area is larger for the 675 °C sample, it is much less reactive than the 700 °C sample. Since the FTIR spectrum shows that there is still carbonate present at 675 °C, the nucleophile concentration has probably not risen to sufficient quantities to afford a fast reaction rate.

Several literature sources describe the sintering of hydroxyapatites in different atmospheres. Carbon dioxide is sometimes used to inhibit the decomposition of carbonate to oxide or hydroxide, and highly humid air is used to increase the rate of surface area change.<sup>17, 18</sup> To explore these phenomena with extracted bone, I sintered powdered bone samples under a hard vacuum at the same temperatures chosen

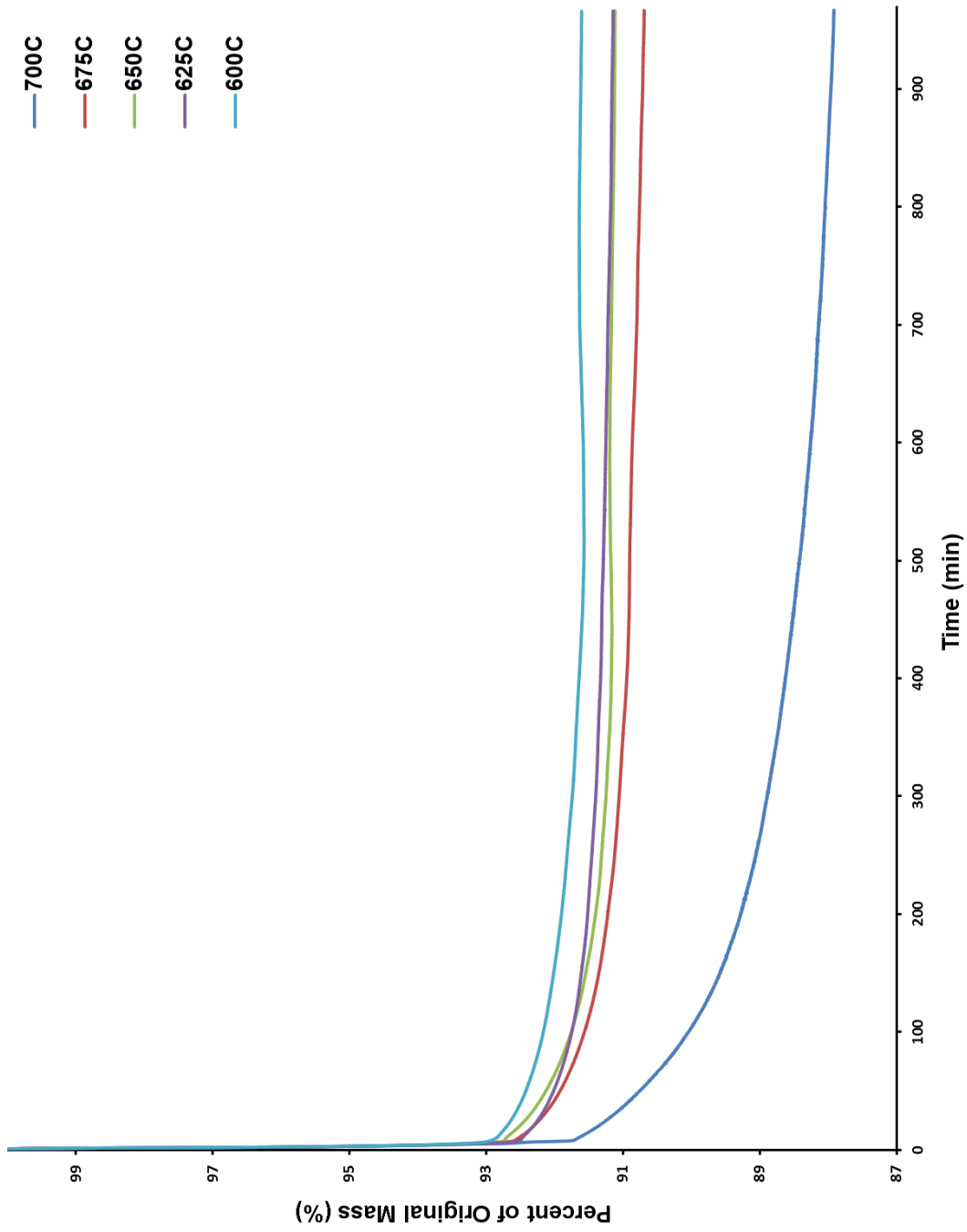


Figure 5.9. Thermogravimetric mass loss plots for bovine HA heated at 600 °C, 625 °C, 650 °C, 675 °C, and 700 °C for 16 hours

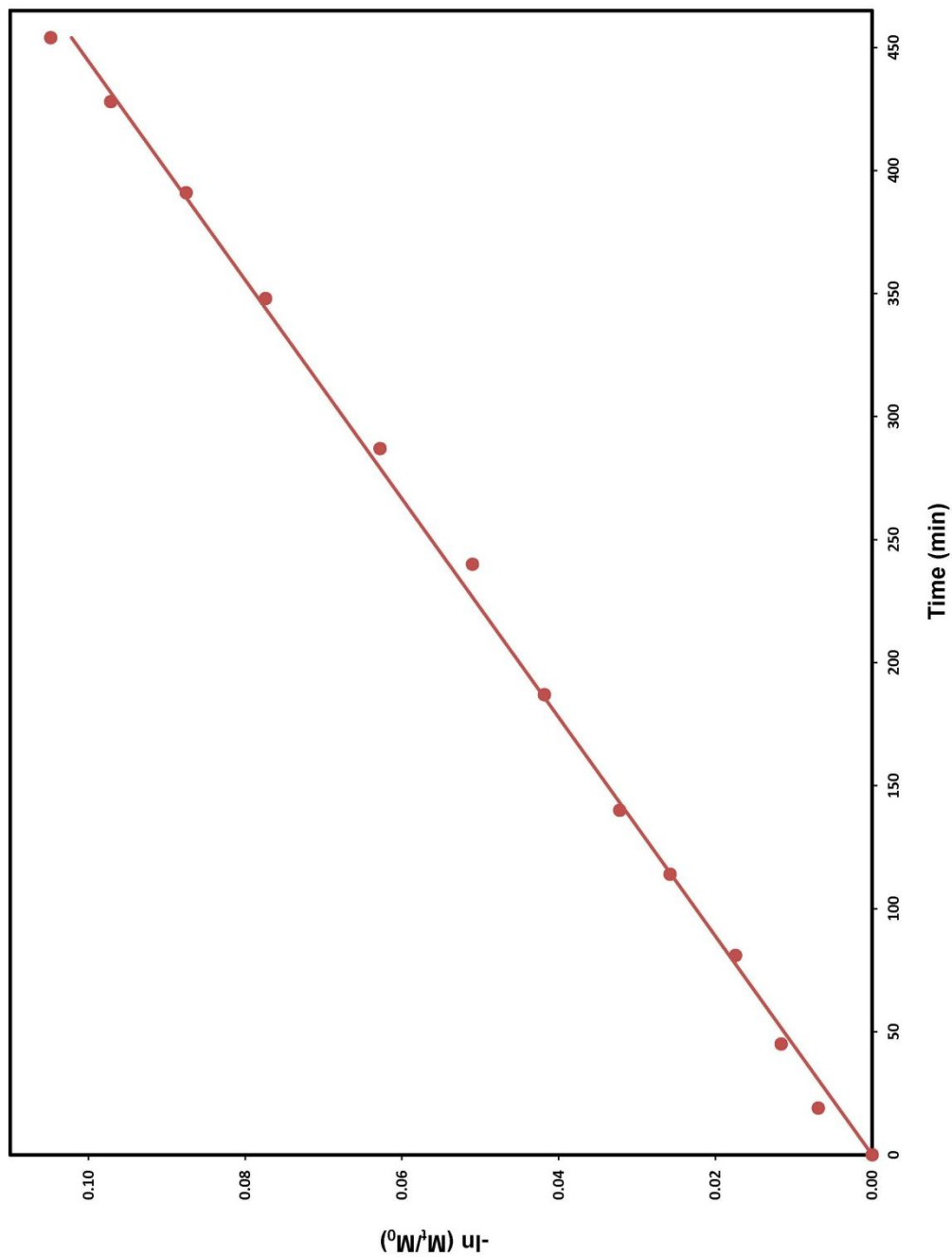


Figure 5.10. Plot of  $-\ln \frac{M_t}{M_0}$  versus time for the polymerization reaction of bovine HA sintered at 675 °C in air for 16 hours and L-lactide

previously. For these samples FTIR spectra reveal that the atmosphere clearly influences the chemical composition of the sintered bone (Figures 5.11, 5.12, 5.13, and 5.14).

For the four sintering temperatures examined, it is clear that the amount of hydroxide present in the samples sintered in air is much higher than any other. Using the libration at  $632\text{ cm}^{-1}$  as an indicator shows that samples sintered in air contain levels of hydroxide that increase with increased temperature. For the samples sintered under vacuum, no appreciable libration peak can be seen until the temperature is raised to  $700\text{ }^{\circ}\text{C}$ , and even then the libration is barely discernable. When comparing analogous samples sintered in air and in vacuum, I saw no differences in the amount of carbonate present in the FTIR spectra. At  $700\text{ }^{\circ}\text{C}$ , all carbonate is lost when sintering under vacuum. The XRD patterns reveal a reflection at  $37.5^{\circ}$  in the  $700\text{ }^{\circ}\text{C}$  and  $675\text{ }^{\circ}\text{C}$  samples indicating that instead of forming hydroxide, sintering under vacuum favors the formation of oxide from the decomposition of carbonate (Figure 5.15). As deduced from Equation 2.12, this lack of hydroxide is most likely due to the lack of water during sintering.

Surface area measurements carried out on vacuum sintered samples show that the rate of decrease in specific surface area is not as pronounced when compared to samples sintered in air (Table 5.3). This is most likely due to the absence of available water. Heughebaert et. al. report that crystal morphology and grain size growth is facilitated by vapor phase water.<sup>17, 19, 20</sup> It is logical to infer that if water were not present, then the crystal remodeling would not happen at such an increased rate. Since water is necessary for the formation of hydroxide instead of oxide, then sintering under vacuum should yield a hydroxyapatite that is high in surface area and rich in oxide. This hypothesis is

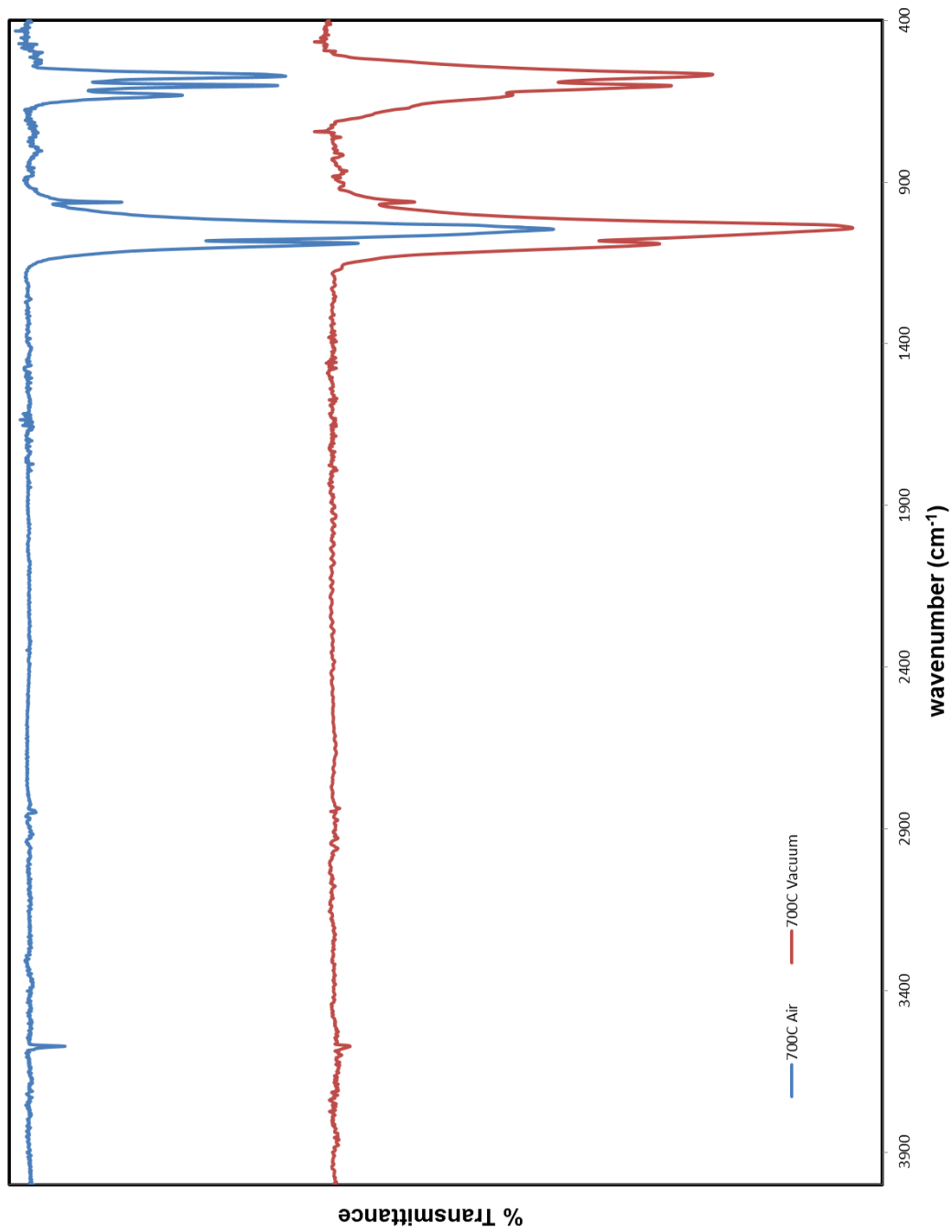


Figure 5.11. FTIR spectra of bovine HA sintered at 700 °C for 16 hours in air and in vacuum



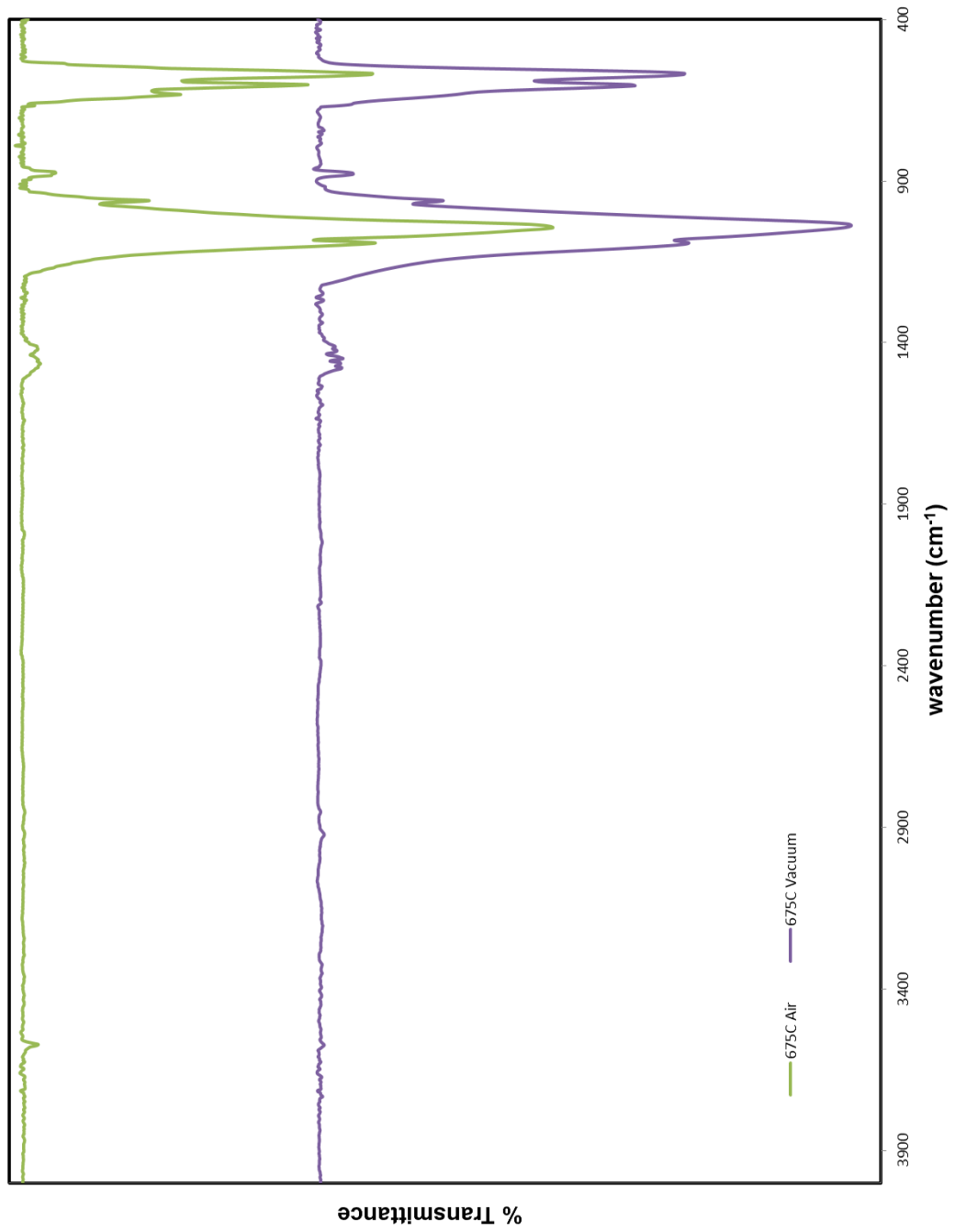


Figure 5.12. FTIR spectra of bovine HA sintered at 675 °C for 16 hours in air and in vacuum

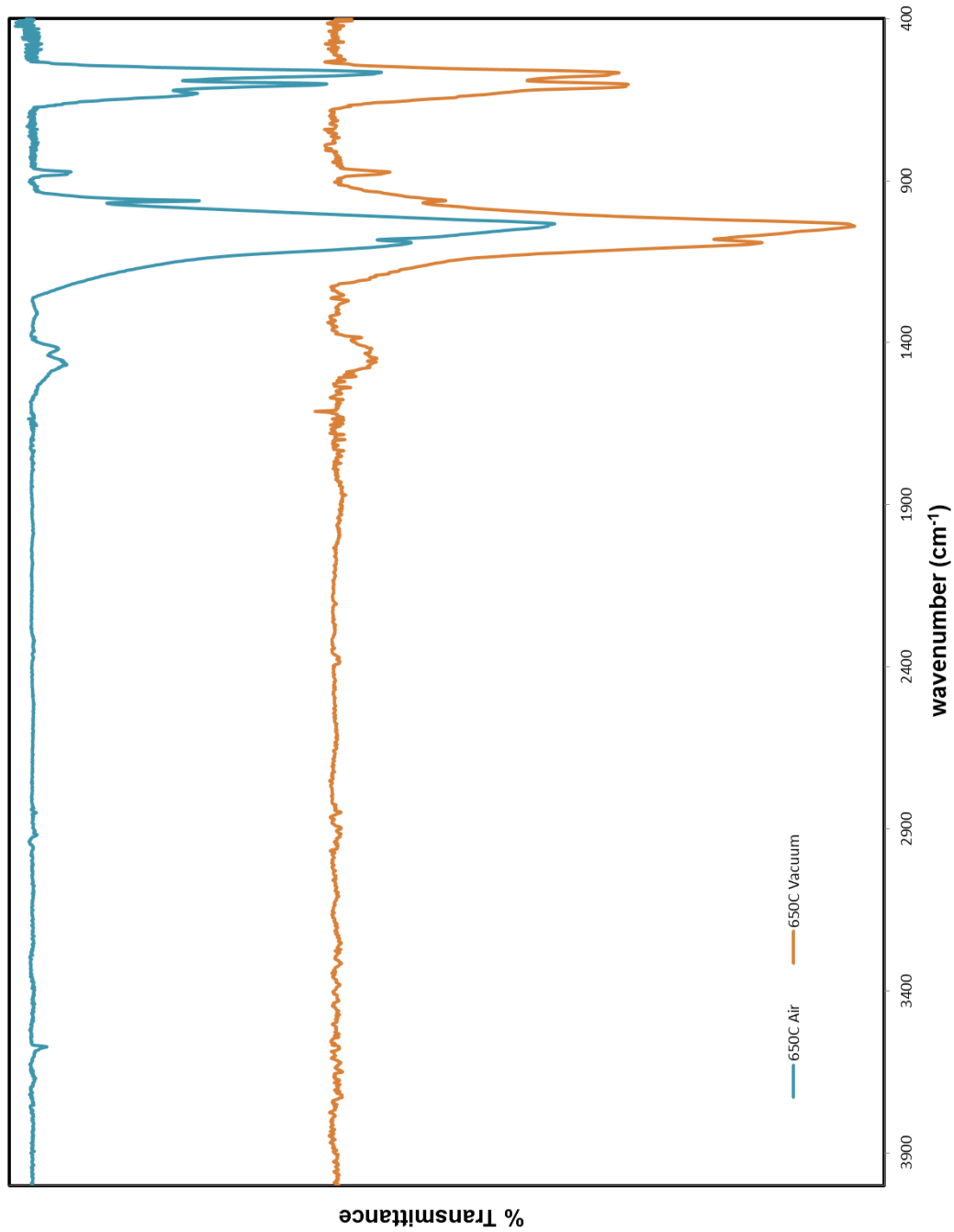


Figure 5.13. FTIR spectra of bovine HA sintered at 650 °C for 16 hours in air and in vacuum

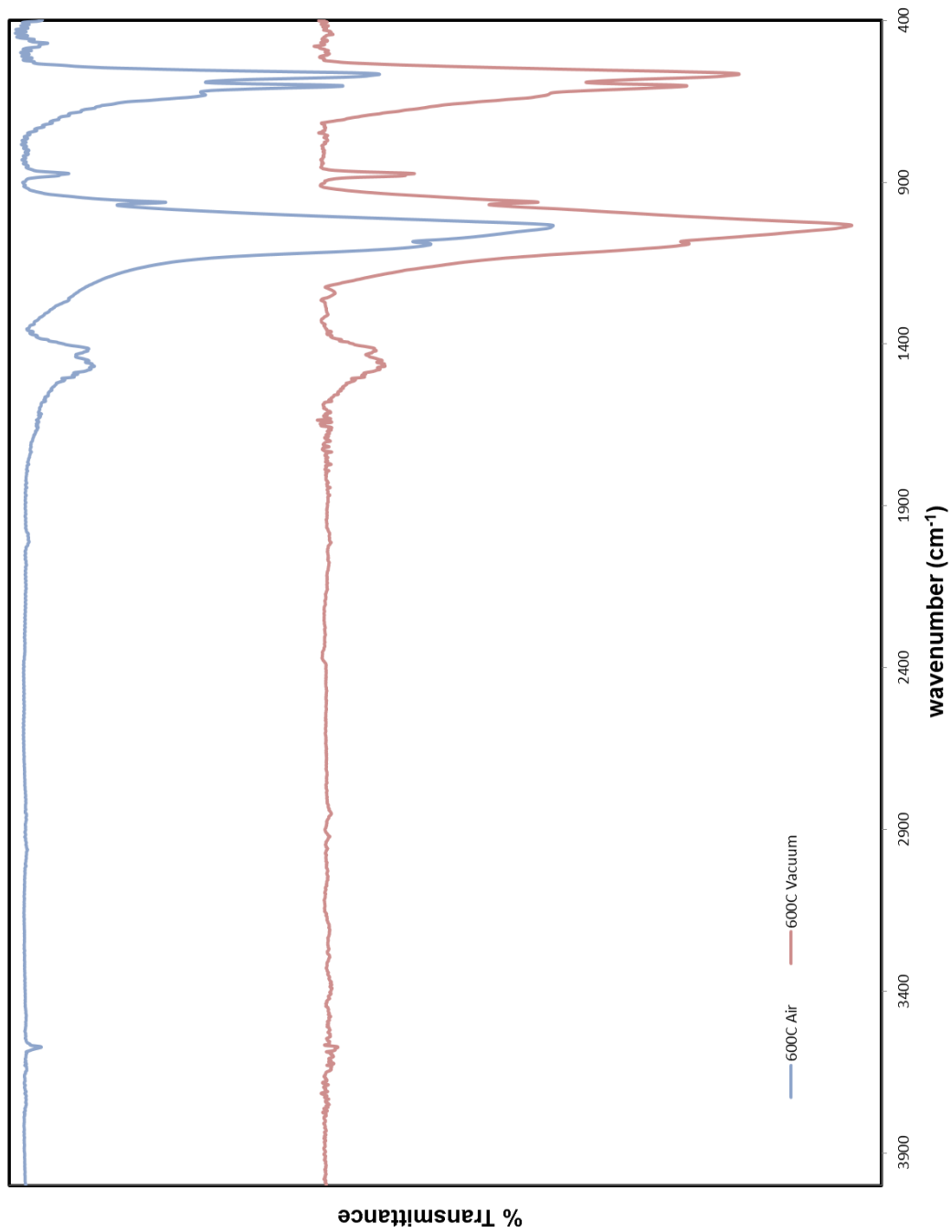


Figure 5.14. FTIR spectra of bovine HA sintered at 600 °C for 16 hours in air and in vacuum

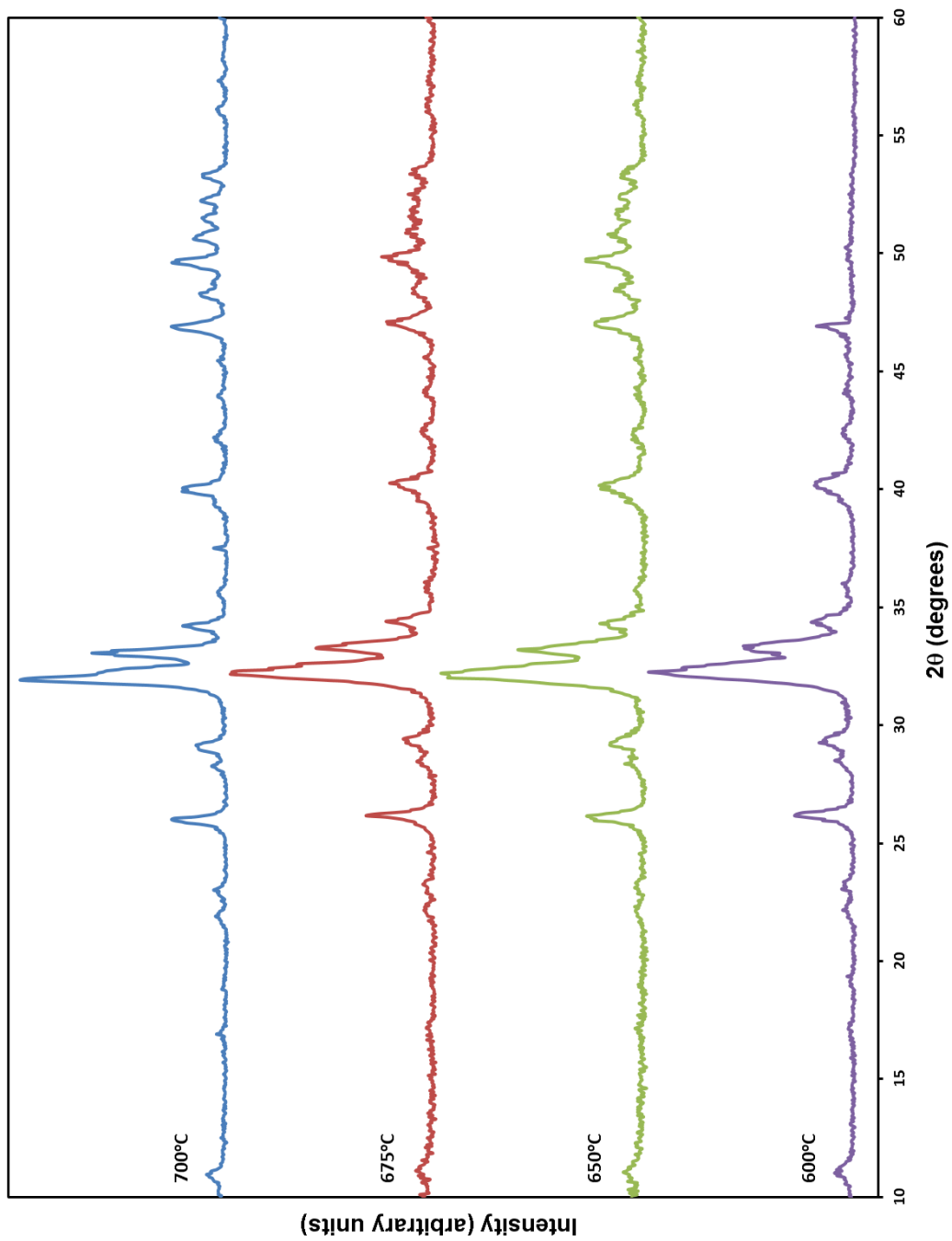


Figure 5.15. XRD patterns for bovine HA sintered at 700 °C, 675 °C, 650 °C, and 600 °C in vacuum

confirmed by the presence of the  $37.5^\circ$  reflection corresponding to an oxide phase in the XRD pattern, the lack of any sizeable peak at  $632\text{ cm}^{-1}$  for the hydroxide libration, and the noticeably higher surface areas measured for vacuum sintered samples.

When comparing the results from the dimensional analysis study for bone plugs sintered in vacuum to those sintered at identical temperatures in air, I observed that the dimension change and mass loss are similar at low temperatures. As the temperature rises the differences between sintering in air and sintering in vacuum become more pronounced. The mass changes and volume changes for samples sintered at  $600^\circ\text{C}$  and  $650^\circ\text{C}$  are essentially the same. At  $675^\circ\text{C}$  these values begin to diverge, and at  $700^\circ\text{C}$  the shrinkage when sintering in air is almost triple the shrinkage when the samples are sintered in vacuum, and the mass loss doubles from roughly 0.4% to 0.8%.

When a standard kinetics reaction was run using powdered HA that was sintered at  $700^\circ\text{C}$  under vacuum, I observed the usual pseudo-first order relationship when plotting  $-\ln \frac{M_t}{M_0}$  versus time (Figure 5.16). The previously determined rate constant for HA sintered at  $700^\circ\text{C}$  in air is  $7.52 \pm 0.04 \times 10^{-6}\text{s}^{-1}$ . The rate constant obtained for the vacuum sintered sample is  $6.3 \pm 0.2 \times 10^{-6}\text{s}^{-1}$ , which is slightly slower than the air sintered sample, even though the surface area is over five times higher. When the rate constants are normalized for surface area, the  $k_{\text{app}}/S_A$  for samples sintered in air is  $1.66 \times 10^{-7}\text{ g/sm}^2$  but for samples sintered in vacuum the number drops to  $2.8 \times 10^{-8}\text{ g/sm}^2$ . These changes show that the surface in air sintered samples is far more reactive than that of the vacuum sintered material.

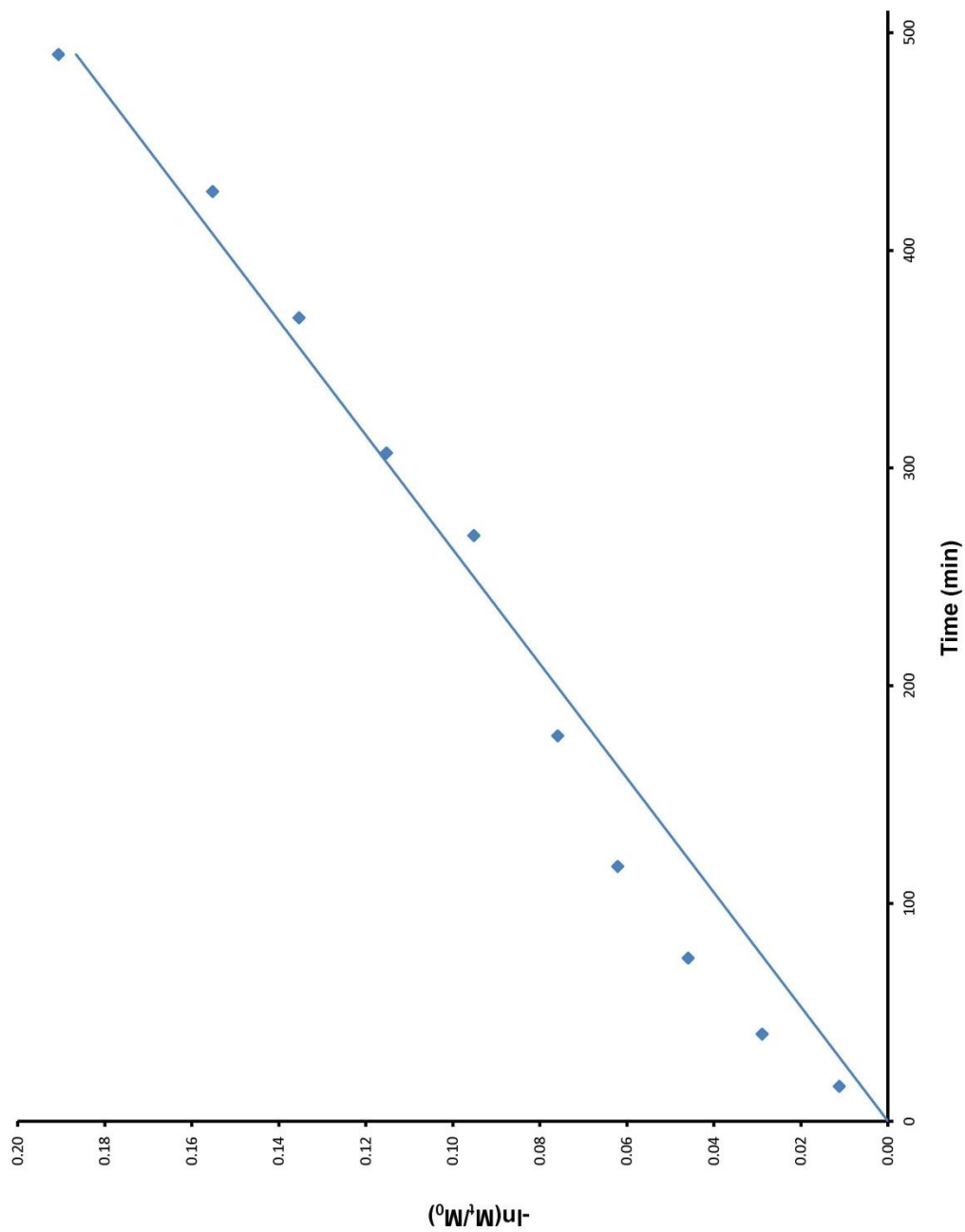


Figure 5.16. Plot of  $-\ln(M_t/M_0)$  versus time for the polymerization reaction of bovine HA sintered at 700 °C in vacuum for 16 hours and L-lactide

From the spectroscopic analyses, surface area measurements, and the kinetics results it is clear that even though sintering HA under vacuum yields a material with much greater specific surface area, it may not be suitable for making a polymer-HA composite due to the reduced reactivity of the surface. It appears that the sintering temperature should be kept below 700 °C to ensure that a high surface area can be maintained while allowing for suitable decomposition of carbonate to hydroxide thereby making the pseudo first order rate constant large enough such that the polymerization reaction is complete in a reasonable period of time.

The kinetics for the polymerization of dioxanone, L-lactide, DL-lactide, and  $\epsilon$ -caprolactone all appear to be first order in mole fraction of monomer. When powdered bovine bone (sintered in air at 700 °C for 16 hours) was used to initiate the polymerization of these monomers, plots of  $-\ln \frac{M_t}{M_0}$  versus time produced linear relationships that are indicative of systems that obey first order kinetics (Figure 5.17)(Table 5.4) L-lactide and DL-lactide have essentially equivalent rates of polymerization, which should be expected since DL-lactide is a racemic mixture of L-lactide and D-lactide. Hydroxyls should show no preference for attacking the carbonyl carbon in either the D or L isomer, since both adopt a pseudo chair conformation making the electrophilic carbon equally open to attack in each enantiomer.<sup>21, 22</sup> Of these four monomers, dioxanone exhibits the fastest rate of polymerization and  $\epsilon$ -caprolactone the slowest.

When plotting  $-\ln \frac{M_t}{M_0}$  versus time for the reaction of L-lactide with bioglass in mass ratios of 4 to 1, 15 to 1 and 31 to 1, I observed a linear relationship that is indicative of

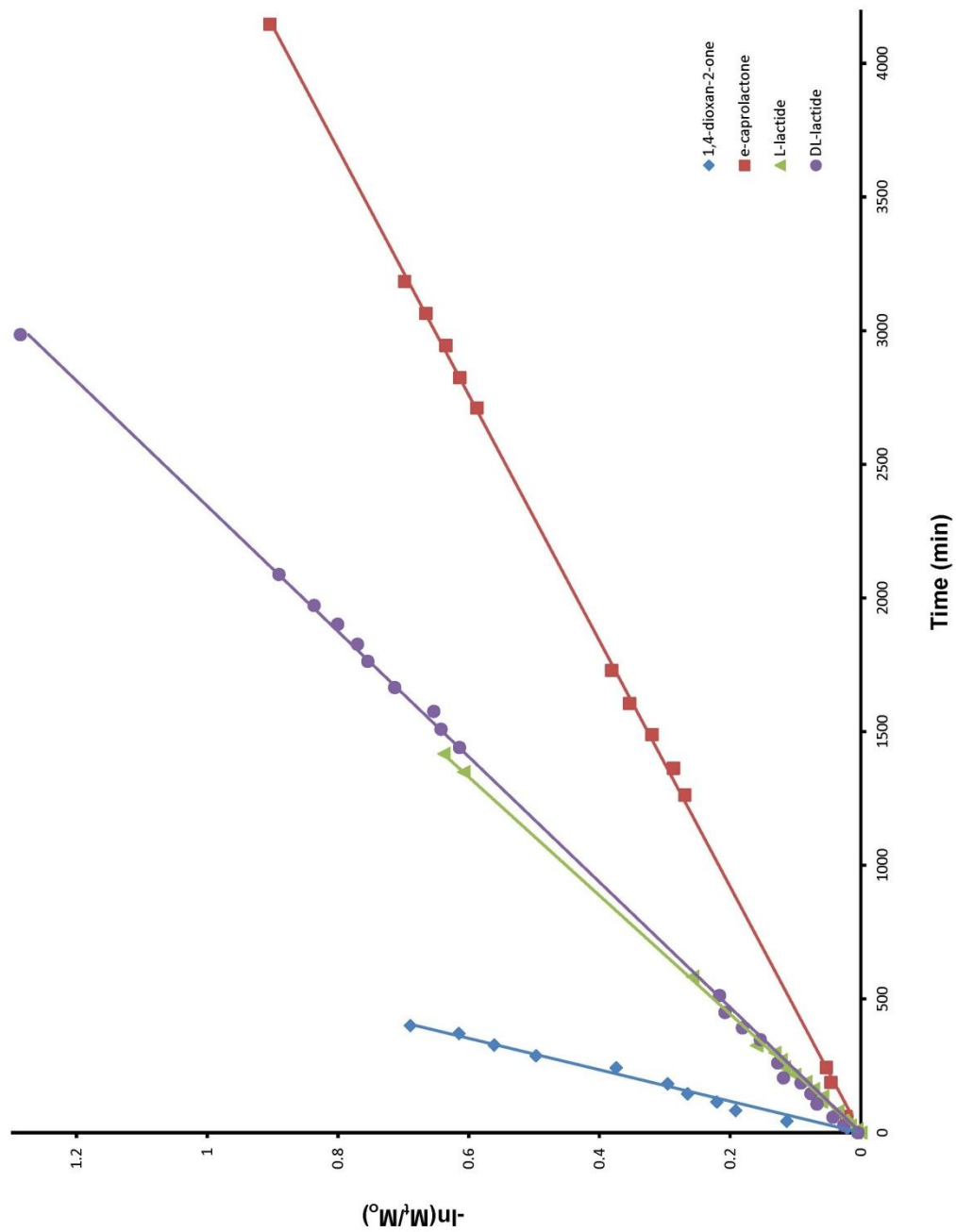


Figure 5.17. Plots of  $-\ln \frac{M_t}{M_0}$  versus time for the polymerization reaction of bovine HA sintered at 700 °C in air for 16 hours with L-lactide, DL-lactide,  $\epsilon$ -caprolactone, and dioxanone



| Monomer                  | $k_{app}$<br>( $10^{-7} \text{ s}^{-1}$ ) | $10^6 \times k_{app}/SA$ ( $\text{g}/\text{sm}^2$ ) |
|--------------------------|---|---|
| 1,4-dioxan-2-one         | 283.2 $\pm$ 5.4                           | 5.91 $\pm$ 0.14                                     |
| $\epsilon$ -caprolactone | 36.2 $\pm$ 0.1                            | 0.76 $\pm$ 0.01                                     |
| L-lactide                | 75.2 $\pm$ 0.4                            | 1.57 $\pm$ 0.01                                     |
| DL-lactide               | 71.1 $\pm$ 0.4                            | 1.48 $\pm$ 0.01                                     |

Table 5.4. Kinetic rate constants for the polymerizations reactions of dioxanone,  $\epsilon$ -caprolactone, L-lactide, and DL-lactide with powdered bovine hydroxyapatite sintered at 700 °C in air for 16 hours. In all cases, a 4:1 mass ratio of monomer to HA was used.

first order kinetics. Of all of the nucleophilic surfaces examined, bioglass exhibited the highest surface activity. Given the apparent first order rate constant of  $4.84 \pm 0.07 \times 10^{-5} \text{ s}^{-1}$  and a specific surface area of  $8.57 \pm 0.64 \text{ m}^2/\text{g}$ ,  $k_{\text{app}}/S_A$  for the bioglass is  $5.65 \pm 0.12 \times 10^{-6} \text{ g}/\text{sm}^2$ , making the normalized first order rate constant larger than for any other system I examined. (Figure 5.18)(Table 5.5).

Interpretations of the kinetics results for the mixed monomer experiment are more complicated than simply plotting  $-\ln \frac{M_t}{M_0}$  versus time. From the  $^1\text{H}$  NMR peak integrals it is still possible to obtain meaningful data and gain an understanding of how the reaction is taking place (Table 5.6). The first relationship that can be studied is the decrease of total monomer as the reaction proceeds. Using the integrals obtained from the  $^1\text{H}$  NMR spectra a formula for the total mole fraction of monomers can be written as

$$M_{\text{mono}} = M_l + M_g \quad (5.2)$$

Where  $M_{\text{mono}}$  is the mole fraction of all monomers,  $M_l$  is the mole fraction of L-lactide, and  $M_g$  is the mole fraction of glycolide. The mole fraction of L-lactide can be calculated as

$$M_l = \frac{I_l}{I_l + I_{\text{PLLA}} + \frac{I_g + I_{\text{PGA}}}{2}} \quad (5.3)$$

and the mole fraction of glycolide can be calculated as

$$M_g = \frac{\frac{I_g}{2}}{I_l + I_{\text{PLLA}} + \frac{I_g + I_{\text{PGA}}}{2}} \quad (5.4)$$

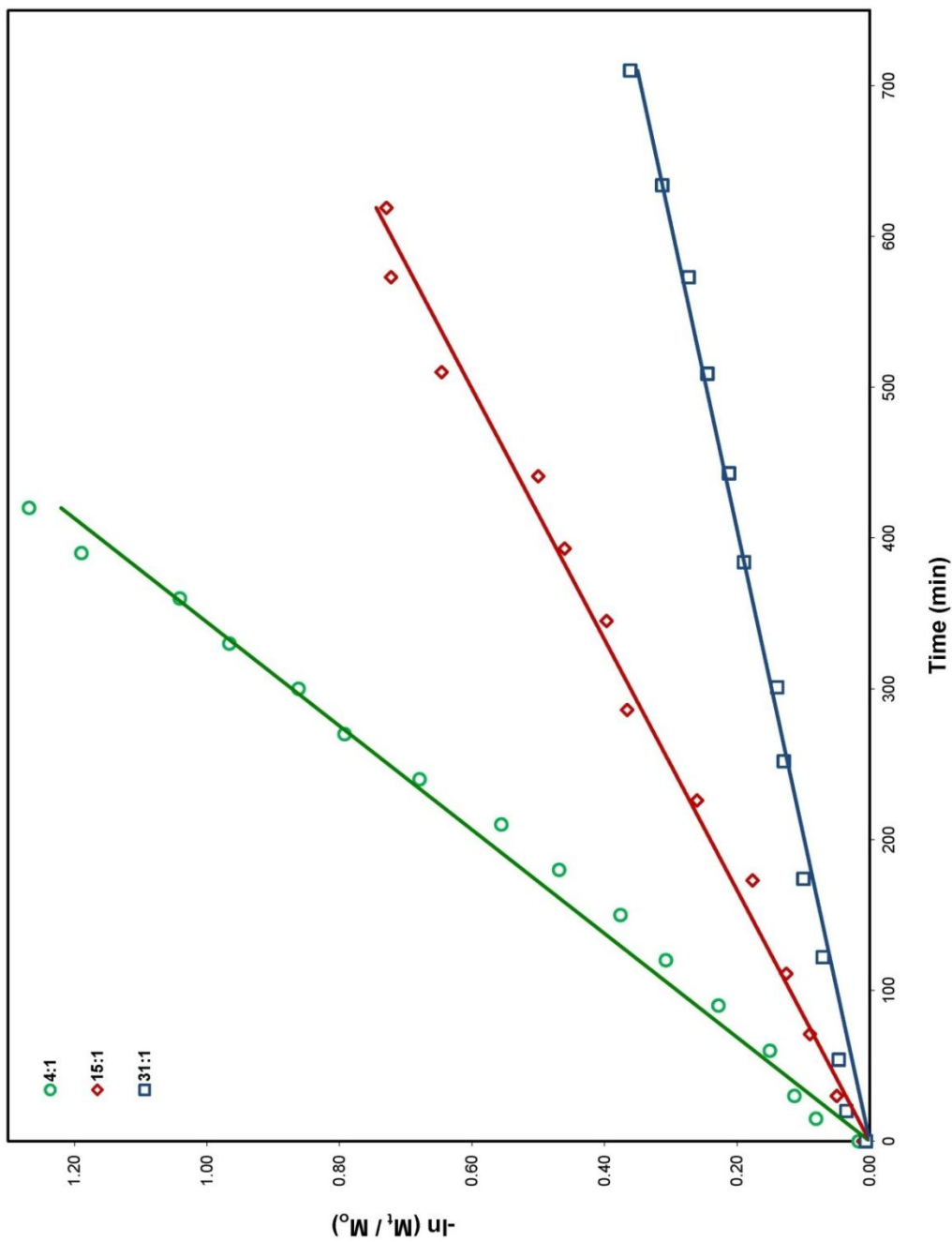


Figure 5.18. Plots of  $-\ln \frac{M_t}{M_0}$  versus time for the reaction of bioglass and L-lactide in 4:1, 15:1, and 31:1 monomer to bioglass mass ratios

| L-lactide to<br>Bioglass Mass<br>Ratio | $k_{app}$<br>( $10^{-5} \text{ s}^{-1}$ ) | $10^5 \times k_{app}/SA$ ( $\text{g}/\text{sm}^2$ ) |
|--|---|---|
| 4:1                                    | 4.84 $\pm$ 0.07                           | 5.65 $\pm$ 0.12                                     |
| 15:1                                   | 2.31 $\pm$ 0.05                           | 2.70 $\pm$ 0.07                                     |
| 31:1                                   | 1.22 $\pm$ 0.03                           | 1.43 $\pm$ 0.05                                     |

Table 5.5. Kinetic rate constants for the reaction of L-lactide with bioglass in 4:1, 15:1, and 31:1 monomer to initiator ratios.

| Sample Number | Elapsed Time (min) | PLLA    | Lactide | PLLA hydroxyl end group | PGA     | Glycolide | PGA hydroxyl end group | Mole Fraction L-lactide (M <sub>l</sub> ) | Mole Fraction Glycolide (M <sub>g</sub> ) | Total Monomer Mole Fraction | M <sub>l</sub> / (M <sub>l</sub> + M <sub>g</sub> ) | M <sub>g</sub> / (M <sub>l</sub> + M <sub>g</sub> ) |
|---------------|--------------------|---------|---------|-------------------------|---------|-----------|------------------------|---|---|-----------------------------|---|---|
| 1             | 0                  | 0.5866  | 89.0750 | 0.5964                  | 1.1463  | 8.1469    | 0.4489                 | 0.8908                                    | 0.0815                                    | 0.9722                      | 0.916   | 0.084   |
| 2             | 30                 | 1.5393  | 88.5409 | 0.9969                  | 2.2857  | 6.1083    | 0.5290                 | 0.8854                                    | 0.0611                                    | 0.9465                      | 0.935   | 0.065   |
| 3             | 60                 | 2.0396  | 90.2043 | 0.9879                  | 3.4362  | 2.9576    | 0.3744                 | 0.9020                                    | 0.0296                                    | 0.9316                      | 0.968   | 0.032   |
| 4             | 100                | 4.2890  | 86.3251 | 1.7342                  | 5.0491  | 2.2770    | 0.3256                 | 0.8633                                    | 0.0228                                    | 0.8860                      | 0.974   | 0.026   |
| 5             | 160                | 10.4904 | 77.0972 | 2.2486                  | 8.4581  | 1.4121    | 0.2937                 | 0.7710                                    | 0.0141                                    | 0.7851                      | 0.982   | 0.018   |
| 6             | 213                | 15.4384 | 70.5889 | 2.4895                  | 10.5401 | 0.6980    | 0.2451                 | 0.7059                                    | 0.0070                                    | 0.7129                      | 0.990   | 0.010   |
| 7             | 274                | 20.0520 | 64.9984 | 2.7364                  | 11.6380 | 0.3786    | 0.1966                 | 0.6500                                    | 0.0038                                    | 0.6538                      | 0.994   | 0.006   |
| 8             | 333                | 24.1096 | 60.2138 | 3.1070                  | 12.1812 | 0.2153    | 0.1731                 | 0.6021                                    | 0.0022                                    | 0.6043                      | 0.996   | 0.004   |
| 9             | 381                | 26.8636 | 58.1590 | 2.6172                  | 12.1203 | 0.1570    | 0.0829                 | 0.5816                                    | 0.0016                                    | 0.5832                      | 0.997   | 0.003   |
| 10            | 429                | 29.8049 | 55.2761 | 2.4708                  | 12.2699 | 0.1230    | 0.0553                 | 0.5528                                    | 0.0012                                    | 0.5540                      | 0.998   | 0.002   |
| 11            | 498                | 33.8391 | 50.8783 | 2.8899                  | 12.2502 | 0.0776    | 0.0649                 | 0.5088                                    | 0.0008                                    | 0.5096                      | 0.998   | 0.002   |
| 12            | 561                | 37.0596 | 47.9363 | 2.5071                  | 12.3951 | 0.0539    | 0.0479                 | 0.4794                                    | 0.0005                                    | 0.4799                      | 0.999   | 0.001   |
| 13            | 607                | 39.4496 | 45.5223 | 2.3990                  | 12.5357 | 0.0444    | 0.0489                 | 0.4552                                    | 0.0004                                    | 0.4557                      | 0.999   | 0.001   |
| 14            | 1543               | 68.8523 | 17.0085 | 1.3080                  | 12.7853 | 0.0213    | 0.0247                 | 0.1701                                    | 0.0002                                    | 0.1703                      | 0.999   | 0.001   |
| 15            | 1849               | 73.8440 | 12.9084 | 0.6041                  | 12.6190 | 0.0152    | 0.0094                 | 0.1291                                    | 0.0002                                    | 0.1292                      | 0.999   | 0.001   |

Table 5.6. Representative Excel® spreadsheet for a reaction of bioglass and an 82% L-lactide and 18% glycolide mixture of monomers

in a similar manner to that used in chapter 2 where integrated areas from the  $^1\text{H}$  NMR spectra were used to calculate relative proton abundances. The integrated area terms in equations 5.3 and 5.4 are defined as follows, glycolide monomer ( $I_g$ ), L-lactide monomer ( $I_l$ ), PLLA ( $I_{\text{PLLA}}$ ), and PGA ( $I_{\text{PGA}}$ ). Recall equation 2.8 where  $I_p$  for PLLA is defined. For the purposes of this mixed monomer system  $I_{\text{PLLA}} = I_p$  from equation 2.8. An analogous equation for PGA was needed that accounted for the internal polymer protons ( $I_{P_{\text{PGA}}}$ ) as well as the carboxylate ( $I_{C_{\text{PGA}}}$ ) and alcohol ( $I_{A_{\text{PGA}}}$ ) end groups.

$$I_{\text{PGA}} = I_{P_{\text{PGA}}} + I_{A_{\text{PGA}}} + I_{C_{\text{PGA}}} \quad (5.5)$$

All integrated areas obtained for the glycolide monomer and for PGA need to be divided by two because there are two methylene protons that are analogous to the single methine proton used for PLLA and L-lactide.

When examining the mole fraction of glycolide as the reaction progressed, I saw it decreased at a rate much greater than that of the L-lactide. When plotting  $-\ln \frac{M_t}{M_0}$  versus time for both monomers a linear relation is seen in each instance, I obtained pseudo-first order rate constants of  $14.44 \pm 0.66 \times 10^{-5} \text{s}^{-1}$  for glycolide and  $2.00 \pm 0.07 \times 10^{-5} \text{s}^{-1}$  for L-lactide (Figures 5.19 and 5.20). This shows that glycolide is almost an order of magnitude more reactive than L-lactide.

If we consider only the monomers in the reaction mixture, the mole fraction of L-lactide ( $X_l$ ) and glycolide ( $X_g$ ) can be defined as shown in equations 5.6 and 5.7 where

$$X_l = \frac{I_l}{I_l + \frac{I_g}{2}} \quad (5.6)$$

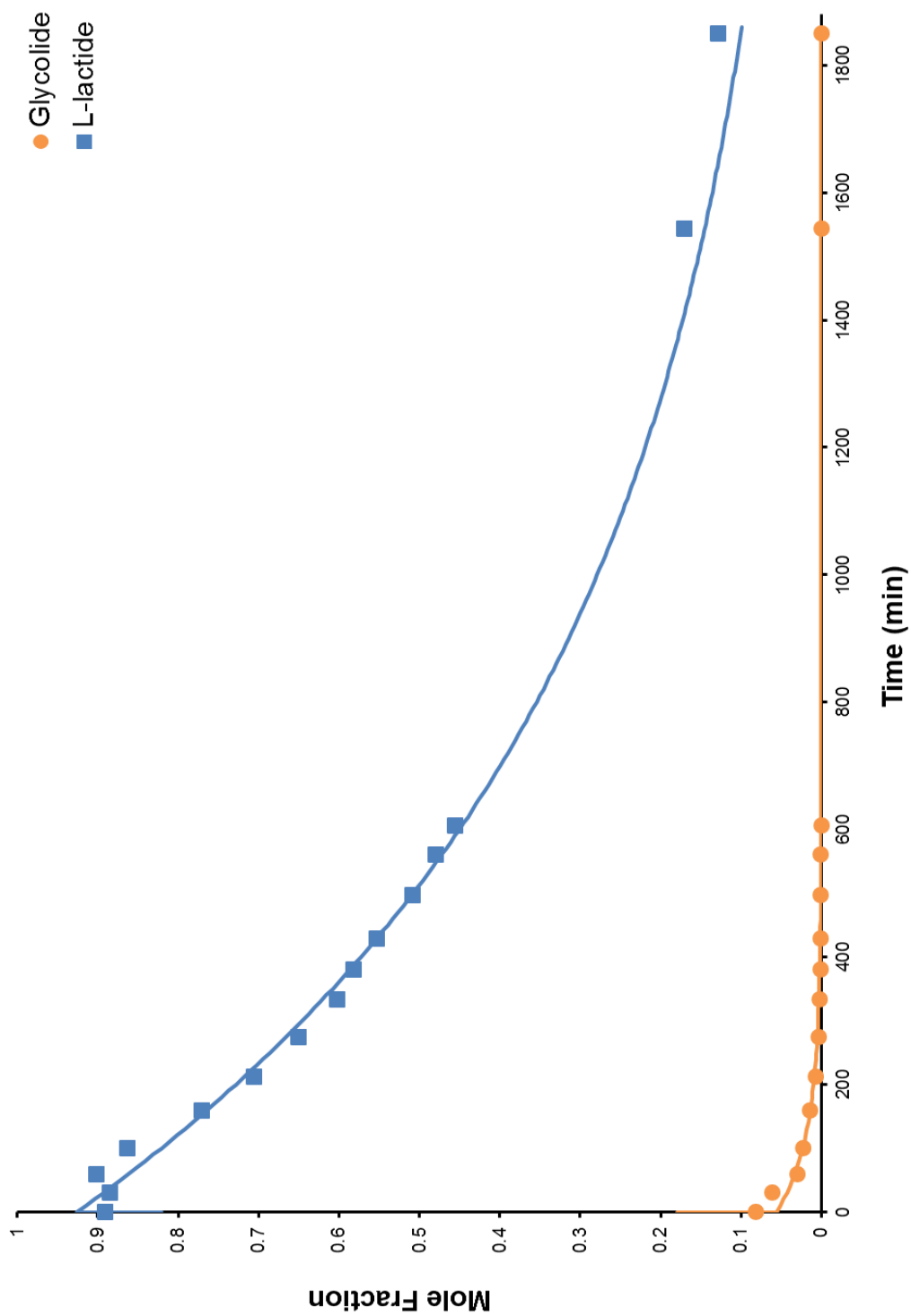


Figure 5.19. Plots of mole fraction of monomer versus time for the polymerization reaction of bioglass with an 82% L-lactide and 18% glycolide monomer mix

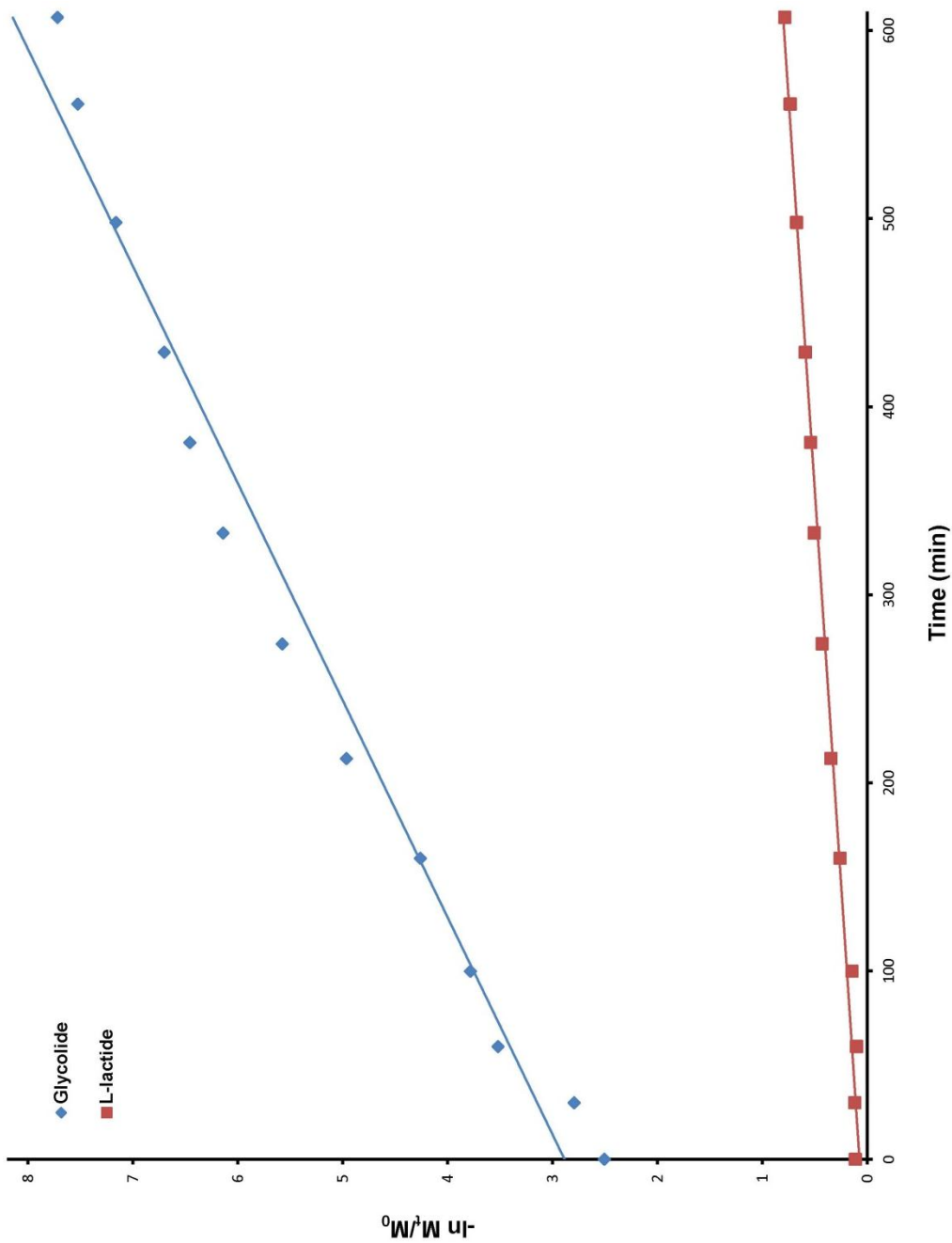


Figure 5.20. Plots of  $-\ln \frac{M_t}{M_0}$  versus time for the polymerization reaction of bioglass with an 82% L-lactide and 18% glycolide monomer mix



and

$$X_g = \frac{\frac{I_g}{2}}{I_l + \frac{I_g}{2}} \quad (5.7)$$

can be seen to decrease until it becomes barely imperceptible by  $^1\text{H}$  NMR spectroscopy. By definition the sum of all monomers is one.

$$X_g + X_l = 1 \quad (5.8)$$

Over time  $X_l$  rapidly approaches one while  $X_g$  approaches zero. (Figure 5.21) The glycolide in the reaction mixture is nearly completely consumed before the L-lactide is. This result agrees with the measured rate constants for each monomer.

At  $t = 0$ , the starting mole fractions of L-lactide and glycolide should be 0.82 and 0.18 respectively, but the observed values were measured to be 0.916 for L-lactide and 0.084 for glycolide. This deviation from the theoretical value is most likely due to the extreme reactivity of glycolide. In the time scale on which the first sample aliquot could be taken, a significant fraction of the glycolide had ring opened. The kinetics of this event is not accessible given the manner in which the experiment was executed. It is clear that some of these glycolide ring opening events occurred during the time in which the reaction mixture is warmed and completely melted.

A consequence of the difference in reactivities of L-lactide and glycolide is that the polymer created at long times is not a mixture of PLLA with regular intervals of PGA but rather a polymer that is weighted toward high fractions of PGA at the carboxylate end and high fractions of PLLA at the alcohol end. At long reaction times the polymer

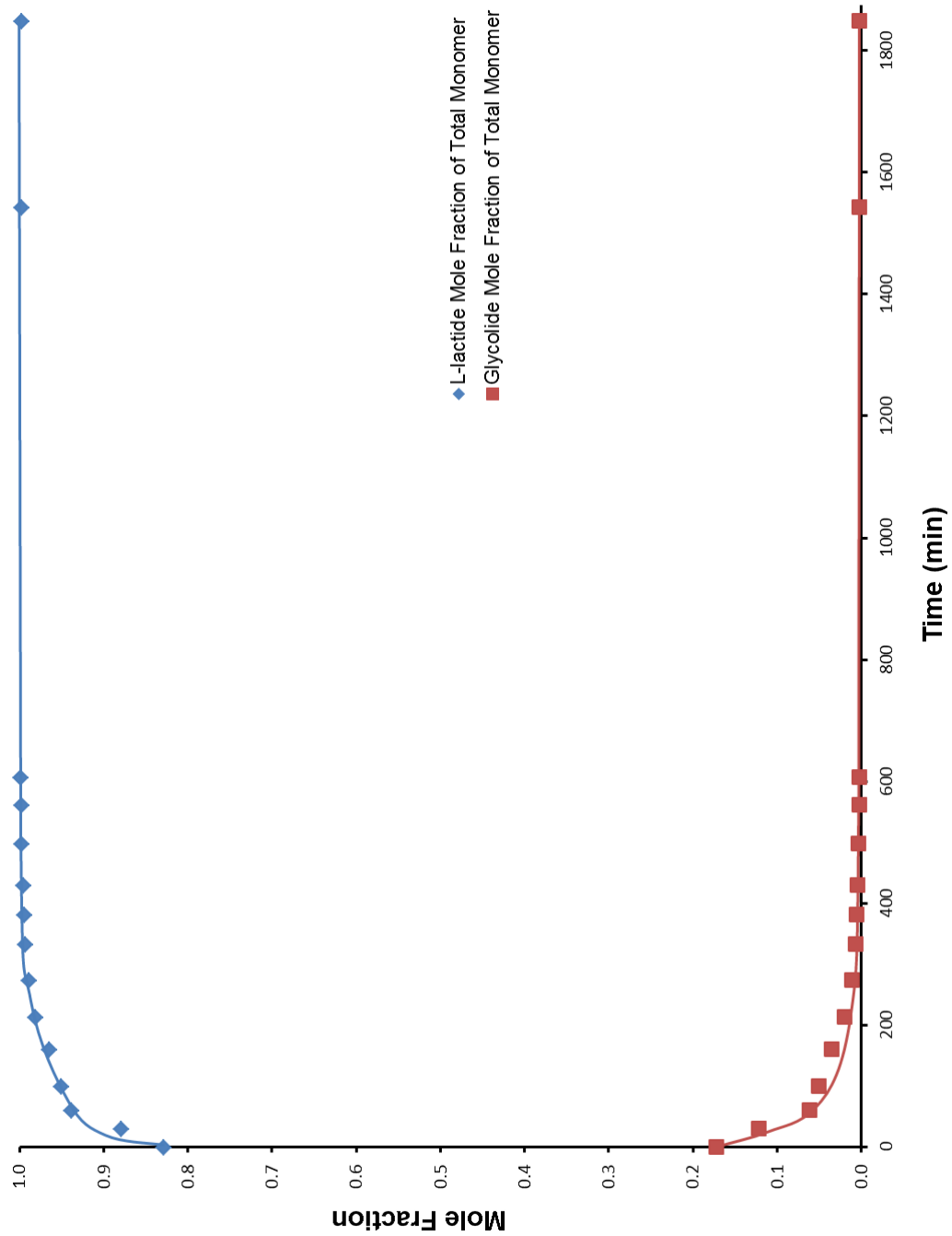


Figure 5.21. Plots of mole fraction versus time for the polymerization reaction of bioglass with an 82% L-lactide and 18% glycolide monomer mix considering only the monomer fraction of the reaction mixture

structure on the alcohol end approaches that of pure PLLA. This result is directly relevant to the resorption of the polymer when placed in biological systems. The PGA ester and the PLLA ester do not hydrolyze at the same rate. This should lead to different degradation patterns and fragmentation that could affect the physical strength of composites manufactured using this method.

### References

1. Bernache-Assollant, D.; Ababou, A.; Champion, E.; Heughebaert, M., Sintering of calcium phosphate hydroxyapatite  $\text{Ca}_{10}(\text{PO}_4)_6(\text{OH})_2$ . I. Calcination and particle growth. *Journal of the European Ceramic Society* **2002**, *23*, 229-241.
2. Ooi, C. Y.; Hamdi, M.; Ramesh, S., Properties of hydroxyapatite produced by annealing of bovine bone. *Ceramics International* **2007**, *33*, (7), 1171-1177.
3. Haberko, K.; Bucko, M. M.; Brzezinska-Miecznik, J.; Haberko, M.; Mozgawa, W.; Panz, T.; Pyda, A.; Zarebski, J., Natural hydroxyapatite - its behaviour during heat treatment. *Journal of the European Ceramic Society* **2006**, *26*, (4-5), 537-542.
4. Bailliez, S.; Nzihou, A., The kinetics of surface area reduction during isothermal sintering of hydroxyapatite adsorbent. *Chemical Engineering Journal* **2004**, *98*, (1-2), 141-152.
5. Nishida, H.; Yamashita, M.; Endo, T.; Tokiwa, Y., Equilibrium Polymerization Behavior of 1,4-Dioxan-2-one in Bulk. *Macromolecules* **2000**, *33*, 6982-6986.
6. Fischmen, G.; Clare, A.; Hench, L.; Editors In *Proceedings of the Biomedical and Biological Applications of Ceramics and Glass Symposium*, Bioceramics: Materials and Applications, Indianapolis, IN, April 25-27, 1994, 1995; American Ceramic Society: Indianapolis, IN, 1995; p 329 pp.
7. Gross, U.; Strunz, V., The interface of various glasses and glass ceramics with a bony implantation bed. *Journal of Biomedical Materials Research* **1985**, *19*, 251-71.
8. Hench, L. L., Bioceramics. *Science of Ceramics* **1977**, *9*, 193-211.
9. Hench, L. L., Bioceramics, a clinical success. *The American Ceramic Society: Bulletin* **1998**, *77*, 67-74.

10. Jones, J. R.; Hench, L. L. In *Challenges for bioceramics in the 21st century*, 2007; Wiley-Liss, Inc.: 2007; pp 189-196.
11. Wilson, J.; Hench, L. L.; Greenspan, D.; Editors, *Bioceramics: Volume 8. (Proceedings of the 8th International Symposium on Ceramics in Medicine, held in Ponte Vedra, Florida, November 1995.)*. Pergamon: 1995; p 512 pp.
12. Wilson, J.; Pigott, G. H.; Schoen, F. J.; Hench, L. L., Toxicology and biocompatibility of bioglasses. *Journal of Biomedical Materials Research* **1981**, 15, 805-17.
13. Zini, E.; Scandola, M.; Dobrzynski, P.; Kasperczyk, J.; Bero, M., Shape memory behavior of novel (L-Lactide- glycol ide-trimethylene carbonate) terpolymers. *Biomacromolecules* **2007**, 8, (11), 3661-3667.
14. Dechy-Cabaret, O.; Martin-Vaca, B.; Bourissou, D., Controlled ring-opening polymerization of lactide and glycolide. *Chemical Reviews* **2004**, 104, (12), 6147-6176.
15. Cai, Q.; Bei, J. Z.; Wang, S. G., Synthesis and degradation of a tri-component copolymer derived from glycolide, L-lactide, and epsilon-caprolactone. *Journal of Biomaterials Science-Polymer Edition* **2000**, 11, (3), 273-288.
16. Dobrzynski, P.; Kasperczyk, J.; Bero, M., Application of calcium acetylacetonate to the polymerization of glycolide and copolymerization of glycolide with epsilon-caprolactone and L-lactide. *Macromolecules* **1999**, 32, (14), 4735-4737.
17. Ababou, A.; Bernache-Assollant, D.; Heughebaert, M., Influence of water vapor on grain growth during the calcination of hydroxyapatite. *Ceramic Transactions* **1995**, 51, 111-15.

18. Haberko, K.; Bucko, M. M.; Mozgawa, W.; Pyda, A.; Brzezinska-Miecznik, J.; Carpentier, J., Behaviour of bone origin hydroxyapatite at elevated temperatures and in O<sub>2</sub> and CO<sub>2</sub> atmospheres. *Ceramic International* **2009**, *35*, 2537-2540.
19. Gruy, F.; Pijolat, M., Kinetics of anatase titania surface area reduction in a mixture of hydrogen chloride, water, and oxygen: I. Experimental study. *Journal of the American Ceramic Society* **1992**, *75*, 657-62.
20. Beruto, D.; Barco, L.; Belleri, G.; Searcy, A. W., Vapor-phase hydration of submicrometer calcium monoxide particles. *Journal of the American Chemistry Society* **1981**, *64*, 74-80.
21. Koeller, S.; Kadota, J.; Deffieux, A.; Peruch, F.; Massip, S.; Leger, J. M.; Desvergne, J. P.; Bibal, B., Ring-Opening Polymerization of L-Lactide Efficiently Triggered by an Amido-Indole. X-ray Structure of a Complex between L-Lactide and the Hydrogen-Bonding Organocatalyst. *Journal of the American Chemical Society* **2009**, *131*, (42), 15088-+.
22. Inai, Y.; Ogawa, H., Theoretical Studies on Conformational Features of Poly(lactic acid) Chain Containing a Racemic Unit. *Kobunshi Ronbunshu* **2010**, *67*, (3), 214-223.

## Chapter Six

### Physical Properties of Composite Devices Created from a Bioresorbable Polymer and Bovine Derived Hydroxyapatite

#### Introduction and Background

As described in earlier chapters of this thesis, the use of hydroxyapatite to initiate the ring opening polymerization of lactones can be controlled through the HA sintering time and sintering temperature, which influence the specific surface area and chemical composition of the surface. Control of these parameters is only part of the puzzle when attempting to make a material for replacement of hard tissues. The morphologies of these materials are often complex. As a result, biomechanical efficacy is not certain *a priori*. However, it is possible to screen the materials for possible biomechanical efficacy of a device by determining the mechanical properties of the materials themselves. To that end, in this chapter I provide a discussion of compression and torsional properties measured for the samples I prepared.

The compressive strength of materials is measured by applying a force to a section of the sample material such that the dimensions of the sample along one axis are decreased. A load cell is used to record the force applied to the sample as a function of the distance between the surfaces of the load cell. Ceramic-polymer composites such as the type prepared from bone and resorbable polyester polymers are usually treated as brittle materials, such as glass or concrete, rather than being treated as flexible materials such as elastomers or plasticized polymers. (Figure 6.1) In graphical presentations of data from such tests, strain is plotted on the x-axis in units of travel distance over sample height.

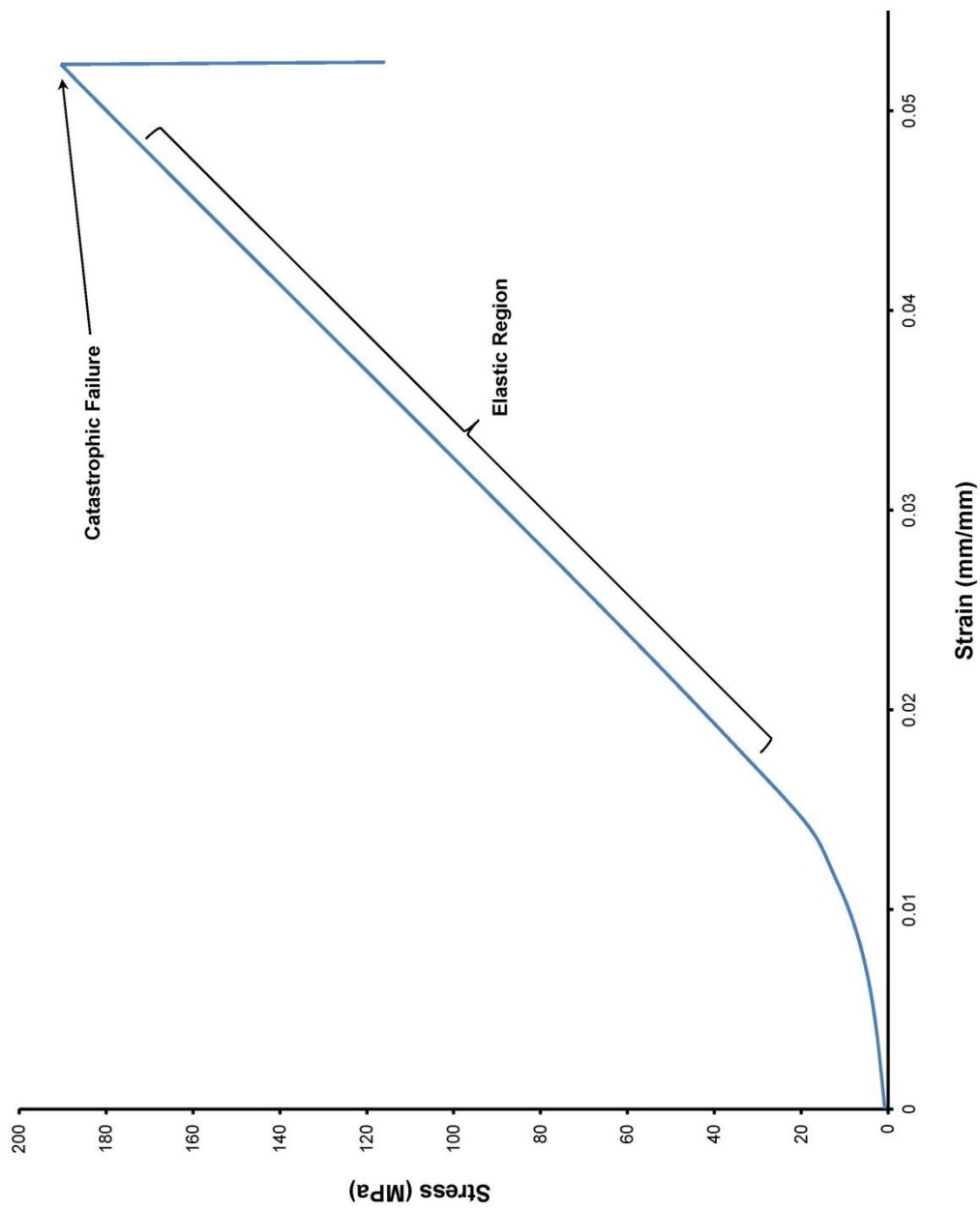


Figure 6.1. Representative compressive stress strain curve for a brittle solid



Stress is plotted on the y-axis. Stress is reported in pressure units since it is defined as the applied force divided by the sample's cross-sectional area. The linear region of the stress strain curve is the elastic region. In the elastic region the sample will return to its original shape if the load is removed. The slope of the stress-strain curve in this linear region is defined as the elastic modulus, which has units of pressure. The apex of the stress-strain curve (the point where the derivative of the stress with respect to strain is zero) is the maximum stress a sample can withstand before failure. One characteristic of brittle materials is a clearly defined failure point, sometimes referred to as the point of catastrophic failure, where the sample usually breaks into several smaller shards. For failure to happen the downward force  $F_D$  must exceed the critical force,  $F_C$ , inherent in the sample where  $F_C$  is defined as

$$F_C = \frac{(\text{Elastic Modulus})(\text{Cross Sectional Area})^2}{(\text{Sample Height})^2} \quad (6.1)$$

The equation can be rewritten for cylindrical samples as

$$F_C = \frac{E\pi^2r^4}{h^2} \quad (6.2)$$

where E is the elastic modulus, r is the radius, and h is the sample height.<sup>1-3</sup>

Modulus can be thought of as the resistance to deformation. Brittle samples generally have higher moduli than elastomeric materials. For later comparison to the mechanical properties of my materials, it is useful to note that the measured compressive strength of wet human femoral bone is 167 MPa, and the modulus of elasticity is 17.2 GPa.<sup>4,5</sup>

Integrating the area under the stress strain curve gives a value referred to as material toughness. This is the total amount of energy a material can absorb before failure. Toughness has units of  $\text{energy}/\text{volume}$ .

In some applications envisioned for my materials, devices such as pins or screws would be subjected to twisting deformations. Consequently, I measured the torsional properties of rods constructed from my composites. In a typical torsional measurement, one end of the rod is fixed in place and a force is applied to a lever arm attached the other end, causing the arm to rotate about the axis of the rod. (Figure 6.2) This produces a force called torque that can be defined by the equation

$$\tau = r\mathbf{F} \sin \theta \quad (6.3)$$

where  $\tau$  is the torque force in Nm,  $r$  is the radius, and  $\mathbf{F}$  is the force applied perpendicularly to the lever arm. The torque equation can also be rewritten for static systems to yield

$$\tau = r\mathbf{F}_{\perp} \quad (6.4)$$

where  $\mathbf{F}_{\perp}$  is the force applied perpendicularly to the radial vector. The  $\sin \theta$  term becomes  $\sin \frac{\pi}{2}$ , which is one, simplifying the equation. This treatment is theoretically valid for samples that are either fixed at both ends or free to rotate at both ends. Stress strain curves for torsion can be generated analogously to those for compression. (Figure 6.3) In the actual measurements I performed, one end of a sample rod was fixed in a static jaw and the other was attached to a drive motor to twist the sample. A load cell was mounted on the stationary end to measure the torque when the sample was twisted.

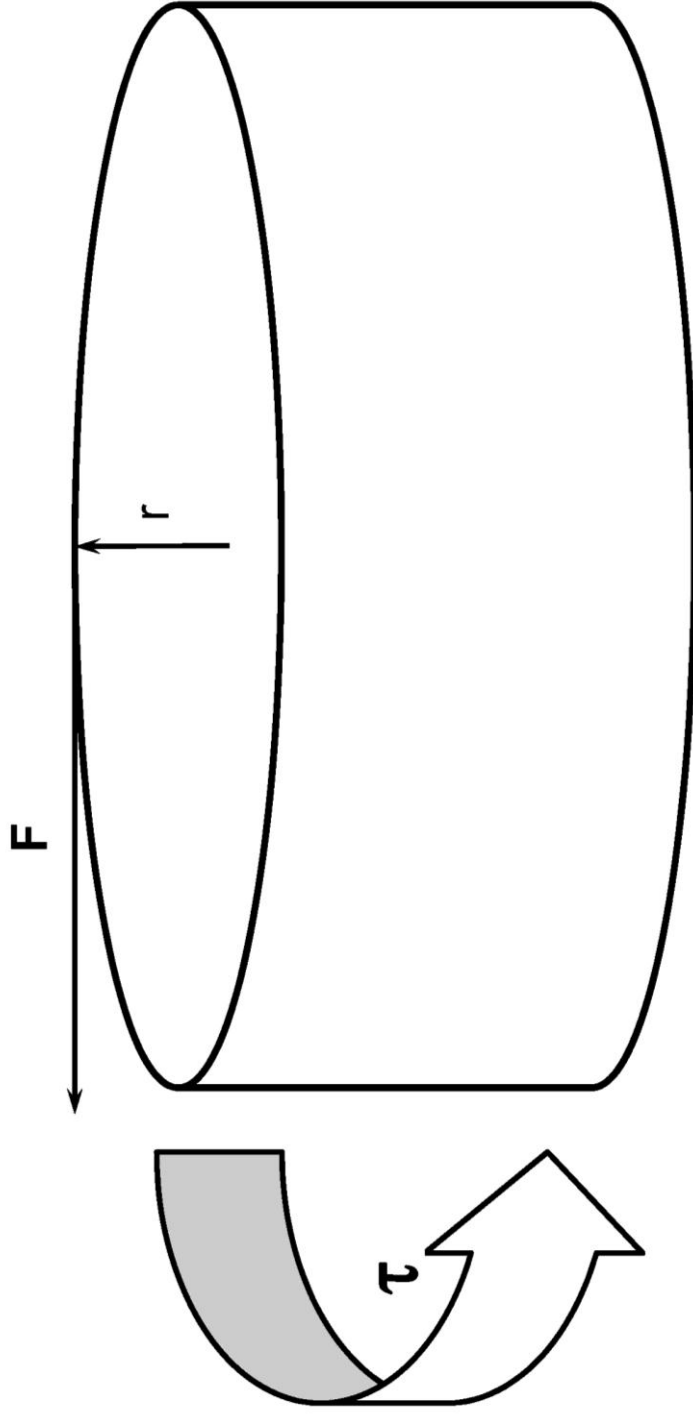


Figure 6.2. Diagram showing a force,  $F$ , acting tangent to the radius,  $r$ , of a round solid generating a torsion,  $\tau$

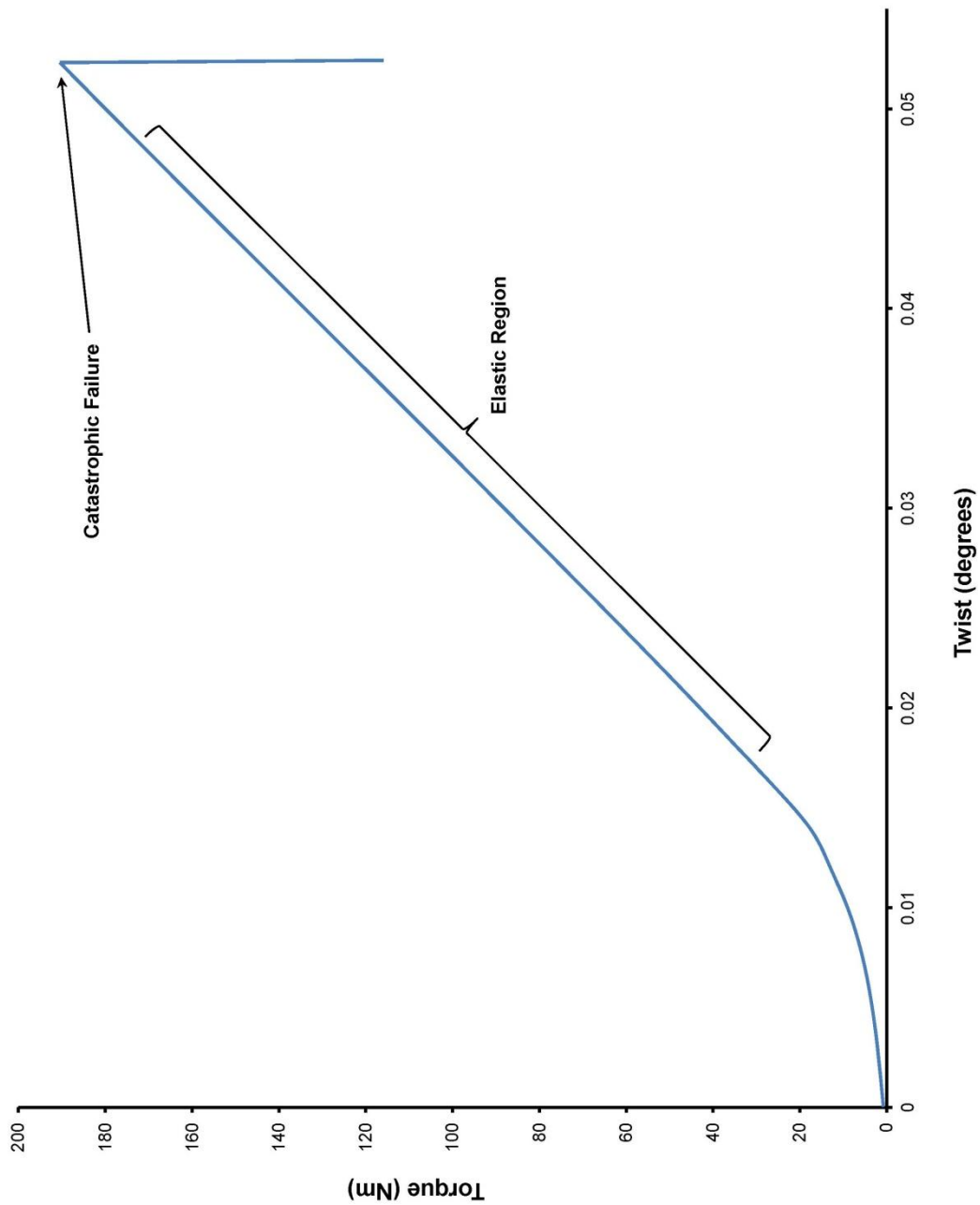


Figure 6.3. Representative torsion plot of torque versus twist

For this particular geometry, the equations introduced above must be expanded to account for the height of the test sample. This equation is

$$G = \frac{TL}{J\theta} \quad (6.5)$$

for cylindrical rods where  $L$  is the sample length,  $J$  is the polar moment of inertia of the section around its center,  $\theta$  is twist angle,  $T$  is the measured torque in the sample, and  $G$  is the modulus of rigidity or shear modulus.<sup>2,6,7</sup> Higher moduli are associated with stiffer or more brittle samples.<sup>3,7</sup>  $J$  is defined as

$$J = \frac{\pi D^4}{32} \quad (6.6)$$

where  $D$  is the outside diameter of the shaft.

The modulus of rigidity for the sample can be calculated using a rearranged form of equation 6.5, i.e., equation 6.7.

$$T = \frac{GJ}{L} \theta \quad (6.7)$$

The modulus of rigidity for the sample can be calculated from the slope of the stress strain curve obtained when  $T$  is plotted versus  $\theta$ , as shown in Figure 6.3.

Although there is no torsional data available for bioresorbable polymer-hydroxyapatite composites such as those I have produced from bovine cortical bone, data does exist for some commercially available fixation screws. All of the screws are made completely of resorbable polymer with no mineral filler or metal substructure.<sup>8</sup> The screws studied were between 7 and 10 mm in diameter and as would be expected the screws with larger

diameter required a higher torque before failure. Screws with a 9 mm diameter or higher had a maximum torque at failure of roughly 2.5 to 3.0 Nm and the smaller screws with a diameter of 7 mm fail at about 1.1 to 1.75 Nm. Modulus of rigidity was not reported for either bone or the tested fixation screws.

Polymers often exhibit different properties depending on the rate at which a force is applied. These are called viscoelastic properties.<sup>13</sup> All non-Newtonian fluids exhibit such properties. If the stress is applied quickly then the material will respond as a solid, but if the stress is applied slowly the sample will respond as a liquid. A material that exemplifies this property is Silly Putty®, which is a low molecular weight silicone polymer. If the material is pulled slowly, it will stretch and sag. If the material is pulled quickly it resists flow and breaks cleanly instead. This has consequences when designing orthopaedic implants, since the force loading is not constant. The loading of a device implanted in the leg is much faster when a recipient is running as opposed to standing in place.

Polymer molecular weights for the devices tested were also measured. Two specific mathematic treatments of molecular weight were used in the characterizations. The first is the number average molecular weight ( $M_n$ ), which is defined as

$$M_n = \frac{\sum M_i N_i}{\sum N_i} \quad (6.8)$$

This is the arithmetic average of all molecular weights of the polymer chains present in the polymerized bone plug.<sup>9</sup> The second is the weight average molecular weight ( $M_w$ ).<sup>9</sup> It is defined mathematically as

$$M_w = \frac{\sum M_i^2 N_i}{\sum M_i N_i} \quad (6.9)$$

and is best described as the contribution that any one molecular weight has toward the total molecular weight. The ratio of the different averages is called the polydispersity index (PDI) and is defined as

$$PDI = \frac{M_w}{M_n} \quad (6.10)$$

PDI is a measure of the distribution of molecular weight of the polymer chains in the polymer mixture. A PDI of 1 means that there is no distribution in the polymer chains and that they are all exactly the same molecular weight. A large PDI means that there is a large distribution in molecular weights.

### Experimental

Chemicals: Deuterated chloroform ( $\text{CDCl}_3$ , 99.8% D from Sigma-Aldrich), deuterated 1,1,2,2-tetrachloroethane ( $\text{C}_2\text{D}_2\text{Cl}_4$ , 99.5% D from Sigma-Aldrich), 1,4-dioxan-2-one (Dioxanone, DX, from Ethicon),  $\epsilon$ -caprolactone (CL, 99% from Fluka), ethylene diamine (99% from Sigma Aldrich), were used as purchased from the respective supplier. L-lactide (from Purac) was sublimed at 90 °C and then transferred into a  $\text{N}_{2(g)}$  atmosphere glove box for further use. Biologic hydroxyapatite was derived from bovine femur (Premium Protein Products in Lincoln, Nebraska).

Methodology: Biologically derived hydroxyapatite bone plugs, were prepared by extracting bovine bone and then sintering it as described on page 47 in Chapter 2. (Figure 6.4) Plugs were machined into cylinders by the method set forth in chapter 3 on page 124.



Figure 6.4. Extraction of bovine bone plugs used in the manufacture of compression and torsional test devices



The next step in creating specimens for compression or torsional testing was to sinter the extracted bone plugs in a manner that best duplicates methods used to sinter powder samples. Extracted bone plugs, were placed into crucibles and then the crucibles were placed into a preheated muffle furnace and allowed to sinter in air for a specified time. The plugs were allowed to cool in a vacuum desiccator under vacuum at 50 millitorr. The plugs were then transferred into a  $N_{2(g)}$  atmosphere glove box.

Some samples were also sintered under vacuum. Roughly 7 bone plugs were placed into a ½ inch inner diameter quartz tube. The tube was then directly attached to a vacuum pump and placed under vacuum at 50 millitorr. The tube was then lowered into the preheated muffle furnace until all of the plugs were well into the chamber. Approximately 9 inches of quartz tube was left to protrude from the top of the furnace. This allowed for the vacuum tube to stay cool and not compromise the seal. The plugs were then sintered for a specified time. The sintered plugs were transferred into a vacuum desiccator and cooled under hard vacuum at 50 millitorr. The plugs were then transferred into a  $N_{2(g)}$  atmosphere glove box.

The sintered plugs were then placed into small pieces of PTFE tubing which acted as a sleeve around the plug. The plug and sleeve were then placed into a 12 mm outer diameter, medium wall glass tube that is approximately 12 inches long. To this, roughly 1.3 times the mass of the plug of the desired monomer was added. A ¾ inch piece of latex tubing was fitted over the top of the glass tube. A pinch clamp was placed on the latex tube to seal it. The entire setup was transferred out of the box and attached to a vacuum manifold. The piece of latex tubing was placed over the brass nipple on the

vacuum manifold and the pinch clamp was slowly removed to expose the interior of the glass tube to vacuum. Removing the pinch clamp too quickly causes the monomer to be pulled into the manifold. The lower two inches of the tube were immersed in liquid nitrogen to ensure that excess heat from sealing the tube would not affect the monomer or bone plug. The tube was allowed to evacuate for five to ten minutes after submersion. An oxy/acetylene torch was used to seal the glass tube so that the monomer and bone plug were under vacuum. The torch was used to put two small indentions on opposite sides of the tube so that the plug could not slide past the center point of the tube after sealing. The tube was then placed into a 130 °C convection oven for L-lactide so that the bone plug was completely surrounded by molten monomer. As soon as the viscosity of the excess monomer had thickened to the point where it had the consistency of honey, a period which averaged approximately 4 days for samples sintered at 700 °C for 16 hours, the tube was inverted to allow the excess to run to the bottom while the plug remained suspended at the indentions. The polymerization reaction was then allowed to run to completion. The tube was taken out of the oven and allowed to cool to room temperature. If the polymer runoff cooled and was cloudy, due to excess monomer content, then the tube was placed back into the oven to continue to react. If the polymer runoff cooled into a clear solid, this was an indication that the reaction had run to completion. Once the bone plugs were finished reacting they were removed from the oven, the tubes were cracked open, and the plugs were removed from their PTFE sleeves.

Compressive properties for the polymer-HA composite cylinders were obtained on an Instron 5967 with a 30 kN load cell. Instrument control, data acquisition, and data processing were performed by Blue Hill version 2.23 proprietary software. Samples were

prepared for compression testing by machining the polymerized bone plugs on a Colchester-Clausing lathe. The rotation speed was set to 800 rpm and the plugs were machined into cylinders with a 1 to 2 diameter to height ratio. The shavings from the machining process were collected and saved for further characterization. The cross head speed for testing was  $1.0 \text{ mm}/\text{min}$  for standard testing. Raw bone samples were machined into cylinders on a lathe with a 1 to 2 diameter to height ratio from cut bone plugs and tested as machined.

Compression tests were run on machined composite cylinders with crosshead speeds of  $0.5 \text{ mm}/\text{min}$  and  $2.0 \text{ mm}/\text{min}$  to explore the viscoelastic properties of a polymer-HA composite.

Torsional studies were performed on an Instron MT1 fitted with a 200 in-lb torque load cell. Instrument control, data processing, and data acquisition were performed by Partner version 8.4d proprietary software. Specimens for torsional testing were prepared on a Colchester-Clausing lathe set at 800 rpm. The plugs were machined into cylinders with a recess cut out of the center (Figure 6.5). This recess was the weakest portion of the sample, consequently the dimensions of the recess were used as the test specimen dimensions. (Figure 6.5) The turn rate for testing was  $0.5 \text{ rev}/\text{min}$ . Raw bone samples were machined on a lathe in the same manner as the polymerized plugs and were tested as machined.

Gel permeation chromatography (GPC) was employed to determine the polymer molecular weights of the devices used in compression and torsion testing. GPC is a chromatographic separation technique based on the hydrodynamic volume of the analyte.

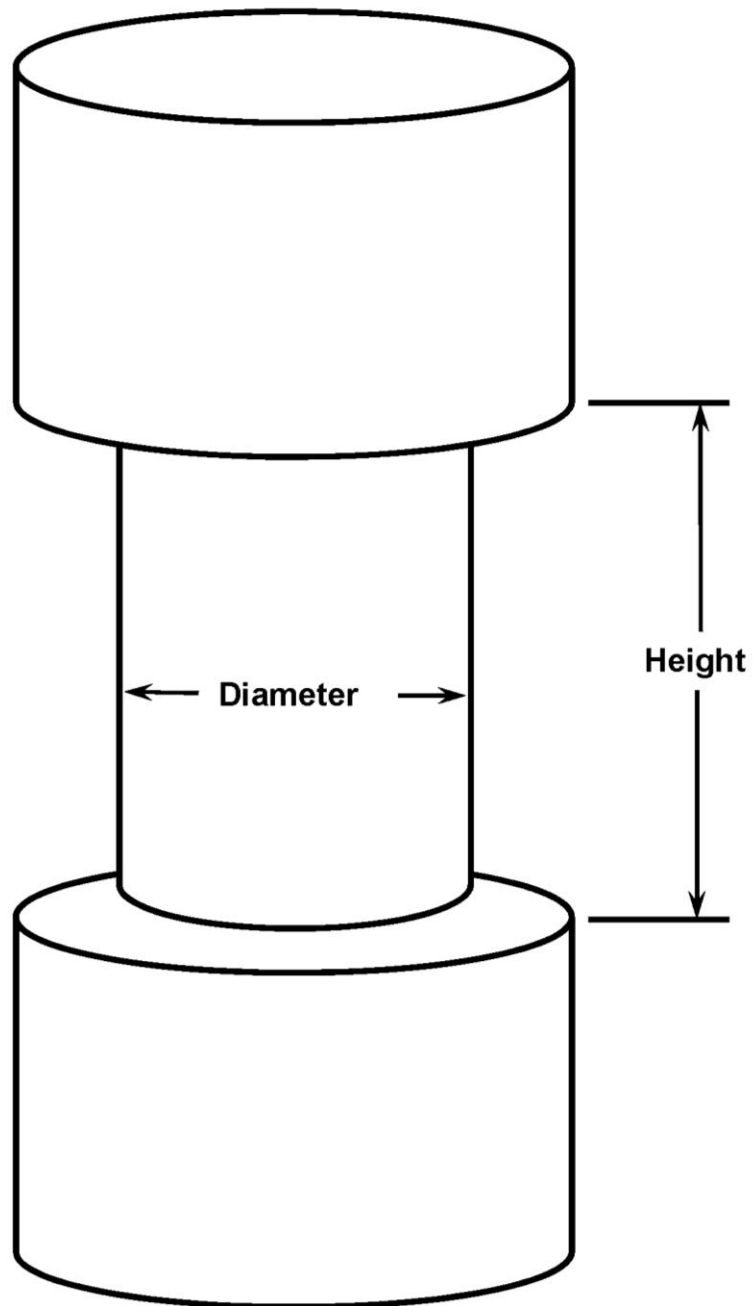


Figure 6.5. Representative diagram of devices used for torsional testing

Smaller molecules are trapped in the pores in the stationary phase while larger molecules remain in the mobile phase and pass through the column. For molecular weight determinations of PLLA the mobile phase was tetrahydrofuran (THF). The instrument was a Viscotek VE2001 GPCmax with a Jordi Gel DVB 10,000A column heated to 35 °C in an Eldex CH-150 column heater. The exclusion limit of the column was 400,000 Da. The detector was a VE3580 refractive index detector also manufactured by Viscotek. The flow rate was 1.0 ml/min. Polystyrene standards with molecular weights from 1,000 Da to 150,000 Da with polydispersity indices of less than 1.2 were used to build a requisite calibration curve. A second order fit was used to construct the calibration curve. (Figure 6.6)

### Results and Discussion

Compression and torsion tests were run on raw bone to establish a base line. (Figures 6.7 and 6.8) The modulus of elasticity for raw bovine cortical bone was measured to be  $13.5 \pm 0.9$  GPa. This is slightly lower than the literature reported for human femoral bone of 17.2 GPa. The compressive strength of tested bovine samples was  $291 \pm 23$  MPa, which is higher than the value reported of 167 MPa for human bone. (Table 6.1)

The modulus of rigidity for raw bovine bone was measured as  $3.91 \pm 0.80$  GPa. The bone samples exhibited the traditional brittle failure in both compression and torsion. These values are used as the basis for comparison for the polymer composite devices created. For a relative scale, the shear modulus of steel is a 79.3 GPa and it exhibits a brittle failure. Polyethylene has a shear modulus of 0.117 GPa but its failure mode is elastic.

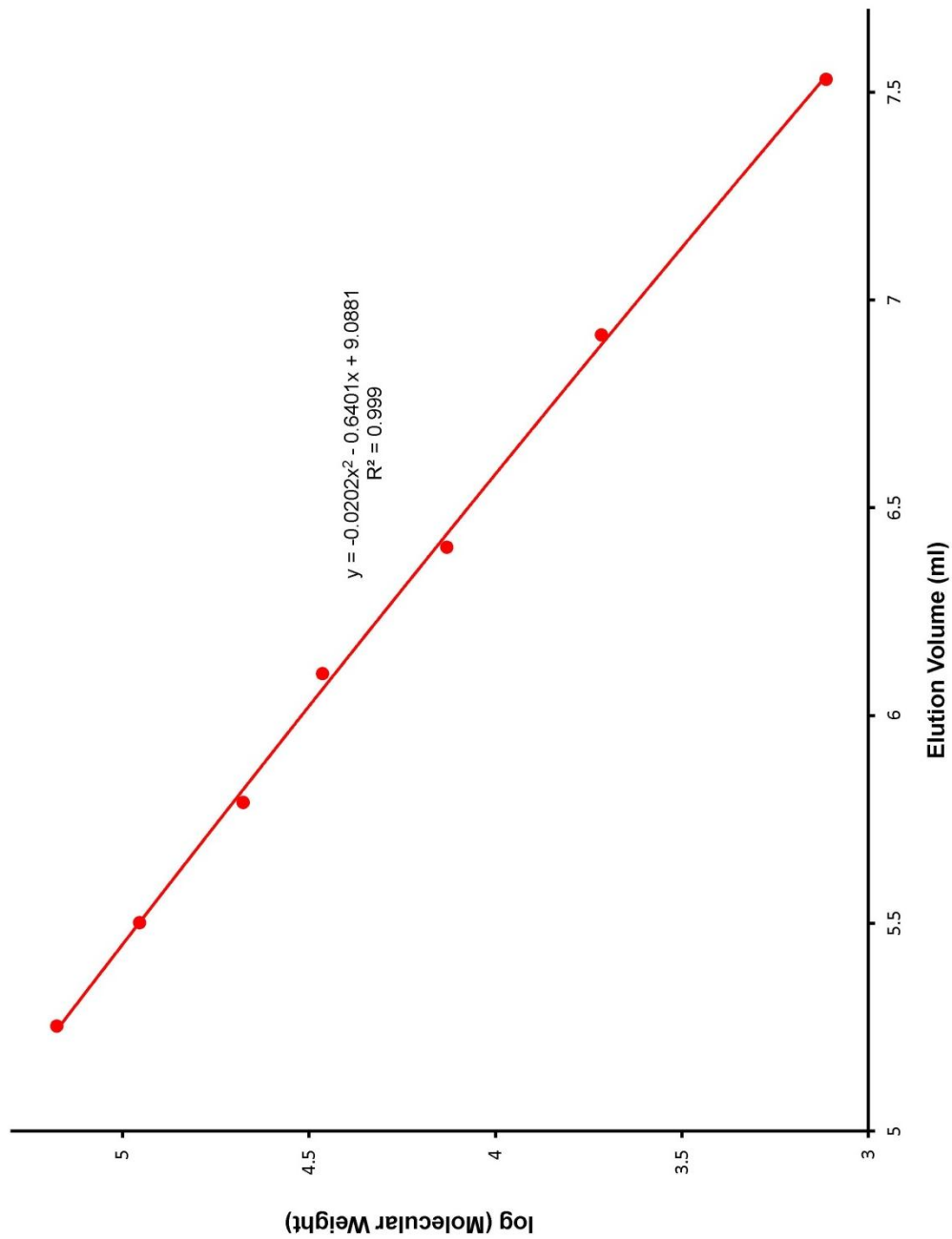


Figure 6.6. GPC calibration curve using 150,000 Da, 90,000 Da, 47,500 Da, 29,100 Da, 13,500 Da, 5200 Da, and 1300 Da polystyrene standards

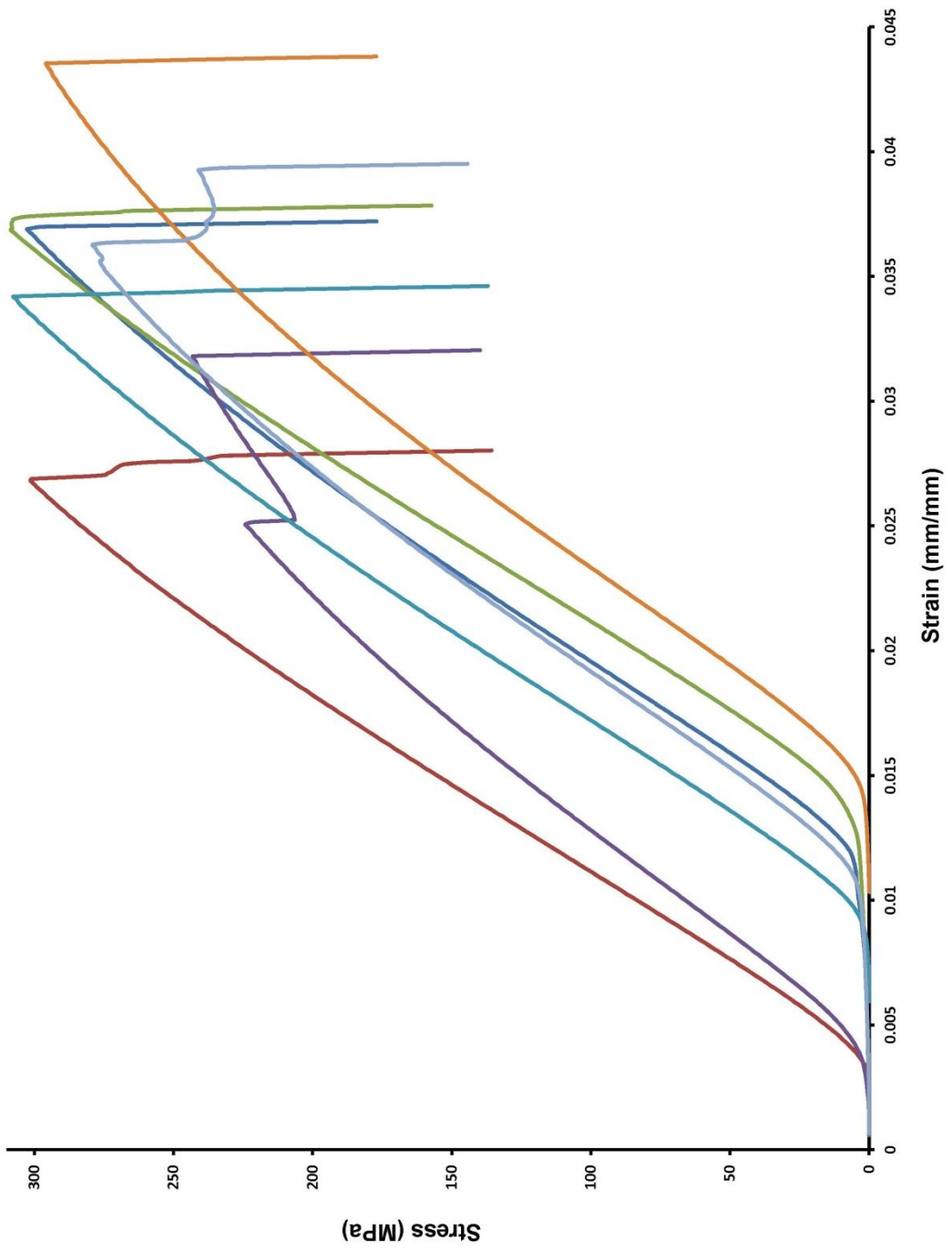


Figure 6.7. Compressive stress strain curves for raw bovine bone

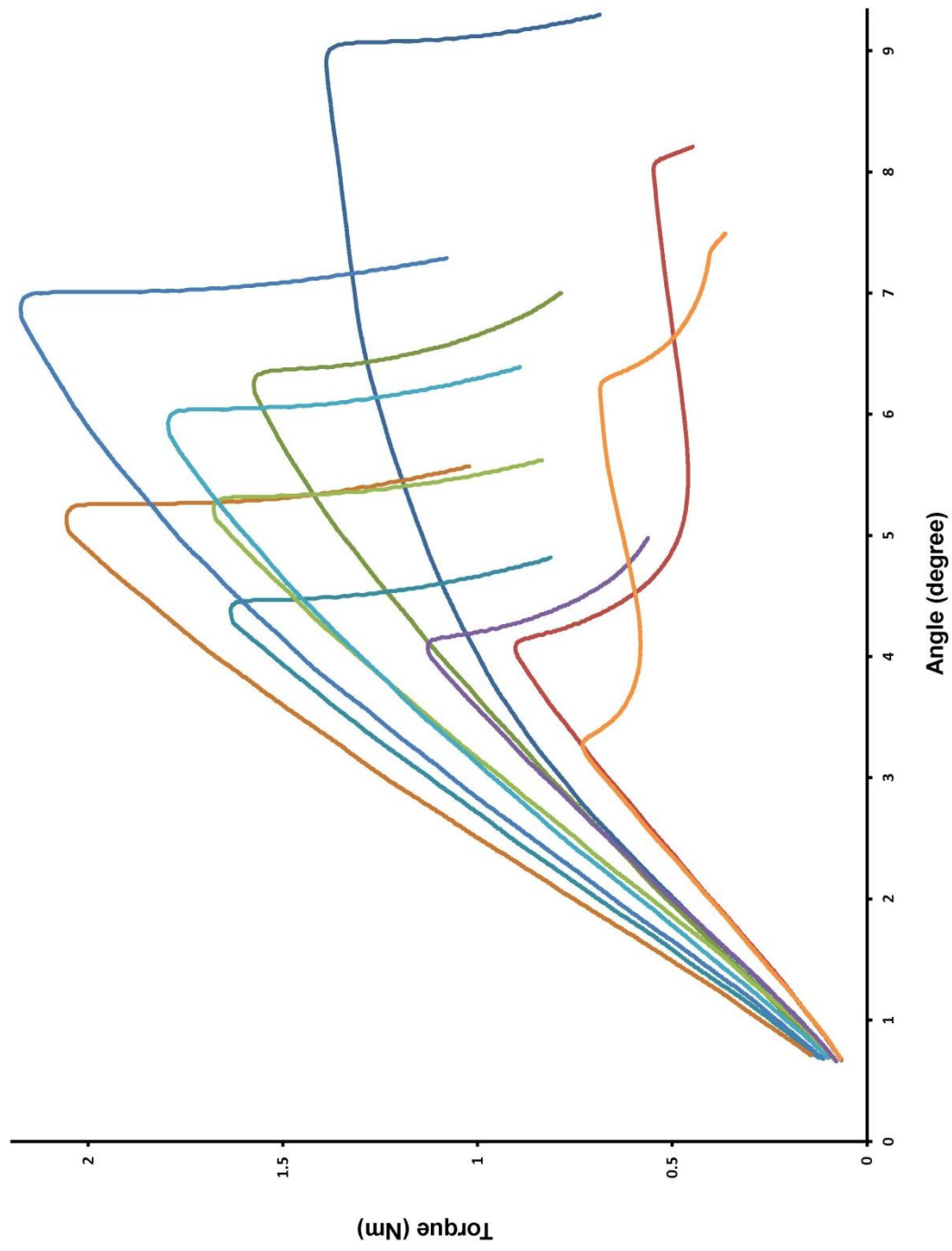


Figure 6.8. Torsion plots for raw bovine bone



| Sample | Height (mm) | Diameter (mm)      | Compressive Strength (MPa) | Modulus of Elasticity (GPa) |
|--------|-------------|--------------------|----------------------------|-----------------------------|
| 1      | 11.85       | 5.87               | 303                        | 13.7                        |
| 2      | 11.75       | 5.89               | 301                        | 14.3                        |
| 3      | 12.13       | 5.96               | 309                        | 14.5                        |
| 4      | 11.97       | 6.05               | 243                        | 12.1                        |
| 5      | 11.53       | 5.70               | 308                        | 13.9                        |
| 6      | 10.96       | 5.42               | 296                        | 12.8                        |
| 7      | 10.57       | 5.55               | 279                        | 13.0                        |
|        |             | Average            | 291                        | 13.5                        |
|        |             | Standard Deviation | 23                         | 0.9                         |

| Sample | Height (mm) | Diameter (mm)      | Peak Torque (Nm) | Modulus of Rigidity (GPa) |
|--------|-------------|--------------------|------------------|---------------------------|
| 1      | 11.63       | 4.93               | 1.389            | 3.65                      |
| 2      | 8.77        | 4.63               | 1.359            | 3.18                      |
| 3      | 10.65       | 5.10               | 1.575            | 2.88                      |
| 4      | 9.63        | 4.84               | 1.200            | 2.26                      |
| 5      | 11.13       | 5.06               | 1.635            | 4.36                      |
| 6      | 10.85       | 5.13               | 2.056            | 4.42                      |
| 7      | 9.44        | 4.95               | 2.174            | 3.84                      |
| 8      | 7.27        | 3.88               | 0.903            | 4.93                      |
| 9      | 11.29       | 4.83               | 1.678            | 4.58                      |
| 10     | 10.07       | 4.59               | 1.128            | 4.33                      |
| 11     | 9.66        | 4.85               | 1.795            | 3.85                      |
| 12     | 5.49        | 3.69               | 0.731            | 4.63                      |
|        |             | Average            | 1.469            | 3.91                      |
|        |             | Standard Deviation | 0.437            | 0.80                      |

Table 6.1. Tabulated compressive and torsional data for raw bovine bone samples

Compression testing for bone plugs that were sintered at 700 °C for 16 hours in air and then polymerized, yielded a compressive strength of  $194 \pm 26$  MPa and an elastic modulus of  $8.85 \pm 0.49$  MPa when tested with a cross head speed of  $1.0 \text{ mm}/\text{min}$ . (Table 6.2) The compression value is lower than the initial raw bovine cortical bone, but it is notable that this value exceeds accepted values for human cortical bone. The elastic modulus is much lower than that of either the raw bovine bone or the reported values for human bone.

Composite devices created from bone plugs sintered for 16 hours at 675 °C in air gave a compressive strength of  $212 \pm 62$  MPa and an elastic modulus of  $13.2 \pm 1.7$  GPa when tested with a cross head speed of  $1.0 \text{ mm}/\text{min}$ . (Table 6.3) The compressive strength is not statistically different than that of the 700 °C samples but the elastic modulus is much higher.

Polymerized bone plugs were also made from samples sintered at 600 °C for 8 days in vacuum. The extended sintering time was necessary to remove all the carbonaceous organic material. The compressive strength of these samples was  $213 \pm 65$  MPa and the elastic modulus was  $12.7 \pm 0.8$  GPa. (Table 6.4) These values are not statistically different than those obtained for the samples sintered at 675 °C.

Torsion tests were also performed on devices manufactured from bovine bone plugs sintered at the three afore mentioned sets of conditions. Plugs sintered at 700 °C for 16 hours in air yielded devices with a modulus of rigidity of  $3.13 \pm 0.65$  GPa. This value is slightly lower than the value for wet bovine bone. The samples sintered at 675 °C for 16 hours in air gave devices with a modulus of rigidity of  $3.98 \pm 1.14$  GPa. This mean value

| Sample | Height (mm) | Diameter (mm)      | Compressive Strength (MPa) | Modulus of Elasticity (GPa) | M <sub>n</sub> (Da) | M <sub>w</sub> (Da) | PDI |
|--------|-------------|--------------------|----------------------------|-----------------------------|---------------------|---------------------|-----|
| 1      | 12.15       | 6.28               | 217                        | 9.00                        | 4,600               | 8,600               | 1.9 |
| 2      | 12.01       | 6.29               | 217                        | 8.61                        | 4,200               | 8,400               | 2.0 |
| 3      | 12.73       | 6.23               | 167                        | 9.28                        | 3,000               | 5,800               | 1.9 |
| 4      | 11.18       | 6.28               | 226                        | 9.06                        | 4,100               | 7,500               | 1.8 |
| 5      | 10.53       | 6.30               | 160                        | 7.73                        | 4,400               | 7,700               | 1.8 |
| 6      | 12.03       | 6.29               | 171                        | 8.42                        | 4,600               | 8,600               | 1.9 |
| 7      | 12.05       | 6.28               | 169                        | 8.90                        | 4,100               | 7,100               | 1.7 |
| 8      | 11.86       | 6.27               | 225                        | 9.21                        | 2,000               | 4,100               | 2.1 |
| 9      | 11.80       | 6.26               | 202                        | 9.33                        | 4,000               | 7,900               | 2.0 |
| 10     | 11.65       | 6.29               | 181                        | 8.97                        | 4,400               | 9,000               | 2.0 |
|        |             | Average            | 194                        | 8.85                        | 3,900               | 7,500               | 1.9 |
|        |             | Standard Deviation | 26                         | 0.49                        | 820                 | 1,500               | 0.1 |

| Sample | Height (mm) | Diameter (mm)      | Peak Torque (Nm) | Modulus of Rigidity (GPa) | M <sub>n</sub> (Da) | M <sub>w</sub> (Da) | PDI |
|--------|-------------|--------------------|------------------|---------------------------|---------------------|---------------------|-----|
| 1      | 8.12        | 4.43               | 0.484            | 2.55                      | 4,400               | 8,900               | 2.0 |
| 2      | 8.72        | 4.61               | 0.540            | 2.44                      | 5,000               | 9,100               | 1.8 |
| 3      | 8.12        | 5.03               | 0.428            | 3.32                      | 3,100               | 7,100               | 2.3 |
| 4      | 8.19        | 4.65               | 0.552            | 3.36                      | 3,900               | 7,300               | 1.9 |
| 5      | 8.84        | 4.62               | 0.674            | 3.51                      | 4,700               | 8,600               | 1.8 |
| 6      | 7.78        | 4.66               | 0.424            | 4.23                      | 5,100               | 9,200               | 1.8 |
| 7      | 7.98        | 4.84               | 0.343            | 3.52                      | 2,300               | 4,500               | 2.0 |
| 8      | 5.61        | 5.43               | 0.826            | 2.12                      | 3,100               | 6,800               | 2.2 |
| 9      | 10.88       | 5.53               | 0.868            | 3.11                      | 4,500               | 8,500               | 1.9 |
|        |             | Average            | 0.571            | 3.13                      | 4,000               | 7,800               | 2.0 |
|        |             | Standard Deviation | 0.183            | 0.65                      | 980                 | 1,500               | 0.2 |

Table 6.2. Tabulated compressive and torsional data for PLLA-HA devices made from bovine bone plugs sintered at 700 °C for 16 hours in air

| Sample | Height (mm) | Diameter (mm)      | Compressive Strength (MPa) | Modulus of Elasticity (GPa) | M <sub>n</sub> (Da) | M <sub>w</sub> (Da) | PDI |
|--------|-------------|--------------------|----------------------------|-----------------------------|---------------------|---------------------|-----|
| 1      | 10.96       | 5.39               | 317.08                     | 14.9                        | 3,800               | 12,000              | 3.2 |
| 2      | 11.86       | 5.84               | 221.89                     | 13.6                        | 4,200               | 14,000              | 3.3 |
| 3      | 11.05       | 5.44               | 177.06                     | 11.7                        | 4,300               | 14,000              | 3.3 |
| 4      | 10.56       | 5.19               | 243.6                      | 14.7                        | 5,000               | 17,000              | 3.4 |
| 5      | 10.69       | 5.31               | 118.75                     | 10.2                        | 4,500               | 15,000              | 3.3 |
| 6      | 10.33       | 5.22               | 220.47                     | 13.0                        | 3,300               | 13,000              | 3.9 |
| 7      | 11.71       | 5.85               | 187.52                     | 14.1                        | 4,600               | 16,000              | 3.5 |
|        |             | Average            | 212                        | 13.2                        | 4,200               | 14,000              | 3.4 |
|        |             | Standard Deviation | 62                         | 1.7                         | 560                 | 1,700               | 0.3 |

| Sample | Height (mm) | Diameter (mm)      | Peak Torque (Nm) | Modulus of Rigidity (GPa) | M <sub>n</sub> (Da) | M <sub>w</sub> (Da) | PDI |
|--------|-------------|--------------------|------------------|---------------------------|---------------------|---------------------|-----|
| 1      | 6.13        | 4.54               | 0.826            | 4.23                      | 5,000               | 19,000              | 3.8 |
| 2      | 6.7         | 4.86               | 0.879            | 4.25                      | 5,600               | 17,000              | 3.0 |
| 3      | 5.73        | 4.52               | 0.143            | 1.79                      | 4,800               | 16,000              | 3.3 |
| 4      | 4.97        | 4.15               | 0.729            | 3.51                      | 5,700               | 19,000              | 3.3 |
| 5      | 6.8         | 4.91               | 0.943            | 4.67                      | 4,800               | 15,000              | 3.1 |
| 6      | 5.45        | 4.52               | 0.289            | 3.23                      | 5,100               | 16,000              | 3.1 |
| 7      | 6.48        | 4.77               | 0.916            | 4.60                      | 4,700               | 15,000              | 3.2 |
| 8      | 6.78        | 5.06               | 1.129            | 5.58                      | 3,800               | 13,000              | 3.4 |
|        |             | Average            | 0.732            | 3.98                      | 5,000               | 16,000              | 3.3 |
|        |             | Standard Deviation | 0.340            | 1.14                      | 590                 | 2,000               | 0.2 |

Table 6.3. Tabulated compressive and torsional data for PLLA-HA devices made from bovine bone plugs sintered at 675 °C for 16 hours in air

| Sample | Height (mm) | Diameter (mm)      | Compressive Strength (MPa) | Modulus of Elasticity (GPa) | M <sub>n</sub> (Da) | M <sub>w</sub> (Da) | PDI |
|--------|-------------|--------------------|----------------------------|-----------------------------|---------------------|---------------------|-----|
| 1      | 9.64        | 4.85               | 203                        | 12.9                        | 5,700               | 31,000              | 5.4 |
| 2      | 11.62       | 5.71               | 234                        | 13.6                        | 6,900               | 35,000              | 5.1 |
| 3      | 10.91       | 5.39               | 255                        | 12.2                        | 5,500               | 32,000              | 5.8 |
| 4      | 11.02       | 5.40               | 130                        | 12.5                        | 5,700               | 26,000              | 4.6 |
| 5      | 12.05       | 5.93               | 307                        | 13.7                        | 5,800               | 33,000              | 5.7 |
| 6      | 11.43       | 5.61               | 269                        | 11.7                        | 6,200               | 33,000              | 5.3 |
| 7      | 11.09       | 5.43               | 245                        | 13.0                        | 6,500               | 32,000              | 4.9 |
| 8      | 11.78       | 5.75               | 133                        | 12.7                        | 6,500               | 36,000              | 5.5 |
| 9      | 12.00       | 5.86               | 141                        | 11.5                        | 5,800               | 26,000              | 4.5 |
|        |             | Average            | 213                        | 12.7                        | 6,100               | 32,000              | 5.2 |
|        |             | Standard Deviation | 65                         | 0.8                         | 480                 | 3,500               | 0.5 |

| Sample | Height (mm) | Diameter (mm)      | Peak Torque (Nm) | Modulus of Rigidity (GPa) | M <sub>n</sub> (Da) | M <sub>w</sub> (Da) | PDI |
|--------|-------------|--------------------|------------------|---------------------------|---------------------|---------------------|-----|
| 1      | 7.87        | 5.00               | 0.494            | 4.44                      | 5,600               | 32,000              | 5.7 |
| 2      | 6.95        | 4.74               | 0.189            | 3.52                      | 6,600               | 31,000              | 4.7 |
| 3      | 5.39        | 5.01               | 0.863            | 5.44                      | 6,100               | 34,000              | 5.6 |
| 4      | 5.06        | 4.51               | 0.575            | 4.86                      | 6,400               | 32,000              | 5.0 |
| 5      | 5.58        | 4.72               | 0.597            | 6.02                      | 5,900               | 31,000              | 5.3 |
| 6      | 6.25        | 4.85               | 0.491            | 3.97                      | 5,800               | 34,000              | 5.9 |
|        |             | Average            | 0.535            | 4.71                      | 6,100               | 32,000              | 5.4 |
|        |             | Standard Deviation | 0.217            | 0.93                      | 380                 | 1,400               | 0.4 |

Table 6.4. Tabulated compressive and torsional data for PLLA-HA devices made from bovine bone plugs sintered at 600 °C for 8 days in vacuum

is more in line with the value for wet bone but the large standard deviation shows that at the 95% confidence level it is not statistically different than the value obtained for samples sintered at 700 °C. Finally the samples sintered at 600 °C in vacuum gave a modulus of  $4.71 \pm 0.93$  GPa. This torsional value is higher than the moduli for the other PLLA-HA devices produced.

Standard compression tests were conducted to examine the viscoelastic properties of the devices manufactured where the rate at which the stress was applied was varied. Three different crosshead speeds were tested. Each speed was double the previous speed. The first rate tested was  $0.5 \text{ mm}/\text{min}$ . This tested yielded an elastic modulus of  $9.39 \pm 1.25$  GPa. Samples tested at  $1.0 \text{ mm}/\text{min}$  and  $2.0 \text{ mm}/\text{min}$  gave elastic moduli of  $8.85 \pm 0.49$  GPa and  $8.73 \pm 1.50$  GPa respectively. (Table 6.5) All three of these results are statistically equivalent showing that PLLA-HA composite material produced will respond to stresses applied at different rates in the same manner. This is important since implants are subjected to a variety of loading rates from the lowest that occurs while a recipient is standing in place to more severe loading that would result from the recipient running.

Several sintering treatments for bovine bone plugs were tested with a PLLA reinforcing polymer.  $^1\text{H}$  NMR spectroscopy, and molecular weight determinations were performed on all samples. The  $^1\text{H}$  NMR spectra for all PLLA-HA devices manufactured were comparable. The percent polymerization ( $P\%$ ) was calculated for all samples and varied from 95% to 98% completion. (Figure 6.9) The percent polymerization was calculate by

$$P\% = \frac{I_P + I_C + I_A}{I_P + I_C + I_A + I_M} \times 100 \quad (6.11)$$

| 2.0 mm/min |             |                    |                            |                             |        |                    | 0.5 mm/min    |                            |                             |        |             |               |                            |                             |
|------------|-------------|--------------------|----------------------------|-----------------------------|--------|--------------------|---------------|----------------------------|-----------------------------|--------|-------------|---------------|----------------------------|-----------------------------|
| Sample     | Height (mm) | Diameter (mm)      | Compressive Strength (MPa) | Modulus of Elasticity (GPa) | Sample | Height (mm)        | Diameter (mm) | Compressive Strength (MPa) | Modulus of Elasticity (GPa) | Sample | Height (mm) | Diameter (mm) | Compressive Strength (MPa) | Modulus of Elasticity (GPa) |
| 1          | 11.79       | 5.61               | 162                        | 9.83                        | 1      | 11.28              | 5.57          | 155                        | 8.74                        | 2      | 10.53       | 5.65          | 186                        | 10.24                       |
| 2          | 11.64       | 5.72               | 110                        | 6.32                        | 2      | 11.81              | 5.83          | 181                        | 10.51                       | 3      | 11.12       | 5.49          | 162                        | 7.36                        |
| 3          | 10.93       | 5.36               | 93                         | 7.98                        | 3      | 11.94              | 5.81          | 176                        | 10.51                       | 4      | 11.71       | 5.74          | 161                        | 11.08                       |
| 4          | 11.20       | 5.49               | 76                         | 7.27                        | 4      | 11.58              | 5.71          | 138                        | 8.50                        | 5      | 11.54       | 5.68          | 163                        | 8.44                        |
| 5          | 10.10       | 5.03               | 181                        | 8.05                        | 5      | 11.93              | 6.00          | 159                        | 9.10                        | 6      | Average     |               | 165                        | 9.39                        |
| 6          | 11.65       | 5.73               | 202                        | 9.58                        | 6      | Standard Deviation |               | 15                         | 1.25                        | 7      |             |               |                            |                             |
| 7          | 11.71       | 5.61               | 120                        | 10.08                       | 7      |                    |               |                            |                             | 8      |             |               |                            |                             |
| 8          | 11.92       | 5.82               | 207                        | 11.01                       | 8      |                    |               |                            |                             | 9      |             |               |                            |                             |
| 9          | 11.74       | 5.78               | 140                        | 8.45                        | 9      |                    |               |                            |                             |        |             |               |                            |                             |
|            |             | Average            | 143                        | 8.73                        |        |                    |               |                            |                             |        |             |               |                            |                             |
|            |             | Standard Deviation | 48                         | 1.50                        |        |                    |               |                            |                             |        |             |               |                            |                             |

| 1.0 mm/min |             |                    |                            |                             |
|------------|-------------|--------------------|----------------------------|-----------------------------|
| Sample     | Height (mm) | Diameter (mm)      | Compressive Strength (MPa) | Modulus of Elasticity (GPa) |
| 1          | 12.15       | 6.28               | 217                        | 9.00                        |
| 2          | 12.01       | 6.29               | 217                        | 8.61                        |
| 3          | 12.73       | 6.23               | 167                        | 9.28                        |
| 4          | 11.18       | 6.28               | 226                        | 9.06                        |
| 5          | 10.53       | 6.30               | 160                        | 7.73                        |
| 6          | 12.03       | 6.29               | 171                        | 8.42                        |
| 7          | 12.05       | 6.28               | 169                        | 8.90                        |
| 8          | 11.86       | 6.27               | 225                        | 9.21                        |
| 9          | 11.80       | 6.26               | 202                        | 9.33                        |
| 10         | 11.65       | 6.29               | 181                        | 8.97                        |
|            |             | Average            | 194                        | 8.85                        |
|            |             | Standard Deviation | 26                         | 0.49                        |

Table 6.5. Tabulated compressive data for PLLA-HA devices made from bone plugs sintered at 700 °C for 16 hours in air with cross head speeds of 2.0 mm/min, 1.0 mm/min, and 0.5 mm/min

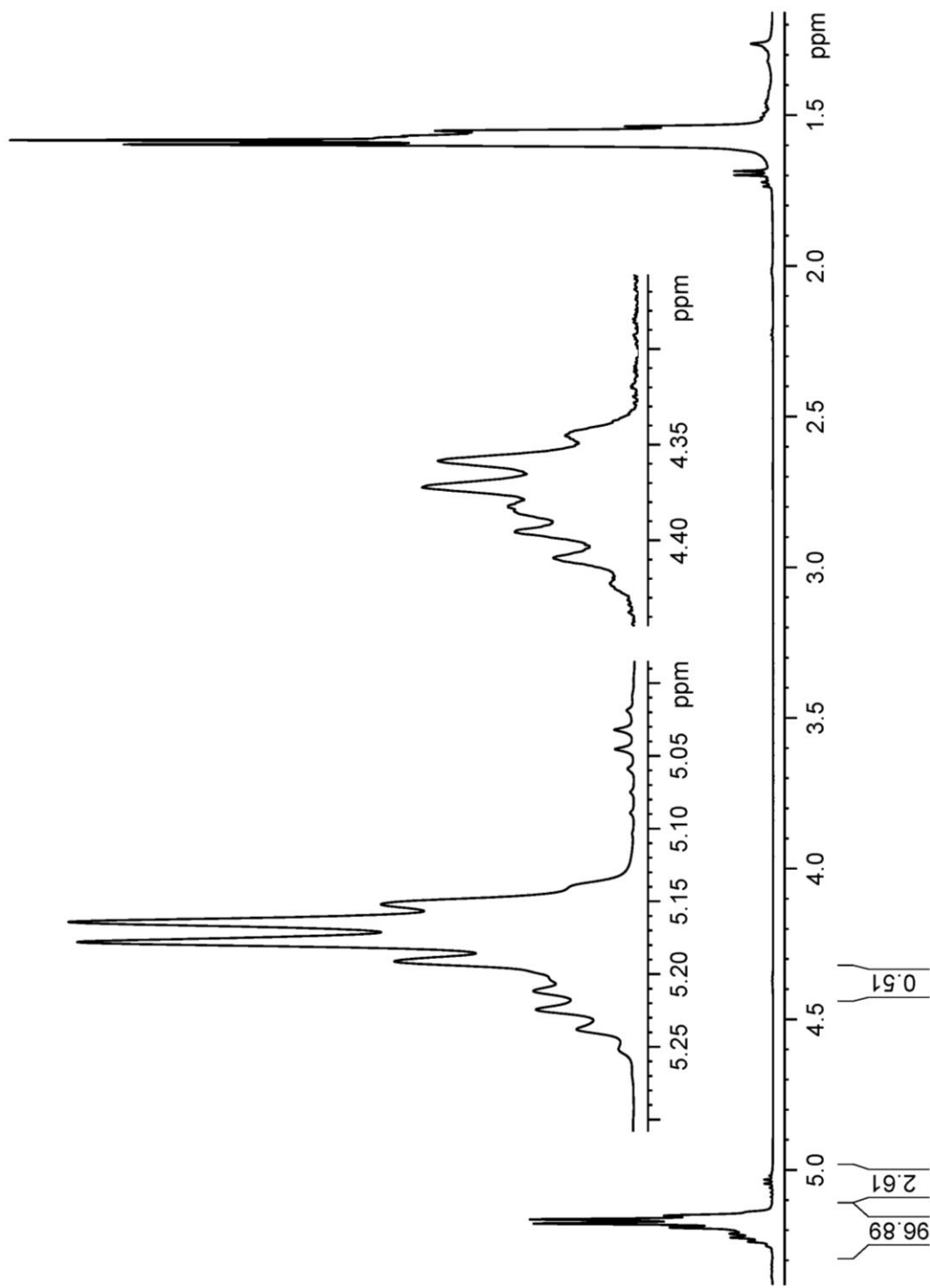


Figure 6.9. Representative  $^1\text{H}$  NMR spectrum of a polymerized bone plug showing over 97% polymerization



GPC analysis of the molecular weights from the devices made by the three different sintering methods does show some differences in the methods. Samples sintered at 700 °C for 16 hours in air took 7 days to completely polymerize. Samples sintered at 675 °C needed 14 days to react completely, and the samples sintered at 600 °C for 8 days in vacuum took 9 weeks to polymerize. These extended reaction times appear to affect the molecular weight distributions of the resulting polymer in the test devices. The 700 °C samples gave a  $M_n$  of  $4000 \pm 800$  Da and  $M_w$  of  $7600 \pm 1500$  Da for a PDI of  $1.9 \pm 0.1$ . The samples sintered at 675 °C had a  $M_n$  of  $4600 \pm 660$  Da and a  $M_w$  of  $15,400 \pm 2100$  Da which yields a PDI of  $3.4 \pm 0.2$ . For these two sintering conditions the  $M_n$  are statistically indistinguishable but the  $M_w$  values differ by a factor of roughly two. The similar  $M_n$  values show that the overall number of polymer chains has not increased between the 700 °C and 675 °C samples. Commutatively this means that the number of initiating sites must also be similar. The large difference in  $M_w$  illustrates that there is great difference in the molecular weight distributions between the two sample sets. This is also evident from the PDI values.

From previous chapters it was established that there is a much higher surface area for HA sintered at 675 °C for 16 hours than for HA sintered at 700 °C at 16 hours. It was also shown via FTIR that not all of the carbonate had decomposed to hydroxide and oxide at 675 °C as it had at 700 °C. This higher surface area, combined with a lower nucleophile surface density at 675 °C must result in an overall number of initiation sites that is the same for the 700 °C material and the 675 °C material. The lengthened reaction time results in a larger distribution of molecular weights. This is most likely due to chain scission and chain transfer reactions.<sup>14, 15</sup> (Figure 6.10)

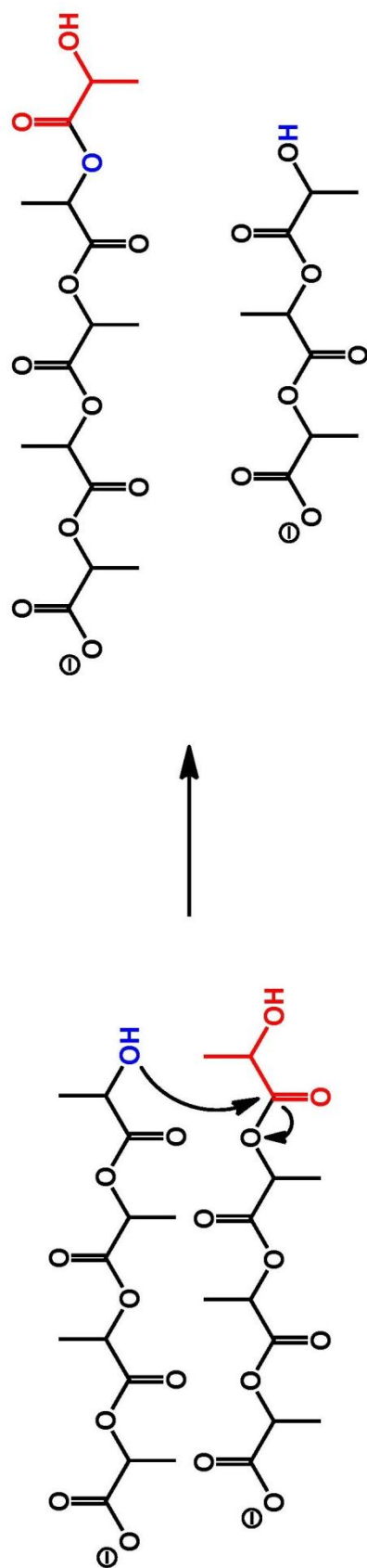


Figure 6.10. Mechanism showing transesterification chain transfer resulting in increased molecular weight distribution

The samples sintered at 600 °C under vacuum had a  $M_n$  of  $6100 \pm 430$  Da and  $M_w$  of  $32,000 \pm 2800$  Da. This gives a PDI of  $5.3 \pm 0.5$ . The increased  $M_n$  shows that there are few initiation sites present in the 600 °C hydroxyapatite than at either the 700 °C or 675 °C materials. With longer reaction time came a wider distribution of molecular weights as is attested by the PDI value. From the GPC results it appears that to get higher molecular weight, a material with fewer initiation sites must be used, but this also results in a slower polymerization reaction which requires more time. The longer reaction times serve to increase the distribution of molecular weights. This large distribution may have consequences for the long term strength of an implant and its resorbability.

### References

1. Osswald, T. A.; Menges, G., *Materials Science of Polymers for Engineers*. 2nd ed.; Hanser Gardner Publications: 2003.
2. Brown, R., *Handbook of Polymer Testing: Physical Methods of Plastics Engineering*. 1st ed.; CRC Press: 1999; p 845.
3. Nielsen, L. E.; Landhl, R. F., *Mechanical Properties of Polymers and Composites*. Revised and Expanded Edition ed.; CRC Press: 1993; p 580.
4. Park, J. B., *Biomaterials Science and Engineering*. 1st ed.; Springer: 1984.
5. Yamada, H., *Strength of Biological Materials*. 1st ed.; Williams & Wilkins: 1970.
6. Beer, F. P.; E. Russell Johnston, J.; Dewolf, J. T., *Mechanics of Materials*. 4th ed.; McGraw-Hill Publishing Company: New York, New York, 2006; p 787.
7. International, A., Standard Test Method for Shear Modulus at Room Temperature. In *E143-02*, ASTM International: West Conshohocken, Pennsylvania, 2008; Vol. 3.01.
8. Costi, J. J.; Kelly, A. J.; Hearn, T. C.; Martin, D. K., Comparison of torsional strengths of bioabsorbable screws for anterior cruciate ligament reconstruction. *American Journal of Sports Medicine* **2001**, 29, (5), 575-580.
9. Hiemenz, P. C.; Lodge, T. P., *Polymer Chemistry*. 2nd ed.; CRC Press: 2007; p 608.
10. Rapkin, E. Anorganic bone. 2,968,593, January 17, 1961.
11. Bassett, C. A. L.; Hurley, L. A.; Stinchfield, F. E., Fate of long-term anorganic bone implants. *Transplant Biology* **1962**, 29, 51-5.
12. Williams, J. B.; Irvine, J. W., Jr., Preparation of the inorganic matrix of bone. *Science* **1954**, 119, 771-2.

13. Shaw, M. T.; MacKnight, W. J., *Introduction to Polymer Viscoelasticity*. 3rd ed.; Wiley-Interscience: 2005.
14. Korhonen, H.; Helminen, A.; Seppala, J. V., Synthesis of polylactides in the presence of co-initiators with different numbers of hydroxyl groups. *Polymer* **2001**, *42*, 7541-7549.
15. Mori, T.; Nishida, H.; Shirai, Y.; Endo, T., Effects of chain end structures on pyrolysis of poly(L-lactic acid) containing tin atoms. *Polymer Degradation and Stability* **2004**, *84*, 243-251.

## Chapter Seven

### Preliminary Biologic Compatibility Studies and Early Proof of Concept Prototype Devices

#### Introduction and Background

Previous chapters have been concerned with the specifics of understanding variables that control lactone ring opening polymerizations initiated by hydroxyapatite derived from mammalian bone. A specific goal was the manipulation of these variables to control the physical properties of composite materials. In most cases, the development of orthopedic devices prepared from new materials require a series of biocompatibility studies. Biocompatibility studies are also important to the possible use of my materials as orthopedic devices.

A set of preliminary cell culture studies were initiated to assess the immunological response toward my polymer-HA materials. Macrophages are the primary cells associated with immune response and chronic inflammation. So materials that induce their response are thought to be unsuitable for screening new materials.<sup>1</sup> Fibroblasts are the first cells to attach to implanted materials and are also the first cells present in wound healing.<sup>2</sup> An ideal material would not induce macrophage activity and would not interfere with fibroblast activity.

A biocompatible material is useless unless it can be fashioned into a functional, implantable device. As stated in chapter one, the two most needed implant devices are for segmental defect repair and maxillofacial reconstruction. For segmental bone defects,

one potential method to create a device would be to obtain a section of bone similar in size and shape to the defect and use previously outlined methods of organic material removal and polymerization. If the defect were in the ulna, then a potential source could be bone from a cadaver or pig tibia. This donor bone could easily be converted into a polymer-HA composite suitable for implantation. For maxillofacial reconstruction, a similar process utilizing cadaver bone could be used.

If donor bone is not available or is not desirable an alternative would be to make an injection molded device from a composite material derived from the polymerization initiated by powdered HA. This material could be molded into any shape allowing greater flexibility of use for the surgeon. Standard stock pieces could also be created and stored for later use. These stock pieces could be machined on a lathe or mill into a multitude of shapes to fit the specific need.

### Experimental

Chemicals: Deuterated chloroform ( $\text{CDCl}_3$ , 99.8% D from Sigma-Aldrich), deuterated 1,1,2,2-tetrachloroethane ( $\text{C}_2\text{D}_2\text{Cl}_4$ , 99.5% D from Sigma-Aldrich), 1,4-dioxan-2-one (Dioxanone, DX, from Ethicon), ethylene diamine (99% from Sigma Aldrich), were used as purchased from the respective supplier. L-lactide (from Purac) was sublimed at 90 °C and then transferred into a  $\text{N}_{2(\text{g})}$  atmosphere glove box for further use.

Preparation of samples: Small polymer-HA discs were manufactured for cell culture studies in the following manner. Biologically derived hydroxyapatite plugs were created using the extraction procedure set forth on page 47 in chapter 2 and the polymerization

method used for plugs on page 225 in chapter 6. Polymerizations were carried out at 130 °C for L-lactide or 100 °C for dioxanone.

The polymerized bone plugs were sectioned with a parting tool into discs that were approximately 1.0 mm thick and 6.0 mm in diameter. A Colchester-Clausing lathe was used for the sectioning. The discs were then polished sequentially with 1200 grit wet sandpaper, 3 µm alumina polishing powder, and then finally with 0.5 µm alumina polishing powder. This method produced discs with a smooth surface free of tooling imperfections. The discs were then cleaned ultrasonically in a 50% methanol / 50% water solution to remove any residual polishing compound. A representative SEM image of a PLLA/HA disc, where the HA is derived from a bovine femur, is shown in figure 7.1. Experienced observers might note that the macroscopic structure of the bovine cortical bone is largely conserved.

An additional step was required to prepare polydioxanone (PDX) discs because it was necessary to remove the relatively large quantities of residual dioxanone monomer. The discs were placed in a vacuum sublimator where the pressure was reduced to approximately 50 millitorr. The temperature of the cold finger was set to 0 °C. After seven days of sublimation at room temperature, <sup>1</sup>H NMR spectroscopy showed no presence of residual monomer. (Figure 7.2)

All cell culture studies were performed by Dr. Haiying Yu at the Orthopaedic Research Institute at Via Christi Hospital in Wichita, Kansas. Biocompatibility of composite materials with respect to cell viability and related cellular functions was studied using the cell lines NIH/3T3 fibroblast and Raw 264.7 macrophage. Quantitative (MTT and Real



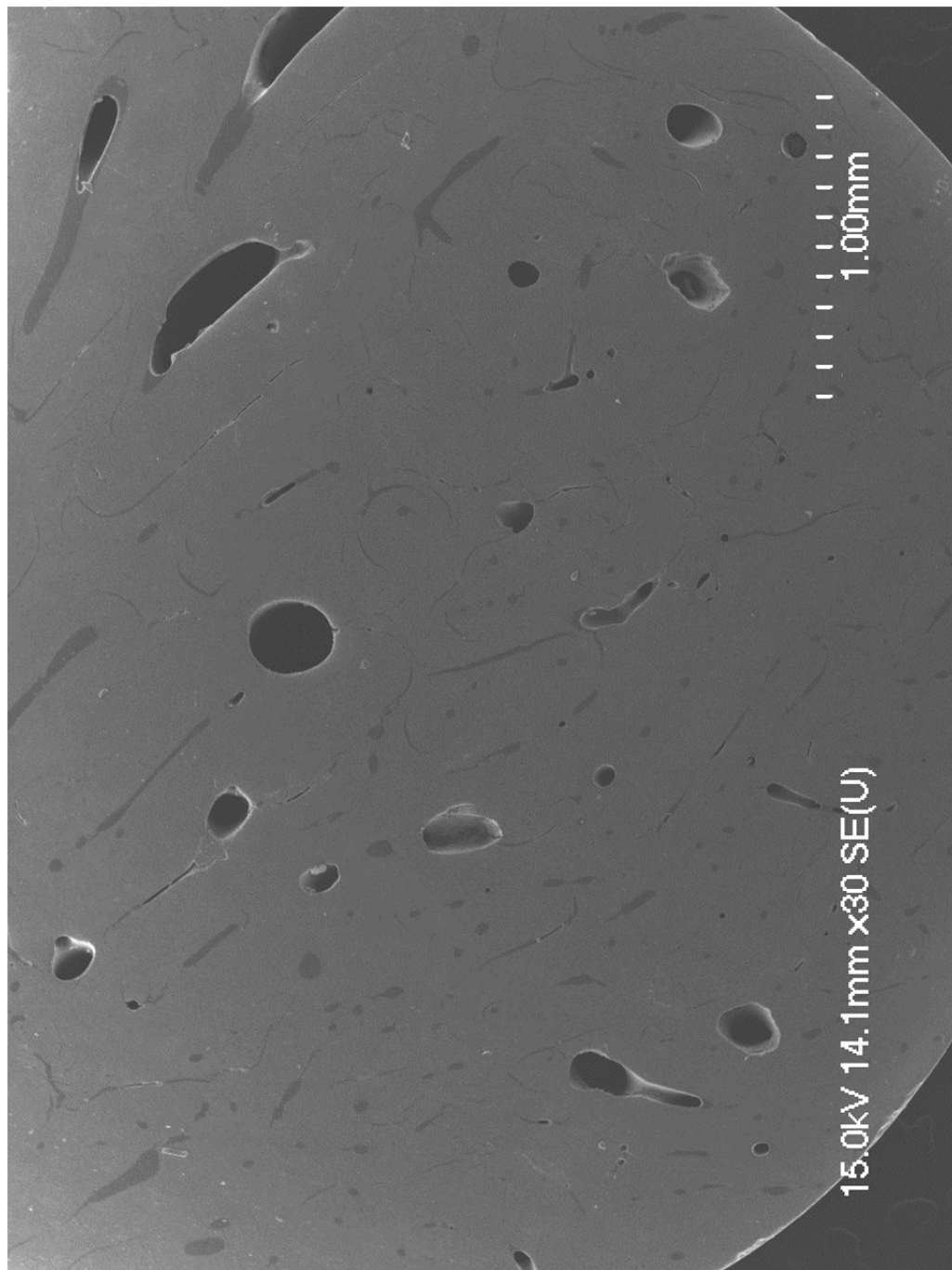


Figure 7.1. Representative SEM image of PLLA-HA discs used for cell culture studies

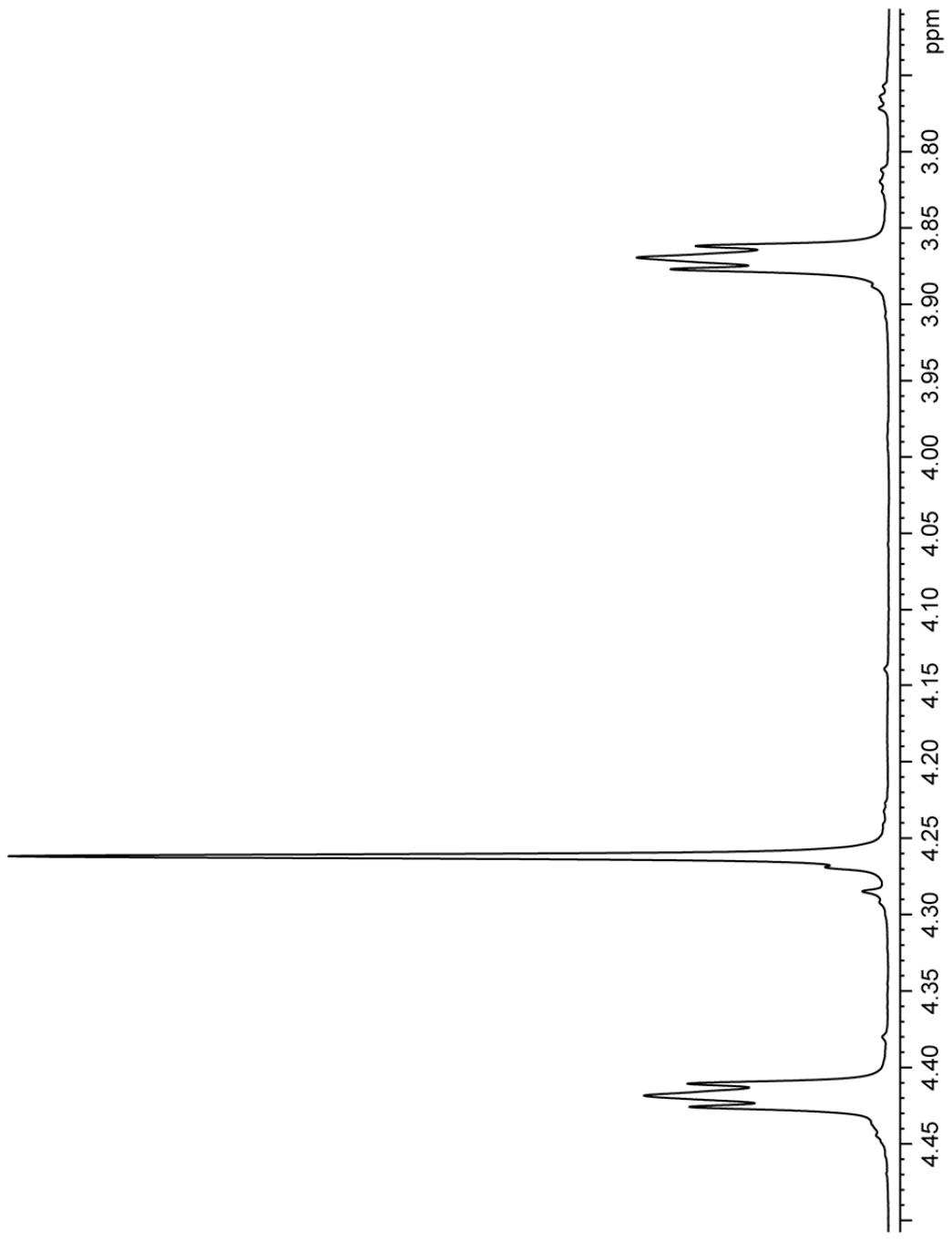


Figure 7.2. Representative <sup>1</sup>H NMR spectrum for a PDX-HA disc used for cell culture studies

time-PCR) and qualitative (SEM) experiments were established to analyze the biological effects of the aforementioned composites to macrophage and fibroblast cells.

Successful polymerization of both the rat femurs and rat skulls shows that this polymerization technology can be applied to more complex shapes that have direct medical applications. Proof of concept prototype devices were manufactured by polymerizing rat femurs and skulls. All organic matter was removed from the constituent bones to prepare them for sintering. This was done using an extraction method similar to the one previously described. One detached rat cranium was placed into a large Soxhlet extractor to extract the skull. Five to seven femurs were extracted in a medium size Soxhlet extractor. After all extractions were completed the skull and femurs were removed from the Soxhlet extractor and allowed to air dry for 24 hours before further processing. Since the rats were juveniles, the skull plates were still discrete bones and needed to be treated with extreme care. Any rigorous motion would cause the skull to lose structural integrity.

The skull and femurs were sintered at 700 °C for 16 hours in air. After the specimens were sintered they were transferred into a  $N_{2(g)}$  atmosphere glove box for further processing. Polymerizations of the skull and femurs were carried out in sealed glass tubes similar to those used in chapter six to create mechanical testing devices. The skull was gently placed into a 35 mm inner diameter glass tube that was about 18 inches long. Roughly 65 g of L-lactide was placed into the tube with the skull. This was far more monomer than was used in the mechanical testing device method, but was necessary to ensure that the skull was completely submerged in monomer. The femurs were sealed in

15 mm inner diameter glass tubes with roughly 4 grams of L-lactide. This is about 15 times more L-lactide than would be needed if producing a bovine bone plug of equal mass. This extra monomer was needed to ensure that the entire femur was submerged during the polymerization reaction. Once the polymerization reactions were completed, the glass tubes were opened and the prototypes were removed for further analysis.

### Results and Discussion

Preliminary cell culture results: Results from the cell culture studies revealed that PLLA-HA, and PCL-HA devices showed the most promise. (Figure 7.3 and 7.4) Each had a low immunologic response when tested with RAW 264.7 macrophages. In comparison to a polystyrene control, there was no increase in expression of the inflammation associated gene interleukin-1  $\beta$  (IL-1  $\beta$ ) and tumor necrosis factor- $\alpha$  (TNF- $\alpha$ ) as determined by polymerase chain reaction (PCR). (Figure 7.5) Additionally, there was no decrease in succinate dehydrogenase activity as tested in the MTT Assay.<sup>3</sup> (Figure 7.6) Succinate dehydrogenase is a mitochondrial enzyme involved in the citric acid and the electron transport chain. Its activity is often used as an indicator for cell viability.<sup>4-7</sup>

These results show that PLLA and PCL composites are good materials for cell growth and do not inhibit cell function. The PDX discs showed no cell growth of either macrophages or fibroblasts. Due to the poor cell viability with PDX, IL-1  $\beta$  and TNF- $\alpha$  were not tested.

Prototype device construction: Successful polymerization of both the rat femurs and rat skulls shows that this polymerization technology can be applied to more complex shapes that have direct medical applications. (Figure 7.7 through 7.12) The process for

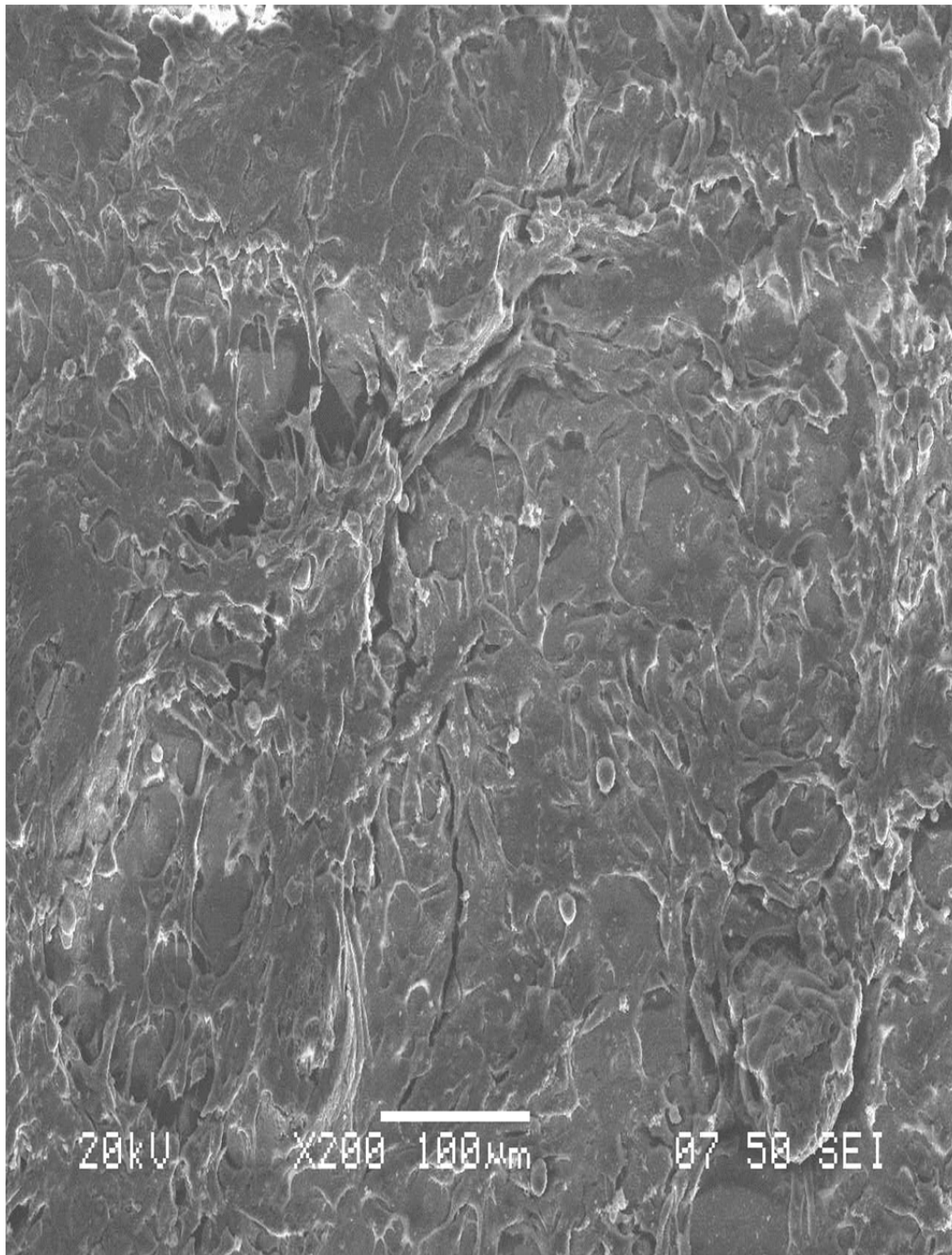


Figure 7.3. SEM image of NIH/3T3 fibroblast cells colonizing a PLLA-HA disc

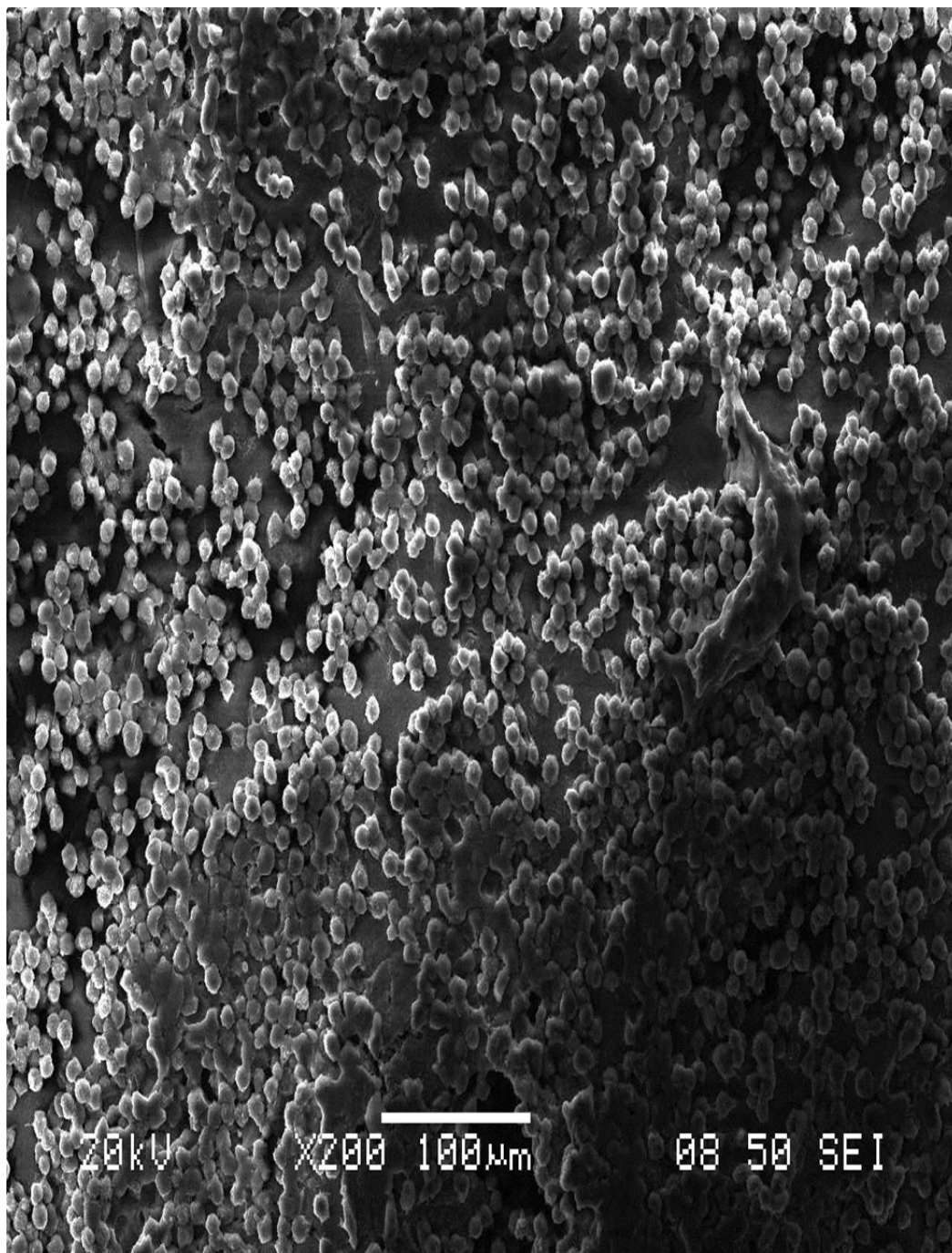


Figure 7.4. SEM image of RAW264.7 macrophage cells colonizing a PLLA-HA disc

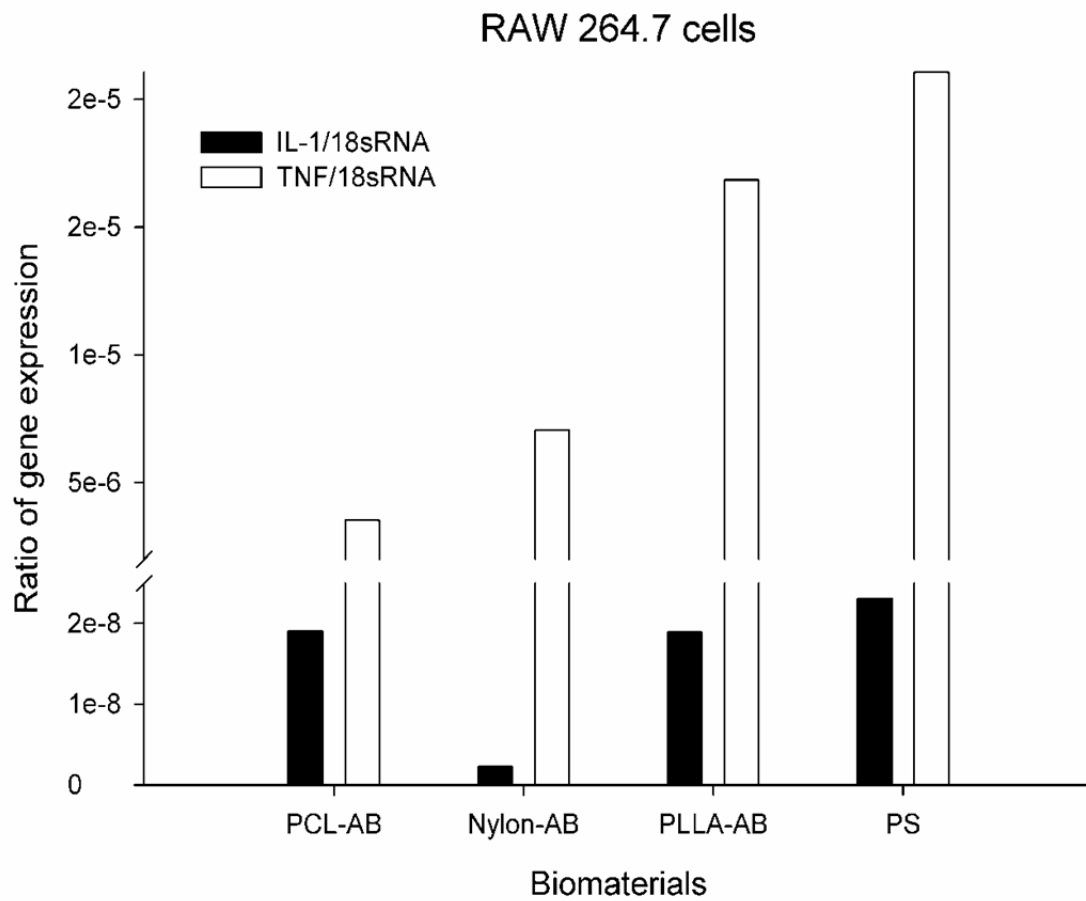


Figure 7.5. Expression of IL-1 $\beta$  and TNF- $\alpha$  in Raw 264.7 cells in response to cell seeding on various polymer-anorganic bone (AB) composites and a PS control

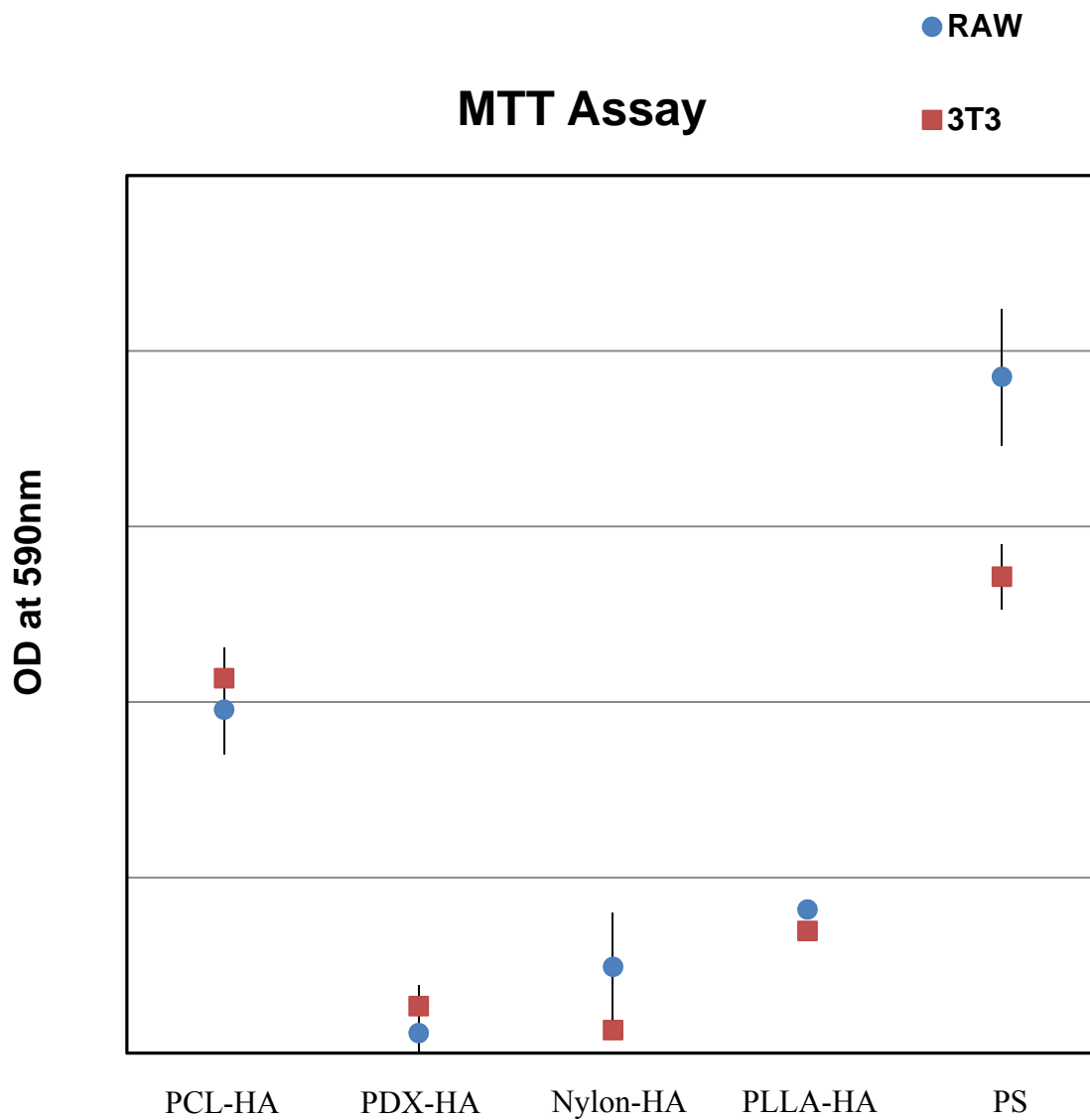


Figure 7.6. MTT assay results for various polymer-HA composites and a PS control





Figure 7.7. Rat femur that has been extracted and polymerized with PLLA

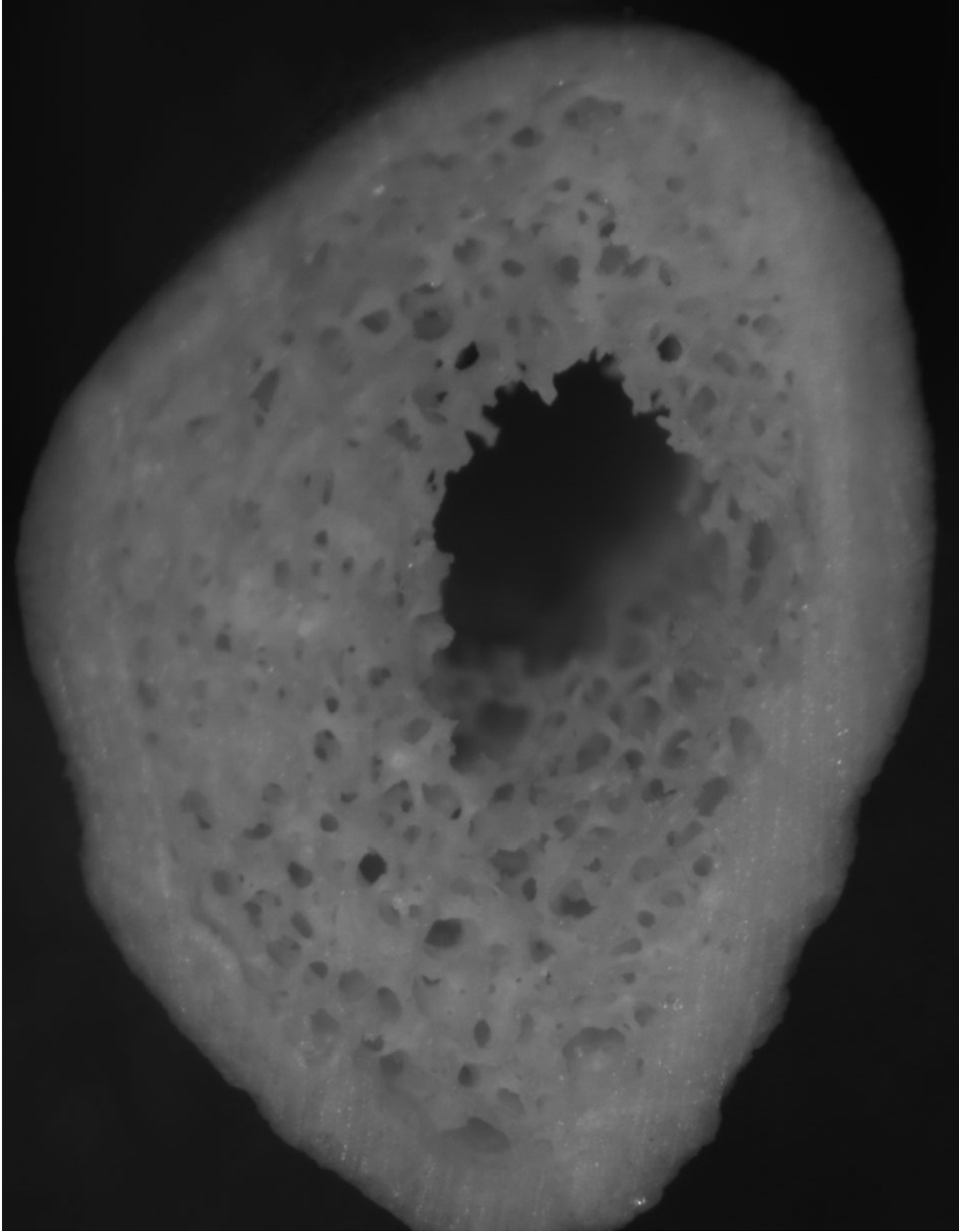


Figure 7.8. End-on image of a rat femur that has been extracted and polymerized with PLLA showing the conserved trabecular bone structures

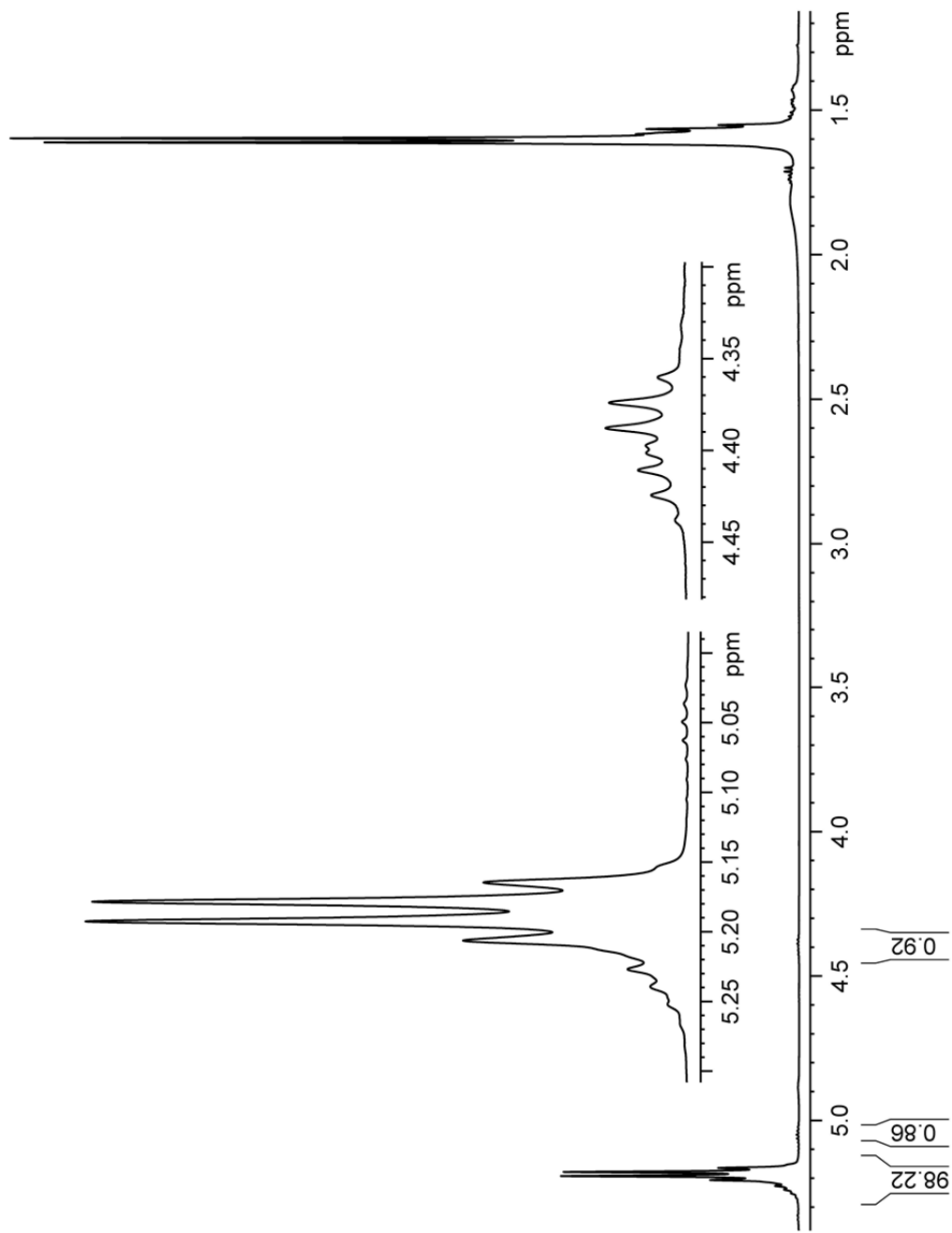


Figure 7.9.  $^1\text{H}$  NMR spectrum for the polymerized rat femur showing less than 1% monomer remains



Figure 7.10. Rat skull that has been extracted and polymerized with PLLA

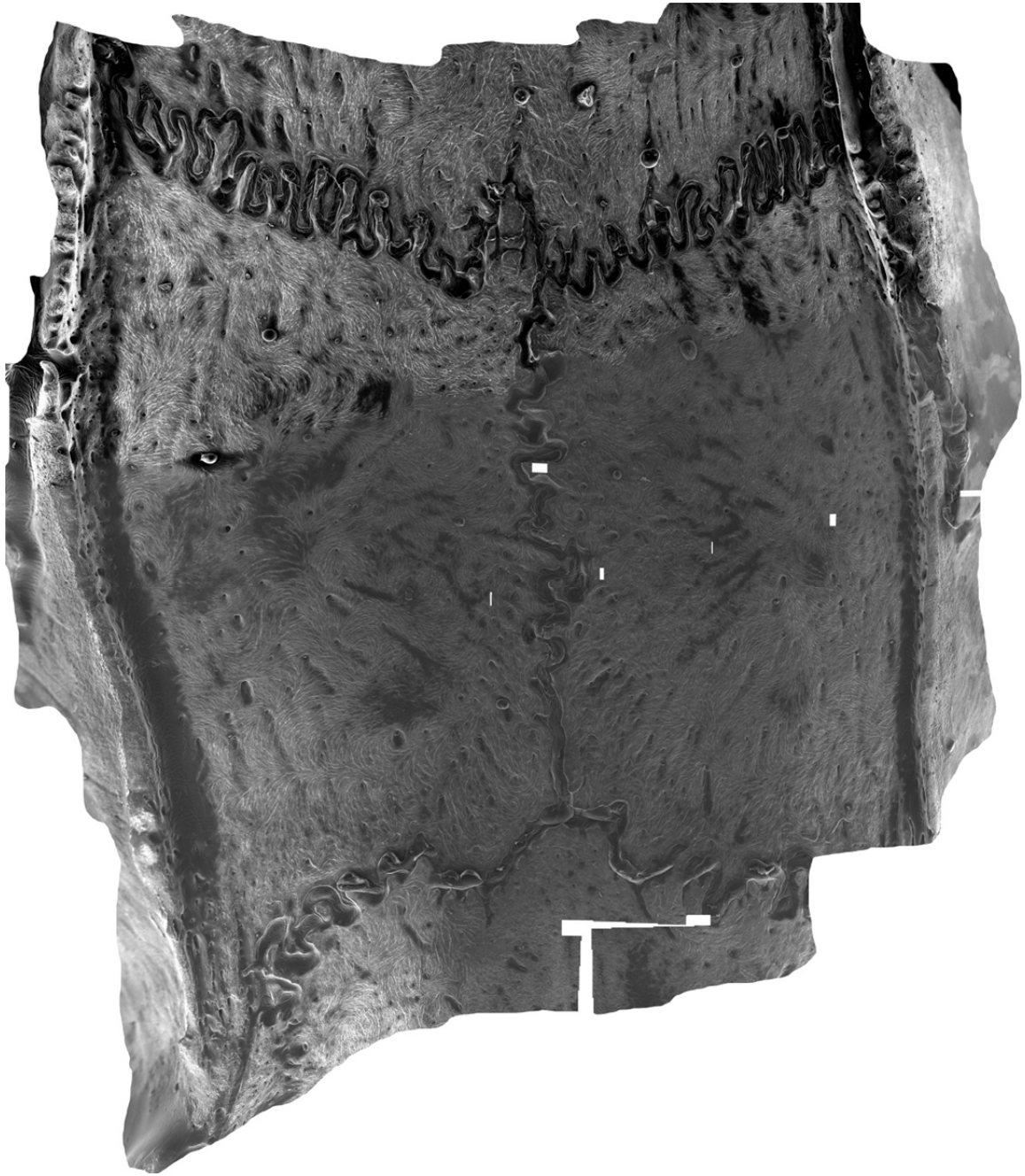


Figure 7.11. Composite SEM image of the polymerized rat skull, note the retention of surface morphology in the bone structure

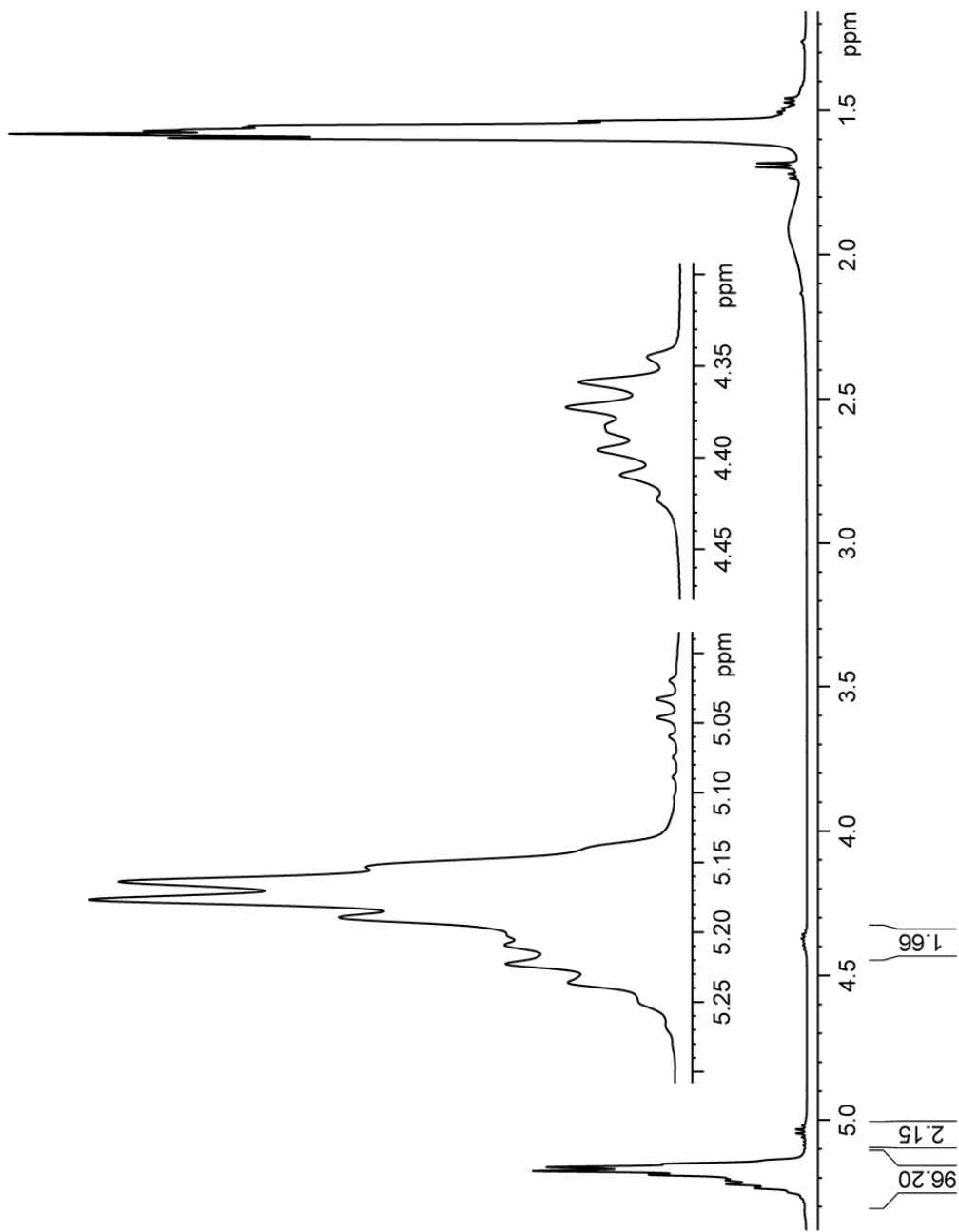


Figure 7.12.  $^1\text{H}$  NMR spectrum for the polymerized rat skull showing approximately 2% monomer remains

polymerizing a rat femur could easily be scaled up to use larger mammalian bones with dimensions similar to human bone. These could then be used to repair segmental defects in the limbs. The same procedures could also be applied to smaller bones such as the metacarpals or phalanges, where one might speculate that the entire bone could be replaced.

Finally, the culmination of my thesis research in constructing these prototype devices lends credence to the exciting possibility that traumatic injuries of the face and skull can be repaired using this technology to reconstitute cranial-facial bones from donors. Since the processes described in this thesis render the bone immunologically mundane, the need for donor screening could be greatly reduced, or possibly eliminated. The most common current therapy involves attempts to rebuild the shattered facial bones by implanting metal wires that hold remaining fragments, if they exist, in place.<sup>8,9</sup> These wires are not removed and remain in the patient. Use of resorbable PLLA-HA composites such as the ones described in my thesis could eliminate the need for the wire reinforcements, and provide an important new alternative for repairing highly fragmented trauma or large defects in complex craniofacial and maxillofacial structures in military and civilian segments of our society.

The preferred material formulations from which a device may be constructed are presently uncertain. Common resorbable polymers offer a combination of attractions and draw backs. PLLA and PGA are used frequently in orthopaedic devices. By far, PLLA is the most commonly used synthetic resorbable polymer. It is approved by the FDA for use in a variety of applications; it is relatively inexpensive but suffers from long

resorption times. A recent study using PLLA implants in the rabbit model showed that PLLA remained even after 69 months *in vivo*.<sup>10</sup> PGA can resorb at rates up to an order of magnitude greater than PLLA, but the monomer is much more costly, and the polymer is intractable in common solvents, making it difficult to process. PCL exhibits resorption properties that are more attractive than PLLA, with resorption times of roughly two years, but its physical properties (specifically compressive strength and tensile strength) make it undesirable for some load bearing applications implants.<sup>11</sup> Polydioxanone is currently used in resorbable sutures because of its quick resorption rate but recent studies involving rats show that prolonged exposure to the monomer, as would happen during implant degradation, adversely affects the kidneys and brain.<sup>12</sup> Polycaprolactam does exhibit superior physical properties, but its resorption times are deleteriously long due to its polyamide nature. Amides are far less susceptible to hydrolysis than the analogous esters.

No matter what the preferred materials for various applications prove to be, additional *in vitro* cell testing will be needed to screen possible candidates. Initial studies will be done without the purposeful addition of adjuvants such as TGF $\beta$  and growth factors such as BMP-2, which are known to induce differentiation of osteoprogenitor cells to osteoblasts through a complex sequence of coupled events that are believed to involve biomechanical feedback loops that are not well understood. It should also be noted that there are a variety of means by which cell adhesion and proliferation might be improved on my materials. For example, Yang, et al. recently provided some compelling examples in which RGD peptides and fibronectin modifications of PLLA films "...to promote human osteoprogenitor adhesion, spreading, growth, and differentiation."<sup>13</sup> At the time of this



writing, two other graduate students and a postdoc in my present research group are engaging in collaborative efforts to measure osteoclast and osteoblast cell activity. Thin sections of polymerized bone will be cultured with bone marrow-derived stem cells using conditions designed to enhance osteoclastogenesis. Osteoclasts will be examined for cell activation status, and the composites will be examined for degradation using image analysis of culture microphotographs, histological evaluation using trichrome staining, and assays of bone and polymer breakdown products, including calcium release into the tissue culture medium. All of this work will be performed in collaboration with Professor Paul Wooley's group at Via Christi Hospital in Wichita, KS. Dr. Wooley is the Research Director of the Orthopaedic Research Institute, which is located at Via Christi.

Materials that appear to perform well in cell culture screenings will be subjected to additional biocompatibility assessments using the murine air pouch model developed by our collaborators.<sup>14</sup> These experiments will use a mouse osteolysis model. The model has the advantage of exposing biomaterials to a pre-existing inflammatory condition, resembling conditions that exist during normal wound healing, but, more pertinently, the inflammation consequential to severe trauma encountered in military injuries. In short, male BALB/c mice will be injection subcutaneously with 2.5 mL air to establish an air pouch. Six days later, a sterile saline solution will be introduced to fill the pouch, followed two days later by the composite of interest. Mice will be sacrificed 14 days after composite implantation, and the pouch fluid will be collected for evaluation. Histology and immunohistochemical evaluations using image analysis will determine the tissue inflammation status and implanted bone matrix morphology. Pathology analysis of the cell morphology and the relationship to the interface between inflammatory tissue and

implanted bone tissue will be conducted. Microcomputerized tomography (MicroCT) imaging analysis will be used to measure bone density, bone volume fraction, and bone structure of the implanted bones using Microview software provided by the manufacturer. The final step in this phase of the research will be to use the data from the biocompatibility screening studies, coupled with the mechanical characterizations described in this thesis, to select materials to repair and segmental bone defect introduced in the femur of a 200 – 250 g male Lewis rat. A section of bone from a donor rat will be processed using our preferred conditions and the resulting processed bone will be implanted into a defect in the recipient. The performance of the implant will be characterized through a variety of means including histological, immunohistological, and biomechanical assessments.

### References

1. Hatefi, Y., The mitochondrial electron transport and oxidative phosphorylation system. *Annual Review of Biochemistry* **1985**, 54, 1015-69.
2. Ziats, N. P.; Miller, K. M.; Anderson, J. M., In vitro and in vivo interactions of cells with biomaterials. *Biomaterials* **1988**, 9, 5-13.
3. Mosmann, T., Rapid colorimetric assay for cellular growth and survival: Application to proliferation and cytotoxicity assays. *Journal of Immunological Methods* **1983**, 65, (1-2), 55-63.
4. Chakrabarti, R.; Kundu, S.; Kumar, S., Vitamin A as an enzyme that catalyzes the reduction of MTT to formazan by vitamin c. *Journal of Cellular Biochemistry* **2000**, 80, (1), 133-138.
5. Griffiths, G. D.; Lindsay, C. D.; Upshall, D. G., Examination of the Toxicity of Several Protein Toxins of Plant Origin Using Bovine Pulmonary Endothelial Cells. *Toxicology* **1994**, 90, (1-2), 11-27.
6. Lacy, A.; O'Kennedy, R., Studies on coumarins and coumarin-related compounds to determine their therapeutic role in the treatment of cancer. *Curr Pharm Design* **2004**, 10, (30), 3797-3811.
7. Melo, A. R.; Lasunskaja, E. B.; de Almeida, C. M. C.; Schriefer, A.; Kipnis, T. L.; da Silva, W. D., Expression of the virulence factor, BfpA, by enteropathogenic *Escherichia coli* is essential for apoptosis signalling but not for NF-kappa B activation in host cells. *Scand J Immunol* **2005**, 61, (6), 511-519.
8. Ellis, E.; Zide, M. F., *Surgical Approaches to the Facial Skeleton*. 2nd ed.; Lippincott Williams and Wilkins: 2005.

9. Haerle, F.; Champy, M.; Terry, W., *Atlas of Craniomaxillofacial Osteosynthesis: Microplates, Miniplates, and Screws*. 2nd ed.; Thieme: 2009.
10. Matsusue, Y.; Hanafusa, S.; Yamamuro, T.; Shikinami, Y.; Ikada, Y., Tissue reaction of bioabsorbable ultra high strength poly (L-lactide) rod. A long-term study in rabbits. *Clinical Orthopaedics and Related Research* **1995**, 246-53.
11. Middleton, J. C.; Tipton, A. J., Synthetic biodegradable polymers as orthopedic devices. *Biomaterials* **2000**, 21, (8), 2335-2346.
12. Kano, H. U., Y.; Saito, M.; Senoh, H.; Ohbayashi, H.; Aiso, S.; Yamazaki, K.; Nagano, K.; Fukushima, S. , Thirteen-week oral toxicity of 1,4-dioxanone in rats and mice *Journal of Toxicological Sciences* **2008**, 33, (2), 141-153.
13. Yang, X. B.; Roach, H. I.; Clarke, N. M. P.; Howdle, S. M.; Quirk, R.; Shakesheff, K. M.; Oreffo, R. O. C., Human osteoprogenitor growth and differentiation on synthetic biodegradable structures after surface modification. *Bone* **2001**, 29, (6), 523-531.
14. Ottaviani, R. A.; Wooley, P. H.; Song, Z.; Markel, D. C., Inflammatory and immunological responses to hyaluronan preparations using a murine biocompatibility model. *Journal of Bone and Joint Surgery-American Volume* **2007**, 89, 148.